UNIVERSIDADE DE LISBOA

FACULDADE DE CIÊNCIAS

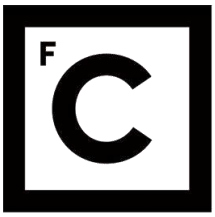

Ciências
ULisboa

The use of remotely sensed Land Surface Temperature for climate monitoring

Doutoramento em Ciências Geofísicas e da Geoinformação
Especialidade de Deteção Remota

Virgílio Alexandre da Silva Marques Bento

Tese orientada por:
Professor Doutor Carlos da Camara
Doutora Isabel Trigo

Documento especialmente elaborado para a obtenção do grau de doutor

2018

UNIVERSIDADE DE LISBOA

FACULDADE DE CIÊNCIAS

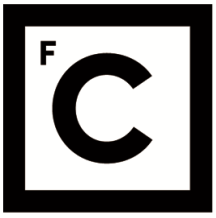

Ciências
ULisboa

The use of remotely sensed Land Surface Temperature for climate monitoring

Doutoramento em Ciências Geofísicas e da Geoinformação
Especialidade de Deteção Remota

Virgílio Alexandre da Silva Marques Bento

Tese orientada por:
Professor Doutor Carlos da Camara
Doutora Isabel Trigo

Júri:
Presidente:

- Doutor João Manuel de Almeida Serra, Professor Catedrático
  Faculdade de Ciências da Universidade de Lisboa.

Vogais:

- Doutora Renata Libonati dos Santos, Professora Adjunto I
  Departamento de Meteorologia da Universidade Federal do Rio de Janeiro (Brasil);
- Doutor Mário Jorge Modesto Gonzalez Pereira, Professor Auxiliar
  Escola de Ciências e Tecnologia da Universidade de Trás-os-Montes e Alto Douro;
- Doutora Isabel Alexandra Martinho Franco Trigo, Investigadora Principal
  Instituto Português do Mar e da Atmosfera (Orientadora);
- Doutor Carlos Alberto Leitão Pires, Professor Auxiliar
  Faculdade de Ciências da Universidade de Lisboa;
- Doutora Célia Marina Pedroso Gouveia, Professora Auxiliar Convidada
  Faculdade de Ciências da Universidade de Lisboa.

Documento especialmente elaborado para a obtenção do grau de doutor

Fundação para a Ciência e Tecnologia, SFRH/BD/52559/2014

2018

Acknowledgments

I want to start by thanking my advisers, Professor Carlos da Camara and Doctor Isabel Trigo, for their scientific guidance and support, and for the opportunity to work with them. To Professor Carlos da Camara, I want to leave a special thank you for the unconditional belief in my aptitudes, for his always welcome ideas and his unstoppable humour, which lightened the day in many occasions. I also want to leave a special thank you to Doctor Isabel Trigo for the extremely helpful guidance and speedy responses and comments to my questions and work, for the pragmatic and down to earth perspective, which helped me to define a common thread for this thesis, and for the patience shown in the moments I went "off track".

I also want to thank Doctor Anke Duguay-Tetzlaff at Meteoswiss and Doctor Célia Gouveia at IPMA for their help and insight on two different stages of this thesis. Finally, I want to thank Doctor João Martins, who helped me grow as a scientist both with his arguing efforts (first in the MSc thesis and then in the yearly presentations I had to do in the scope of this PhD) and with his suggestions during these last 4 years.

Last, but not least, I want to thank the unconditional (and sometimes conditional) support, the adventures, the gastronomical experiences and the philosophical and pertinent discussions I had with my esteemed colleagues and friends Maria and Diogo.

To my parents, who have always supported my decisions and were always there when I needed them, and to Daniela, who willingly decided to put up with me, I leave a very special thank you because without you three this thesis wouldn't be a reality.

This work was supported by FCT under the grant SFRH/BD/52559/2014.

Abstract

Satellite remote sensing of the Earth has been continuously performed from different satellite platforms/constellations since the 1960s. The amount of radiometric information available in organisations like the European Organisation for the Exploitation of Meteorological Satellites (EUMETSAT) may be compiled in Fundamental Climate Data Records (FCDRs), allowing the retrieval of climate records of geophysical variables, such as Land Surface Temperature (LST). Climate Data Records (CDRs) may then be used in a wide range of applications – such as drought monitoring or climate change studies, among others.

Nevertheless, instruments onboard satellites of the same series, spanning decades of observations, may have different characteristics, which imposes a difficulty in the retrieval of LST. One of the most notable examples is the electromagnetic channels at which the earth is observed by these instruments. EUMETSAT Meteosat First Generation (MFG) – first launched in 1977 and last launched in 1997 – was designed to carry an instrument with only one channel in the thermal infrared region of the electromagnetic spectrum. On the other hand, Meteosat Second Generation (MSG) satellites – first launched in 2004 and currently still in operation – were designed to cover two thermal infrared channels. Since retrievals of LST are based on information from that window of the electromagnetic spectrum, and retrieval algorithms are usually based on a split-windows (two adjacent thermal infrared windows) methodology – typically the Generalised Split Windows (GSW) – a different approach must be taken to homogenise the retrievals over a long period of time, with the aim of compiling an LST CDR.

In this context, this thesis aims at developing single-channel/mono-window algorithms that can be used with information from MFG and MSG constellations of satellites. Two algorithms were developed – the Statistical Mono-Window (SMW) and the Physical Mono-Window (PMW) – and consequently two climate data records were compiled in partnership with the Satellite Application Facility on Climate Monitoring (CM SAF) and Land Surface Analysis (LSA SAF). These CDRs are now available to download at the CM SAF website.

The mentioned retrieval algorithms are sensitive to the amount of water vapor present on the atmosphere and use information from ECMWF ERA-Interim fields. However, its relatively coarse spatial resolution may lead to systematic errors in the humidity profiles with implications in LST, particularly over mountainous areas. This limitation was studied, and its implications discussed in this thesis with focus on the improvement of the LST retrievals over these high-altitude regions. Also, a discussion is provided focusing on the best process for the calibration of regression coefficients that constitute SMW and GSW.

Another objective of this thesis is to use an LST CDR for an application focused on drought monitoring. The Vegetation Health Index (VHI) has been widely used for monitoring and characterising droughts. This index takes into account ecosystem features in terms of fluctuations between prescribed maxima and minima of NDVI (Vegetation Condition Index, VCI) and of Land Surface Temperature (LST; Thermal Condition Index, TCI), and is estimated as the weighted sum of these two contributions. Since there is no a priori knowledge about vegetation and temperature contributions, VHI is typically taken as the average of both contributions, i.e., a weight of 0.5 is assumed. It is shown that by maximising the correlations between VHI and the multiscalar drought indicator SPEI (Standardized Precipitation-Evapotranspiration Index) it is possible to evaluate the relative roles of VCI and TCI for different climate regions. This application is developed over a Euro-Mediterranean region and then further applied on a global scale and over the Meteosat disk, using the LST CDR previously developed.

In summary, this thesis is focused on the development, improvement and application of LST climate data records.

Keywords: Climate Data Record, EUMETSAT, Land Surface Temperature, Remote Sensing, Vegetation Health Index.

Resumo

A utilização de Deteção Remota através de satélites que orbitam a Terra com o objetivo de estimar a temperatura da superfície do solo (aqui abreviada utilizando o acrónimo inglês LST proveniente de "Land Surface Temperature") é uma técnica cuja origem remonta às décadas de 1960/70. Foi por esta altura que satélites meteorológicos, com o intuito de estudar a atmosfera e a superfície da Terra, começaram a ser desenvolvidos por organizações como a EUMETSAT, a ESA, a NASA ou a NOAA. Ao longo dos anos foram lançados diversas séries de satélites, nomeadamente as séries Meteosat da EUMETSAT (atualmente lançados 11 satélites), GOES da NOAA (lançados 16 satélites) ou os satélites japoneses Himawari (lançados 9). Estes satélites podem apresentar dois tipos de órbitas distintas: órbita geostacionária e órbita polar. A primeira é uma órbita circular definida sobre o equador e que segue a direção da rotação da Terra, ao passo que uma órbita polar (ou neste caso específico uma órbita polar aproximada ou órbita sincronizada com o sol) se distingue por se realizar a altitudes mais baixas, observando um determinado ponto da superfície da Terra aproximadamente à mesma hora local. Exemplos de satélites meteorológicos com órbita geostacionária são os operados pela EUMETSAT "Meteosat First and Second Generation" (MFG e MSG), cuja relevância para esta tese é central.

Uma mais valia de já existirem décadas de informação de satélite é a possibilidade de se poder começar a desenvolver aplicações climatológicas baseadas em variáveis como a LST. No entanto, é importante referir que apesar de existirem séries de satélites operados continuamente ao longo do tempo, com o evoluir do tempo evoluem também os sensores que esses satélites transportam a bordo. A LST é recuperada utilizando sensores capazes de "ver" em janelas correspondentes ao infravermelho térmico – tipicamente correspondente ao intervalo entre os 8 e 15 μm no espectro electromagnético – sendo que um dos algoritmos mais utilizados para esse efeito é o denominado "Generalised Split-Windows" (GSW). Este algoritmo utiliza duas janelas adjacentes na região do infravermelho térmico para estimar a LST. Ora, de forma a produzir-se uma base de dados climatológica de LST é necessário utilizar sensores equipados em várias gerações de satélites. No caso dos anteriormente mencionados MFG e MSG, a

utilização do GSW para recuperar LST não é possível. Isto deve-se ao facto do sensor a bordo do MFG (o MVIRI) estar limitado à utilização de um canal no infravermelho térmico. De salientar que apesar do sensor a bordo do MSG (o SEVIRI) ser capaz de ver em dois canais diferentes, é importante que uma base de dados climatológica seja consistente e homogénea ao longo do tempo.

Neste contexto, o primeiro objetivo desta tese é focado no desenvolvimento de algoritmos de recuperação de LST capazes de ser aplicados a satélites/instrumentos equipados para ver apenas num canal da região do espectro caracterizada anteriormente, de forma a ser possível produzir uma base de dados climatológica homogénea. Este objetivo foi cumprido em cooperação com a LSA SAF e a CM SAF, e a base de dados climatológica de LST encontra-se disponível ao público através do site da CM SAF. Foram desenvolvidos e estudados dois algoritmos: o mono-canal estatístico e mono-canal físico. O primeiro é baseado numa relação empírica que relaciona a LST com a temperatura de brilho no topo da atmosfera, enquanto a segunda consiste numa inversão da equação de transferência radiativa em ordem à LST. O desempenho dos dois algoritmos mono-canal foi avaliado comparando com o algoritmo mais comum GSW, e os três foram verificados utilizando mais de 60,000 observações de LST à superfície, em locais caracterizados por atmosferas tanto húmidas como secas. Os resultados mostram que, com exceção das atmosferas mais húmidas (água precipitável total superior a 45 mm), a LST recuperada com algoritmos mono-canal compara-se bem com a mesma variável recuperada usando o GSW (diferenças de 0.1 a 0.5 K).

Bases de dados climatológicas de LST são de extrema importância para diversos estudos. Como tal é necessário entender quais as suas maiores vulnerabilidades, procurar mitigá-las a fim de melhorar a qualidade da informação. Neste sentido, e tendo em conta a importância que os estudos de alterações climáticas em zonas de elevada altitude têm tido nos últimos anos, é importante perceber se a LST recuperada é fidedigna em regiões montanhosas. Verifica-se que os algoritmos dependentes de informação de vapor de água, podem apresentar erros sistemáticos devido à fraca resolução da reanálise usada (ERA-Interim). Com o objetivo de corrigir as estimativas de vapor de água, foram desenvolvidos dois métodos: uma parametrização exponencial do integral da água precipitável (apropriado para algoritmos dependentes de regressões lineares – GSW e SMW); e

um método de redução do nível (apropriado para algoritmos que utilizem o perfil de vapor de água em vez do seu integral – PMW). Os resultados mostram que, para uma região teste nos Alpes, os algoritmos originais falharam a classe do integral de água precipitável em cerca de 87% dos casos. Utilizando o método da parametrização exponencial esse número foi reduzido para cerca de 9%. No caso em que se usa o método da redução de nível, as LST apresentam uma correção que pode ir até 1.7 K. Em geral, estas correções no vapor de água devido à orografia levam a correções na LST que são relevantes para garantir que a base de dados climatológica de LST apresenta valores adequados para os requerimentos climáticos.

Noutro ponto referente ao melhoramento de algoritmos, procedeu-se a um estudo sobre a melhor forma de se calibrar os modelos estatísticos (aqui representados pelo GSW e SMW). Como referido anteriormente, este tipo de métodos assenta numa relação linear entre a temperatura de brilho no topo da atmosfera e a LST. Os coeficientes empíricos que constituem estes algoritmos são estimados com o apoio de bases de dados próprias para o seu desenvolvimento, onde se usam grandes quantidades de perfis atmosféricos para calibrar os modelos para o maio número de condições. A escolha destas bases de dados é, portanto, fulcral para o bom funcionamento dos algoritmos. Aqui foram analisadas várias estratégias de calibração, considerando bases de dados construídas com diferentes perfis atmosféricos. Foi depois feita uma análise de sensibilidade utilizando uma base de dados de validação para perceber qual a melhor estratégia de calibração.

Finalmente, bases de dados climatológicas de LST foram aplicadas ao estudo de secas. Um dos índices de seca, baseado em dados de Deteção Remota, mais usado é o índice da saúde da vegetação ("Vegetation Health Index", VHI). Este é formulado com um termo tipicamente dependente da temperatura de brilho no topo da atmosfera ou da LST ("Temperature Condition Index", TCI) e com um outro termo dependente do "Normalised Difference Vegetation Index" NDVI. O VHI é estimado através da soma pesada desses dois termos, sendo que normalmente não existe conhecimento prévio sobre o peso de cada um, utilizando-se, por isso, um peso igual para as duas componentes (0.5). Ora, com a utilização de bases de dados climatológicas de LST e NDVI é avaliada a importância relativa de cada um dos termos, através da comparação com o índice de precipitação e evapotranspiração

estandardizado ("Standardized Precipitation Evapotranspiration Index", SPEI). Os resultados mostram que dependendo do local estudado, os dois termos do VHI não se comportam de igual forma. Nalguns locais o VCI é mais importante ao passo que noutros é o TCI. Finalmente, procedeu-se à maximização das correlações entre o VHI e o SPEI e verificou-se que através desta metodologia, se podem avaliar as contribuições relativas dos termos de VCI e TCI para o VHI aplicado em diferentes regiões climatológicas. Procedeu-se então ao desenvolvimento de um mapa global de contribuições relativas de VCI e TCI. Neste caso, um método de análise de correlações canónicas também foi usado para estimar as contribuições relativas. Os seus benefícios e limitações são discutidos. Finalmente, a mesma metodologia foi aplicada utilizando para o cálculo do TCI a base de dados climatológica de LST desenvolvida no âmbito desta tese, e as contribuições foram estimadas para o disco do Meteosat.

Resumindo, nesta tese são desenvolvidos dois algoritmos de recuperação de LST através de satélite, com a particularidade de poderem ser adotados por instrumentos com apenas um canal no infravermelho térmico – os algoritmos mono-canal estatístico e físico. Consequentemente, e em parceria com a LSA SAF e CM SAF, foram desenvolvidas duas bases de dados climatológicas de LST (que atualmente podem ser descarregadas no site da CM SAF). Depois do desenvolvimento dos algoritmos, é introduzida uma forma de melhoramento destes sobre regiões montanhosas, e é também estudada a forma como algoritmos baseados em regressões estatísticas são calibrados. Finalmente, depois do desenvolvimento e melhoramento, uma base de dados climatológica de LST é aplicada com o objetivo de perceber a melhor forma de monitorizar secas utilizando índices baseados em informação de Deteção Remota.

Palavras Chave: Bases de Dados Climatológicas, Deteção Remota, EUMETSAT, Índice da Saúde da Vegetação; Temperatura da Superfície do Solo.

Contents

Acknowledgments ..... **i**

Abstract ..... **iii**

Resumo ..... **v**

List of Acronyms and Abbreviations ..... **xiii**

List of Symbols ..... **xix**

List of Figures ..... **xxiii**

List of Tables ..... **xxvii**

Chapter 1 ..... **1**

1. Thesis Framework **1**

1.1. Motivation 1

1.2. Objectives 3

1.3. Layout 3

1.4. Remarks 4

Chapter 2 ..... **7**

2. Theoretical Introduction **7**

2.1. From Remote Sensing to Land Surface Temperature 7

2.2. Land Surface Temperature retrieval algorithms 15

2.2.1. A general review 15

2.2.2. Single-Channel and Split-Windows Algorithms 17

2.3. LST as a climate asset 19

2.3.1. LST as an Essential Climate Variable 19

2.3.2. Drought monitoring 21
Chapter 3 25
3. Development of Land Surface Temperature Climate Data Record 25
3.1. Introduction 26
3.2. Data and Mehods 28
3.2.1. Satellite Data 28
3.2.2. Generalized Split-Windows 29
3.2.3. Physical Mono-Window 30
3.2.4. Statistical Mono-Window 32
3.2.5. Theoretical Uncertainty Characterisation 34
3.2.6. Ground-Based LST Measurements 36
3.3. Results and Discussion 38
3.3.1. The Impact of the Calibration Database on Statistical Models 38
3.3.2. Theoretical Uncertainty Analysis 40
3.3.3. Ground-Based Validation 42
3.4. Conclusions 45
Chapter 4 47
4. Improvement of LST retrieval algorithms over mountainous regions ... 47
4.1. Introduction 48
4.2. Data and Methods 50
4.2.1. Data 50
4.2.1.1. Study Area 50
4.2.1.2. Satellite Data 50
4.2.1.3. Model Data 51
4.2.1.4. LST Retrieval Algorithms 53
4.2.1.5. Orographic Correction of Atmosphere Profiles 55
4.3. Results 57
4.3.1. Differences between ERA-Int and COSMO TPW 57
4.3.2. Sensitivity Analysis 58
4.4. Discussion 60
4.5. Conclusions 63

Chapter 5 65

5. Assessing drought using Remote Sensing data: Understanding the combined use of thermal (LST) and visible (NDVI) observations 65

5.1. Introduction 66

5.2. Development of the methodology over a Mediterranean region 69

5.2.1. Data 69

5.2.1.1. Study Area 69

5.2.1.2. NDVI and LST 69

5.2.1.3. SPEI 71

5.2.2. Methods 71

5.2.3. Results and Discussion 73

5.2.3.1. Month of maximum NDVI 73

5.2.3.2. Correlations between VHI and SPEI 76

5.2.3.3. The relative importance of VCI and TCI 78

5.3. A global application 84

5.3.1. Data and Methods 84

5.3.2. Results and Discussion 87

5.3.2.1. Iterative maximisation of the VHI-SPEI correlation 87

5.3.2.2. Canonical Correlation Analysis 89

5.4. Using Meteosat LST CDR 93

5.5. Conclusions 96

Chapter 6 99

6. Overall Conclusions and Final Remarks 99

Bibliography 105

Annexes 121

List of Acronyms and Abbreviations

AATSR	Advanced Along-Track Scanning Radiometer
AHI	Advanced Himawari Imager
AIRS	Atmospheric Infrared Sounder
ASTER	Advanced Spaceborne Thermal Emission and Reflection Radiometer
ATBD	Algorithm Theoretical Basis Document
ATI	Apparent Thermal Inertia
ATSR	Along-Track Scanning Radiometer
AVHRR	Advanced Very High-Resolution Radiometer
CDR	Climate Data Record
CFSR	Climate Forecast System Reanalysis
CGIAR	Consultative Group for International Agriculture Research
CM-SAF	Satellite Application Facility on Climate Monitoring
CMIP	Coupled Model Intercomparison Project
COSMO	Consortium for Small-Scale Modelling
CRU	Climate Research Unit
CSI	Consortium for Spatial Information (GCIAR-CSI)
CWSI	Crop Water Stress Index
DJF	December – January – February
ECMWF	European Centre for Medium-Range Weather Forecasts
ECV	Essential Climate Variable
EDW	Elevation Dependent Warming
ENSO	El-Niño Southern Oscillation

ERA-Int	ECMWF Interim Reanalysis
ERS	European Remote Sensing Satellite
ESA	European Space Agency (former ESRO)
ESI	Evaporative Stress Index
ESRO	European Space Research Organisation (now ESA)
EUMETSAT	European Organization for the Exploitation of Meteorological Satellites
FCI	Flexible Combined Imager
FVC	Fraction of Vegetation Cover
GCOS	Global Climate Observing System
GEO	Geostationary Earth Orbit
GIMMS	Global Inventory Modelling and Mapping Studies
GMS	Geostationary Meteorological Satellite “Himawari”
GOES	Geostationary Operational Environment Satellite
GSW	Generalised Split-Windows
HIRS	High-Resolution Infrared Radiation Sounder
IASI	Infrared Atmospheric Sounding Interferometer
IGBP	International Geosphere-Biosphere Programme
IP	Iberian Peninsula
IPCC	Intergovernmental Panel for Climate Change
IR	InfraRed
ISCCP	International Satellite Cloud Climatology Project
JJA	June – July – August
KIT	Karlsruhe Institute of Technology
LEO	Low Earth Orbit

LSA-SAF	Land Surface Analysis Satellite Applications Facility
LSE	Land Surface Emissivity
LST	Land Surface Temperature
LUT	Look-Up Table
LWIR	Long-Wave Infrared
MAM	March – April – May
MFG	Meteosat First Generation
MODIS	Moderate Resolution Imaging Spectroradiometer
MODTRAN	Moderate Resolution Atmospheric Transmission
MSG	Meteosat Second Generation
MTG	Meteosat Third Generation
MTSAT	Multi-Functional Transport Satellite “Himawari”
MVIRI	Meteosat Visible and InfraRed Imager
MW	Mono-Window
MWIR	Medium Wavelength Infrared
NASA	National Aeronautics and Space Administration
NCEP	National Centres for Environmental Prediction
NDTI	Normalised Difference Temperature Index
NDVI	Normalized Difference Vegetation Index
NIR	Near Infrared
NOAA	National Oceanic and Atmospheric Administration
NWC-SAF	Nowcasting and Very Short-Range Forecasting Satellite Application Facility
NWP	Numerical Weather Prediction
PATMOS-x	Pathfinder Atmospheres-Extended dataset

PDSI	Palmer Drought Severity Index
PET	Potential Evapotranspiration
PMW	Physical Mono-Window
POES	Polar Operational Environmental Satellites
PUM	Product User Manual
RED	Red colour in the visible part of the electromagnetic spectrum
RMSD	Root Mean Square Deviations
RMSE	Root Mean Square Error
RMZ	Rust Mijn Ziel (region in Namibia, Kalahari bush)
RTE	Radiative Transfer Equation
RTM	Radiative Transfer Model
RTTOV	Radiative Transfer for TOVS
SEVIRI	Spinning Enhanced Visible and InfraRed Imager
SLSTR	Sea and Land Surface Temperature Radiometer
SMW	Statistical Mono-Window
SON	September – October – November
SPEI	Standardized Precipitation Evapotranspiration Index
SPI	Standardized Precipitation Index
SST	Sea Surface Temperature
SURFRAD	Surface Radiation Budget Network
SWIR	Short-Wave Infrared
TCI	Temperature Condition Index
TIR	Thermal InfraRed
TIROS	Television InfraRed Observation Satellite Program

TIRS	Thermal Infrared Sensor
TOA	Top of Atmosphere
TOVS	TIROS Operational Vertical Sounder
TCWV	Total Column Water Vapor
TM	Thermal Mapper
TPW	Total Precipitable Water
TVDI	Temperature Vegetation Dryness Index
UN	United Nations
UNESCO	United Nations Educational, Scientific and Cultural Organization
USA	United States of America
USGS	United States Geological Survey
UV	Ultraviolet
VCI	Vegetation Condition Index
VHI	Vegetation Health Index
VNIR	Visible and Near Infrared
VSWI	Vegetation Supply Water Index
VZA	Viewing Zenith Angle
WDI	Water Deficit Index
WMO	World Meteorological Organisation

List of Symbols

a_k $(k = 1,2)$	Statistical Mono-Window (SMW) coefficients
b_k $(k = 0, \dots, 6)$	Generalised Split-Windows (GSW) coefficients
B	Planck function
c	Speed of Light ($\sim 3.00 \times 10^8\ m/s$)
c_1	Constant ($1.19104 \times 10^{-5}\ mW(cm^{-1})^{-4}m^{-2}sr^{-1}$)
c_2	Constant ($1.43877\ Kcm$)
h	Planck constant ($6.63 \times 10^{-34}\ J.s$)
H_0	ERA-Int altitude field
H_1	COSMO altitude field
i, j	Given sensor channel (window) of the electromagnetic spectrum
k_b	Boltzmann constant ($1.38 \times 10^{-23}\ J/K$)
LST	Land Surface Temperature
L	Radiance measured by a sensor onboard a satellite
L^s	Direct solar radiance reflected by the surface that reaches the sensor
L_d^a	Radiance emitted by the atmosphere directed to the surface that reflects upwards and reaches the sensor
L_d^s	Solar radiance scattered by the atmosphere that is directed downwards to the surface and reaches the sensor
L_u^a	Thermal radiance emitted upwards by the atmosphere and reaches the sensor
L_u^s	Solar radiance scattered upwards by the atmosphere
$NDVI$	Normalised Difference Vegetation Index
NIR	Near Infrared

r	Bi-directional reflectivity
RED	Red colour in the visible part of the electromagnetic spectrum
$\overline{T_a}$	Mean temperature of the atmospheric column
T_b	Brightness temperature measure by a sensor onboard a satellite
T_k	Temperature of the atmosphere layer
T_*	Arbitrary temperature near $\overline{T_a}$, T_b and LST
TPW_0	Reference Total Precipitable Water
TPW_1	Estimated Total Precipitable Water
VCI	Vegetation Condition Index
TCI	Temperature Condition Index
VHI	Vegetation Health Index
α	Weight used to estimate VHI associated with VCI
β	Weight used to estimate VHI associated with TCI
γ	Parameter depend on the spectral characteristics of the channel
δ	Scale parameter
ε	Pixel integrated emissivity (surface emissivity)
ε_m	Mean emissivity of channels 10.8 and 12 μm
$\Delta\varepsilon$	Difference of emissivities from channels 10.8 and 12 μm
η	Parameter depend on the spectral characteristics of the channel
θ	Satellite Viewing Zenith Angle (VZA)
θ_s	Solar Zenith Angle
λ	Wavelength
ν	Frequency
ρ	Spectral reflectivity

τ	Transmissivity
ϕ	Satellite Azimuthal Angle
ϕ_s	Solar Azimuthal Angle

List of Figures

Figure 2.1 – A schematic view of wavelength and energy carried by electromagnetic radiation (adapted from Essentials of Meteorology: An Invitation on the Atmosphere by C. Donald Ahrens). 11

Figure 2.2 – Portion of the transmission Spectrum (adapted from Remote Sensing: The Image Chain Approach by John R. Schott). 12

Figure 2.3 – Relationship between terms in the radiative transfer equation and energy paths associated with photon flux onto the sensor. 14

Figure 2.4 – List of LST retrieval algorithms with known and unknown surface emissivity (Li et al. 2013). 15

Figure 2.5 – Schematic of the GSW calibration 19

Figure 3.1 – Locations of the Karlsruhe Institute of Technology's (KIT) validation stations on the Meteosat Second Generation (MSG)/Spinning Enhanced Visible and Infrared Imager (SEVIRI) disk. 36

Figure 3.2 – Distribution of (a) TCWV and (b) skin temperature on the SeeBor dataset; (c) bivariate distribution of the previous parameters. 39

Figure 3.3 – Distribution of (a) TCWV and (b) skin temperature on the calibration dataset; (c) bivariate distribution of the previous parameters. 40

Figure 3.4 – Theoretical uncertainty for MSG/SEVIRI LST estimates. (a) Physical radiative transfer-based mono-window model (PMW); (b) statistical mono-window model (SMW). The values are the root mean square differences, assuming model and input uncertainties. VZA, satellite viewing angle. 41

Figure 3.5 – Comparison of LST between in situ measurements from the KIT sites and Meteosat-based retrievals for different TCWV classes. The boxplots show the median, the first and third quartile with whiskers at the 95th and fifth

percentiles. GSW: the Satellite Application Facility on Land Surface Analysis's (LSA SAF) operational GSW. (a) KIT Gobabeb station; (b) KIT Evora station; (c) KIT Dahra station; (d) KIT RMZ station. 43

Figure 4.1 – COSMO-2 orography field for the studied area. 51

Figure 4.2 – Histogram of orographic differences between Era-Int and COSMO for the studied area. 52

Figure 4.3 – Map of orographic differences between Era-Int and COSMO for the studied area. 53

Figure 4.4 – Scatterplot of the ratio of COSMO TPW with respect to its surrounding neighbours, $TPWi$, versus differences in height ΔH (grey dots). The black curve represents an exponential fit to the data. Circles and whiskers respectively represent the mean and standard deviation of $TPW/TPWi$, considering classes ΔH in steps of 100 m. 56

Figure 4.5 – Histogram representing the relative frequency of ERA-Int TPW departures from COSMO reference TPW (in blue) for classes of 0.25 cm over the Alps for 2014. Median, 25th and 75th percentiles of differences of height between ERA-Int and COSMO are shown in black lines. 57

Figure 4.6 – Contingency tables of the COSMO and ERA-Int TPW (in mm), for the April-September period (only cases with height differences between models greater than 1000 m are used) a) uncorrected ERA-Int; b) ERA-Int with exponential correction. 58

Figure 4.7 – Scatterplots of corrected- versus original- values of retrieved LST for the four different classes of ΔH (yellow, red, green and blue dots) when PMW (left panels), SMW (middle panels) and GSW (right panels) retrieval algorithms, are applied during extended summer (top panels) and extended winter (bottom panels). 62

Figure 5.1 – Geographical domain of the study area over Europe. Colours represent the aridity index classes (based on the CGIAR-CSI Global-Aridity and Global-PET Database). Desert zones are masked (in white) according to the IGBP land cover. 70

Figure 5.2 – Spatial distributions of the climatological month of maximum NDVI (A) and of respective maximum value (B); and annual cycles of spatial averages of NDVI (C) over pixels having maximum NDVI in the months of March, April, May, June and July. 73

Figure 5.3 – Spatial distribution of the Pearson's linear correlation coefficient (A) between VHI of the maximum NDVI month and the SPEI time scale (B) for which the correlation is maximum. 78

Figure 5.4 – Relationship between the correlations of VCI-SPEI and TCI-SPEI for the significant pixels of the maximum NDVI months and its spatial distribution. 79

Figure 5.5 – Values of α for which the pixel-by-pixel correlation between VHI and SPEI is maximised. 82

Figure 5.6 – Distribution of α (top) for the different aridity classes and (bottom left) for the IGBP classes of landcover. Both panels show the mean of α for each of the maximum NDVI clusters in a given distribution (filled circles). The spatial distribution of the IGBP landcovers for the regions where correlations of VHI-SPEI is significant is also displayed (bottom right). 83

Figure 5.7 – Aridity index classes (top) based on the CGIAR-CSI Global-Aridity and Global-PET Database and biomes classes (bottom) based on the IGBP landcover. Deserts are masked in white following the IGBP definition. 86

Figure 5.8 – Global map of coefficient α as estimated through the stepwise maximisation of the correlation between VHI and SPEI. 87

Figure 5.9 – Boxplots representing the aridity intervals for $\alpha > 0.5$ (larger VCI contribution) and $\alpha < 0.5$ (larger TCI contribution). The black dot represents the median value, the box represents the 25th and 75th percentiles, and the whiskers the 5th and 95th percentiles. The coloured circles represent the landcovers associated to that interval of α. The size of the circles is proportional to the percentage of the total number of pixels in each combination (numbers above the circles). The sum of the coloured circles in each combination is 100%. 88

Figure 5.10 – Relation between α and the aridity index. Black dots represent the mean of α in an interval of 0.05 in aridity index. Blue lines represent the 25th and 75th percentiles. 89

Figure 5.11 – Global map of α and β coefficient combinations as estimated through canonical correlation analysis. 90

Figure 5.12 – Boxplots representing the aridity index distribution and its associated climatic class over the different coefficient combinations. The black dot represents the median value, the box represents the 25th and 75th percentiles, and the whiskers the 5th and 95th percentiles. The coloured circles represent the landcovers associated to that combination of coefficients. The size of the circles is proportional to the percentage of the total number of pixels (numbers above the circles) in each combination (as displayed in Table 5.3). The sum of the coloured circles in each combination is 100%. 92

Figure 5.13 – Comparison of α estimated with TCI dependent on: Princeton University (PU) merged LST (left), CM SAF PMW LST (center), CM SAF SMW LST (right). 94

Figure 5.14 – Histogram of the differences between estimated with PMW – PU (top left), SMW – PU (top center) and PMW – SMW (top right); and distribution of the number of pixels with values of α with PMW against PU (bottom left), SMW against PU (bottom center) and SMW against PMW (bottom right). The black line represents the diagonal. 95

List of Tables

Table 2.1 – List of some of the missions, satellites and instruments capable of peeking through the TIR window. 10

Table 2.2 – Essential Climate Variables (ECVs). 20

Table 3.1 – Overview of KITs validation stations. 37

Table 3.2 – Theoretical uncertainty for MSG/SEVIRI LST estimates for the PMW and SMW. RMSD and bias associated with both model and input uncertainty. 42

Table 3.3 – Statistics for the comparison of LST between in situ measurements and the operational LSA SAF dataset for dry to medium-moist atmospheres (TCWV ≤45 mm)..... 44

Table 3.4 – Statistics for the comparison of LST between in situ measurements and the operational LSA SAF dataset for very moist atmospheres (TCWV >45 mm) experienced at the KIT 'Dahra' station..... 45

Table 4.1 – LST RMSD (K) when comparing LST derived with COSMO profiles (reference) and LST derived with ERA-Int original profiles (Orig) and ERA-Int corrected with the different methods (Corr), for PMW (a), SMW (b) and GSW (c). N represents the number of profiles in a determined class of altitude difference and season. The seasons are the extended winter (Nov-Mar) and extended summer (Apr-Sep). 59

Table 5.1 – Percentage of climate classes defined by the CGIAR-CSI Aridity Index in the different NDVI months of maximum vegetation activity for all pixels (AP) and for the ones where the VHI-SPEI correlation is significant (SP). Hyper arid climatic class is missing as a consequence of the desert mask applied to the data. 76

Table 5.2 – Number of pixels and percentage of SPEI time scales of 3, 6, 9 and 12 months and SPEI/VHI interquartile correlation over the regions defined by the maximum NDVI month. 77

Table 5.3 – Number and percentage of pixels for each coefficient α and β combination (and its rationale). Only pixels with statistically significant correlations are considered. 91

Chapter 1

Enclosed in this chapter is the thesis framework, which includes the motivation and main objectives of the PhD. Furthermore, the organisation of the manuscript is briefly explained in the layout section, and a number of remarks about its development – including the problems and limitations that originated during the process, and also the main achievements – are listed.

1. Thesis Framework

1.1. Motivation

Land Surface Temperature (hereafter abbreviated by its acronym LST) is one of the most important parameters in the physics of land surface processes since not only it drives long-wave radiation and turbulent heat fluxes at the surface-atmosphere interface, as these processes influence LST evolution. Consequently, an accurate knowledge of LST estimates is crucial to several earth system applications, such as: climate change and climate monitoring (Siemann et al. 2016); urban climate (Arnfield 2003; Weng 2009); land-atmosphere coupling (Trigo et al. 2015); data assimilation (Ghent et al. 2010); hydrological cycle (Kustas and Norman 1996; Kalma et al. 2008); vegetation and drought monitoring (Wan et al. 2004; Kogan 1997, 2001); among others. However, in situ measurements of LST are very sparse and costly to maintain, preventing monitoring to be thorough and efficient for global or regional analyses.

Remote Sensing from space has been a major tool to monitor the Earth since the 1960/70s (Neeck et al. 2005). During these decades the primary platform used to carry remote sensing instruments changed from airplanes to satellites, which could cover larger areas continuously in time. This revolution in the way we monitor the Earth led to the development of algorithms to estimate several geophysical variables, including LST, which is usually derived from satellite

thermal infrared (TIR) channels (Schott 2007). Thus far, many LST retrieval methods have been theorised and/or applied to both polar-orbit and geostationary satellites, with different spatial, temporal and spectral resolutions (Li et al. 2013). Examples of widely used instruments with LST products are the Spinning Enhanced Visible and Infrared Imager (SEVIRI) on-board of Meteosat Second Generation (MSG) satellites operated by the European Organisation for the Exploitation of Meteorological Satellites (EUMETSAT) (Trigo et al. 2009), NASA's Moderate-resolution imaging spectroradiometer (MODIS) on-board the Terra and Aqua satellites (Zhengming 1999), or the sounder aboard the Geostationary Operational Environmental Satellite (GOES) system operated by the National Oceanic and Atmospheric Administration (NOAA) (Yunyue 2010). However, the problem of retrieving LST is mathematically defined as an ill-posed inversion problem, since the number of unknowns in the radiative transfer equations is always larger than the number of equations (Peres and DaCamara 2004). To solve this problem numerous algorithms were developed with the sole objective of accurately retrieving LST (Li et al. 2013). However, one method considered the "best" was still not achieved.

Climate Monitoring has been a fundamental task performed by scientists in the last decades to identify and attribute the signature of climate change (Wentz and Schabel 2000; Zhang et al. 2017; Goddard Institute for Space Studies 1992; Vicente-Serrano et al. 2018). By monitoring a diverse range of climate variables (e.g. temperature, precipitation, vegetation, amongst others), and implementing the correct policies, society can adapt to future conditions and plan for the inherent socioeconomic needs. To achieve that objective, the development of Climate Data Records (CDRs), defined by the US National Research Council committee as "a time series of measurements of sufficient length, consistency and continuity to determine climate variability and change", has been the main goal of many climate groups all over the world (Yu et al. 2008; Cao et al. 2008; Hollmann et al. 2013; Verhoef et al. 2017; Schulz et al. 2009).

The use of remotely sensed Land Surface Temperature for climate monitoring is still in early stages of development, but represents a golden opportunity to understand, study and prepare for climate change with a new observational tool. As such, EUMETSAT's Meteosat First (MFG) and Second (MSG) Generation

satellites provide the unique opportunity to compile more than 30 years of 30 min temporal- and 5 km spatial- resolution LST CDR over Africa and Europe.

1.2. Objectives

A compilation of data through several generations of satellites has its inherent problems. In the case of EUMETSAT instruments, the Meteosat Visible and Infrared Imager (MVIRI) on-board MFG is equipped with a single TIR channel. On the other hand, the SEVIRI instrument on-board MSG has two TIR channels within the atmospheric window part of the spectrum. The algorithm operationally used in the Land Surface Analysis Satellite Application Facility (LSA SAF; Trigo et al. 2011) (lsa-saf.eumetsat.int) consists of a so called Generalized Split Windows (GSW) (Wan and Dozier 1996) LST estimate, which uses the two TIR channels available on MSG (Freitas et al. 2013; Trigo et al. 2008). This algorithm cannot be used for the first generation Meteosat satellites.

The aim of this thesis is to develop, improve, implement and apply CDRs of LST, consisting of satellite observations, with appropriate spatial and temporal resolutions to be used for climate studies. For that purpose, the development of a single-channel algorithm able to retrieve LST and ensure consistency across all Meteosat satellite generations is required. Furthermore, the implementation of such algorithm in the chain of command of the Climate Monitoring Satellite Application Facility (CM SAF; cm-saf.eumetsat.int) is envisioned. This LST CDR is to be provided by CM SAF as part of its product portfolio. Furthermore, LST can be used directly for several applications, being drought monitoring one of them (Kogan 1997, 2001). The social and economic importance, combined with the increasing severity of drought episodes in Southern Europe, requires a better understanding and monitoring of the phenomenon. Therefore, using LST CDRs as an asset to achieve this objective is another topic discussed here.

1.3. Layout

The present thesis is organised in 6 chapters covering the different stages of work. Chapter 1 introduces the thesis and its framework, focusing in providing a general picture of what composes this manuscript. Chapter 2 contains a theoretical

introduction with the main mathematical and physical definitions as well as an historic context relevant to a better understanding of the manuscript. Chapter 6 summarises the overall conclusions of the thesis. The remaining chapters contain the main original research and are organised as follows:

- Chapter 3 contains the development of the single-channel LST retrieval algorithms, its uncertainty analysis and a validation against in situ stations; it is based on a paper published in *Remote Sensing* and defines the base for the implementation of the algorithm on the CM-SAF chain of command. A very brief discussion, adapted from another paper published in the same journal, is also presented about the calibration of the algorithms;

- Chapter 4 addresses sources of uncertainty in LST algorithms and how these can be minimised. In particular it describes an improvement of the algorithms developed in Chapter 3 for mountainous regions. The chapter is based on a paper published in *Remote Sensing*;

- In Chapter 5 LST and NDVI CDRs are used to estimate a widely used drought index – the Vegetation Health Index, VHI. The study aims at assessing whether one of the assumptions undertaken in its development is valid when the index is applied to a Mediterranean region. Furthermore, a similar methodology is applied on a global scale and over the Meteosat disk, using the LST CDR developed in Chapter 3. The chapter consists of a paper currently in revision in *Agricultural and Forest Meteorology*, and another paper in preparation.

1.4. Remarks

To clarify the scope of the thesis a few remarks about the underlying work should be pointed out.

The development of the single-channel algorithms – the so-called Physical (PMW) and Statistical (SMW) Mono-Window algorithms – was part of a joint effort between the LSA-SAF and CM-SAF with the aim of providing an LST CDR product to the public through the CM-SAF website. This effort was successfully achieved, and the data record is now available at:

http://www.cmsaf.eu/EN/Home/home_node.html

The Algorithm Theoretical Basis Document (ATBD) may be downloaded using the following link:

http://www.cmsaf.eu/EN/Documentation/Documentation/ATBD/ATBD_node.html

and searching for Land Surface Temperature (SUMET); other documents related with this dataset may also be downloaded from the CM-SAF website.

The Edition 1 of the above-mentioned dataset, consisting of hourly and monthly diurnal cycle LST covering the 1991 - 2009 period, was released a few months before the submission of this thesis. The underlying algorithm is described in Chapter 3 and has been published in Remote Sensing journal in co-authorship with the CM- and LSA-SAF teams. However, the development of the algorithms and the results concerning the theoretical uncertainty analysis were produced within the scope of this thesis.

Other work published in co-authorship with the LSA-SAF and the CM-SAF teams, namely the validation of LST CDR and a thorough analysis of the impact of calibration datasets on the uncertainty of statistical LST algorithms, are briefly presented in Chapter 3 while the full articles are presented as annexes to this thesis. It is worth mentioning that the idea to further explore the latter arose partially from problems found when developing the single channel algorithms. Chapter 4 is mainly composed by a paper published in *Remote Sensing*, concerning the improvement of LST retrieval algorithms developed in Chapter 3 over mountainous regions.

Finally, great part of the results comprised in Chapter 5 do not use the LST CDR developed in Chapter 3 due to delays in the processing and in the release of this dataset by the CM-SAF with respect to the initially planned schedule. Given the time constraints to develop the work in this thesis, it was decided to pursue the investigation with a different CDR of LST. However, in the last section of this chapter a brief analysis using CM SAF LST CDR is performed.

As above-mentioned, some of the chapters that comprise the thesis in hands are versions of published or submitted peer-reviewed articles in international

journals. The author decided to adapt the entirety of the papers to thesis format, which includes the introductory sections. Therefore, some repetition of ideas or concepts will be present. Also, regarding the papers, a definition of the main equations used in this thesis is presented in the theoretical introduction chapter. To keep homogeneity with symbols and terms throughout the manuscript, equations encapsulated in the papers may have been changed in relation to the published version.

Chapter 2

Land Surface Temperature is a key parameter for several climate applications. This chapter aims at introducing the variable, focusing in its physical and mathematical derivations and on its retrieval from instruments on-board earth viewing meteorological satellites. Furthermore, the interest of Land Surface Temperature as an essential climate variable is addressed, and a climatologic application on drought monitoring is introduced.

2. Theoretical Introduction

2.1. From Remote Sensing to Land Surface Temperature

In the last decades Remote Sensing has been widely used by different branches of science and society as an asset. Examples of its usage go from the use of satellites in space to track a hurricane to the use of satellite imagery to count the number of vehicles in a parking lot so that investors can predict retail earnings and market share. But not all the applications depend on satellite imagery. Military surveillance using planes also counts as a remote sensing application or back in World War II when the Germans used photographic cameras attached to pigeons. With so many and disparate applications a general definition of remote sensing is hard to achieve. The broadest definitions usually found in the literature revolve around the idea that "Remote Sensing is the field of study associated with the acquisition, processing and interpretation of information about an object without being in physical contact with it" (Schott 2007; Lillesand et al. 2004; Sabins 1997; Elachi and van Zyl 2006). An implication from this definition is that when we look at the window just before leaving home to see if it is raining and decide about the need an umbrella, we are indeed applying a remote sensing technique. In fact, our eyes are acquiring data, that will be processed by our brain and finally interpreted to assess the necessity of an umbrella. Many of our daily based observations can be described as remote sensing in its broader definition. However, for the purpose

intended here – Earth Observation from space – a more specific definition is required. The United Nations (UN), in their General Assembly Resolutions and International Treaties Pertaining to the Peaceful Uses of Outer Space, defined the term Remote Sensing as the "sensing of the Earth's surface from space by making use of the properties of electromagnetic waves emitted, reflected or diffracted by the sensed objects, for the purpose of improving natural resources management, land use and the protection of the environment". This definition is much more pertinent for the topics discussed in this thesis since it specially addresses the sensing from space– that requires instruments onboard earth viewing satellites – and presupposes an understanding of the behavior of electromagnetic radiation.

Satellite remote sensing has been a major tool to monitor the earth's weather and surface environment since 1960, when the Television Infrared Observation Satellite (TIROS-1) was launched (Neeck et al. 2005). This scientific and technical achievement was followed by several other satellite launches helping researchers to study and develop methods to better understand land surface and atmospheric processes (House et al. 1986; Davis 2007). The European Space Research Organisation (ESRO), that preceded the European Space Agency (ESA), received funding (in 1968) for studies of application satellites, which included weather satellites, and decided to incorporate in 1972 the Meteosat programme that introduced the concept of a global system of geostationary platforms capable of observing the atmospheric circulation and weather around the equator, in near real-time. Meteosat-1, the first European Geostationary Earth Orbit (GEO) meteorological satellite was then launched in November 23, 1977, followed by Meteosat-2 on June 19, 1981 (Tessier 1989). In 1986, an Intergovernmental Conference of 17 European countries convened to consider the matter of long-term continuity of Meteosat satellites, creating a new specialised operational organisation, named EUMETSAT (www.eumetsat.int). Today this Organisation is responsible for the operation of Meteosat satellites in orbit. Meteosat-1 through -7 are considered the Meteosat First Generation (MFG) constellation of satellites. In 2002, Meteosat-8 was launched, being the first satellite from the Meteosat Second Generation (MSG) constellation (Schmetz et al. 2002). The Second Generation was designed in response to user requirements with the aim of serving the needs of Nowcasting and Numerical Weather Prediction (NWP). The last MSG satellite,

Meteosat-11, was launched on July 15, 2015. The launch of the first Meteosat Third Generation (MTG) (Rodriguez et al. 2009; Aminou et al. 2009; Stuhlmann et al. 2005) satellite is expected to take place in 2018/2019. An advantage of this kind of satellite mission – spanning 30 years of combined earth observation – is the emerging opportunity to study several climate applications using remote sensing observations. However, a global study cannot be achieved with the Meteosat constellation alone, which provides images of Africa and Europe. Other GEO satellites provide images of different regions – NOAA GOES (Menzel and Purdom 1994; Schmit et al. 2005) offers imagery for South and North America while the Himawari geostationary satellites (BESSHO et al. 2016) deliver imagery for east Asia and Australia. Additionally, meteorological polar satellites (or Low Orbit Satellites, LEO) cover the earth in sun-synchronous orbits, observing vast regions on Earth twice a day with similar illumination conditions due to passages at about the same local solar time. LEO satellites offer a better spatial resolution than GEO due to their closeness to the Earth. Conversely, the time resolution for each pixel is much more degraded. Currently operating LEO satellites include NASA's Aqua and Terra (Savtchenko et al. 2004) or the ESA/EUMETSAT MetOp (Clerbaux et al. 2009). Table 2.1 shows a summarised list of GEO and LEO weather satellites.

As emphasised by the UN definition of remote sensing, sensors onboard meteorological satellites use the properties of electromagnetic waves that interact with the sensed objects. These waves consist of energy transported through space (energy path) in the form of periodic disturbances of electric and magnetic fields, travelling at the speed of light c. An electromagnetic wave is characterised by a frequency ν and a wavelength λ. These two quantities are related to the speed of light according to:

$$\lambda = \frac{c}{\nu} \qquad \text{Eq. 2.1}$$

The frequency (and the wavelength) of an electromagnetic wave depends on its source. There is a wide range of frequencies encountered in the physical world, ranging from the low frequency of electric waves generated by the power transmission lines to the very high frequency of the gamma rays originating from the atomic nuclei. This wide range of electromagnetic waves constitute the

Table 2.1 – List of some of the missions, satellites and instruments capable of peeking through the TIR window.

Mission	Satellites (launch date)	Orbit	TIR instrument
EUMETSAT			
Meteosat First Generation (MFG)	Meteosat-1 (1977) to Meteosat-7 (1997)	GEO	Meteosat Visible and Infrared Imager (MVIRI)
Meteosat Second Generation (MSG)	Meteosat-8 (2002)‡ to Meteosat-11 (2015)‡	GEO	Spinning Enhanced Visible and Infrared Imager (SEVIRI)
MetOp (developed by ESA)	MetOP-A (2006)‡ to MetOP-B (2012)‡	LEO	Advanced Very High-Resolution Radiometer (AVHRR) High-Resolution Infrared Radiation Sounder (HIRS) Infrared Atmospheric Sounding Interferometer (IASI)
NASA			
Terra (EOS AM-1)	Terra (1999)‡	LEO	Moderate-Resolution Imaging Spectroradiometer (MODIS) Advanced Spaceborne Thermal Emission and Reflection Radiometer (ASTER)
Aqua (EOS PM-1)	Aqua (2002)‡	LEO	MODIS Atmospheric Infrared Sounder (AIRS)
NOAA			
GOES	GOES-1 (1975) to GOES-16 (2016)‡	GEO	Imager
POES (in partnership with EUMETSAT)	TIROS-1 (1960) to NOAA-19 (2009)‡	LEO	AVHRR HIRS
ESA			
ERS	ERS-1 (1991) to ERS-2 (1995)	LEO	Along-Track Scanning Radiometer (ATSR-1/2)
Envisat	Envisat (2002)	LEO	Advanced Along-Track Scanning Radiometer (AATSR)
Sentinel	Sentinel-1A (2014)‡ to Sentinel-3 (2016)‡	LEO	Sea and Land Surface Temperature Radiometer (SLSTR)*
Others			
Himawari (includes GMS and MTSAT)	GMS-1 (1977) to Himawari-9 (2016)‡	GEO	IMAGER Advanced Himawari Imager (AHI)
Landsat (USGS/NASA)	Landsat-1 (1972) to Landsat-8 (2013)‡	LEO	Thematic Mapper (TM) Thermal Infrared Sensor (TIRS)

‡ Still operational

* Only available on Sentinel-3

Electromagnetic Spectrum. Figure 2.1 shows an infographic containing the type of radiation in different regions of the Electromagnetic spectrum, its relative and typical wavelengths, and the energy carried per wave.

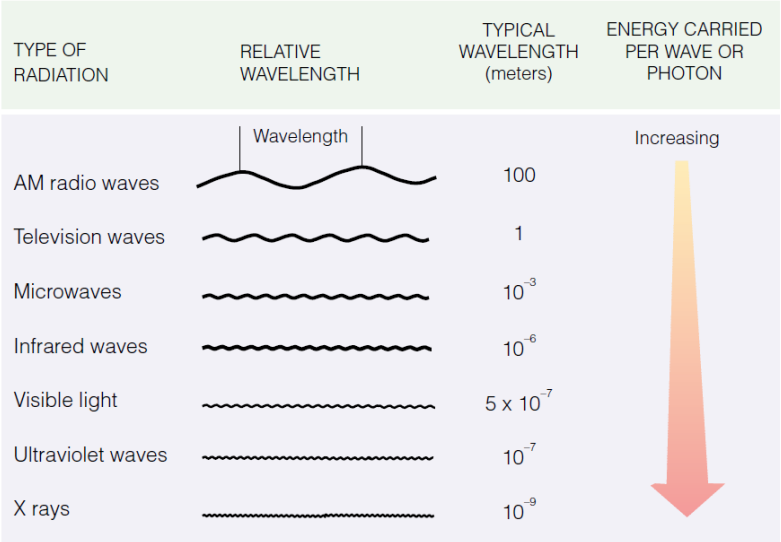

Figure 2.1 – A schematic view of wavelength and energy carried by electromagnetic radiation (adapted from Essentials of Meteorology: An Invitation on the Atmosphere by C. Donald Ahrens).

The parametrisation of most fluxes at the surface/atmosphere interface, such as long wave or latent and sensible heat fluxes, require knowing Land Surface Temperature (LST). Consequently, it is crucial to have access to reliable estimates of this variable over large spatial and temporal scales. Since this task is very difficult to achieve from in situ observations, the use of satellite remote sensing in the thermal infrared (TIR) – also called Long-Wave infrared (LWIR) – channel appears as an advantage to pursue these estimates. TIR sensors measure a radiance, which can be translated to a top-of-atmosphere (TOA) brightness temperature that depends on the transmission band (or window) through which the sensor is peaking. Satellite retrieval of LST is performed using remote-sensed information in a part of the transmission spectrum (Figure 2.2) where the atmosphere is almost transparent (typically between the 10.5 and 12.5 μm on the so-called window of the TIR part of the spectrum). Since the atmosphere is not completely transparent, a first problem is to address this non-negligible effect. Another problem of LST retrieval is surface

emissivity, a usually unknown parameter when land surface is not taken as a black or even grey body. Also, emissivity is generally frequency dependent.

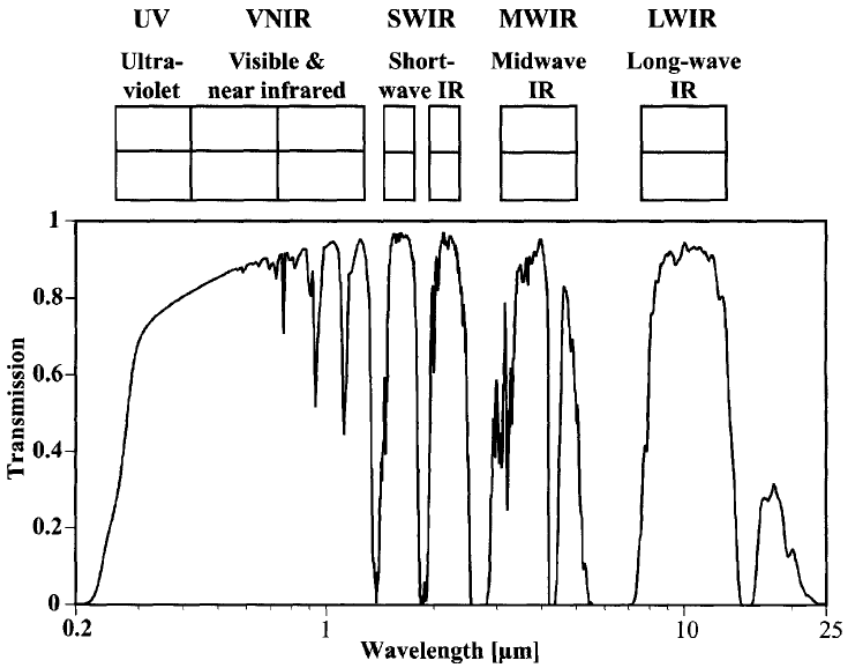

Figure 2.2 – Portion of the transmission Spectrum (adapted from Remote Sensing: The Image Chain Approach by John R. Schott).

A sensor on-board a satellite records values of the energy flux reaching its system. These energy paths can be divided into two groups. The first group of energy paths are the ones that follow radiation originated from the sun, while the second group are the ones from radiating objects other than the sun. Figure 2.3 displays a very simplified schematic of these two groups. Let θ and ϕ be the satellite zenith and azimuth angles, and θ_s and ϕ_s the solar zenith and azimuthal angles, respectively. The infrared radiance L reaching a sensor, in a given channel i, may be expressed according to the Radiative Transfer Equation (RTE):

$$L_i(\theta,\phi) = \underbrace{\varepsilon_i(\theta,\phi)B_i(LST)\tau_i(\theta,\phi)}_{(1)} + \underbrace{L_i^S\, cos(\theta_s)\,\tau_i(\theta,\phi)r_i\tau_i(\theta_s,\phi_s)}_{(2)} +$$

$$+ \underbrace{[1-\varepsilon_i(\theta,\phi)]L_i^{a_d}\tau_i(\theta,\phi)}_{(3)} + \underbrace{[1-\varepsilon_i(\theta,\phi)]L_i^{s_d}\tau_i(\theta,\phi)}_{(4)} + \qquad \text{Eq. 2.2}$$

$$+ \underbrace{L_i^{a_u}(\theta,\phi)}_{(5)} + \underbrace{L_i^{s_u}(\theta,\phi)}_{(6)}$$

where ε_i is the pixel integrated emissivity of the land surface, τ_i is the transmissivity of the atmosphere, r_i is bi-directional reflectivity of the land surface, B_i represents the Planck function, superscripts s, s_d, s_u, a_d, a_u represent the direct solar radiation reaching the land surface, the solar radiation scattered by the atmosphere, the solar scattered upwelling components, and atmospheric downwelling and upwelling components, respectively. Term (1) of Eq. 2.2 characterises the thermal radiance emitted by the surface at a given LST and emissivity that reaches the sensor; term (2) represents the direct solar radiance reflected by the surface that reaches the sensor, attenuated by the path through the atmosphere taken when it is directed downwards (directed to the surface) and upwards (directed to the sensor); term (3) characterises the integrated radiance emitted by the atmosphere directed to the surface that reflects upwards and reaches the sensor; term (4) describes the solar radiance scattered by the atmosphere that is directed downwards to the surface and then reflected to the sensor; term (5) represents the integrated thermal radiance emitted upwards by the atmosphere and reaches the sensor; and finally, term (6) describes the solar radiance scattered upwards by the atmosphere. The terms of the radiative transfer equation (RTE) are schematised in Figure 2.3. However, for different regions of the electromagnetic spectrum some of the terms are more important than others, and some simplifications can be therefore introduced. In the TIR window (8 – 14 μm) – the window used throughout this thesis – the contribution of solar radiation is negligible. Consequently, the governing equation of radiation reaching a sensor in the thermal infrared region can be simplified as:

$$L_i(\theta,\phi) = \underbrace{\varepsilon_i(\theta,\phi)B_i(LST)\tau_i(\theta,\phi)}_{(1)} + \underbrace{[1-\varepsilon_i(\theta,\phi)]L_i^{a_d}\tau_i(\theta,\phi)}_{(3)} + \underbrace{L_i^{a_u}(\theta,\phi)}_{(5)} \quad \text{Eq. 2.3}$$

where the Planck function for a given channel with frequency ν_i is given by:

$$B_i(LST) = \frac{2h\nu_i^3}{c^2}\left(e^{\frac{h\nu_i}{K_b LST}}\right)^{-1} \quad \text{Eq. 2.4}$$

where h is the Planck constant and K_b the Boltzmann constant. Eq. 2.3 represents therefore an approximation of the thermal radiation that is emitted by the earth surface and its atmosphere, and reaches a sensor situated at the top-of-atmosphere.

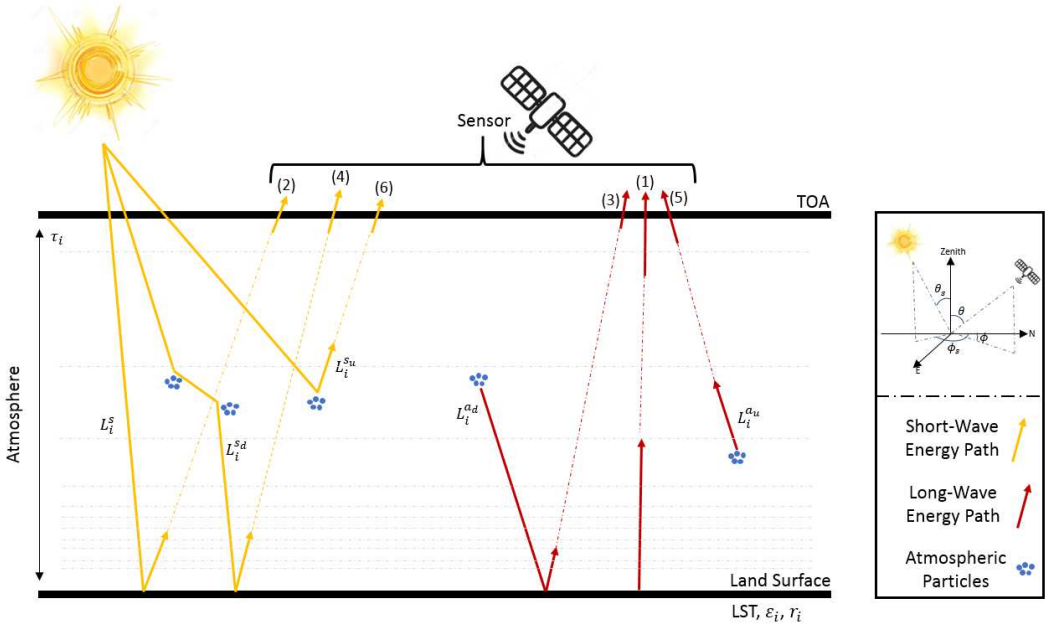

Figure 2.3 – Relationship between terms in the radiative transfer equation and energy paths associated with photon flux onto the sensor.

Eq. 2.3 also displays the relationship between LST and radiance measured by the sensor. However, inverting the equation to estimate LST knowing the radiance on top-of-atmosphere is an ill-posed inversion problem. If the radiance is measured in N channels, there will always be $N+1$ unknowns, corresponding to the N emissivities in each channel and unknown LST for N equations. To make LST deterministic, one or more of the emissivities must be known, or the LST and emissivity must be simultaneously solved with the aid of some other assumptions or constraints. Besides, estimated LST will also be dependent on the directionality, i.e., satellites look to a determined pixel in one direction (e.g. GEO satellites look at the same pixel with approximately the same angle through all its life). This implies that variables dependent on satellite viewing angle θ may have a directional bias, which will propagate to the retrieved LST.

Due to the problems that LST retrieval arises, several different algorithms have been developed during the last decades. Next section is intended as a

summarised overview focusing on the most relevant algorithms for the aim of this thesis.

2.2. Land Surface Temperature retrieval algorithms

2.2.1. A general review

Following Li et al. 2013, LST retrieval algorithms can be divided into three categories if the surface emissivity is known, and into another three if surface emissivity is not known, as shown in Figure 2.4.

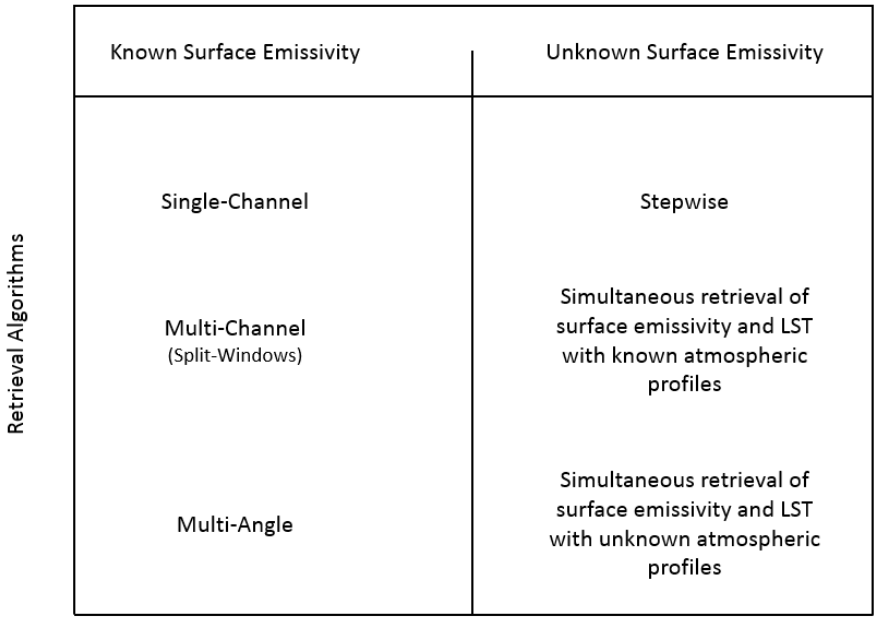

Figure 2.4 – List of LST retrieval algorithms with known and unknown surface emissivity (Li et al. 2013).

Single channel algorithms (Qin et al. 2001; Jiménez-Muñoz and Sobrino 2003) use the radiance measured by the sensor in a single TIR channel, requiring input data from accurate atmospheric profiles to correct for the atmospheric attenuation and emission. Furthermore, this method requires radiative transfer models (RTMs) to estimate the atmospheric quantities like transmissivity or upwelling and downwelling path radiance on Eq. 2.3. On the other hand, multi-channel algorithms (Wan and Dozier 1996; Becker and Li 1990a) use two or more adjacent TIR channels, which implies the requirement of *a priori* knowledge of the pixel emissivity in both. There are many parametrisations of the RTE available,

leading to different split-windows algorithms with different performance characteristics. The multi-angle retrieval (Chedin et al. 1985; Prata 1993; Sobrino et al. 2004) algorithm relies on differential atmospheric absorption due to the different path-lengths when the same object is observed in a given channel from different viewing angles. This method assumes that LST is independent of satellite viewing zenith angle (VZA) and that the atmosphere is horizontally uniform and stable over the observation time.

Retrieval algorithms when the surface emissivity is unknown include the stepwise method (Peres and DaCamara 2005; Snyder et al. 1998; Sun and Pinker 2003; Valor and Caselles 1996; Becker and Li 1990b) where LST is retrieved using two consecutive steps. First, the surface emissivity is empirically determined from visible/near-infrared measurements or physically estimated from pairs of atmospherically corrected MIR and TIR radiances at ground level. Then, LST is estimated using one of the three algorithms introduced in the last paragraph. On the other hand, the simultaneous retrieval of LST and surface emissivity with known atmospheric information can be classified into two categories: the multi-temporal (Watson 1992; Wan and Li 1997; Peres and DaCamara 2006) and multi (hyper)-spectral retrieval methods (Barducci and Pippi 1996; Gillespie et al. 1998; Borel 2008; Wang et al. 2011). The multi-temporal retrieval methods primarily make use of measurements at different times to retrieve the LST and the surface emissivity under the assumption that the latter is time-invariant. The multi (hyper)-spectral retrieval methods rely on the intrinsic spectral behavior of the surface emissivity rather than temporal information. Based on some reasonable assumptions or constraints, these methods can retrieve both the LST and surface emissivity from the atmospherically corrected radiances at the ground level either by reducing the number of unknowns or by increasing the number of equations. Although LST and surface emissivity can be accurately retrieved in case the atmospheric corrections are performed properly, accurate atmospheric profiles are usually unavailable, leading to a degradation in quality of retrieved LST and surface emissivity. A solution is to simultaneously retrieve LST, surface emissivity and the atmospheric parameters (Wang et al. 2010; Ma et al. 2002).

For the purpose of this thesis, the surface emissivity will be always taken as a known parameter, and since the satellite sensors used do not have the ability to

operate in biangular-mode (eliminating the possibility of using multi-angle retrieval methods), the remaining are the single- and multi-channel algorithms. A detailed description of these algorithms is provided in the following subsection.

2.2.2. Single-Channel and Split-Windows Algorithms

As discussed in the previous subsection, retrieval of LST from the RTE poses a problem of inversion. A main feature of this inversion is that it is a set of nonlinear integro-differential equations, where radiance is a nonlinear function of temperature, and the atmospheric transmission (in a given set of frequencies) is a nonlinear function of atmospheric composition. If the emissivities are known, then the determination of LST under clear-sky conditions is straightforward. When retrieving LST with a single-channel algorithm the a priori knowledge of surface emissivity is mandatory. To solve the RTE, the remaining atmospheric radiative contributions are estimated with a radiative transfer model fed with atmospheric profiles representing the state of the atmosphere in a given pixel. However, errors in surface emissivity, atmospheric profiles, and in the RTM itself propagate to the retrieved LST. Errors of a few percent in surface emissivity alone can lead to an error up to 2 K in LST (Dash et al. 2002, 2005). Many variations of the single-channel algorithm were developed in the past decades, including algorithms that only depend on near-surface air temperature and Total Column Water Vapor (TCWV) instead of the atmospheric profiles (Qin et al. 2001), which uses linear relationships between atmospheric transmissivity and TCWV, and between mean atmospheric and near surface air temperature; or the generalised single-channel algorithm (Jiménez-Muñoz and Sobrino 2003; Jiménez-Muñoz et al. 2009; Cristóbal et al. 2009).

Accurate knowledge of the atmospheric profiles in a given pixel, synchronised with the satellite pass is a very difficult task to achieve. To overcome this problem a different method was developed: the split-windows algorithm. This algorithm, initially used to retrieve Sea Surface Temperature (SST) from space (McMillin 1975), relies on the differential atmospheric absorption in the two adjacent channels of the TIR window.

Many different versions of the split-windows have been developed through the years (Becker and Li 1990a; Sobrino et al. 1991; Ulivieri et al. 1994; Sobrino et al. 1994, 1996; Wan and Dozier 1996; Tang and Li 2008) to retrieve LST. Differences relate to the parametrisation of the coefficients based on assumptions on surface emissivity, water vapour content, and/or VZA (θ). Here we adopt the so-called Generalized Split-Windows (GSW) algorithm that takes into account the three mentioned factors.

A typical formulation of the GSW is the following (Wan and Dozier 1996):

$$LST = b_0 + \left(b_1 + b_2\frac{1-\varepsilon_m}{\varepsilon_m} + b_3\frac{\Delta\varepsilon}{\varepsilon_m^2}\right)\frac{T_{b_i} + T_{b_j}}{2} + \\ + \left(b_4 + b_5\frac{1-\varepsilon_m}{\varepsilon_m} + b_6\frac{\Delta\varepsilon}{\varepsilon_m^2}\right)\frac{T_{b_i} - T_{b_j}}{2} \quad \text{Eq. 2.5}$$

where T_{b_i} and T_{b_j} are the brightness temperatures measured at channels i and j, b_k $(k = 1, \dots, 6)$ are the empirically parametrised coefficients, and

$$\varepsilon_m = \frac{\left[\varepsilon_i(\theta,\phi) + \varepsilon_j(\theta,\phi)\right]}{2}, and \quad \text{Eq. 2.6}$$

$$\Delta\varepsilon = \left[\varepsilon_i(\theta,\phi) - \varepsilon_j(\theta,\phi)\right] \quad \text{Eq. 2.7}$$

are the mean emissivity and the difference between emissivities in the channels i and j. For simplicity, the dependence on the satellite zenith (θ) and azimuthal (ϕ) angles is dropped in the terms of Eq. 2.5.

This algorithm is currently used by the LSA SAF, which routinely disseminates LST from SEVIRI onboard MSG on an operational basis (Freitas et al. 2010; Trigo et al. 2008a, 2011; Freitas et al. 2013). The empirical coefficients b_k of the LSA SAF GSW were estimated for classes of TCWV and VZA, relying on linear regressions of synthetic brightness temperatures in the 10.8 and 12 μm channels, obtained from radiative transfer simulations performed over a set of clear-sky atmospheric profiles covering a wide variety of atmospheric conditions. Figure 2.5 shows a schematic of the GSW algorithm calibration procedure.

After the calibration of the GSW coefficients, LST is estimated with surface emissivity and the measured pixel brightness temperature. The validation of the coefficients is then performed by comparing the estimated LST with the prescribed initial LST. Validation of the GSW presents errors in the retrieved LST between 1 K and 2 K, which is below the operational acceptable error (Freitas et al. 2010).

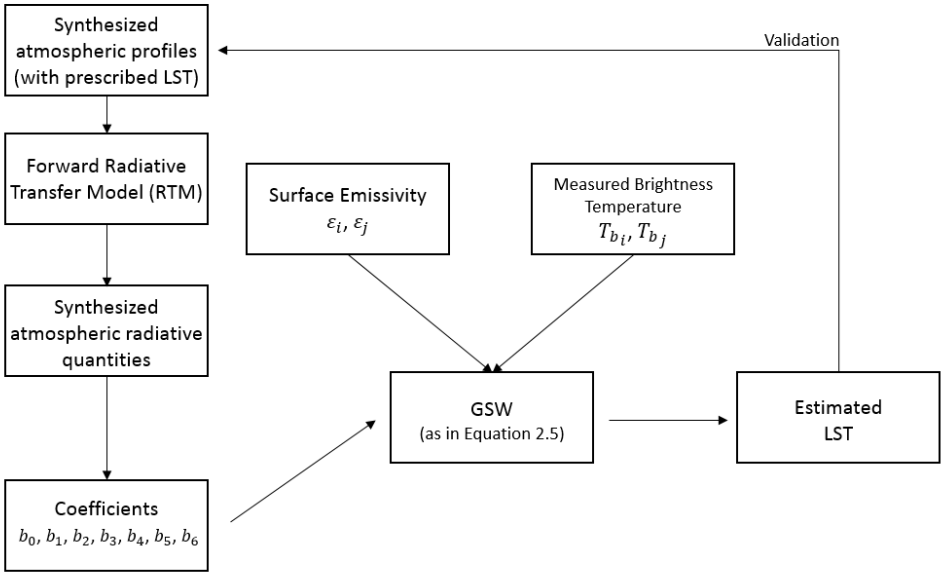

Figure 2.5 – Schematic of the GSW calibration.

2.3. LST as a climate asset

2.3.1. LST as an Essential Climate Variable

Recently LST was recognised as an Essential Climate Variable (ECV). As defined by the World Meteorological Organisation (WMO) an ECV is a physical, chemical or biological variable or a group of linked variables that critically contributes to the characterisation of Earth climate. ECV datasets provide the empirical evidence needed to understand and predict the evolution of climate on Earth, to guide mitigation and adaptation measures, to assess risk and enable attribution of climate events to underlying causes, and to underpin climate services (Bojinski et al. 2014). Since its establishment in 1992, the Global Climate Observing System (GCOS) has assured the availability of systematic climate

observations, establishing through its science panels the variables to be monitored (the ECVs) and the user requirements for measuring them (WMO 2016).

Table 2.2 – Essential Climate Variables (ECVs).

Measurement Domain	Essential Climate Variables (ECVs)
Atmospheric	**Surface** – Air temperature, Wind speed and direction, Water vapour, Pressure, Precipitation, Surface radiation budget;
	Upper-Air – Temperature, Wind speed and direction, Water vapour, Cloud properties, Earth radiation budget, Lightning;
	Composition – Carbon Dioxide (CO2), Methane (CH4), Other long-lived greenhouse gases (GHGs), Ozone, Aerosol, Precursors for aerosol and ozone;
Oceanic	**Physics** – Temperature: Sea surface and Subsurface, Salinity: Sea Surface and Subsurface, Currents, Surface Currents, Sea Level, Sea State, Sea Ice, Ocean Surface Stress, Ocean Surface heat Flux;
	Biogeochemestry – Inorganic Carbon, Oxygen, Nutrients, Transient Tracers, Nitrous Oxide (N2O), Ocean Colour;
	Biology/Ecosystems – Plankton, Marine habitat properties;
Terrestrial	**Hydrology** – River discharge, Groundwater, Lakes, Soil Moisture;
	Cryosphere – Snow, Glaciers, Ice sheets and Ice shelves, Permafrost;
	Biosphere – Albedo, Land cover, Fraction of absorbed photosynthetically active radiation, Leaf area index, Above-ground biomass, Soil carbon, Fire, Land Surface Temperature;
	Human use of natural resources – Water use, GHG fluxes;

ECVs for which global observation is currently feasible are divided into three categories: atmospheric, oceanic and terrestrial (Table 2.2). The LST ECV is fundamental for applications such as the development of land surface components of climate models, to perform climate model intercomparison and verification studies (e.g. Coupled Model Intercomparison Project CMIP projects). The LST ECV is also used by developers and providers of climate services (e.g. agriculture, heat stress), as well in studies of drought, wildfires and desertification processes, and impacts of climate change on agriculture, in research on the elevation dependent climate warming, as well on land cover, snow, permafrost and soil moisture ECVs (Hollmann et al. 2013).

The increasing relevance of LST has led several organisations to develop long-term homogeneous CDRs of LST from geostationary satellites (typically chosen over its polar counterparts due to its stronger diurnal variation). Examples of available LST

CDRs are the International Satellite Cloud Climatology Project (ISCCP) (Rossow and Schiffer 1999) and the Pathfinder Atmospheres-Extended dataset (PATMOS-x) (Heidinger et al. 2013) – both briefly discussed in the following chapter.

2.3.2. Drought monitoring

Drought is considered to be one of the most costly hazards since it can lead to reduced water supply and consequently have substantial effects on agriculture and socioeconomic activities (Riebsame et al. 1991). The severity of drought depends on factors like its duration, intensity, spatial extent and socioeconomic conditions of the affected region. Due to global warming the precipitation patterns have changed (Milly et al. 2002), triggering the increase of duration and intensity of droughts in recent years (Mishra and Singh 2009; Vicente-Serrano et al. 2014). This increase affects crop productions and therefore have high socioeconomic costs. To reduce possible impacts on crop production, the monitoring of droughts at a regional scale is of primary importance (Tang and Li 2014).

Droughts are most commonly classified into four different types (Wilhite and Glantz 1985):

- A meteorological drought, defined as a deviation from normal precipitation conditions due to climate variability or an increase in temperature over a period of time for a specific region, further causing higher evaporation and transpiration;
- An agricultural drought, which occurs after a meteorological drought, and where a characteristic lack of adequate soil moisture causes a certain crop or plant water stress and obstructs its ability to grow and thrive during a particular time;
- A hydrological drought, which occurs when precipitation has been reduced for an extended period of time and water supplies found in streams, lakes, rivers, and reservoirs are deficient with demand exceeding supply;

- A socioeconomic drought that is defined as a condition when the physical water supplies are so low that they negatively affect the community where the drought is occurring.

Satellite-based remote sensing is largely suited for monitoring drought conditions since its instruments and sensors allow for both regional and global scale observations of land surfaces, providing spatially continuous measurements across the landscape (Kogan 1997). Satellite observations can also have a high repeat visit frequency over the same geographic area (geostationary satellites), allowing for comparisons of data collected over time. TIR data which are sensitive to soil moisture are suitable for drought monitoring. Several indexes to monitor drought based on satellite TIR data where developed through the years. Some examples are the Apparent Thermal Inertia (ATI) (Mitra and Majumdar 2004; Verstraeten et al. 2006), the Vegetation Health Index (VHI) and its individual terms: the Vegetation Condition Index (VCI) and Temperature Condition Index (TCI) (Kogan 1997, 2000, 2001), the Normalised Difference Temperature Index (NDTI) (McVicar and Jupp 1998), the Vegetation Supply Water Index (VSWI) (Li et al. 1998), the Temperature Vegetation Dryness Index (TVDI) (Sandholt et al. 2002), the Crop Water Stress Index (CWSI) (Idso et al. 1981; Jackson et al. 1981), the Water Deficit Index (WDI) (Moran et al. 1994), or the Evaporative Stress Index (ESI) (Anderson et al. 2007). An intercomparison between this indices (Sun et al. 2011), using MODIS products, indicates that they do not lead to the same results, which is expected since they do not use the same features of land surface to represent drought.

For this thesis the focus will be on the VHI and its additive terms VCI and TCI:

$$VHI = \alpha VCI + (1 - \alpha)TCI \qquad \text{Eq. 2.8}$$

The first term of Eq. 2.8 is a function of the Normalised Difference Vegetation Index (NDVI), which is an indicator of the greenness of the biome, and is defined as the normalised difference of spectral reflectances ρ measured in the near infrared (NIR) and visible red (RED) windows:

$$NDVI = \frac{\rho_{NIR} - \rho_{RED}}{\rho_{NIR} + \rho_{RED}} \quad \text{Eq. 2.9}$$

The second term of Eq. 2.8 is a function of satellite-based temperature, which is usually top-of-atmosphere brightness temperature or – as in the case of this thesis – LST.

Due to the observed rise in drought duration and intensity (e.g. Vicente-Serrano et al. 2014), there is a growing need for a proper monitoring of vegetation. A CDR of LST can be an asset when applied to VHI both to better understand the past in order to prepare for the present and to improve the use of the index. An example of the latter application is to tackle the problem of the generalised use of $\alpha = 0.5$ in Eq. 2.8 (due to the lack of a better estimate of VCI and TCI contributions). With a climatological record of LST it may be possible to understand if this assumption is appropriate to estimate VHI in different regions.

In the next chapters, two LST CDRs retrieved using single-channel algorithms are developed. Its formulations will be addressed and a comprehensive LST validation is performed against the GSW and in-situ stations. Furthermore, the process of calibration of the statistical algorithms is briefly assessed, and an improvement of the single-channel algorithms over mountainous regions is discussed. Finally, the above-mentioned application of VHI using LST CDRs is analysed.

Chapter 3

Records of climatological data are required to understand the past, with the aim of understanding the future and take the social and economic precautions needed. In this chapter the retrieval algorithms needed to compile a climatological record of satellite Land Surface Temperature are developed, and its accuracy and uncertainties are estimated.

3. Development of Land Surface Temperature Climate Data Record[1]

Abstract

The European Organization for the Exploitation of Meteorological Satellites' (EUMETSAT) Meteosat satellites has operated satellites for more than 3 decades, therefore providing a unique opportunity to generate a long-term land surface temperature (LST) data record. Since the Meteosat instrument on-board Meteosat 2–7 is equipped with a single thermal channel, single-channel LST retrieval algorithms are used to ensure consistency across Meteosat satellites. This chapter describes two single-channel LST retrieval algorithms: (1) a physical radiative transfer-based mono-window (PMW); and (2) a statistical mono-window model (SMW). Their performances are assessed using a database of synthetic radiances for a wide range of atmospheric profiles and surface variables. Furthermore, the two single-channel algorithms are evaluated against the generalized split-window (GSW) model used operationally by the LSA-SAF to derived LST from SEVIRI/MSG.

[1] Adapted from Duguay-Tetzlaff, A., Bento, V. A., Göttsche, F. M., Stöckli, R., Martins, J. P. A., Trigo, I. F., Olesen, F., Bojanowski, J. S., DaCamara, C. C., Kunz, H. Meteosat Land Surface Temperature Climate Data Record: Achievable Accuracy and Potential Uncertainties. Remote Sens. 2015, 7, 13139-13156; doi:10.3390/rs71013139

The expected algorithm uncertainties, taking into account propagation of input errors and algorithm calibration / limitations are also assessed. This also includes a short analysis of the impact of the calibration databases on the statistical methods (the GSW and SMW). Finally, a summary of the comparison of LST derived by the three algorithms against ground observations is also presented, showing that, except for very moist atmospheres (TCWV >45 mm), Meteosat single-channel retrievals are in agreement with those of the GSW algorithm by 0.1–0.5 K.

3.1. Introduction

Land surface temperature (LST) is a key climate state variable. Accurate estimates of LST are essential to compute the radiative and sensible heat balance of the surface (Bodas-Salcedo al. 2008). Furthermore, LST is an important variable for several Earth system applications associated to land surface processes, where drought monitoring (Wan et al. 2004) and evaporation monitoring (Kustas and Norman 1996) are examples. Satellite remotely sensed LSTs are also important for the assessment of surface-emitting temperatures in climate models at several time scales (Bodas-Salcedo et al. 2008), and they can also be assimilated into land surface models (Bosilovich et al. 2007; Reichle et al. 2010; Ghent et al. 2010) with the aim of improving numerical weather and climate model predictions.

The wide range of possible applications for which LST is a key variable makes the compilation of a long-term homogeneous LST climate data record (CDR) highly desirable (GCOS 2011). Instruments onboard geostationary satellites are ideal to measure large-scale LST (Heidinger et al. 2013) since those are subject to strong diurnal variation (Garand 2003; Göttsche and Olesen 2009), and therefore a good choice to produce a LST CDR. Geostationary LST climate data records like the International Satellite Cloud Climatology Project (ISCCP) (Rossow and Schiffer 1999) and the Pathfinder Atmospheres-Extended dataset (PATMOS-x) (Heidinger et al. 2013) are already available. However, the global ISCCP LST CDR is limited by its spatial and temporal resolutions of 30-km and 3 hours (Rossow and Schiffer 1999), respectively, and by estimating LST by assuming all pixels has a black body (unitary emissivity), which may lead to LST retrieval errors particularly

in dry regions (Freitas et al. 2010). These limitations arise since the primary goal of the ISCCP analysis was the retrieval of cloud properties. On the other hand, PATMOS-x geostationary LST CDR is available for the Geostationary Operational Environmental Satellite (GOES) disk, which only encompasses North and South America.

Instruments onboard the European Organization for the Exploitation of Meteorological Satellites (EUMETSAT) Meteosat First (MFG) and Second (MSG) Generation satellites provide the opportunity to compile a CDR with more than three decades of LST data (from 1983 onwards) with a 30-min temporal and 5-km spatial resolution over the Meteosat disk (enclosing Africa and Europe). However, the instrument onboard MFG satellites (Meteosat Visible and Infra-Red Imager, MVIRI) does not have the same characteristic as the one onboards MSG satellites (Spinning Enhanced Visible and Infra-Red Imager, SEVIRI). In particular, MVIRI is equipped with a single thermal infrared channel, while SEVIRI is equipped with two thermal infrared channels. To ensure consistency across all Meteosat satellites a single channel LST retrieval algorithm must be used. A consistent retrieval approach maximises long-term and inter-satellite consistency (Heidinger et al. 2013).

The Generalized Split-Windows (GSW) (Wan and Dozier 1996; Trigo et al. 2008a) algorithm is employed by most state-of-the-art satellite-based LST retrieval models, such as the one from the Satellite Application Facility on Land Surface Analysis (LSA SAF). In this algorithm the atmospheric absorption is estimated through a two thermal infrared channel regression of top-of-atmosphere (TOA) brightness temperatures. This atmospheric correction is less dependent on atmospheric ancillary data than single channel algorithms. The latter algorithms are fully dependent of ancillary data from numerical weather prediction (NWP) models to estimate the atmospheric state. These range from Statistical Mono-Window (SMW) algorithms, which use the observed 11-μm TOA radiance, the total column water vapor (TCWV) from NWP models and *a priori* fitted LST model parameters (Sun et al. 2004; Jiménez-Muñoz and Sobrino 2003) to Physical Mono-Window (PMW) algorithms, which are based on radiative transfer models (RTMs; Heidinger et al. 2013; Reutter et al. 1994; Scarino et al. 2013). Since PMW algorithms run RTMs for each satellite observation, while SMW algorithms estimate the correction

term using a previously calibrated look up table of statistical coefficients, it is expected that the PMW requires a significantly larger processing time than SMW. Previous works reported LST accuracies of 1–2 K for GSW (Freitas et al. 2010; Yu et al. 2014), a maximum of 2.5 K for PMW (Heidinger et al. 2013; Scarino et al. 2013) and 2–4 K for SMW (Freitas et al. 2013). However, these performance metrics found in the literature are not comparable, since they were estimated for different satellite sensors with different viewing geometries, with variations in instrument calibration and different validation sets of data for a physical parameter (LST), which is highly variable in time and space (Heidinger et al. 2013; Göttsche and Olesen 2009, 2001). With the aim of performing a study of the achievable accuracy of Meteosat single channel LST retrieval algorithms the calibration and validation settings must be comparable. The objective of this chapter is to understand if the accuracy of the single channel algorithms is comparable to the accuracy of the GSW; to investigate which of the single channel algorithms (SMW and PMW) present the best results; and to characterise uncertainties for the single channel Meteosat LST retrievals. The expected algorithm uncertainties are tested with a series of sensitivity analysis, where propagation of input errors towards the final LST is considered and algorithm calibration and limitations are assessed. A brief analysis of the impact of the calibration databases on the statistical methods (GSW and SMW) is also investigated. Finally, a comprehensive summary of the comparison of LST derived with GSW, SMW and PMW against more than 60,000 in situ LST measurements from four dedicated LST validation stations (located in different climate zones including dry to very moist atmospheres) operated by the Karlsruhe Institute of Technology (KIT), is presented.

3.2. Data and Mehods

3.2.1. Satellite Data

Data used in this chapter is from the EUMETSAT MSG satellite. The MSG satellite carries the Spinning Enhanced Visible and Infrared Imager (SEVIRI), a radiometer that measures the Earth every 15 min with a footprint of about 3 km at nadir. MSG is positioned at 0° longitude over the Equator and views KIT's four validation stations at low (25°, Dahra site) to moderate satellite viewing angles (45°,

Evora site). LST was estimated in this study from TOA radiances of SEVIRI's 10.8-μm channel.

The LSA SAF provided MSG-2 TOA 10.8-μm brightness temperatures, the LSA SAF cloud mask, the LSA SAF surface emissivity and the LSA SAF GSW LST retrieval on a 3 × 3 pixel window centred on the ground stations for the year 2010. The extracted time series had a temporal resolution of 15 minutes. The CM SAF team collocated satellite data and available KIT *in situ* measurements from the year 2010 and ran a PMW and a SMW model using the TOA 10.8-μm brightness temperature together with the LSA SAF surface emissivity. The CM SAF team only considered satellite data that were classified as cloud free in the entire 3 × 3 pixel window by the cloud masking. Overall, this analysis included about 60,000 collocated in situ and satellite observations. The in-situ data, as well as the different LST models are described in detail in the following subsections.

3.2.2. Generalized Split-Windows

The LSA SAF applies the GSW model with a formulation similar to that proposed by Wan and Dozier (Wan and Dozier 1996; Trigo et al. 2008a) and adapted by Trigo et al. (Trigo et al. 2009) and (Freitas et al. 2010) to the SEVIRI split-window channels. LST is obtained through a semi-empirical regression of SEVIRI 10.8- and 12.0-μm TOA brightness temperatures, where the correction of atmospheric influences is based on the different absorption of two adjacent infra-red bands (Freitas et al. 2010). The LST is estimated through a linear regression of the split-window TOA brightness temperatures. The regression coefficients depend explicitly on the land surface emissivity and implicitly on the TCWV obtained from the European Centre for Medium-Range Weather Forecasts (ECMWF) operational forecasts and the satellite view zenith angles (VZA) (Trigo et al. 2009). The surface emissivity is provided for the split-window channels using a method based on the fraction of vegetation cover (FVC), also estimated by the LSA SAF from SEVIRI visible and near-infrared channels (Freitas et al. 2010; Peres and DaCamara 2005). Thus, the emissivity computation is driven by the vegetation state and takes into account daily FVC estimates from SEVIRI measurements and a global land cover classification (Freitas et al. 2010; Peres and DaCamara 2005).

Reported uncertainties for the LSA SAF LST dataset are in the range of 1–2 K (Freitas et al. 2010), except for very moist atmospheres. A detailed description of the LSA SAF model can be found in the corresponding Algorithm Theoretical Base Document (Trigo et al. 2009); see also (Freitas et al. 2010). LST data from the LSA SAF archive is used for model inter-comparisons, which is labelled "GSW" LST in the following subsections.

3.2.3. Physical Mono-Window

A PMW model is applied to the Meteosat time series as described in Section 2.1. The PMW model used here is based on radiative transfer runs. Radiative transfer models can be used to estimate the upward and downward atmospheric path radiance ($L_i^{a_u}$, $L_i^{a_d}$) and the atmospheric transmittance (τ_i) in the thermal infrared for a specific atmospheric profile (Reutter et al. 1994). The downward atmospheric path radiance ($L_i^{a_d}$) is the hemispherically-averaged downward radiance. Approximating the Earth's surface as a Lambertian emitter-reflector and neglecting atmospheric scattering, the radiance $L_i(\theta, \phi)$ recorded in channel i of a sensor onboard a satellite observing the Earth's surface under view zenith θ and azimuthal ϕ angles may be written as (e.g., Li et al. 2013):

$$L_i(\theta,\phi) = \underbrace{\varepsilon_i(\theta,\phi)B_i(LST)\tau_i(\theta,\phi)}_{(1)} + \underbrace{[1-\varepsilon_i(\theta,\phi)]L_i^{a_d}\tau_i(\theta,\phi)}_{(3)} + \\ + \underbrace{L_i^{a_u}(\theta,\phi)}_{(5)} \qquad \text{Eq. 2.3}$$

where ε_i and LST denote land surface emissivity and land surface temperature, respectively. The calibrated Planck function B_i (LST) provides the radiance emitted by a blackbody at temperature LST in channel i. The parameters τ_i, $L_i^{a\uparrow}$ and $L_i^{a\downarrow}$ in Eq. 2.3 are the corresponding surface to top of the atmosphere (TOA) transmittance and the atmospheric upward and downward radiances, respectively. These three parameters can be estimated based on the atmospheric humidity and temperature profiles. For a channel of finite spectral band width, the calibrated Planck function in the frequency domain may be approximated as:

$$B_i(LST) \approx \frac{c_1 \nu_i^3}{exp\left(\frac{c_2 \nu_i}{\gamma LST + \eta}\right) - 1} \qquad \text{Eq. 3.1}$$

where c_1, c_2 are constants and γ, η and ν_i depend on the spectral characteristics of the channel to be used.

Inverting Eq. 2.3 and Eq. 3.1 (see, e.g., Yu et al. 2014; Li et al. 2013), the thermal radiance $L_i(\theta, \phi)$ measured at the sensor level can then be used to estimate LST:

$$LST \approx \left(\frac{c_2 \nu_i}{ln\left(\frac{c_1 \nu_i^3 \tau_i(\theta,\phi)\varepsilon_i(\theta,\phi)}{L_i(\theta,\phi) - L_i^{a\uparrow}(\theta,\phi) - [1-\varepsilon_i(\theta,\phi)]L_i^{a\downarrow}\tau_i(\theta,\phi)} + 1\right)} - \eta \right) / \gamma \qquad \text{Eq. 3.2}$$

The PMW LST in this study was estimated with Eq. 3.2 for SEVIRI 10.8-µm clear-sky TOA brightness temperatures described in subsection 3.2.1, together with surface emissivities (ε_i) taken from the operational LSA SAF dataset (Trigo et al. 2008b). Values of $L_i^{a_u}(\theta, \phi)$, $L_i^{a_d}$ and $\tau_i(\theta, \phi)$ were obtained via the Radiative Transfer for the Television Infrared Observation Satellite Operational Vertical Sounder code (RTTOV, Version 11.2), which is a fast-radiative transfer model used operationally at the ECMWF (Saunders et al. 1999). RTTOV is significantly faster than the commonly-used Moderate Resolution Atmospheric Transmission (MODTRAN) line-by-line radiative transfer code (Berk et al. 1999). It uses pre-computed transmittance look-up-tables (LUTs) calculated from a spectroscopic database (Hocking et al.). PMWs require radiative transfer runs during the satellite data processing. For large data processing, it is hence crucial to run a fast-radiative transfer model. Bento (2013) has compared simulated MODTRAN and RTTOV TOA brightness temperatures and reports an overall bias of about 0.2 K in the SEVIRI spectral range, which is close to the SEVIRI instrumental noise.

RTTOV runs performed in this study used atmospheric profiles (temperature and specific humidity) from the ECMWF ERA-Interim reanalysis dataset as input (Dee et al. 2011), which are available 6-hourly at a spatial resolution of about 75 km. RTTOV simulations for model atmospheres with 21 pressure levels (1000–1

hPa) were performed using the ERA-Interim profiles closest in time and space to each satellite observation.

3.2.4. Statistical Mono-Window

The third tested LST model is a SMW model. SMWs consist of empirical approaches that relate TOA brightness temperatures of a single atmospheric window channel to LST (Sun et al. 2004; Freitas et al. 2013; Li et al. 2013), generally via a simple linear regression.

Considering Eq. 2.3 and dropping the azimuth term ϕ for simplicity and assuming that: TOA radiance depends on brightness temperature T_b; that term (5) depends on temperature in each atmospheric layer T_j; and that the TOA radiance may be approximated by the Planck distribution; the RTE may be written as:

$$B_i(\theta, T_b) = \varepsilon_i(\theta) B_i(LST) \tau_i(\theta) + [1 - \varepsilon_i(\theta)] L_i^{a_d} \tau_i(\theta) + \\ + L_i^{a_u}(\theta, T) \qquad \text{Eq. 3.3}$$

Then, assuming a mean atmospheric temperature $\overline{T_a}$, and that each atmospheric layer j may be approximated to a black body and then applying the mean-value theorem to radiance emitted by each atmospheric layer:

$$L_i^{a_u}(\theta, T) = \int_{\tau_i}^{1} B_{i,j}(\theta, T_j)\, d\tau = [1 - \tau_i(\theta)] B_i(\theta, \overline{T_a}) \qquad \text{Eq. 3.4}$$

Writing the downwelling term in its integral form and applying the same reasoning, then:

$$[1 - \varepsilon_i(\theta)] L_i^{a_d} \tau_i(\theta) = [1 - \varepsilon_i(\theta)] \tau_i^2(\theta) \int_{\tau_i}^{1} \frac{B_{i,j}(\theta, T_j)}{\tau_{i,j}^2(\theta)} d\tau \qquad \text{Eq. 3.5}$$

$$[1 - \varepsilon_i(\theta)] L_i^{a_d} \tau_i(\theta) = \tau_i(\theta) [1 - \tau_i(\theta)] B_i(\theta, \overline{T_a}) [1 - \varepsilon_i(\theta)] \qquad \text{Eq. 3.6}$$

Using a Taylor series to expand Planck's distribution around some temperature T_* near T_b, LST and $\overline{T_a}$:

$$B_i(\theta, LST) \approx B_i(\theta, T_*) + \frac{\partial B_i(\theta, T_*)}{\partial T}(LST - T_*) \quad \text{Eq. 3.7}$$

$$B_i(\theta, T_b) \approx B_i(\theta, T_*) + \frac{\partial B_i(\theta, T_*)}{\partial T}(T_b - T_*) \quad \text{Eq. 3.8}$$

$$B_i(\theta, \overline{T_a}) \approx B_i(\theta, T_*) + \frac{\partial B_i(\theta, T_*)}{\partial T}(\overline{T_a} - T_*) \quad \text{Eq. 3.9}$$

Substituting Eq. 3.4 and Eq. 3.6 on Eq. 3.3 and rearranging terms:

$$B_i(\theta, T_b) = \varepsilon_i(\theta) B_i(LST)\tau_i(\theta) + \\ +[1 - \tau_i(\theta)] B_i(\theta, \overline{T_a})\left[1 + \left(1 - \varepsilon_i(\theta)\right)\tau_i\right] \quad \text{Eq. 3.10}$$

Then, merging Eq. 3.7, Eq. 3.8 and Eq. 3.9 with Eq. 3.10, neglecting τ_i^2 and rearranging terms, the equation becomes:

$$\frac{\partial B_i(\theta, T_*)}{\partial T}(T_b - T_*) = \\ = \varepsilon_i(\theta)\tau_i(\theta)\frac{\partial B_i(\theta, T_*)}{\partial T}(LST - T_*) + \\ +[1 - \tau_i(\theta)]\left[1 + \left(1 - \varepsilon_i(\theta)\right)\tau_i\right]\frac{\partial B_i(\theta, T_*)}{\partial T}(\overline{T_a} - T_*) \quad \text{Eq. 3.11}$$

Eliminating the derivatives:

$$(T_b - T_*) = \varepsilon_i(\theta)\tau_i(\theta)(LST - T_*) + \\ +[1 - \tau_i(\theta)]\left[1 + \left(1 - \varepsilon_i(\theta)\right)\tau_i\right](\overline{T_a} - T_*) \quad \text{Eq. 3.12}$$

Solving for LST and rearranging the terms dependent on T_b, $\overline{T_a}$ and T_*:

$$LST = \frac{1}{\varepsilon_i(\theta)\tau_i(\theta)}T_b - \frac{1}{\varepsilon_i(\theta)\tau_i(\theta)}T_* + T_* - \frac{1}{\varepsilon_i(\theta)\tau_i(\theta)}\overline{T_a} + \\ +\overline{T_a} + \frac{1}{\varepsilon_i(\theta)\tau_i(\theta)}T_* - T_* \quad \text{Eq. 3.13}$$

Rearranging and simplifying Eq. 3.13:

$$LST = \frac{1}{\varepsilon_i(\theta)\tau_i(\theta)}T_b - \frac{1}{\varepsilon_i(\theta)\tau_i(\theta)}\overline{T_a} + \overline{T_a} \quad \text{Eq. 3.14}$$

Since transmissivity is a function of only TCWV and VZA and $\overline{T_a}$ is a function of only TCWV, the two terms may be replaced by coefficients:

$$a_1 = \frac{1}{\tau_i(\theta)} \quad \text{Eq. 3.15}$$

$$a_2 = -\frac{\overline{T_a}}{\tau_i(\theta)} \quad \text{Eq. 3.16}$$

$$a_3 = \overline{T_a} \quad \text{Eq. 3.17}$$

Finally, Eq. 3.14 may be written as:

$$LST(\theta,\phi) = a_1 \frac{T_b(\theta,\phi)}{\varepsilon_i(\theta,\phi)} + a_2 \frac{1}{\varepsilon_i(\theta,\phi)} + a_3 \quad \text{Eq. 3.18}$$

where $T_b(\theta,\phi)$ is the TOA brightness temperature in channel i and $\varepsilon_i(\theta,\phi)$ stands for the corresponding spectral surface emissivity.

The regression coefficients a_1, a_2 and a_3 are estimated for different classes of TCWV and VZA. Following Freitas et al. (2010) for the operational LSA SAF GSW model and Freitas et al. (2013) for a single-channel LST model for the GOES satellite series, the calibration/validation of Eq. 3.18 made use of synthetic radiances obtained with the radiative transfer model MODTRAN 4.0. We selected MODTRAN and not RTTOV to tune the SMW model, as we assume the line-by-line MODTRAN model to be slightly more accurate than the "broad band" RTTOV model. In contrast to the PMW model, the processing speed of the radiative transfer model is less relevant for SMW, as the radiative transfer simulations are only computed once to establish the model coefficients.

3.2.5. Theoretical Uncertainty Characterisation

In order to ensure a good fit under all possible conditions, a study to determine the best algorithm calibration dataset is developed. After choosing the best calibration dataset the potential LST retrieval errors were assessed using the remaining synthetic validation database further described in subsection 3.3.1, which contained over 15,000 independent simulations. For the uncertainty analysis

presented in this study, we followed the approach of Freitas et al. 2010. We provided TOA brightness temperatures, surface and atmospheric information from the database as input to the SMW and PMW model; the calculated LST output was then compared with the corresponding ("true") surface temperature from the database. In addition to the model error, we assessed the sensitivity of the SMW and PMW to radiometric noise, uncertainty in surface emissivity and NWP by superimposing artificial errors to PMW and SMW inputs.

The value used for SEVIRI 10.8-μm radiometric noise is based on radiometric performances for SEVIRI IR 10.8-μm compared to the Infrared Atmospheric Sounding Interferometer (IASI) (bias <0.2 K) (Hewison and König 2008). Values for noise in brightness temperature were generated from a uniform random distribution within the conservative interval (−0.3 K, 0.3 K).

For the estimation of the surface emissivity error, we took into account that bare ground and semiarid surfaces (generally with lower emissivities) present higher variability and, therefore, higher uncertainty than areas covered by vegetation. As such, emissivity uncertainties used in this study were obtained from random uniform distributions within the intervals (−0.04, 0.04) for $\varepsilon_c < 0.95$, (−0.02, 0.04) for $0.95 \leq \varepsilon_c < 0.98$ and (−0.01, 0.01) for $\varepsilon_c \geq 0.98$ The rationale for this choice is based on emissivity variability for bare ground surfaces ($\varepsilon_c < 0.95$), sparsely- ($0.95 \leq \varepsilon_c < 0.98$) and densely- ($\varepsilon_c \geq 0.98$) vegetated areas (Freitas et al. 2010).

The PMW model requires a characterisation of the errors associated with the atmospheric profiles. Since these are obtained from ERA-Interim nearest in space and time to the satellite observation, we assume that the uncertainty in collocation may be used as a measure of the profile uncertainty. Thus, the impact of profile errors on retrieved LST values was estimated by replacing the profiles at hour h by the corresponding ones at hour $h + 6$. A similar procedure was used to determine the impact of TCWV errors on LST estimates from the SMW. It is worth recalling that TCWV is an implicit input to the SMW: this variable is used to determine the regression coefficients (Eq. 3.18). Therefore, and as explained in detail in (Freitas et al. 2010), studies of the impact of TCWV uncertainties on LST need to combine:

(1) the effect on the LST estimate due to the choice of the wrong set of coefficients; and (2) the probability of that event.

3.2.6. Ground-Based LST Measurements

The KIT operates four permanent validation stations for satellite-based LST retrieval. These stations were specifically chosen and designed to validate LST derived from MSG/SEVIRI and are located in large homogenous areas within the field of view of the METEOSAT satellites and lie in different climate regions, which provides a broad range of atmospheric conditions for product validation (Göttsche et al. 2013). Figure 3.1 shows the locations of the four validation stations on the SEVIRI Earth disk. An overview of the KITs validation sites is provided in Table 3.1.

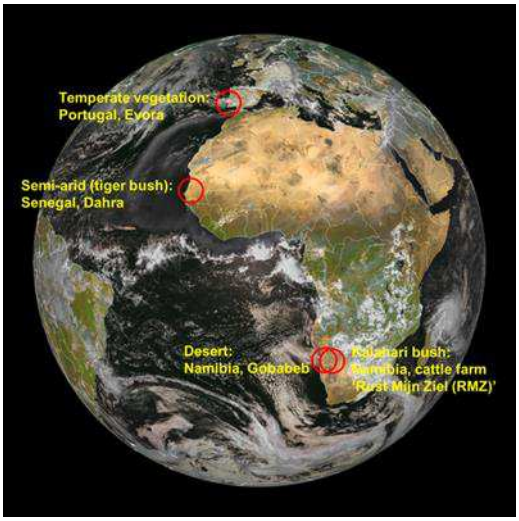

Figure 3.1 – Locations of the Karlsruhe Institute of Technology's (KIT) validation stations on the Meteosat Second Generation (MSG)/Spinning Enhanced Visible and Infrared Imager (SEVIRI) disk.

Theoretically, LST datasets can be validated with ground-truth radiometric measurements. However, this so-called 'temperature-based validation' is largely complicated by the spatial scale mismatch between satellite- and ground-based sensors: areas observed by ground radiometers usually cover about 10 m^2, whereas satellite measurements in the thermal infrared typically cover between 1 km^2 and 100 km^2 (Göttsche et al. 2013). Furthermore, natural land covers and the corresponding land surface temperatures are spatially quite heterogeneous. Then, for validation measurements to be representative for satellite-derived LST, they

must be performed in areas that are homogenous at the satellite pixel scale. The size of the area that needs to be viewed by the validation instrument at the ground depends on the within-pixel variability of the surface and on how well measurements of several "end members" can be mixed in order to obtain a representative value for the satellite pixel. This so-called end-member-cover method is based on a linear spectral mixing approach and assumes that the total IR radiance emitted by the land surface within a satellite pixel can be reasonably well approximated by a linear mixture of the IR radiance emitted by the relevant surface cover types within that area (Bork-Unkelbach 2012). The mixing of measurements obtained for different end-members requires information on their respective fractions within the sensor's field of view and also on scene emissivity (Trigo et al. 2008b; Göttsche and Hulley 2012; Kabsch et al. 2008). At KIT's validation sites, the relevant spectral end-members (e.g., trees, grassland and background soil) were determined from an independent component analysis of high-resolution satellite data (visible and near-infrared). The fractional coverages of the determined end-members were then obtained by land cover classification (Bork-Unkelbach 2012).

Table 3.1 – Overview of KITs validation stations.

	Dahra	**RMZ**	**Gobabeb**	**Evora**
Location	Senegal Lat: 15.402336 Lon: −15.432744	Namibia Lat: −23.010532 Lon:18.352897	Namibia Lat: −23.550956 Lon: 15.05138	Portugal Lat: 38.540244 Lon: −8.003368
Elevation	90 m	1450 m	406 m	230 m
Climate Zone	Tropical Wet Dry	Steppe	Desert	Mediterranean
TCWV 2010	17 to 56 mm	2 to 28 mm	1 to 38 mm	2 to 43 mm
Vegetation	Grassland; 96% grass, 4% tree	Savanna; 86% grass/soil, 15% tree	Baren; 32% tree; 68% grass	Woody savanna with isolated groups of evergreen oak trees

Accurate estimations of land surface emissivity (LSE) are essential for obtaining satellite LST products, but also for limiting the uncertainty of ground-based LST estimates. Especially sites with larger fractions of bare ground are prone

to be misrepresented in satellite-retrieved LSEs: comparisons with *in situ* LSE revealed that over arid regions, satellite-retrieved LSEs differ by more than 3% (Göttsche and Hulley 2012). Since for vegetated sites, LSE is a dynamic quantity, LSA-SAF's daily LSE is used to derive *in situ* LST from the *in situ* radiance measurements at Dahra (Senegal, tiger bush, 45 m a.s.l.), Rust Mijn Ziel (RMZ) (Namibia, Kalahari bush, 1450 m a.s.l.) and Evora (Portugal, cork-oak tree forest, 230 m a.s.l.). *In situ* LST at the desert site Gobabeb (Namibia, gravel plains, 450 m a.s.l.) is derived using a static emissivity obtained from *in situ* measurements (Göttsche and Hulley 2012).

3.3. Results and Discussion

3.3.1. The Impact of the Calibration Database on Statistical Models[2]

As mentioned in the previous section, GSW and SMW are algorithms that retrieve LST through semi-empirical linear regressions between TOA brightness temperature and LST in a combination of two TIR channels (in the case of GSW) or on a single TIR channel (in the case of SMW). These regressions are performed using ancillary data like TCWV and VZA, which are typically divided in classes, and for each combination a set of coefficients is estimated (Freitas et al. 2013; Li et al. 2013). This procedure requires setting up a comprehensive database for the calibration of the coefficients. However, the choice of this calibration dataset is crucial to the accuracy of the retrieval algorithms, since there is a high risk of leaving out unforeseen situations that lead to systematic retrieval errors. Hence, a good calibration database to fit the coefficients of Eq. 2.5 and Eq. 3.18 must ensure that each artificial pixel (designed for the calibration) is observed by a wide range of VZAs and has a variety of water vapour profiles associated to it (with different boundary layers). Here water vapour is the only atmospheric gas considered since it is the most important absorber and emitter of radiation in the TIR window. The calibration dataset also must take in account the possibility of temperature

[2] Adapted from Martins, J. P. A., Trigo, I. F., Bento, V. A., DaCamara, C. C. A Physically Constrained Calibration Database for Land Surface Temperature Using Infrared Retrieval Algorithms. Remote Sens. 2016, 8, 808; doi:10.3390/rs8100808. Full version of the paper may be found on Annex A.

inversions close to the surface. This effect may be taken in account if several profiles from different locations and times are associated to the artificial pixel, or by artificially varying the differences between LST and the near-surface air temperature ($LST - T_{air}$). Finally, the emissivity difference in Eq. 2.5 is also an important factor to be taken in account when choosing a calibration dataset.

Martins et al. (2016) performed an exhaustive study using a collection of more than 15,000 clear-sky profiles of temperature, water vapor and ozone, with its respective ancillary data, which consists of spectral emissivity, land cover, elevation, skin temperature and surface pressure. These profiles were compiled by Borbas et al. (2005; the SeeBor dataset). Figure 3.2 shows the distribution of TCWV and skin temperature on the SeeBor dataset, and also shows its bivariate distribution.

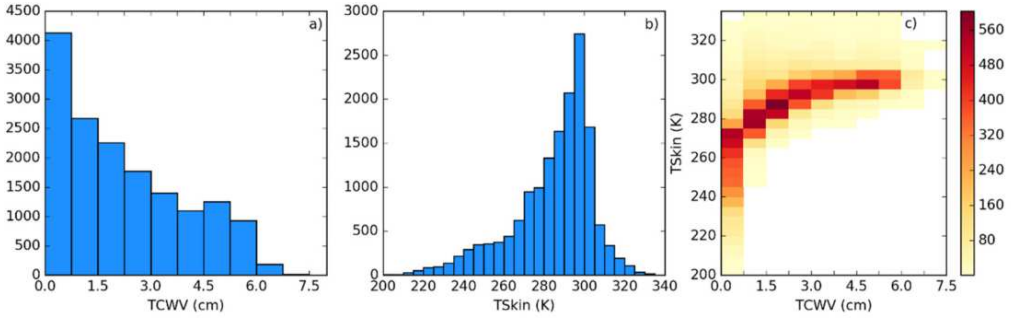

Figure 3.2 – Distribution of (a) TCWV and (b) skin temperature on the SeeBor dataset; (c) bivariate distribution of the previous parameters.

From this dataset of atmospheric profiles and respective ancillary data, only a few are chosen to calibrate LST retrieval algorithms, while the remaining profiles are used for model validation. Following a set of steps (see full article in Annex A) the number of profiles used to calibrate the algorithms is 116, and after changing each profile ground conditions the total number of cases used to calibrate rises to near 900,000. Figure 3.3 shows the same as Figure 3.2 but for the calibration dataset alone. This will be called the baseline calibration dataset.

The calibration database used to fit the coefficients of the SMW algorithm followed the outcome of set of experiments designed precisely to study the sensitivity of different LST algorithms to the calibration set. As further detailed in Martins et al. (2016), these experiments included considering a flat distribution of

TCWV changing the number of chosen profiles, and changing the difference of $LST - T_{air}$ by varying its lower and upper limits using steps of 5 K. Results show that for both GSW and SMW error metrics are very similar for all the calibration dataset experiments (for a detailed review of the experiments and its errors see full article in Annex A), and as such, designing an algorithm calibration dataset that would lead to a good fit under all possible conditions is not an easy task. With this in mind, the calibration dataset chosen to use in the remaining of this chapter will be the baseline built with 116 profiles with TCWV distribution shown in Figure 3.3 and with a range of $LST - T_{air}$ from -15 to 15 K.

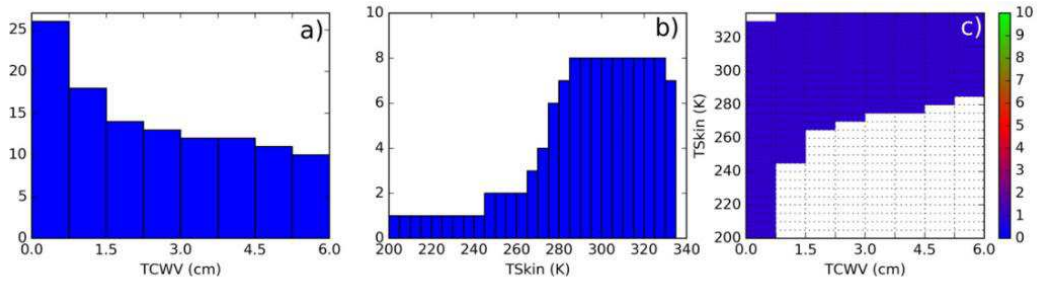

Figure 3.3 – Distribution of (a) TCWV and (b) skin temperature on the calibration dataset; (c) bivariate distribution of the previous parameters.

MODTRAN simulations were performed for the baseline training dataset to determine the SMW coefficients (Eq. 3.18); and for the independent dataset for model validation. A total of over 845,000 simulations were obtained for SMW by varying the viewing geometry and surface conditions for each profile over the following ranges: (1) VZA from 0°–75°; (2) surface emissivity between 0.926 and 0.998; and (3) surface temperatures ranging from near surface air temperature minus 15 K to near surface air temperature plus 15 K. Following the approach of Freitas et al. (2013), coefficients a_1, a_2 and a_3 in Eq. 3.18 were then determined for 8 different TCWV classes (0 cm–6 cm in steps of 7.5 mm) and 15 VZA classes (0°–75° in steps of 5°).

3.3.2. Theoretical Uncertainty Analysis

The total impact of model and input uncertainties, including uncertainties in surface emissivity, NWP and sensor calibration, measured as the root mean square difference (RMSD) of retrieved LST versus the "true" surface temperature in the

database, is presented in Figure 3.4 for different values of VZA and TCWV. RMSD and bias obtained for the validation database are shown in Table 3.2.

The 2 K target accuracy (RMSD) of the LSA SAF LST dataset is reached for the majority of angles and TCWV classes for PMW and SMW, degrading into larger errors for very moist atmospheres with high angles, i.e., for very large optical paths. The slopes of the lines in Figure 3.4 suggest that TCWV errors are most relevant for low-to-moderate view angles. For very moist atmospheres ($TCWV > 50$ mm) and high viewing angles ($VZA > 55$ mm), the SMW performed slightly better than the PMW. We hypothesise that this reflects the implicit sensitivity of the PMW to the NWP input: (Freitas et al. 2010) showed that uncertainties in atmospheric profiles can have a strong impact on LST retrievals. While SMWs only require TCWV as input, PMWs require atmospheric temperature and water vapor profiles, which can introduce additional uncertainties, especially for very moist atmospheres. We found that LST errors associated with emissivity uncertainties are expected to be within 1.0 K and 2.8 K in 90% of the estimates obtained with the SWM and PWM model, respectively. However, the impact of emissivity in both models is much smaller under moist atmospheres.

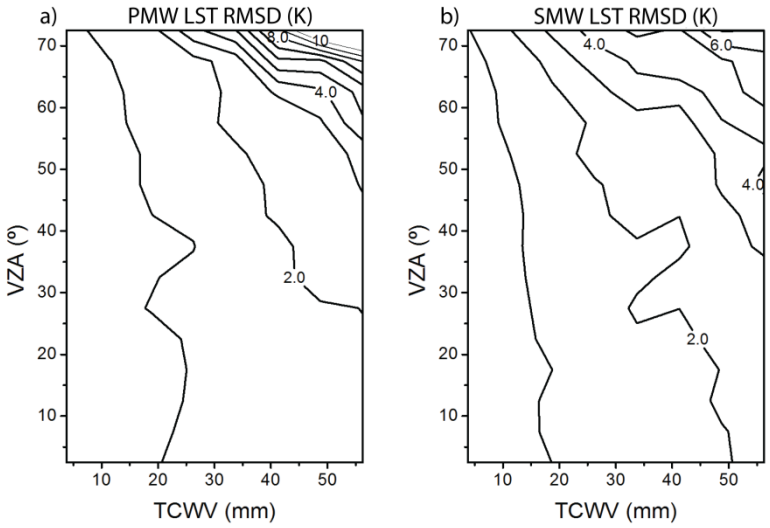

Figure 3.4 – Theoretical uncertainty for MSG/SEVIRI LST estimates. (a) Physical radiative transfer-based mono-window model (PMW); (b) statistical mono-window model (SMW). The values are the root mean square differences, assuming model and input uncertainties. VZA, satellite viewing angle.

The PMW and SMW uncertainties we simulated for $TCWV \leq 45$ mm (RMSD of 1.6 K) more or less correspond to the uncertainties reported by Freitas

et al. (2010) for GSW. For moister atmospheres (TCWV > 45 mm) the PMW and SMW uncertainties (RMSD of up to 10 K and 6 K, respectively) significantly exceed the simulated GSW uncertainties (maximum error about 4.5 K; (Freitas et al. 2010)), particularly for high VZAs. This very likely demonstrates the different sensitivity of the single-channel and GSW models to uncertainties related to inaccurate NWP input. Single-channel models rely entirely on NWP data to estimate the atmospheric state, while the two split-window channels provide additional information about the atmospheric absorption for the GSW model (Heidinger et al. 2013).

Table 3.2 – Theoretical uncertainty for MSG/SEVIRI LST estimates for the PMW and SMW. RMSD and bias associated with both model and input uncertainty.

	PMW		**SMW**	
	RMSD (K)	Bias (K)	RMSD (K)	Bias (K)
TCWV ≤ 45 mm	1.6	-0.2	1.6	-0.1
TCWV > 45 mm	3.3	-1.1	3.4	-0.6

3.3.3. Ground-Based Validation[3]

The results presented above correspond to an assessment of the expected LST uncertainty considering the propagation of input errors and the performance of the PMW and SMW algorithms under different retrieval conditions. To complement that analysis, this section presents the outcome of a brief validation exercise, where actual LST estimates using the mono-channel algorithms were compared against ground observations gathered at KIT stations (Duguay-Tetzlaff et al. 2015). For completeness, these results are shown together with the comparison of LSA-SAF LST product, derived using a GSW (Freitas et al. 2010). The single channel algorithms match the accuracy of GSW for a range of atmospheric conditions

[3] This section of the paper was mainly developed by the CM-SAF team lead by Anke Duguay-Tetzlaff. For that reason, only a brief discussion of the results is presented in this thesis. For the complete version of the paper, see Annex B.

(Figure 3.5). Tables 3.3. and 3.4 show the error metrics between model and in situ LST for TCWV up to 45 mm and above 45 mm, respectively.

Tables 3.3 and 3.4 show that observed RMSD matches the theoretical uncertainties (subsection 3.3.2) to within 0.3–1 K for dry to medium-moist atmospheres. Slightly larger RMSDs may reflect uncertainty and scaling differences of the ground measurements which are not included in the theoretical uncertainty analysis performed in the previous subsection.

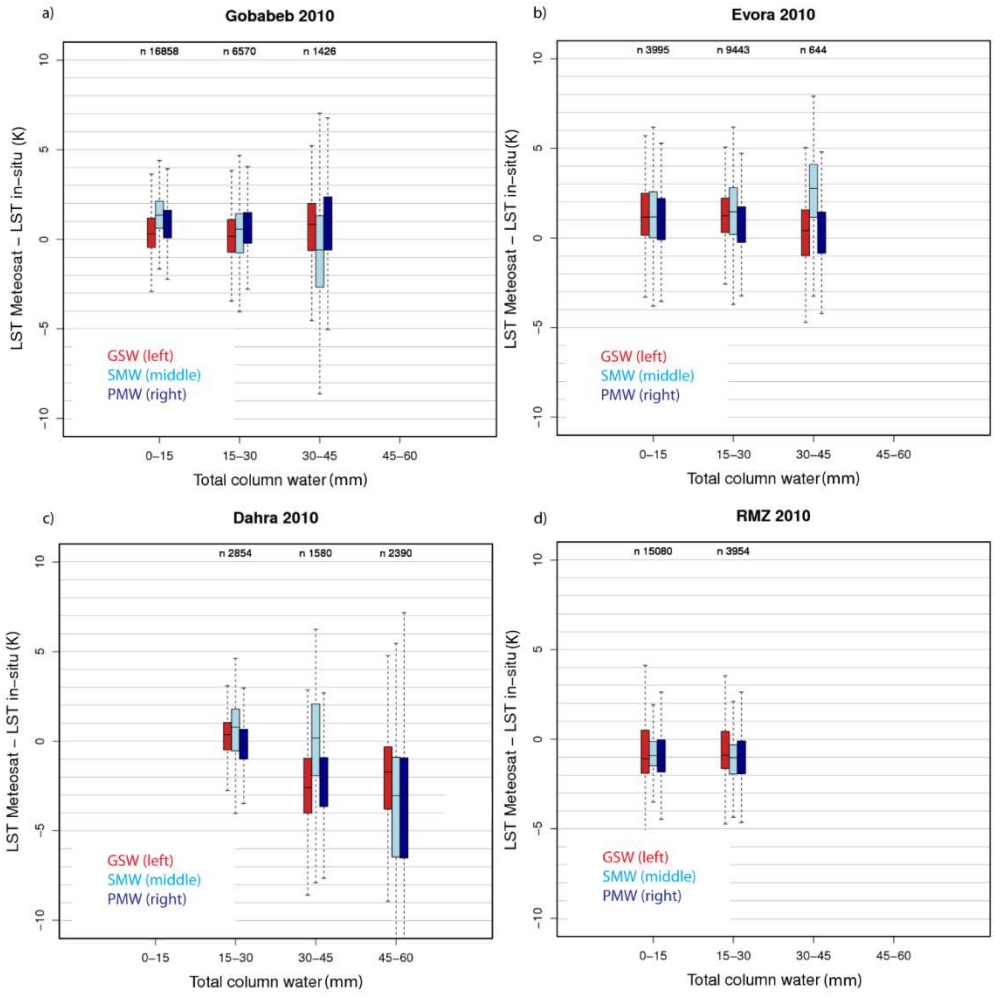

Figure 3.5 – Comparison of LST between in situ measurements from the KIT sites and Meteosat-based retrievals for different TCWV classes. The boxplots show the median, the first and third quartile with whiskers at the 95th and fifth percentiles. GSW: the Satellite Application Facility on Land Surface Analysis's (LSA SAF) operational GSW. (a) KIT Gobabeb station; (b) KIT Evora station; (c) KIT Dahra station; (d) KIT RMZ station.

Table 3.4 shows that for atmospheres with TCWV up to 45 mm (dry to medium-moist), RMSDs of the single channel algorithms range between 1.8 K and

2.6 K. These errors are close to the 2 K target accuracy of the GSW-based LSA SAF dataset. On Evora and RMZ sites, the PMW algorithm matches the accuracy of the GSW with RMSDs of 1.9 K (PMW) and 1.9–2.0 K (GSW) and is defined by an absolute bias below 1 K. For the sites of Gobabeb and Dahra, the PMW shows a RMSD of 1.8 K and 2.6 K, which is slightly less accurate than the GSW algorithm, with RMSD of 1.5 K and 2.3 K, while the SMW RMSD is up to 0.5 K larger (TCWV up to 45 mm; Table 3.4).

Table 3.3 – Statistics for the comparison of LST between in situ measurements and the operational LSA SAF dataset for dry to medium-moist atmospheres (TCWV ≤45 mm).

	GSW		**PMW**		**SMW**	
	RMSD (K)	Bias (K)	RMSD (K)	Bias (K)	RMSE (K)	Bias (K)
Gobabeb	1.5	0.4	1.8	0.8	2.0	0.9
Evora	2.0	1.2	1.9	0.7	2.5	1.4
Dahra	2.3	-0.8	2.6	-1.2	2.4	0.4
RMZ	1.9	-0.5	1.9	-0.8	1.7	-0.8

Yu et al. (2014) have recently compared PMW and GSW LSTs from the Landsat satellite against 41 ground observations from the Surface Radiation (SURFRAD) Budget Networking moderate climate zones. The authors have reported a higher accuracy for the PMW with a difference in RMSD of only 0.1 K when compared to GSW. These results are not in line with the analysis performed here. We show that PMW agrees with GSW to within 0.1–0.5 K for most atmospheric conditions tested here.

PMW and SMW have very similar performances in Gobabeb, RMZ and Dahra, with a Δ RMSD of 0.2 K, for TCWV below 45 mm. Conversely, for Evora site, the PMW had a 0.6 K lower RMSD and 0.7 K lower bias when compared with SMW. For very high TCWVs (greater than 45 mm), PMW shows a RMSD 1 K higher when compared to SMW at Dahra site. This may be due to cloud

contamination, which are not accounted in the theoretical uncertainty analysis, and/or uncertainties in NWP (ECMWF). In conclusion, the computationally-expensive PMW algorithm outperforms the SMW only at one out of four investigated stations.

Table 3.4 – Statistics for the comparison of LST between in situ measurements and the operational LSA SAF dataset for very moist atmospheres (TCWV >45 mm) experienced at the KIT 'Dahra' station.

	GSW		**PMW**		**SMW**	
	RMSD (K)	Bias (K)	RMSD (K)	Bias (K)	RMSE (K)	Bias (K)
Dahra	3.4	-2.2	6.3	-4.3	5.3	-3.0

3.4. Conclusions

Long-term LST climate data records with high temporal and spatial resolution are useful for climate monitoring and several climate applications (GCOS 2011). This requirement can be met by extending LST data records from geostationary satellites into the past. Since heritage sensors provide only one thermal infrared channel, multi-channel LST retrieval approaches, like the Generalized Split-Windows (GSW), cannot be used. In this study the performance of two single channel retrieval algorithms, developed for the geostationary Meteosat satellites, were evaluated – the physical mono-window (PMW) and the statistical mono-window (SMW) – with the objective of assessing if these algorithms can achieve the accuracy of the GSW currently operational in the LSA SAF.

A short analysis on the impact of the dataset chosen to calibrate the coefficients of the statistical algorithms is assessed. The different experiments performed showed that an ideal calibration dataset if very difficult to choose, having very similar error metrics. With that in mind, the chosen calibration was the baseline one, with 116 different profiles. The expected algorithm uncertainties, taking into account propagation of input errors and algorithm calibration was assessed and the 2 K target accuracy (RMSD) of the LSA SAF LST dataset is reached for the

majority of angles and TCWV classes for PMW and SMW, degrading into larger errors for very moist atmospheres with high viewing angles, i.e., for very large optical paths.

Finally, a summary of a comprehensive validation of LST derived by the three algorithms against more than 60,000 in situ observations is also presented, showing that, except for very moist atmospheres (TCWV greater than 45 mm), Meteosat single-channel retrievals are in agreement with those of the GSW algorithm by 0.1–0.5 K and are within (or very close to) the 2 K target accuracy of the LSA SAF LST. Furthermore, results show that most of MSG single-channel LSTs meet the 2–3 K "currently achievable performance" defined by the Global Climate Observing System (GCOS 2011). Plus, single channel algorithms have the added benefit of being capable of retrieving LST across Meteosat generations.

The results presented in this study suggest that the computationally more expensive PMW do not necessarily outperform SMW. A distinct higher accuracy (Δ RMSD >0.2 K) for the PMW compared to SMW was observed only at one at of four validation stations.

Possible improvements of the current PMW and SMW model will be addressed in the next chapter. The presented single-channel models might be improved by including an orographic correction for the atmospheric profiles and by an improved cloud screening in tropical regions.

The results presented here are strictly only valid for MSG, since the MFG thermal sensor has a slightly different spectral response function, a lower digital quantification and a less accurate absolute radiometric accuracy. Accordingly, the LST retrieval errors may be greater than the errors presented in this study. Inaccuracies arising from emissivity retrieval and satellite calibration were not considered here, despite their relevance for the quality of a Meteosat LST CDR. Therefore, future work needs to investigate these error sources. Although it might be difficult to remove inter-Meteosat calibration errors completely, the present work demonstrates that, for the investigated ground stations, LST retrievals from well-calibrated MFG data can reach the accuracy of LSA SAF's operational GSW.

Chapter 4

Once the development and validation of the retrieval algorithms to compile a Climate Data Record of Land Surface Temperature is achieved, the following step is to improve some of its aspects. This chapter focuses in the improvement of Land Surface Temperature retrievals over mountainous regions, where ERA-Interim reanalysis is prone to underestimate land surface altitude.

4. Improvement of LST retrieval algorithms over mountainous regions[4]

Abstract

Algorithms for Land Surface Temperature (LST) retrieval from infrared measurements are usually sensitive to the amount of water vapor present in the atmosphere. The Satellite Application Facilities on Climate Monitoring and Land Surface Analysis (CM SAF and LSA SAF) have been working on the compilation of 25-year LST Climate data record (CDR), which uses water vapor information from ERA-Int reanalysis. However, its relatively coarse spatial resolution may lead to systematic errors in the humidity profiles with implications in LST, particularly over mountainous areas. The present study compares LST estimated with three different retrieval algorithms: a radiative transfer-based mono-window (PMW), a statistical mono-window (SMW), and a Generalized Split-Windows (GSW). The algorithms are tested over the Alpine region, using ERA-Int reanalysis data and relying on the finer spatial scale COSMO model data as reference. Two methods are developed to correct ERA-Int water vapor misestimation: (1) an exponential parametrisation of total precipitable water (TPW) appropriate for SMW/GSW; and (2) a level reduction

[4] Adapted from Bento, V. A., DaCamara, C. C., Trigo, I. F., Martins, J. P. A., Duguay-Tetzlaff, A. Improving Land Surface Temperature Retrievals over Mountainous Regions. Remote Sens. 2017, 9, 38; doi:10.3390/rs9010038

method to be used in PMW. When ERA-Int TPW is used, the algorithm misses the right TPW class in 87% of the cases. When the exponential parametrisation is used, the missing class rate decreases to 9% and when the level reduction method is applied the PMW LST corrections may go up to 1.7 K over the study region. Overall the correction for pixel orography in TPW leads to corrections in LST estimations up to more than 1.5 K, which are relevant to ensure that long-term LST records meet climate requirements, particularly over mountainous regions.

4.1. Introduction

Land surface temperature (LST) is a crucial variable for environmental and climate studies. Together with surface emissivity, LST controls the surface upward thermal radiation. LST also partly controls the surface turbulent heat flux, which modulates the thermodynamic structure of the atmospheric boundary layer (Crago and Qualls 2014). Several studies pointed out the importance of LST in a range of applications, such as general model assessment (Trigo et al. 2003, 2015) data assimilation (Ghent et al. 2010; Reichle et al. 2010; Caparrini et al. 2004; Kalman 1960; Kalman and Bucy 1961), hydrology (Kustas and Norman 1996; Wan et al. 2004) and climate monitoring (Duguay-Tetzlaff et al. 2015; Siemann et al. 2016) among others.

Taking into account the growing interest in LST as an essential climate variable, the Satellite Application Facilities on Climate Monitoring and Land Surface Analysis (CM SAF and LSA SAF) are currently compiling a 25-year LST Climate data record (CDR) with an hourly temporal and 0.05 degree spatial resolutions (Duguay-Tetzlaff et al. 2015), using brightness temperatures measured by the European Organisation for the Exploitation of Meteorological Satellites (EUMETSAT) Meteosat First (MFG) and Second (MSG) Generation satellites. The atmospheric correction makes use of profiles of water vapor and temperature extracted from the European Centre for Medium-Range Weather Forecasts (ECMWF) reanalyses, namely Era-Int (Dee et al. 2011). One of the main advantages of such LST dataset is its high homogeneity, since the used retrieval algorithm and ancillary data are the same for the whole processing period, and the

process makes use of recent EUMETSAT efforts to recalibrate top-of-atmosphere radiances.

A main interest of such long records of remotely sensed LST is to complement the widely used near-surface air temperature in situ measurements in climate monitoring applications (Good 2015; Oyler et al. 2016). *In situ* data present large gaps and uncertainties where station density is low, e.g., over sparsely populated areas like deserts and mountains. According to a recent study (Mountain Research Initiative EDW Working Group 2015) there is growing evidence that the rate of warming is amplified with elevation. However, it has been extremely difficult to define the rate of warming in mountainous regions due to the lack of surface *in situ* measurements at high elevation sites (Lawrimore et al. 2011). This issue may be overcome by using long-term time series of spatially continuous remotely sensed LST datasets. A study addressing the rapid warming over the Tibetan plateau using night time MODIS data and station observations (Qin et al. 2009) may be viewed as a first step in this direction; however, the added value of LST crucially depends on the quality of the dataset over such areas.

LST is usually retrieved from remote sensors using data from one or more channels within the thermal infrared window of the electromagnetic spectrum (Li et al. 2013; Masiello et al. 2015, 2013). LST retrieval algorithms are usually sensitive to the amount of water vapor in the atmosphere (Masiello et al. 2013; Freitas et al. 2010), which is an input either as in the form of water vapor profiles (in the case of physical retrievals) or of total precipitable water (TPW), which is generally used by statistical methods. This information is often obtained from numerical weather prediction (NWP) models or reanalysis. The latter are preferred in the development of CDRs but their relatively coarse spatial resolution (currently of the order of 80 km) may lead to systematic errors in the humidity profiles particularly over mountainous areas with implications in LST CDRs over such regions.

In this study, we address the problem of water vapor misestimation when using Era-Int data at high altitudes and its implications in the retrieval of LST. We also develop orographic correction models with the aim of reducing the propagation of error in LST estimates due to water vapor misestimation.

The structure of this chapter is organised as follows: in section 4.2 the satellite and model data are described, as well as the LST retrieval algorithms used for the study; here the problem of ERA-Int water vapor misestimation is addressed and the methods to overcome this problem are introduced; in section 4.3 the methods described in section 4.2 are applied and LST estimated with and without them is compared for the chosen retrieval algorithms; finally, section 4.4 summarises the main conclusions of this study.

4.2. Data and Methods

4.2.1. Data

4.2.1.1. Study Area

The study focuses on the Alpine region, which is the highest and most extensive mountain range in Europe. The Alps are within MSG/SEVIRI disk and are part of the domain of the high-resolution Consortium for Small-Scale Modelling (COSMO) numerical weather prediction model run at the Swiss Federal Office of Meteorology and Climatology, MeteoSwiss (Figure 4.1). The Alps are therefore our testbed to assess the impact errors in LST retrievals associated with misrepresentation of atmospheric profiles and/or total water vapor content associated with altitude. We use profiles both from high (about 2 km COSMO) and medium (about 80 km ERA-Interim) spatial resolution NWP runs. Used data correspond to 6-hourly fields for 1 day per month over the full year of 2014, covering the area shown in Figure 4.1; however, due to the particularly high cloud frequency over the Alpine region, no data were analysed for October.

4.2.1.2. Satellite Data

We consider LST estimates from Top-of-Atmosphere (TOA) brightness temperatures measured by the Spinning Enhanced Visible and Infrared Imager (SEVIRI) onboard EUMETSAT MSG satellite. SEVIRI is the primary MSG instrument and has the capability to observe the Earth in 12 spectral channels, with view zenith angles (VZA) ranging from 0° to 80°, and with a temporal resolution of 15 min and a spatial resolution of 3-km at the subsatellite point. MSG-3 top-of-

atmosphere 10.8-µm and 12.0-µm brightness temperatures, as well as the respective cloud mask are provided by the LSA-SAF. Cloud masks were determined using the software developed by the SAF on support to Nowcasting and Very Short-Range Forecasting for (NWC SAF) following the algorithm described by (Derrien and Gléau 2011). The LSA SAF also provided surface emissivity values for the split-window channels (centred at 10.8-µm and 12.0-µm) which are obtained via a combination of land cover classification and SEVIRI-based fraction of vegetation cover (FVC) updated daily on a pixel-by-pixel basis (Freitas et al. 2010; Trigo et al. 2011).

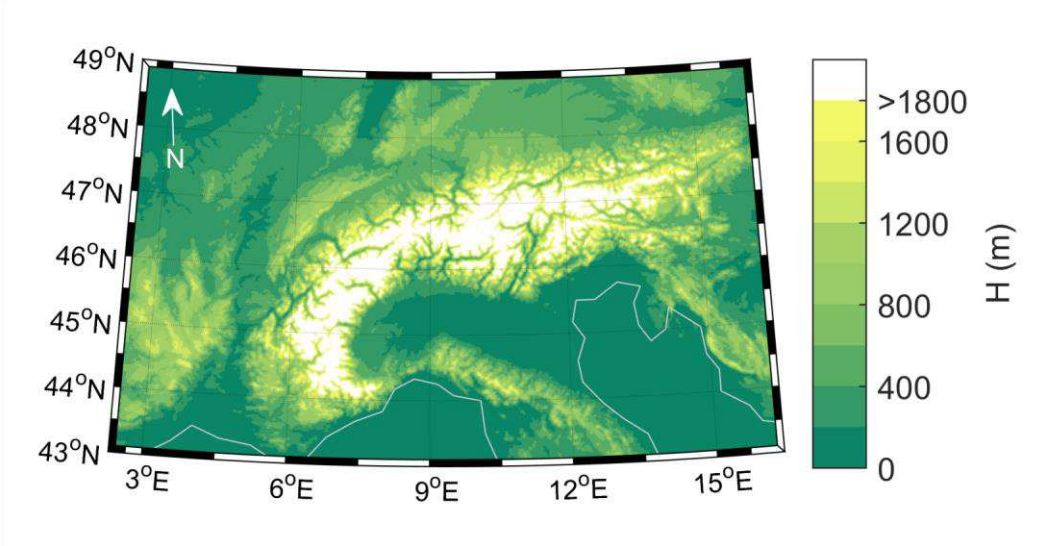

Figure 4.1 – COSMO-2 orography field for the studied area.

4.2.1.3. Model Data

The LST algorithm that is currently being developed by the CM-SAF makes use of Era-Int water vapor and temperature profiles at 60 pressure levels with a horizontal resolution of 80 km (Dee et al. 2011). The base altitude for these profiles is defined by a relatively coarse orographic field representative of the model spatial resolution. For mountainous regions departures of Era-Int height from actual topography can be very large and in the Alps these differences can reach 2 500 m in a reduced number of locations (Figure 4.2).

The COSMO model is a non-hydrostatic operational weather prediction model maintained and continuously improved by the national weather services affiliated in the consortium for small-scale modelling (COSMO) (Baldauf et al.

2011). The COSMO model run at MeteoSwiss has a high-resolution topography (of about 2 km), which makes it more suitable to be used as the reference orography field. Furthermore, the small horizontal scale fluctuations of humidity profiles are expected to be more realistically represented in such a high-resolution model. The differences between COSMO and ERA-Int surface orography fields are shown in Figure 4.2, which clearly puts into evidence the finer details represented in the former.

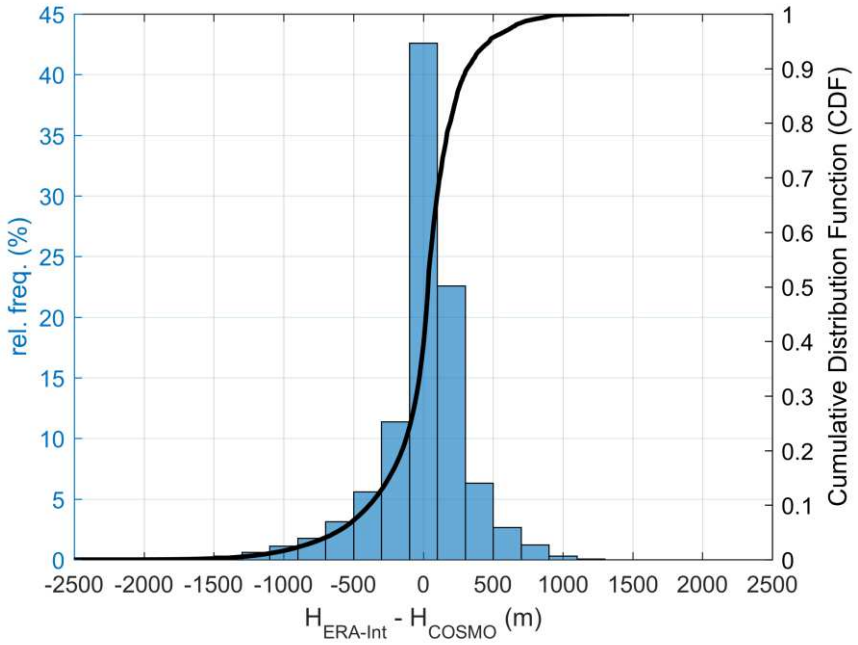

Figure 4.2 – Histogram of orographic differences between Era-Int and COSMO for the studied area.

Figure 4.3 shows that, if COSMOS's grid cells are taken to be a realistic representation of surface orography, then out of the totality of pixels the number of cases where ERA-Int underestimates surface height by more than 1000 m is of 2974-pixel locations over the area of study, leading to a sample of 43 096 retrieved LST values covering the considered year of 2014. Overestimation is less frequent, with only 241-pixel locations where ERA-Int surface height is higher than COSMO's by 1000 m or more. This asymmetry results from the smoothing of the topography performed for numerical stability reasons in medium resolution models and is stronger in those used to build reanalyses datasets. As will be further discussed in the next subsections, this smoothing may lead to systematic errors in

LST estimates over high elevation areas which make use of such reanalyses profiles.

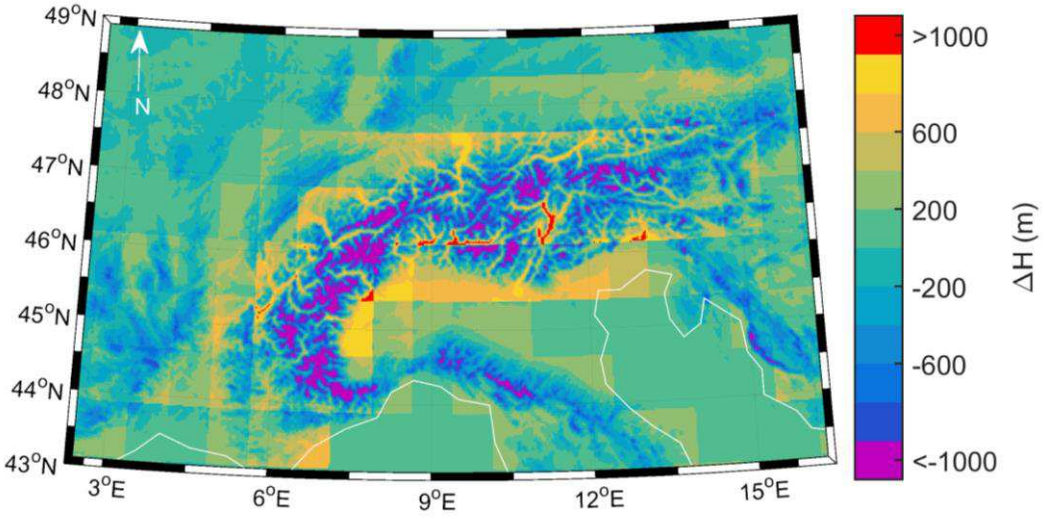

Figure 4.3 – Map of orographic differences between Era-Int and COSMO for the studied area.

4.2.1.4. LST Retrieval Algorithms

A variety of LST retrieval algorithms may be found in the literature (see Li et al. 2013; Masiello et al. 2015) for a comprehensive description). Here we restrict to the three following approaches:

1) The Generalized Split-Windows (GSW), that is based on the formulation by Wan and Dozier for AVHRR and MODIS sensors (Wan and Dozier 1996) and later adapted for MSG/SEVIRI (Freitas et al. 2010; Trigo et al. 2008a,b); LST is computed using a semi-empirical expression involving top-of-atmosphere brightness temperature and surface emissivity in two thermal infrared channels (10.8 and 12 μm),the so-called split-window channels:

$$LST = b_0 + \left(b_1 + b_2\frac{1-\varepsilon_m}{\varepsilon_m} + b_3\frac{\Delta\varepsilon}{\varepsilon_m^2}\right)\frac{T_{b_i}+T_{b_j}}{2} + \left(b_4 + b_5\frac{1-\varepsilon_m}{\varepsilon_m} + b_6\frac{\Delta\varepsilon}{\varepsilon_m^2}\right)\frac{T_{b_i}-T_{b_j}}{2} \quad \text{Eq. 2.5}$$

where in this case $i = 10.8\,\mu m$ and $j = 12.0\,\mu m$, $\varepsilon_m = \frac{\varepsilon_{10.8}+\varepsilon_{12}}{2}$ and $\Delta\varepsilon = \varepsilon_{10.8} - \varepsilon_{12}$ are respectively the mean of and the difference between surface emissivities, $\varepsilon_{10.8}$ and ε_{12}, in the two considered channels, and b_k $(k = 0, \ldots, 6)$ are coefficients calibrated for classes of TPW and VZA.

2) The Statistical Mono-Window (SMW) (Duguay-Tetzlaff et al. 2015), where LST is computed based on an expression involving TOA brightness temperature and emissivity in a single thermal infrared channel (centred at 10.8-μm):

$$LST(\theta,\phi) = a_1 \frac{T_b(\theta,\phi)}{\varepsilon_i(\theta,\phi)} + a_2 \frac{1}{\varepsilon_i(\theta,\phi)} + a_3 \qquad \text{Eq. 3.18}$$

where $T_b(\theta,\phi)$ and $\varepsilon_i(\theta,\phi)$ are the brightness temperature and the surface emissivity of the considered channel, and a_k $(k = 1,2,3)$ are coefficients calibrated for different classes of TPW and VZA.

3) The Physical Mono-Window (PMW) (Duguay-Tetzlaff et al. 2015; Yu et al. 2014), which is based on the direct inversion of the radiative transfer equation for one channel in the thermal infrared window (again centred at 10.8-μm):

$$LST \approx \left(\frac{c_2 \nu_i}{ln\left(\frac{c_1 \nu_i^3 \tau_i(\theta,\phi)\varepsilon_i(\theta,\phi)}{L_i(\theta,\phi) - L_i^{a_u}(\theta,\phi) - [1-\varepsilon_i(\theta,\phi)]L_i^{a_d}\tau_i(\theta,\phi)} + 1 \right)} - \eta \right) / \gamma \qquad \text{Eq. 3.2}$$

where $\varepsilon_i(\theta,\phi)$,$\tau_i(\theta,\phi)$, $L_i(\theta,\phi)$, $L_i^{a_u}(\theta,\phi)$, $L_i^{a_d}\tau_i(\theta,\phi)$ are respectively the surface emissivity, atmospheric transmissivity, top-of-atmosphere radiance, upward atmospheric path radiance and downward atmospheric path radiance for the considered channel i, c_1 and c_2 are constants from Planck's law and γ, η are coefficients that depend on the spectral characteristics of the considered channel, and ν_i is the channel central wavenumber. A radiative transfer model is used to estimate $\tau_i(\theta,\phi)$, $L_i^{a_u}(\theta,\phi)$, $L_i^{a_d}\tau_i(\theta,\phi)$ using information on air temperature and humidity from atmospheric profiles. In this study the Radiative Transfer for TOVS (RTTOV) model is used for this purpose (Matricardi et al. 2001).

These three models were chosen due to the fact that the GSW is the operational model used to retrieve LST in the LSA-SAF (Trigo et al. 2011) and both mono-window algorithms are being used to produce the 25-year LST CDR at the CM-SAF (Duguay-Tetzlaff et al. 2015).

4.2.1.5. Orographic Correction of Atmosphere Profiles

As described above, the three LST algorithms use as input either the total content of water vapor within the column of atmosphere between the surface and the sensor (Eq. 2.5 and 3.3), or the actual atmospheric temperature and humidity profiles (used to solve Eq. 3.2). Here we will describe two methodologies to account for the correction of the profile surface height:

1) The exponential parametrisation of Total Column Water Vapor. Assuming hydrostatic equilibrium, which is a good approximation for the vertical dependence of the pressure field in the real atmosphere, TPW decreases exponentially with height, where the rate of decay depends on the temperature lapse rate. As such, we tested a parametrisation based on the exponential decrease of TPW with altitude (Basili et al. 2004; Morland and Mätzler 2007), i.e.,

$$TPW_1 = TPW_0 \, exp\left(\frac{H_0 - H_1}{\delta}\right) \qquad \text{Eq. 4.1}$$

where TPW_1, TPW_0 are the estimated and reference TPW, respectively. H_1 and H_0 are the high and coarse resolution altitude, respectively. The scale parameter δ is estimated by linear regression using COSMO fields of height and TPW for all grid-points and for all data considered in this study. For each COSMO grid point and observation, we considered the values of height and of TPW over each grid point and the surrounding 8 neighbours. Differences in H and ratios in TPW were then computed between surrounding neighbours and the central grid point (Figure 4.4). Considering COSMO spatial resolution of about 2 km, the rationale is that for the area delimited by the 8 neighbours, changes in TPW are mainly driven by differences in topography, while the thermodynamic properties of the atmospheric profile are maintained. The value of parameter δ is then estimated by linear regression performed between differences in H and the natural logarithm of the

ratios in TPW. Obtained estimate for parameter δ is 1547 m, i.e., TPW decreases by a factor of e when surface elevation increases by 1547 m.

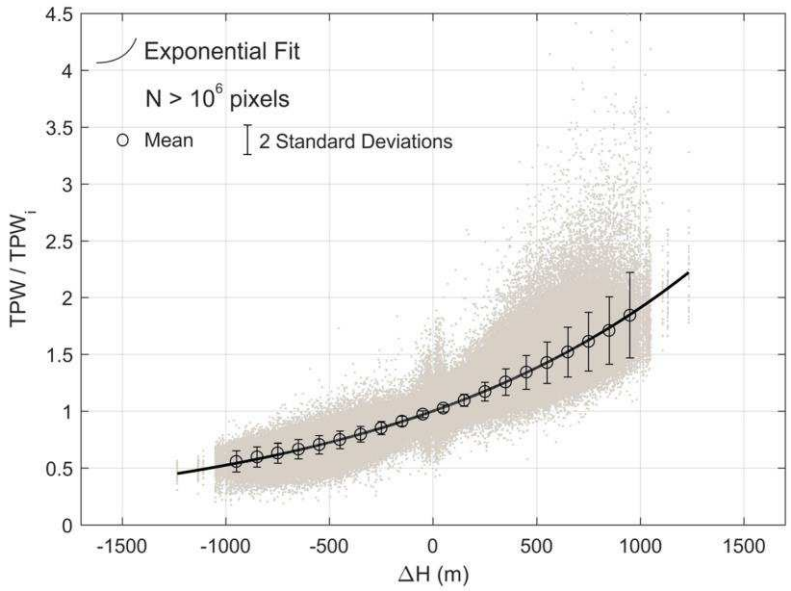

Figure 4.4 – Scatterplot of the ratio of COSMO TPW with respect to its surrounding neighbours, TPW_i, versus differences in height ΔH (grey dots). The black curve represents an exponential fit to the data. Circles and whiskers respectively represent the mean and standard deviation of TPW/TPW_i, considering classes ΔH in steps of 100 m.

2) The Level reduction, which consists of using the surface pressure from COSMO and then, by linear interpolation, truncating the ERA-Int profile at that COSMO pressure level. This method is required for radiative transfer based LST retrieval algorithms (that use water vapor and temperature profiles as input). The method may be also used for statistically based algorithms with the drawback of introducing more variables to the models (thermodynamic profiles, where only TPW is required).

We will restrict to cases where surface height is underestimated, as these correspond to the most critical cases where deviations of ERA-Int surface from actual orography may reach 1000 m or more (Figure 4.2 and Figure 4.3).

4.3. Results

4.3.1. Differences between ERA-Int and COSMO TPW

The comparison between ERA-Int TPW and COSMO reference TPW is shown in Figure 4.5 for grid points with altitude differences (COSMO minus ERA-Int) greater than 1000 m. Differences in TPW reach a maximum of 17.2 mm and present an average of 4 mm and root mean square difference (RMSD) of 5 mm. For each bin of the histogram (Figure 4.5), the median (black solid line), 25th and 75th percentiles of height differences between ERA-Int and the reference COSMO indicate that the differences of height tend to be larger with the increase in the departures of ERA-Int TPW from reference.

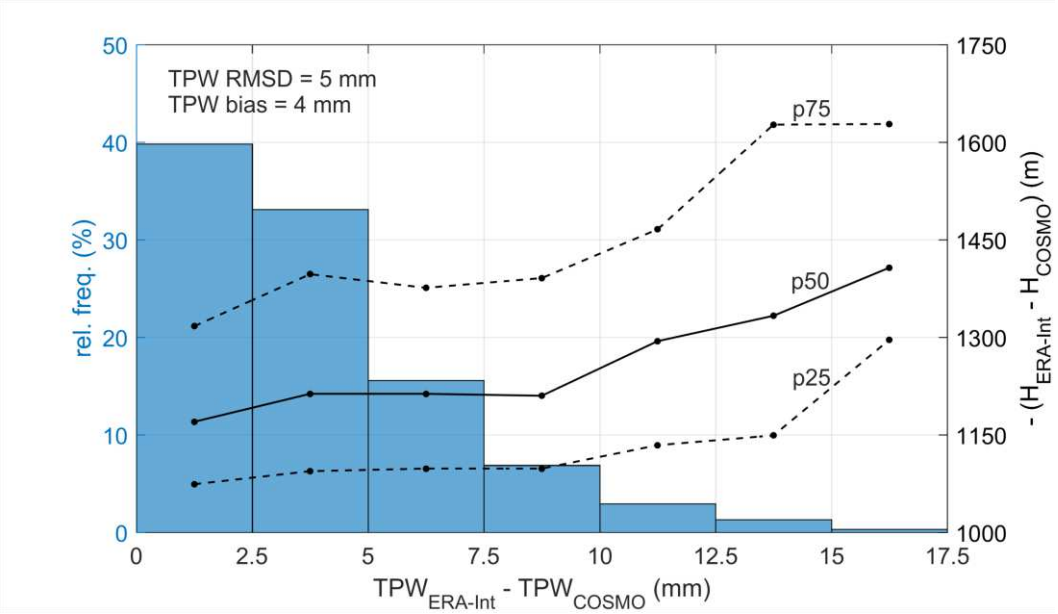

Figure 4.5 – Histogram representing the relative frequency of ERA-Int TPW departures from COSMO reference TPW (in blue) for classes of 0.25 cm over the Alps for 2014. Median, 25th and 75th percentiles of differences of height between ERA-Int and COSMO are shown in black lines.

Figure 4.6 shows the agreement between TPW classes determined by ERA-Int and COSMO profiles, plotting the percentage of cases that fall in different pairs of ERA-Int/COSMO TPW classes for the period between April and September. The selected period corresponds to the season where (clear sky) TPW is most variable, when the atmosphere is warmer and therefore able to hold larger water vapor contents. When ERA-Int is compared with COSMO without any orographic

correction (Figure 4.6a), only 13% (i.e. 10% + 3% along the diagonal) of the total amount of grid-points are in the same TPW class, i.e., about 87% of ERA-Int profiles (i.e. the total of off-diagonal cells) in the wrong TPW class. Furthermore, about 75% of the points miss by one class and 12% by two classes (Figure 4.6a). If the exponential parametrisation (Eq. 4.1) is applied (Figure 4.6b), then the fraction of correct hits rises from 13% to 91% (i.e. 81% + 10% along the diagonal). The remaining 9% differ by one class.

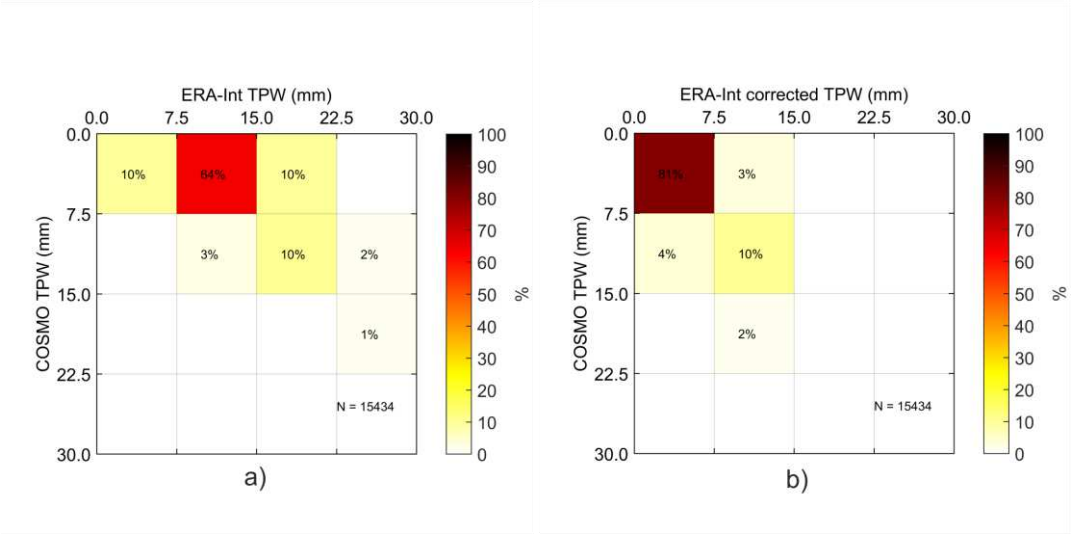

Figure 4.6 – Contingency tables of the COSMO and ERA-Int TPW (in mm), for the April-September period (only cases with height differences between models greater than 1000 m are used) a) uncorrected ERA-Int; b) ERA-Int with exponential correction.

4.3.2. Sensitivity Analysis

Since to our best knowledge there are no LST validation *in situ* stations at high altitudes, a proper validation study of the proposed corrections is still not possible. Instead, a sensitivity study is performed in which LST is retrieved using each of the three abovementioned algorithms using COSMO profiles (for PMW) and COSMO TPW (for GSW and SMW). These LSTs are considered as the reference. Next, LST is retrieved for the same grid-points under the same conditions, but with ERA-Int profiles/TPW. The same procedure is repeated using corrected ERA-Int profiles/TPW. The exponential parametrisation method (Eq. 4.1) is applied to get corrected TPW fields for GSW and SMW, while the level reduction method is applied to adjust the profiles used by the PMW. The RMSD is computed to compare LST retrieved with ERA-Int profiles and the reference LST (retrieved

with COSMO profiles). The same procedure is applied when comparing the corrected LST. Table 4.1 shows LST RMSD per season – November to March and April to September, which for simplicity we will call extended winter and extended summer, respectively – and per difference in ERA-Int and COSMO surface height, for PMW, SMW and GSW.

The RMSD obtained for PMW forced with ERA-Int (Table 4.1a) increase with elevation, regardless of the season. RMSD ranges between 0.3 K (extended winter, for altitude differences between 1000 and 1250 m) and 1.8 K (extended summer, for altitude differences greater than 1750 m). When the level reduction orographic correction is applied, RMSD decreases significantly, with new values ranging between 0 K (several cases) and 0.2 K (extended summer, for altitude differences between 1000 m and 1250 m and between 1250 m and 1500 m). Furthermore, the highest RMSD of 1.8 K in extended summer 2014, for altitudes greater than 1750 m, decreased to 0.1 K.

Table 4.1 – LST RMSD (K) when comparing LST derived with COSMO profiles (reference) and LST derived with ERA-Int original profiles (Orig) and ERA-Int corrected with the different methods (Corr), for PMW (a), SMW (b) and GSW (c). N represents the number of profiles in a determined class of altitude difference and season. The seasons are the extended winter (Nov-Mar) and extended summer (Apr-Sep).

LST (K) (RMSD)	**1000< ΔH <1250**			**1250< ΔH <1500**			**1500< ΔH <1750**			**ΔH >1750**		
	Orig	**Corr**	**N**	**Orig**	**Corr**	**N**	**Orig**	**Corr**	**N**	**Orig**	**Corr**	**N**
	a) PMW											
Nov-Mar	0.3	0.0	16544	0.4	0.0	7230	0.5	0.0	2762	0.6	0.0	1126
Apr-Sep	1.0	0.2	9091	1.2	0.2	4132	1.3	0.1	1582	1.8	0.1	629
	b) SMW											
Nov-Mar	0.1	0.0	16544	0.0	0.0	7230	0.0	0.0	2762	0.0	0.0	1126
Apr-Sep	0.5	0.2	9091	0.5	0.2	4132	0.5	0.1	1582	0.4	0.0	629
	c) GSW											
Nov-Mar	0.1	0.0	16544	0.0	0.0	7230	0.0	0.0	2762	0.0	0.0	1126
Apr-Sep	0.4	0.1	9091	0.4	0.1	4132	0.4	0.1	1582	0.3	0.0	629

The RMSD estimated for SMW LST are shown in Table 4.1b. Here the results are not as striking as for the PMW, where LST has a strong dependence on the season but not on the elevation differences. RMSD ranges between 0 K (in several

cases) and 0.5 K in the extended summer months, a period when TPW values in the clear-sky atmosphere are usually larger. When the exponential parametrisation orographic correction is applied, RMSD also decreases, with a maximum gain of 0.4 K.

Finally, the GSW LST RMSD (Table 4.1c) present the same behaviour as the SMW, showing a higher dependence on month of the year than on altitude differences. Here, RMSD ranges between 0 K (in several cases) and 0.4 K (extended summer, for altitude differences between 1000 m and 1750 m). Again, the most critical cases seem to occur during the warmer period of the year, when the TPW tends to be higher under cloud-free conditions.

These results indicate that PMW is much more sensitive to water vapor than SMW and GSW. This is because PMW requires the whole water vapor profile rather than column integrated values, and for small changes in the water vapor profile the retrieved LST value will also change. Conversely, both SMW and GSW depend on classes of TPW, which means that a small change (or even a substantial change, considering that the TPW classes are generally broad) in water vapor may have no effect on LST. Furthermore, GSW is less sensitive to the TPW input than SMW, as the differences in the two adjacent split-window channels are themselves sensitive to the actual water content in the atmosphere (e.g., Li et al. 2013; Masiello et al. 2015, 2013).

4.4. Discussion

There is growing evidence that the rate of warming is amplified with elevation (Mountain Research Initiative EDW Working Group 2015). Air temperature observations at ground stations are essential to study elevation-dependent warming, but many high-altitude areas are still heavily under-sampled (Lawrimore et al. 2011). To overcome those limitations, spatially continuous remotely sensed land surface temperature (LST) climate data from satellites could be used for elevation dependent warming studies (Mountain Research Initiative EDW Working Group 2015; Qin et al. 2009). This study addresses systematic errors that can be present in satellite-based LST retrievals at high-altitudes and proposes methods to correct for those errors.

Long-term satellite-based LST retrieval algorithms from geostationary satellite sensors rely on reanalyses data (such as ERA-Int) with a relatively coarse horizontal resolution to estimate the atmospheric water vapor content. This implies a rather poor representation of small scale orographic features. In particular, reanalysed water vapor fields can significantly depart from real values for pixels in mountainous regions. For the Alpine region investigated in this study, these differences reach a maximum of 17.2 mm.

The impact of the different water vapor estimates in three different LST retrieval schemes (the SMW, the GSW and the PMW) was assessed. In the case of SMW and GSW, only the vertically integrated water vapor affects the retrieval, as these models are calibrated in classes of TPW (in steps of 7.5 mm). Errors in TPW translate in the selection of the wrong class, i.e. the wrong set of model coefficients will be used, which allows a margin of TPW uncertainty within each correct class.

In terms of class hits (Figure 4.6), ERA-Int profiles miss the TPW class in 87% of the cases, where 75% of these misses reflect a deviation of one class and 12% of two classes. It is shown that the exponential parametrisation orographic correction method dramatically improves the amount of ERA-Int profiles within the correct class (91%). These results correspond to the cases where ERA-Int orography field exceeds the higher resolution orography in more than 1000 m.

Results presented in Table 4.1 show that the radiative transfer-based algorithm (PMW) is much more sensitive to water vapor, when the original ERA-Int profiles are used. The PMW takes the full ERA-Int profiles as one of its inputs, i.e. the atmospheric radiances and transmissivity will be affected by errors in the profile. Furthermore, for the thermal window channels used for LST estimation, radiative transfer is particularly sensitive to the lower levels in the atmosphere where most water vapor content lies. Therefore, when inverting the radiative transfer equation and the calibrated Planck function, LST will be affected even with a relatively small change in the humidity profile.

This work mainly consists of an LST sensitivity study to water vapor errors related to the misrepresentation of the surface orography associated to each atmospheric profile. For that purpose, we compare LST retrievals using water vapor inputs with different spatial resolutions in the Alpine region. We show that RMSD

up to 1.8 K may arise in LST retrievals (Table 4.1) over pixels where the profile surface height deviates by 1000 m or more from a reference orography. We also show that the largest height deviations in models occur for high elevations, where TPW is systematically overestimated and therefore will be a source of systematic errors in LST retrievals. We further show that this may be overcome by an adequate adjustment of reanalyses profiles and/or total column water vapor to the geographic elevation. When using the level reduction method, the highest RMSD of 1.8 K in extended summer 2014, for altitudes greater than 1750 m, decreased to 0.1 K (Table 4.1).

A deeper insight into the impact of height deviations on LST estimates for three LST retrieval algorithms is provided by scatterplots of corrected versus original values of LST for the different classes of ΔH and for extended summer and winter (Figure 4.7).

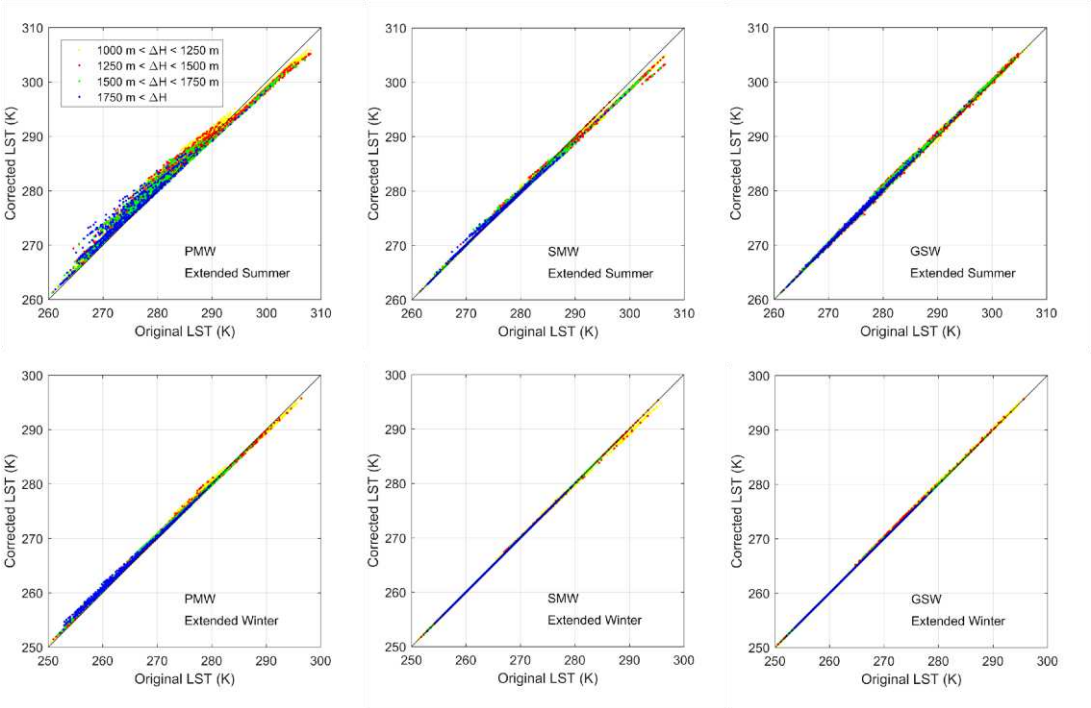

Figure 4.7 – Scatterplots of corrected- versus original- values of retrieved LST for the four different classes of ΔH (yellow, red, green and blue dots) when PMW (left panels), SMW (middle panels) and GSW (right panels) retrieval algorithms, are applied during extended summer (top panels) and extended winter (bottom panels).

The above mentioned larger sensitivity of PMW (followed by SMW) to water vapor translates into the deviations from the 1:1 line which increase from right to

left panels of the figure. As also discussed, deviations are larger during the extended summer than during the extended winter, reflecting the larger amounts of water vapor in the former season than in the latter. It is worth noting that corrections do not present a systematic character, tending to decrease (increase) towards lower (higher) LST values. This implies that on average corrections will have lower values. Finally, it is worth noting that biases in the corrections are strongly conditioned by the value of LST, a major issue that must be taken into account when LST data are used for climatological purposes, namely when building up CDRs.

An ideal validation of results would require data from *in situ* high altitude LST dedicated stations, which were not available during this study. Furthermore, due to the large footprint of MSG/SEVIRI pixel (3-5 km), ideal conditions (as those provided by an LST dedicated station at high altitude in a homogeneous region at the sensor spatial resolution) would be very difficult to achieve.

4.5. Conclusions

Studies focusing on elevation dependent warming related to climate change have been facing difficulties related to the scarceness of air temperature in-situ observations over mountainous regions. The current availability of long-term time series of spatially continuous data of remotely-sensed Land Surface Temperature (LST) appears as a valuable means to overcome this problem. One example of such databases is the one being produced by CM SAF and LSA SAF. However, the algorithms used to retrieve LST depend on reanalysed water vapor profiles defined in a grid associated to a smoothed orography, which leads to misestimations in the water vapor profile.

Two orographic correction methodologies were developed aiming at improving LST retrievals, by correcting the water vapor profile and/or the total precipitable water estimations. Improvements in the LST retrieval vary depending on the method used but may reach 1.7 K (RMSD), an extremely large discrepancy for climatological applications.

Given the lack of *in situ* LST stations in high altitude regions, a direct comparison against ground measurements was not possible at this stage. The relatively large footprint of the MSG/SEVIRI pixel makes the task difficult to

achieve. Nevertheless, LST products derived from MSG/SEVIRI or other sensors would certainly benefit from field campaigns in high-elevation regions, strongly needed to close an important gap in satellite product validation.

This study is performed over the Alpine region, which despite of being the highest mountain range in Europe is not the highest mountain range encompassed in MSG-disk and is far from being the highest mountain range in the world. An example is Mount Kilimanjaro in eastern Africa, which is also within MSG-disk. This mountain reaches an altitude of about 5 900 m, while ERA-Int orographic field has a maximum of 2 115 m. Differences here are of about 3 800 m. This range of amplitude was not studied here, since the maximum difference in the Alps is of about 2 500 m, and of all the grid-points with altitude differences greater than 1000 m, only 1% is greater than 2000 m.

LST estimates in high elevation regions may be affected by other sources of error, namely due to the high spatial (and temporal) variability of surface emissivity associated to the changes in landcover and snow/ice with height. Getting a highly detailed emissivity map over mountain regions is challenging and should be covered in future works.

Chapter 5

Next, Land Surface Temperature climatologies are used on a drought monitoring application. Vegetation Health Index is estimated with Land Surface Temperature and Normalised Differences Vegetation Index climate data records with the objective of assessing if its most common formulation is recommended for different land covers.

5. Assessing drought using Remote Sensing data: Understanding the combined use of thermal (LST) and visible (NDVI) observations

Abstract

Vegetation Health Index (VHI) has been widely used for monitoring and characterising droughts. This index takes into account ecosystem features in terms of fluctuations between prescribed maxima and minima of NDVI (Vegetation Condition Index, VCI) and of Land Surface Temperature (LST; Thermal Condition Index, TCI), and is estimated as the weighted sum of these two contributions. Since there is no a priori knowledge about vegetation and temperature contributions, VHI is typically taken as the average of both contributions, i.e., a weight of 0.5 is assumed. In this work climatologies of NDVI and LST are used to estimate VCI, TCI and VHI on (1) a Mediterranean geographic window; (2) a global scale; and (3) the Meteosat disk; which are then correlated with the multiscalar drought indicator SPEI (Standardized Precipitation-Evapotranspiration Index) with the aim of assessing the effect of drought on each contribution. Results of the correlations between VCI-SPEI and TCI-SPEI show that the relative contribution of VCI and TCI to vegetation health depends on vegetation cover: the effect of drought is more evident in the case of VCI in semiarid climate classes (regions where the limiting factor to vegetation growth is water); while the effect of drought is more obvious in TCI for moistier

climate classes (regions where the limiting factor is solar radiation). This leads to the conclusion that by maximising the correlations between VHI and SPEI, over a climatological period, is possible to evaluate the relative roles of VCI and TCI to VHI for different climate regions.

5.1. Introduction

Drought episodes are a recurrent feature of climate with a wide-range of impacts on the planet and society (Klos et al. 2009; Mishra and Singh 2010; Phillips et al. 2009; Wilhite et al. 2007). Droughts rank among the deadliest (Hillier and Dempsey 2012) and costliest (Cook et al. 2007; Ding et al. 2011) of all natural disasters. Moreover, the observed intensification of evaporative demand associated with the impacts of climate change on temperature and precipitation regimes, have contributed to a widespread increase in drought severity (Dai 2012; Diffenbaugh et al. 2015; Trenberth et al. 2013; Vicente-Serrano et al. 2014). However, a universally accepted definition of drought is still missing (Mishra and Singh 2010; Smakhtin and Schipper 2008; Wilhite and Glantz 1985), which contributes to an even more difficult monitoring of drought episodes and the assessment of their severity. Thus, there is a growing need for a better understanding of the various aspects of drought events that help consolidating monitoring strategies.

The Mediterranean region is known for its vegetation dependence on water availability (Gouveia et al. 2009; Lindner et al. 2010). This is especially true due to its position in a transition region between temperate and tropical climates where, under normal conditions, water availability is low and water demand is high (sometimes surpassing the former). In these regions, the increase of temperature together with the decrease of precipitation will enhance evapotranspiration rate (Hartmann et al. 2013; Iglesias et al. 2009). Also, large areas in this region are dedicated to agriculture, implying a strong consumption of water supplies (Hoerling et al. 2012). Therefore, the role of evapotranspiration on drought frequency and severity has been assessed during the last decades over several areas of the Mediterranean region (Coll et al. 2017; Dai 2012; Páscoa et al. 2017; Sheffield et al. 2012; Vicente-Serrano et al. 2014). Furthermore, according to the Fifth Assessment Report (AR5) of the Intergovernmental Panel on Climate Change

(IPCC) major changes in the mean precipitation and its variability are projected over this area. When combining all these factors with the increased drought frequency observed over the region in the last years (Hoerling et al. 2012; Mariotti 2010; Vicente-Serrano et al. 2014), the need for a proper drought monitoring over the Mediterranean basin becomes a key issue to be dealt with.

Several different indices have been developed during the last decades aiming at characterising the different types of drought, namely meteorological, hydrological and agricultural droughts (Mishra and Singh 2010; Zargar et al. 2011). The Palmer Drought Severity Index (PDSI) (Palmer 1965), the Standardized Precipitation Index (SPI) (Mckee et al. 1993), and the more recent Standardized Precipitation Evapotranspiration Index (SPEI) (Vicente-Serrano et al. 2010) are worth being mentioned among others (Heim 2002; Mishra and Singh 2010). SPEI was specifically designed to assess drought taking into account the climatic balance between precipitation and potential evapotranspiration (Beguería et al. 2014; Vicente-Serrano et al. 2010). Due to the inclusion of the effect of temperature, and therefore evapotranspiration, in drought assessment SPEI has revealed to be very useful for monitoring and characterising drought in climate change context (Vicente-Serrano et al. 2010).

In the last years, remote sensing data have also been used for drought monitoring and drought index development (Gouveia et al. 2017; Kogan 1997; Vicente-Serrano et al. 2015). Indeed, spaceborne observations allow the retrieval of both atmospheric and surface variables – from precipitation, to soil moisture, vegetation indices, amongst others – that have proven useful in this field (Lakshmi 2017; Wardlow et al. 2012). The current availability of accurate satellite-based Climate Data Records (CDRs; Duguay-Tetzlaff et al. 2015; Martins et al. 2016; Bento et al. 2017) opens the way to the application of drought indices derived from remotely-sensed information at large spatial and temporal scales with the aim of better understanding the past behaviour of drought episodes and better anticipating the future.

The vegetation health index (VHI; Kogan 1997, 2001) is a widely used drought index based on remote sensing information (Bhuiyan et al. 2006; Kogan et al. 2012; Quiring and Ganesh 2010a; Singh et al. 2003). It consists of a linear

combination of two components, namely the Vegetation Condition Index (VCI) incorporating information on the visible (VIS) and near infrared (NIR) portions of the electromagnetic spectrum and the Thermal Condition Index (TCI) relying on the thermal infrared (TIR). The VCI component is commonly estimated using the Normalized Difference Vegetation Index (NDVI) and aims to account for the vegetation water stress; the TCI, in turn, is used to assess the temperature stress of vegetation and is estimated based on either top-of-atmosphere brightness temperature or on Land Surface Temperature (LST). The rationale behind the formulation of VHI rests over the following two assumptions:

1. VHI is defined such that the lower the NDVI and the higher the LST, the poorer is vegetation health;

2. Since there is no a priori knowledge about vegetation and temperature contributions to vegetation health, the latter index is commonly computed by simply averaging VCI and TCI.

The first assumption was verified in a number of studies focusing regions located in Mongolia and the USA (Karnieli et al. 2006, 2010; Sun and Kafatos 2007). Results indicate that the way LST and NDVI contribute to vegetation health depends on location, season and vegetation type. For instance, a concurrent contribution of both variables was found when the limiting factor for vegetation development is solar energy (typically at high latitudes and elevations), while opposite contributions occur where water is the limiting factor (typically at arid and semiarid regions).

The first objective of this chapter is to assess the relative contribution of NDVI and LST when characterising vegetation health over a Euro-Mediterranean region, composed of different ecosystems and vegetation landscapes. To accomplish that, VHI and its two components are correlated to SPEI at different time scales, in order to understand the response of vegetation to drought events over different biomes. VHI was chosen, as it allows the quantification of vegetation health under thermal conditions whereas SPEI was selected since it integrates the risen evaporative demand, as obtained through evapotranspiration. The relative contributions of NDVI and LST on vegetation health were then associated to the different aridity regions within the Euro-Mediterranean area. Then, the same

methodology is applied on a global scale with the objective of developing maps of coefficients that can be used to monitor drought. Finally, the same methodology is applied to the Meteosat disk, using the LST CDR developed in Chapter 3.

5.2. Development of the methodology over a Mediterranean region[5]

5.2.1. Data

5.2.1.1. Study Area

This work focuses on the Euro-Mediterranean region encompassed by the geographical window between 30.25 N – 51.25 N and 9.75 W – 37.25 E (Figure 5.1). Desert regions were masked based on land cover data from the International Geosphere-Biosphere Programme (IGBP; Loveland et al. 2000). Figure 5.1 shows the aridity index (Zomer et al. 2006, 2008) from CGIAR-CSI Global-Aridity and Global-PET Database (http://www.cgiar-csi.org) – which uses estimates of evapotranspiration based on the Hargreaves equation (Hargreaves 1994) – divided in different aridity interval values (UNESCO 1979): hyper arid (<0.03), arid (0.03 to 0.2), semiarid (0.2 to 0.5), dry sub-humid (0.5 to 0.65), and humid (>0.65). The study area is characterised by an arid climate in some scattered pixels over north Africa; semiarid climate over north Africa, southern and eastern Iberia, central Turkey and southern Ukraine; dry sub-humid climate is to be found in some regions of north Africa (closer to the Mediterranean), Iberia, Turkey, Ukraine, and the Balkans region; and finally, humid climate, which is the prevailing climate in the area of study, spreads from northern Iberia to eastern Europe.

5.2.1.2. NDVI and LST

Data of NDVI (Myneni et al. 1995) were extracted from NASA/Goddard Space Flight Center's Global Inventory Modelling and Mapping Studies (GIMMS) Group (Tucker et al. 2005). With an 8-km spatial- and a bi-monthly temporal-

[5] Adapted from Bento, V.A., Gouveia, C.M., DaCamara, C.C., Trigo, I.F. A Climatological assessment of drought impact on Vegetation Health Index. Agricultural and Forest Meteorology, Agric. For. Meteorol. 2018, 259, 286–295.

resolution, the GIMMS NDVI dataset is the longest (starting in 1982) and most complete NDVI record available. It is widely used to assess both global and local vegetation dynamics and impacts of climate in the vegetation (Detsch et al. 2016; Ding et al. 2015; Fensholt and Proud 2012).

NDVI data were linearly interpolated to a 0.5º spatial resolution. Then, a centred moving average, with a span of 3 bi-monthly values, was applied to remove high frequency noise. The NDVI trend associated with the greening or browning of the region (de Jong et al. 2011, 2013; Zhu et al. 2016) was also removed by applying a linear regression model to the time-series of each pixel.

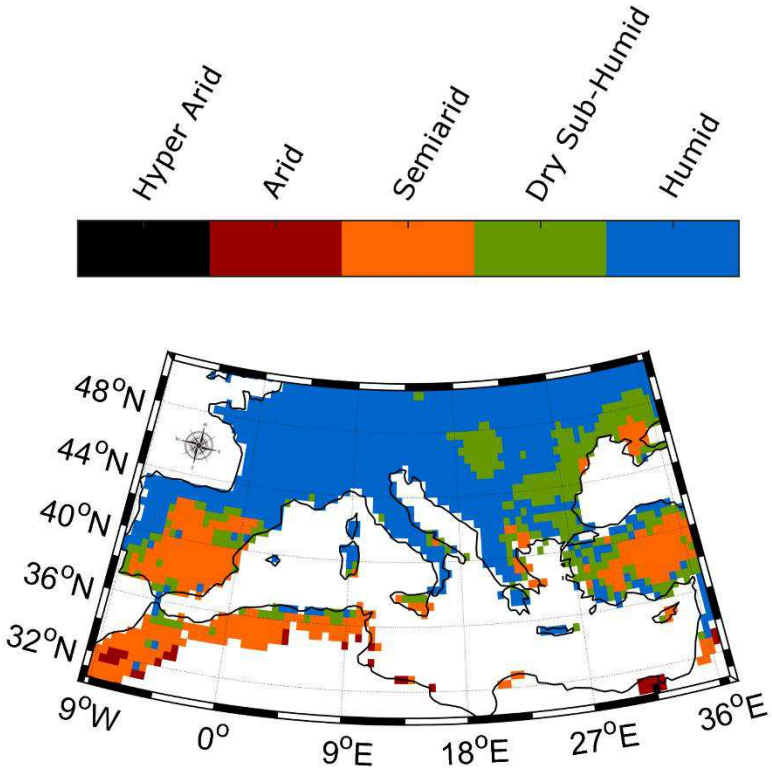

Figure 5.1 – Geographical domain of the study area over Europe. Colours represent the aridity index classes (based on the CGIAR-CSI Global-Aridity and Global-PET Database). Desert zones are masked (in white) according to the IGBP land cover.

Information about land surface temperature was obtained from the LST database developed at the Princeton University (Coccia et al. 2015; Siemann et al. 2016). This high-resolution (0.5°), hourly, long-term (1979 – 2009), temporally and spatially consistent dataset relies on information from the High-resolution Infrared Radiation Sounder (HIRS) LST merged with NCEP's CFSR reanalysed LST

through a Bayesian postprocessing methodology (Siemann et al. 2016). The main advantage of using such a dataset is its all-weather coverage, i.e., LST data are available for both clear- and cloudy- sky conditions due to the filling of unobserved satellite LST with estimates from climate simulations (NCEP CFSR). In contrast most satellite-based LST CDRs are derived from infra-red observations and are therefore biased towards clear sky cases (Duguay-Tetzlaff et al. 2015). Another benefit is the time span of this dataset, covering a 30-year period. The data are calibrated for fixed times (hourly estimates) and locations (0.5º of horizontal resolution) on a global scale, an advantage for the type of analysis to be performed here. It is worth mentioning that an emissivity of one is assumed when deriving LST and therefore the merged variable represents a surface brightness temperature.

Daily means of LST were computed from hourly data and then the maximum value of the fortnight was retained. High frequency and trend components were then removed by applying the same procedure that was used for NDVI.

Climatological datasets of LST and NDVI were finally organised covering the period from 1982 until 2009.

5.2.1.3. SPEI

SPEI is used to characterise drought events in a context of risen evaporative demand, as includes evapotranspiration. The impact of drought on vegetation health is evaluated using SPEI, through the assessment of the relative contribution of the remote sensing derived VCI and TCI. Our analysis relies on the database developed by Russo et al., 2015 and used in previous works (e.g. Páscoa et al. 2017). The data were extracted for time scales of 3, 6, 9 and 12 months, with a resolution of 0.5º. The dataset relies on temperature and precipitation from the Climate Research Unit (CRU) of the University of East Anglia TS3.21 database (Harris et al. 2014), covering the period between 1901 and 2012. A climatological dataset was finally organised spanning from 1982 to 2009.

5.2.2. Methods

Following Kogan (1997), for each pixel and month of a given year, the Vegetation Condition Index (VCI) is computed according to the relation

$$VCI = \frac{NDVI - NDVI_{min}}{NDVI_{max} - NDVI_{min}} \quad \text{Eq. 5.1}$$

where $NDVI$ is the value for the pixel and month and $NDVI_{min}$ and $NDVI_{max}$ are the minimum and maximum values of $NDVI$ over the whole period of 1982-2009, for the considered pixel and month.

Using a similar procedure, the Thermal Condition Index (TCI) is computed according to the relation

$$TCI = \frac{LST_{max} - LST}{LST_{max} - LST_{min}} \quad \text{Eq. 5.2}$$

Finally, the Vegetation Health Index (VHI) is given by

$$\mathrm{VHI} = \alpha\mathrm{VCI} + (1 - \alpha)\mathrm{TCI} \quad \text{Eq. 2.8}$$

where α is a weight parameter that is usually defined as $\alpha = 0.5$ (Kogan 1997, 2001).

The present study will mainly focus on the correlations of VHI (as well as of its two components, VCI and TCI) with previous month SPEI (computed over several time-scales). In order to avoid analysing a very large number of maps of spatial patterns, the following rationale was adopted: i) for each pixel, choose the month of maximum NDVI in the respective climatological annual cycle; ii) use SPEI at time-scales of 3, 6, 9 and 12 months; and iii) for each pixel select the time-scale of SPEI that presents the maximum correlation with VHI. For selected maximum correlations that are statistically significant at the 5% significance level, correlations between VCI and SPEI and between TCI and SPEI were also computed. Finally, in order to estimate the relative contribution of VCI and TCI (at a pixel basis) the correlation between VHI and SPEI was maximised.

5.2.3. Results and Discussion

5.2.3.1. Month of maximum NDVI

Regions with different vegetation characteristics were identified based on the climatological month of maximum NDVI per pixel. This is the month where the annual vegetation peak is reached and therefore when the impact of vegetation and thermal stress is the hardest. As shown in Figure 5.2a, up to 96% of the study area registers maximum NDVI between March and July, with: 11% in March; 14% in April; 18% in May; 40% in June; and 13% in July. As shown in Figure 5.2b, the magnitude of maximum NDVI depends on the latitude. Although desert landscapes in North Africa have been masked, the bordering regions are still covered with poor vegetation, which reflects in very low NDVI values. When comparing Figures 5.2a and 5.2b, it is noticeable that regions with higher NDVI correspond to a later month of maximum NDVI (typically June and July).

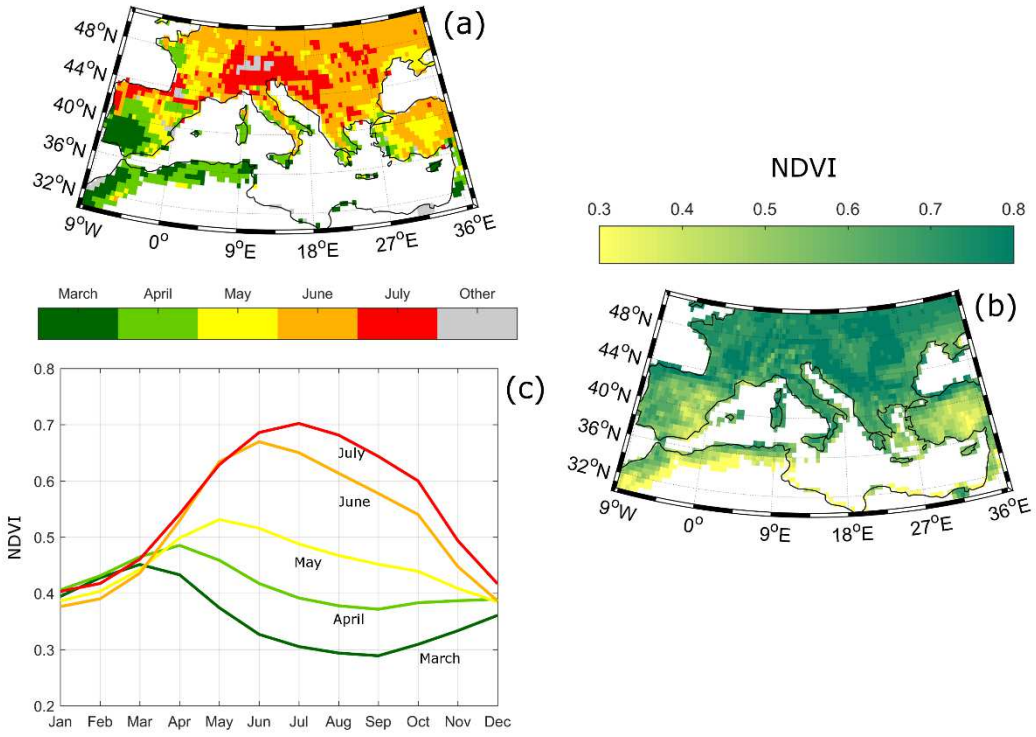

Figure 5.2 – Spatial distributions of the climatological month of maximum NDVI (A) and of respective maximum value (B); and annual cycles of spatial averages of NDVI (C) over pixels having maximum NDVI in the months of March, April, May, June and July.

Pixels where the peak of NDVI occurs in March are mostly located in southwestern Iberia and North Africa. These areas are defined by a typical semiarid vegetation cycle (Figure 5.2c), in which, after attaining the March maximum value (0.46), NDVI declines during spring and summer, until September (0.29). Then, the vegetation starts to grow during autumn and winter. These regions are also characterised by very low values of NDVI in spring, summer and autumn, while having high NDVI values in January and February when compared to the other regions of maximum NDVI. Regions where maximum NDVI happens in April are for the most part located very close to those with maximum in March, in North Africa and Iberia; however other more scattered regions may be identified, along the coasts of Italy, eastern Greece and western Turkey, and northwest France. The vegetation cycle for these areas is very alike to the one in March, with the difference of presenting higher values of NDVI (maximum and minimum of 0.49 and 0.37, respectively).

As shown in Figure 5.2a, regions where May is the month of maximum NDVI are scattered throughout Europe, with the largest clusters in eastern Iberia, France and Turkey. The vegetation cycle of these regions is significantly different from the previous two months. After reaching the peak in May, presenting higher values of NDVI (0.53), vegetation tends to decrease during the rest of the year, until January, when it reaches a minimum value of 0.39 (Figure 5.2c). Here NDVI values are close to those of the previous two cases during the December – April period, and have higher values during summer and autumn. This region can be perceived as a transition zone between the more semiarid regions, which have the NDVI peak early in the year, and the more humid regions, prone to have peaks of vegetation in summer, in the months of June and July. Pixels that have their month of maximum NDVI in June form the largest cluster, spreading from the northern part of the window to eastern Europe, with a few pixels located in Italy and northern Iberia. On the other hand, the July regions concentrate in the Alpine and Pyrenees regions, and in the northern and north-western part of Iberia (Figure 5.2a). As shown in Figure 5.2c the corresponding vegetation cycles consist of a growing season from January until June (or July), with very high values of NDVI in summer (maximum of 0.67 and 0.70 in June and July, respectively), followed by a decrease until

December (reaching a minimum of 0.38 and 0.40 respectively for the cycles with maximum NDVI in June and in July).

The analysis of the month and intensity of maximum NDVI lead to the stratification of the study area into five clusters, defined by the month of greater vegetation activity. Different methods have been used in the literature to characterise the region, including: using Köppen climate classification based on a combination of monthly and seasonal surface air temperature and precipitation (Gao and Giorgi 2008); applying a cluster analysis to monthly NDVI averages (Gouveia et al. 2017); or defining global semiarid regions by means of annual precipitation and evapotranspiration climatologies (Vicente-Serrano et al. 2015). The March/April cluster in North Africa and southern Iberia presents a pattern very similar to the one of semiarid regions estimated in Vicente-Serrano et al. (2015), who have also identified the months of maximum average NDVI that match our results. Gao and Giorgi, 2008 identified these regions as Subtropical Summer Dry climate (or Mediterranean Climate), which is defined by rainy winters and dry-warm summers, while Gouveia et al. (2017) defined the region by dividing it into Mediterranean Dry and Mediterranean Oceanic, following (Rivas-martínez et al. 2011). Regions where maximum NDVI occurs in May are located in eastern Iberia, France, Turkey and a few pixels are scattered through Eastern Europe. These regions encompass different climate types, namely Temperate Oceanic, Temperate Continental and Mediterranean Climates. For pixels with maximum NDVI in June, the geographical pattern resembles the Temperate Continental Climate in Gao and Giorgi (2008), while Gouveia et al. (2017) identified the region as Temperate Continental and Temperate Dry climates. Finally, July is the month of maximum NDVI in regions over and around the Alps and the Pyrenees, the north of Iberia and, for a few pixels, the Balkan region.

The aridity index from CGIAR-CSI Global-Aridity and Global-PET Database (Figure 5.1) is used to estimate the percentages of each maximum NDVI month cluster in four climate classes (Table 5.1) with different aridity interval values. Inside the areas where maximum NDVI month occurs in March and April, the semiarid climatic class is the dominant one, with about 71% and 45 % of the entire region (all pixels, AP in Table 5.1), respectively. However, the region within the March cluster have a much more emphasised semiarid signal than the April

cluster. On the other hand, the May cluster region is composed of a larger percentage of humid climatic class, with about 45 % of the entire area. Finally, June and July cluster regions have a dominant signal of the humid climate, with 78 % and 91 % of the respective areas covered by that class. It is also worth noting that the hyper arid climatic class is missing from the studied region, being a result of the desert mask applied earlier. Furthermore, the climatic class percentages have a linear behaviour with time, except for the dry sub-humid class that increases from March to its maximum in May and then decreases to its minimum percentage in July. Percentages of arid and semiarid classes decrease with time, while the ones of humid class increase in time.

Table 5.1 – Percentage of climate classes defined by the CGIAR-CSI Aridity Index in the different NDVI months of maximum vegetation activity for all pixels (AP) and for the ones where the VHI-SPEI correlation is significant (SP). Hyper arid climatic class is missing as a consequence of the desert mask applied to the data.

Percentage (%) of climate classes in each NDVI cluster		CGIAR-CSI Aridity Index			
		Arid	Semiarid	Dry sub-humid	Humid
All pixels (AP) / Significant pixels (SP)		AP/SP	AP/SP	AP/SP	AP/SP
Month of Maximum NDVI	March	7.8 / 8.5	**71.2 / 73.1**	15.6 / 14.2	5.4 / 4.2
	April	4.0 / 2.9	**44.6 / 57.9**	21.4 / 24.0	30.0 / 15.2
	May	0.3 / 0.7	30.7 / **41.8**	24.3 / 35.6	**44.7** / 21.9
	June	0.0 / 0.0	5.0 / 5.3	17.1 /27.3	**77.9 / 67.4**
	July	0.0 / 0.0	0.7 / 0.0	8.7 / 16.2	**90.6 / 83.8**

5.2.3.2. Correlations between VHI and SPEI

For each pixel, the Pearson's linear correlation coefficients were computed between VHI of the month of maximum NDVI and the SPEI of the previous month, estimated over time scales of 3, 6, 9 and 12 months. A p-value of 0.05 for the two-tailed t-test is used to reject the hypothesis of no correlation. Then, on a pixel-by-pixel basis, the time scale of SPEI that has the maximum correlation NDVI is chosen. Table 5.1 shows the percentage of each NDVI cluster in the four climatic classes for the significant pixels (SP). For the March cluster the percentage of arid and semiarid classes increase when compared to all pixels (AP), while dry sub-humid and humid percentage decreases. The April cluster shows notorious increase/decrease in the semiarid/humid percentages. For the May cluster there is a

decrease of pixels percentage in the humid class and an increase in the semiarid and dry sub-humid classes. It is worth mentioning that this is the only cluster where the climatic class with higher percentage changes (from humid to semiarid), when from AP to SP. Finally, June and July clusters show a decrease in the humid class percentage and an increase in the dry sub-humid class percentage. Table 5.2 shows the number and corresponding fraction of statistically significant pixels for the four chosen time scales of SPEI in each of the clusters. The 3-month time-scale has the highest percentage of pixels in the regions with maximum NDVI in April and May; the 6-month time-scale is found in greater percentage in June and July; on the other hand, March has a higher percentage of pixels with significant correlation at the 9-month time-scale. It is also worth noticing that March is the month with higher correlations (Table 5.2), and that these tend to decrease with time response. Figure 5.3a shows the maximum significant correlations for the region, and Figure 5.3b depicts the SPEI time scale at which that correlation occurs.

Table 5.2 – Number of pixels and percentage of SPEI time scales of 3, 6, 9 and 12 months and SPEI/VHI interquartile correlation over the regions defined by the maximum NDVI month.

Percentage (%) of SPEI time-scales and mean correlation in each NDVI cluster		SPEI time-scales percentages				
		3 month	6 month	9 month	12 month	Interquartile Corr.
Month of Maximum NDVI	March (145)	23%	14%	**37%**	26%	0.50 – 0.65
	April (182)	**48%**	12%	14%	26%	0.45 – 0.59
	May (156)	**39%**	22%	15%	24%	0.43 – 0.61
	June (494)	18%	**36%**	10%	**36%**	0.43 – 0.59
	July (146)	23%	**36%**	13%	28%	0.42 – 0.58

Most of the significant correlations are found in north Africa, southern Europe and the Balkans. It is also worth noticing that the non-significant correlation coefficients are in its majority located in regions defined by the humid class of the aridity index (Figure 5.1), with some notable exceptions, like northern Iberia, some pixels in southern France or the Alps and Pyrenees regions. This is noted with the decrease in the percentage of humid climatic class in all the clusters of maximum NDVI (Table 5.1), when only the significant pixels are retained.

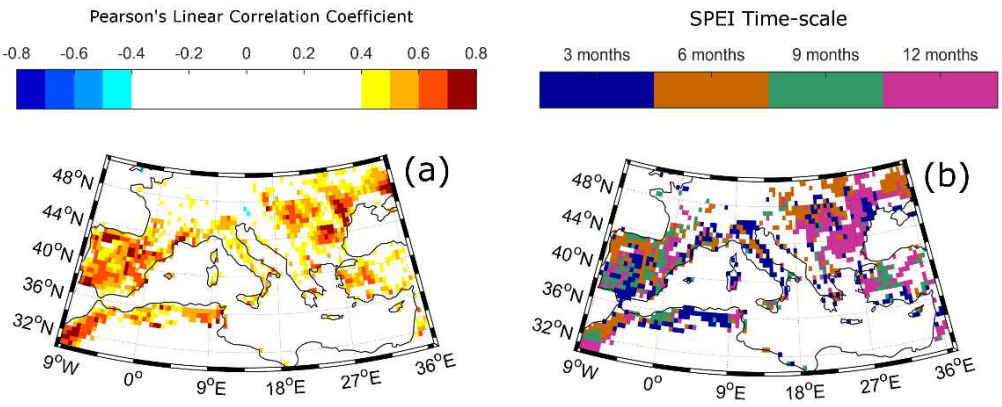

Figure 5.3 – Spatial distribution of the Pearson's linear correlation coefficient (A) between VHI of the maximum NDVI month and the SPEI time scale (B) for which the correlation is maximum.

5.2.3.3. The relative importance of VCI and TCI

The relative importance of VCI and TCI to VHI was assessed based on the values of correlations between each component and SPEI, again restricting to the pixels where VHI and SPEI have significant correlations (with a p-value of 0.05). Figure 5.4 shows the results obtained for the five clusters of maximum NDVI occurring in months from March to July. For each cluster, the correlations between VCI-SPEI are plotted against the ones between TCI-SPEI. Each colour represents one time-scale (blue for 3 months, orange for 6 months, green for 9 months and pink for 12 months), the horizontal and vertical lines extend from the 25th to the 75th percentiles, and the lines intersect at the median values of the two correlations. Clear differences are observed among clusters in terms of VCI and TCI contributions. For instance, when comparing the cluster with maximum NDVI in March and July, the first shows greater correlations of SPEI with VCI, while TCI best correlates with SPEI in the latter.

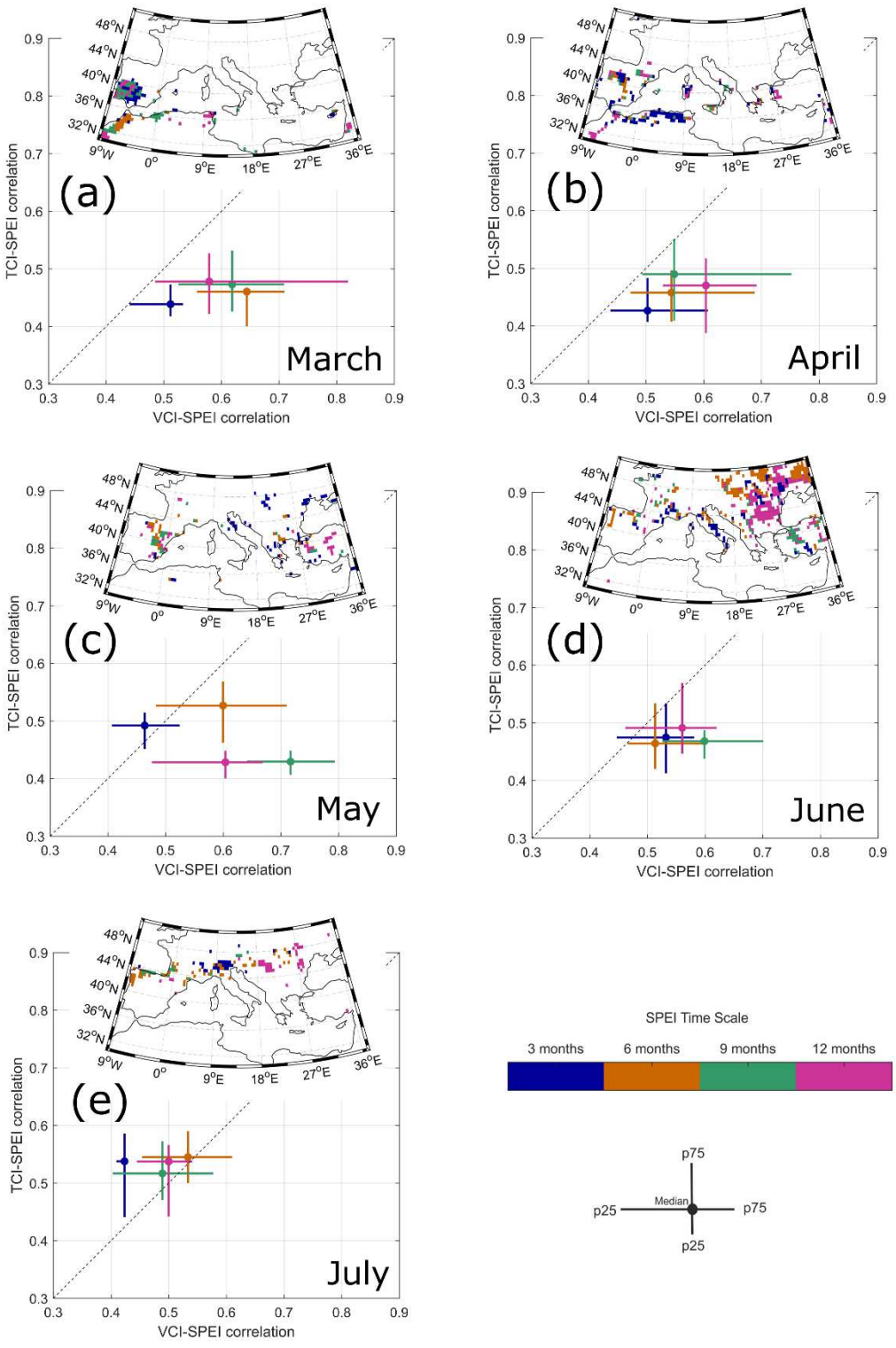

Figure 5.4 – Relationship between the correlations of VCI-SPEI and TCI-SPEI for the significant pixels of the maximum NDVI months and its spatial distribution.

Figure 5.4a shows the relative behaviour of VCI and TCI when correlated with SPEI inside the cluster with maximum NDVI in March. The pixels have higher

VCI-SPEI correlations for all time scales. Nevertheless, the 3 month time scale is the one where the correlation between VCI-SPEI is lower. It is also worth noticing that this time scale is the only one where almost all the pixels are located over Iberia. On the other hand, the time scale of 6 months is almost entirely located in north-western Africa. This is the time scale with higher correlations between VCI-SPEI. Finally, the 9 and 12-month time scales are distributed between northwest Africa and Iberia. These have slightly higher correlations between TCI-SPEI than the shorter time-scales and are much more scattered through the plot than the shorter time scales.

For the cluster of maximum NDVI in April (Figure 5.4b) the results are very similar to those discussed above for the previous cluster. Here the dominant time scale is the 3 months, set in the Mediterranean north Africa (Algeria and Tunisia) and central Iberia. Once again, this shorter time scale is the one with lower correlations between VCI-SPEI. The longer time scales (6, 9 and 12 months) have all higher correlations of both VCI-SPEI and TCI-SPEI than the 3-month time-scale. Most of the pixels are situated in semiarid regions, such as in the previous cluster (Table 5.1).

The cluster where maximum of NDVI occurs in May is located in eastern Iberia and some pixels are scattered over eastern Europe (Figure 5.4c). Some of the pixels are situated in the semiarid region whereas others are located in the dry sub-humid and humid ones (Table 5.1). Here the shorter 3-month time scale is mainly located in pixels on eastern Europe and the correlations between TCI-SPEI tend to be greater than those of VCI-SPEI. On the other hand, the longer time scales of 6, 9 and 12 months have, once again, higher VCI-SPEI correlations. These are situated mainly in Eastern Iberia and central Turkey – semiarid regions.

Figure 5.4d presents the results for the cluster with maximum NDVI in June. Pixels are distributed throughout eastern Europe, with a few pixels located over Italy and northern Iberia. The dominant climates for these regions are the humid and dry sub-humid ones (Table 5.1), with a few pixels in the semiarid region of Turkey. Here, the 3, 6 and 12-month scales have greater VCI-SPEI correlations but are organised closer to the diagonal when compared to earlier months. The 9-month time-scale has the greater VCI-SPEI correlations. However, pixels where this scale

dominates are situated particularly over Turkey, which has a drier vegetation land cover than the remaining regions studied in June. Consequently, temperature extremes will have smaller effect on vegetation health, while its dependence on NDVI will be dominant (Vicente-Serrano et al. 2015).

Finally, the cluster with maximum NDVI in July is situated in eastern Europe, northern Iberia and the Alpine region (Figure 5.4e), which are regions defined by a moistier (Table 5.1) climate (much more sensitive to temperature extremes since solar radiation is the main limiting factor in these regions (Karnieli et al. 2010). Here, the contribution of temperature prevails, since all the scales have higher TCI-SPEI correlations than VCI-SPEI (centroids).

Results presented in Figure 5.4 suggest the existence of a wide variability of VCI and TCI contributions to the overall vegetation stress. Therefore, the relative contribution of VCI and TCI (α in Eq. 2.8), is identified by maximising the correlation between VHI and SPEI on a pixel basis. Figure 5.5 shows the spatial distribution of the optimum weights. Higher values of α, representing a greater contribution of VCI to the overall vegetation health, are found on Western Iberia, north Africa, north-eastern Balkans, Ukraine and central Turkey. Conversely, lower values of α (higher values of $(1-\alpha)$ and therefore a larger contribution of TCI) are found in northern and central Iberia, mountainous regions, Italy, and part of eastern Europe/western Balkans.

The distribution of α with respect to aridity classes and IGBP landcovers are shown in Figure 5.6. Higher values of α are spread over semiarid regions and tend to progress into lower values with the increase of humidity. For each distribution the mean value of α for each month of maximum NDVI cluster is displayed (filled dots in the panels of Figure 5.6). Results show that clusters representing earlier months of maximum NDVI have typically higher/lower values of α inside the humid/semiarid regions while clusters representing later months are characterised by lower/higher values inside the humid/semiarid regions. Vegetation with maximum activity in March present higher values of α for open shrubland and cropland, and lower values for savannas-like land cover types. On the other hand, vegetation with maximum activity in June and July presents generally lower values of α, except over grasslands, which show, as expected, maximum activity in June

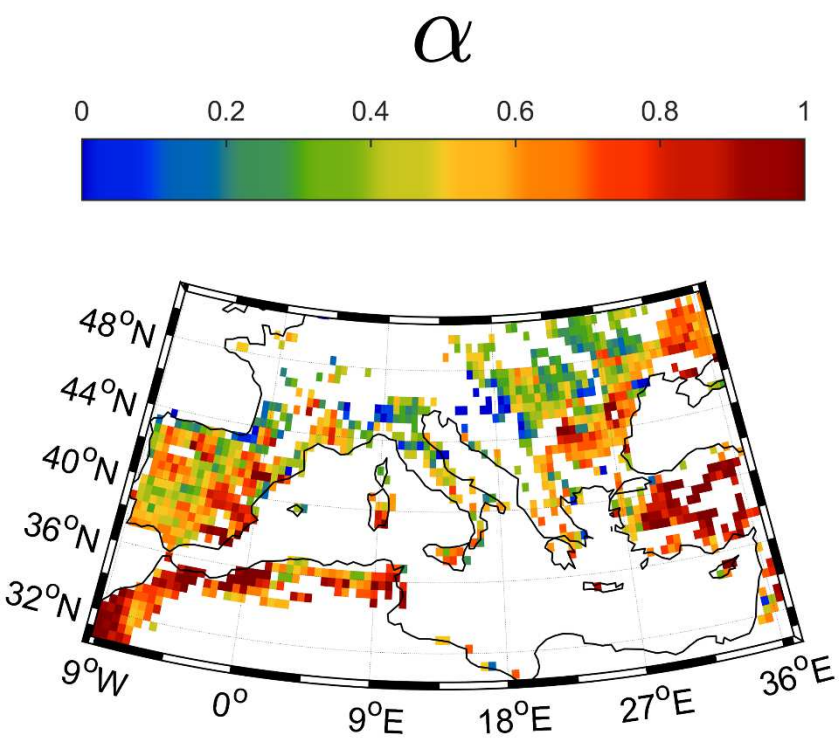

Figure 5.5 – Values of α for which the pixel-by-pixel correlation between VHI and SPEI is maximised.

and high values of α. Furthermore, results shown in Figures 5.4 – 6 suggest that the usual assumption of assigning equal weights to both VCI and TCI to estimate VHI may not be an optimal choice for certain clusters/aridity classes. When comparing both terms to SPEI at different time scales (Figure 5.4) it is shown that, depending on location and time of the year, vegetation health can be more dependent of the intrinsic vegetation stress (measured with NDVI) or temperature stress (measured with LST). Following Liebig's Law of the Minimum, which states that vegetation growth is controlled by the scarcest resource available in the system (Smith and Smith 2015), then the first typically occurs in regions defined by semiarid landscape, where water availability is the limiting factor for vegetation growth (Vicente-Serrano et al. 2015), i.e., a small change in the amount of water in the ecosystem (vegetation) causes a non-negligible change in the vegetation growth. These results are in agreement with (Gouveia et al. 2017) and (Vicente-Serrano et al. 2013), both showing high correlations between NDVI and SPEI in north Africa, Iberia and the Balkan region. Conversely, the latter occurs typically within humid bioclimates and mountainous regions, where energy (solar radiation) is the limiting

factor for vegetation development (Karnieli et al. 2010). The distribution of the estimated α (Figures 5.5 and 5.6) arises as a direct consequence of the asymmetry between VCI-SPEI and TCI-SPEI correlations shown in Figure 5.4. These statements are in agreement and complement the previously mentioned works (Karnieli et al. 2006, 2010) concerning the assumption of the negative correlation between NDVI and LST.

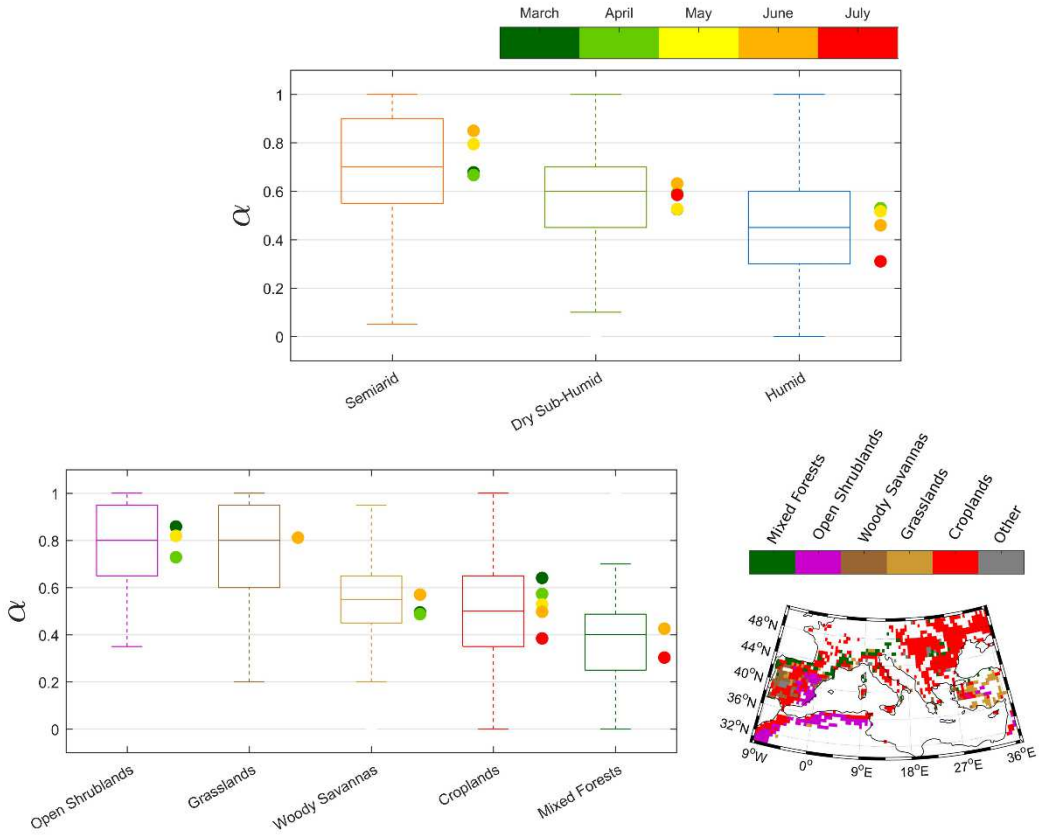

Figure 5.6 – Distribution of α (top) for the different aridity classes and (bottom left) for the IGBP classes of landcover. Both panels show the mean of α for each of the maximum NDVI clusters in a given distribution (filled circles). The spatial distribution of the IGBP landcovers for the regions where correlations of VHI-SPEI is significant is also displayed (bottom right).

5.3. A global application[6]

5.3.1. Data and Methods

NDVI and LST data are the same as described in the previous section, and VHI, VCI and TCI also follow the same methodology, but now estimated for the whole globe. The Standardized Precipitation-Evapotranspiration Index (SPEI; Vicente-Serrano et al. 2010) is used to characterise the impact of drought on vegetation health.

In order to estimate coefficients α and $(1-\alpha)$ two methods are discussed in this section: (1) using an iterative maximisation of the correlation between VHI and SPEI (same as in the previous section); and (2) using canonical correlation analysis (CCA).

In the first approach, and as discussed earlier, the relative contribution of VCI and TCI through weights α and $(1-\alpha)$ are identified by maximising the correlation between VHI and previous month SPEI for each pixel. First, the Pearson's linear correlation coefficients were computed between VHI of the month of maximum NDVI and the SPEI of the previous month, estimated over time scales of 1 up to 12 months. A p-value of 0.05 for the two-tailed t-test is used to reject the null hypothesis of no correlation. Then, on a pixel-by-pixel basis, the time scale of SPEI that has the maximum correlation with NDVI is chosen. Finally, the optimum value of α is identified via an iterative process with the aim of maximising the correlation between VHI and the previous month SPEI: we start with $\alpha = 0.025$; then this value is incremented in steps of 0.05 until 0.975; the value of α for which the correlation is larger is then finally retained.

The second approach relies on CCA to find the best global maps of weights α and β, given by:

$$VHI = \alpha VCI + \beta TCI \qquad \text{Eq. 5.3}$$

[6] Adapted from Bento, V.A., DaCamara, C.C., Gouveia, C.M., Trigo, I.F. On the global assessment of vegetation and temperature contributions to a SPEI based vegetation health index. In preparation.

where the weight β may be different from the term $(1-\alpha)$ shown in Eq. 2.8.

The CCA leads to linear combinations of the time-series of VCI and TCI of the month of maximum NDVI and previous month SPEI (at 1- to 12-month time scales) which have maximum correlation ρ with each other. This results in 12 pairs of canonical coefficients, one for each SPEI time-scale. Then, for each pixel the time-scale with maximum correlation is chosen and the two canonical coefficients associated with that time-scale are retained. Pixels with correlations not statistically significant at the 5% significance level are discarded.

Desert regions, which are of no interest for a vegetation health study, are masked according to land cover data from the International Geosphere-Biosphere Programme (IGBP; Loveland et al. 2000).

Results obtained using the two above-mentioned methodologies are stratified using aridity and biome classes. Based on the aridity index (Zomer et al. 2006, 2008) from the CGIAR-CSI Global-Aridity and Global-PET Database (http://www.cgiar-csi.org), estimated with evapotranspiration based on the Hargreaves equation (Hargreaves 1994), 6 classes are defined: hyper arid, arid, semi-arid, dry sub-humid, moist sub-humid and humid (Figure 5.7, top). The hyper arid class is entirely located over deserts, and therefore, pixels belonging to this class are masked and are discarded in this study. For biome classes, the IGBP (Loveland et al. 2000) land cover is used to further stratify regions into forests, shrublands, grasslands, croplands and savannas (Figure 5.7, bottom).

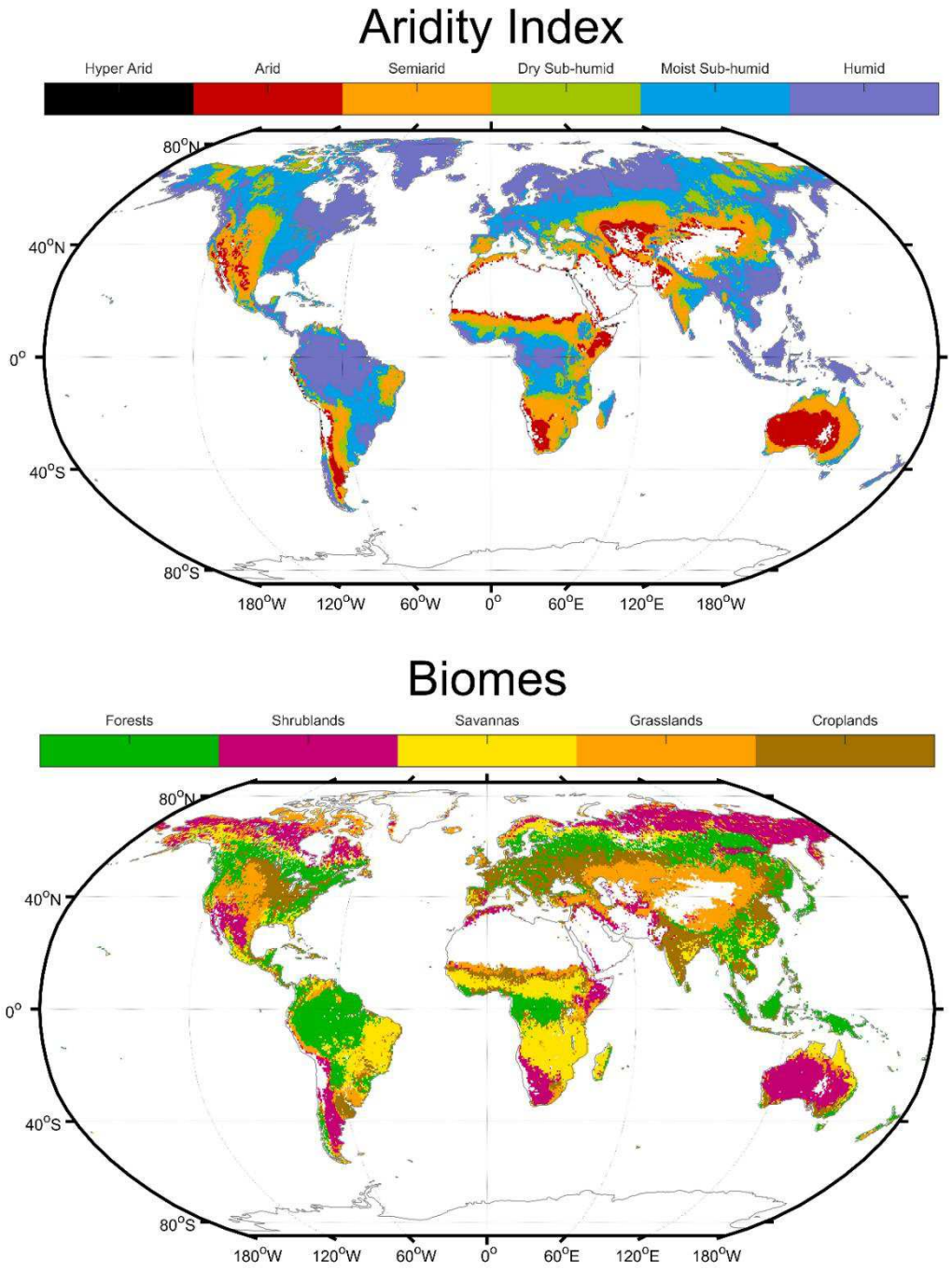

Figure 5.7 – Aridity index classes (top) based on the CGIAR-CSI Global-Aridity and Global-PET Database and biomes classes (bottom) based on the IGBP landcover. Deserts are masked in white following the IGBP definition.

5.3.2. Results and Discussion

5.3.2.1. Iterative maximisation of the VHI-SPEI correlation

Figure 5.8 shows the global map of the coefficient α as obtained by maximising the correlation between VHI and SPEI. The spatial distribution of α suggest the organisation of pixels with similar values (and statistically significant correlations), namely over North America, Brazil and Argentina regions on South America, South Africa, Iberia, Morocco, South Russian territory, the Middle East, India and Australia. It is also possible to note that regions where VCI dominates (yellow to red pixels) or TCI dominates (blue to green pixels) the contribution to vegetation health are well clustered in the map.

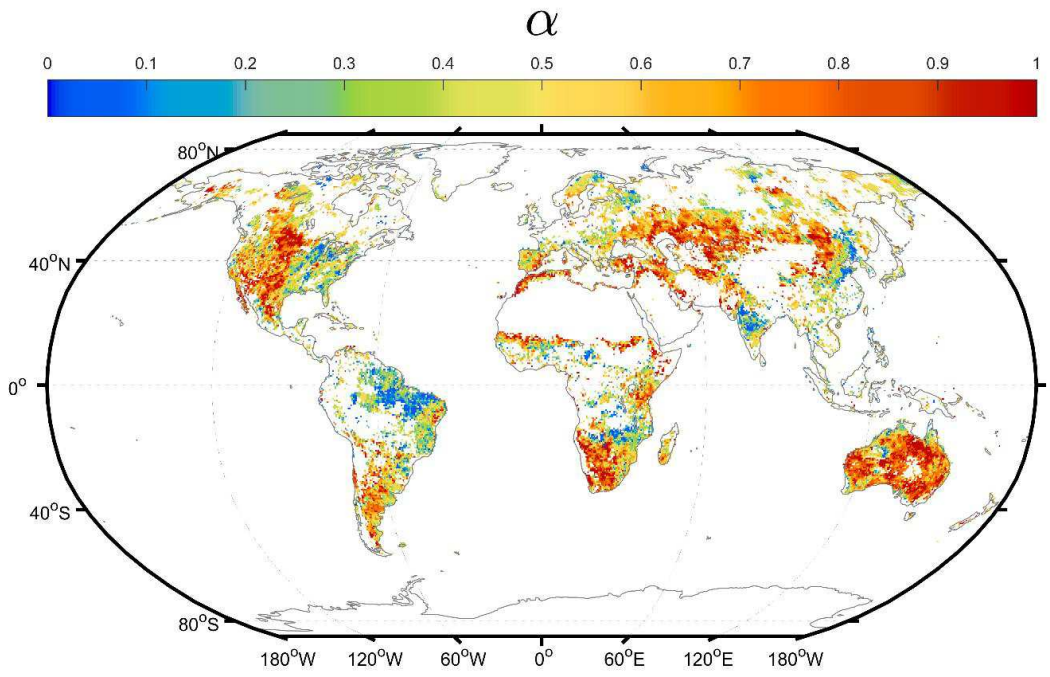

Figure 5.8 – Global map of coefficient α as estimated through the stepwise maximisation of the correlation between VHI and SPEI.

These regions were stratified into classes of aridity and biomes, as shown in Figure 5.9. The boxplots show that regions where TCI dominates ($\alpha < 0.5$) are characterised by a moister climate than regions where VCI dominates ($\alpha > 0.5$). In the first case ($\alpha < 0.5$), the 25th, 50th and 75th percentiles belong to the dry sub-humid, moist sub-humid and humid climatic classes, respectively, while the second set of coefficients ($\alpha > 0.5$) are distributed among the arid, semiarid and moist sub-

humid climatic classes, respectively. These relations are expected to have an impact on the biomes for each class also. Figure 5.9 shows that VCI dominates VHI estimates in regions characterised by less productive biomes like grasslands and shrublands. Conversely, TCI dominates in forests, croplands and savannas, by order of importance. These results indicate that there is a strong global dependency of the weights assigned to VCI and TCI and the properties of the region of interest, to the estimation of the (SPEI-based) vegetation health index.

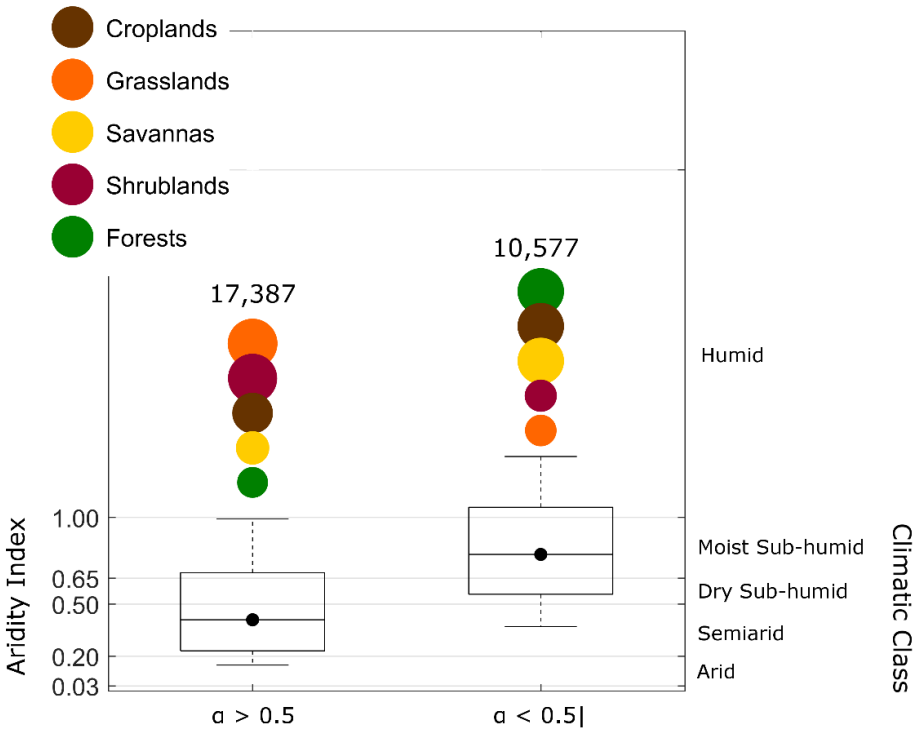

Figure 5.9 – Boxplots representing the aridity intervals for $\alpha > 0.5$ (larger VCI contribution) and $\alpha < 0.5$ (larger TCI contribution). The black dot represents the median value, the box represents the 25th and 75th percentiles, and the whiskers the 5th and 95th percentiles. The coloured circles represent the landcovers associated to that interval of α. The size of the circles is proportional to the percentage of the total number of pixels in each combination (numbers above the circles). The sum of the coloured circles in each combination is 100%.

The dependence of α on the aridity index is further shown in Figure 5.10. For intervals of aridity of 0.05 the respective mean (black dots) and the 25th and 75th percentiles (blue lines) of α are estimated. Here, besides showing once again that drier regions are more dependent on VCI while moister regions tend to be dominated by TCI, it is also observed a well-behaved relation between the two variables. This relation may be of great importance for applications since by fitting

a simple model, one can determine the contribution of VCI and TCI just by having aridity as information.

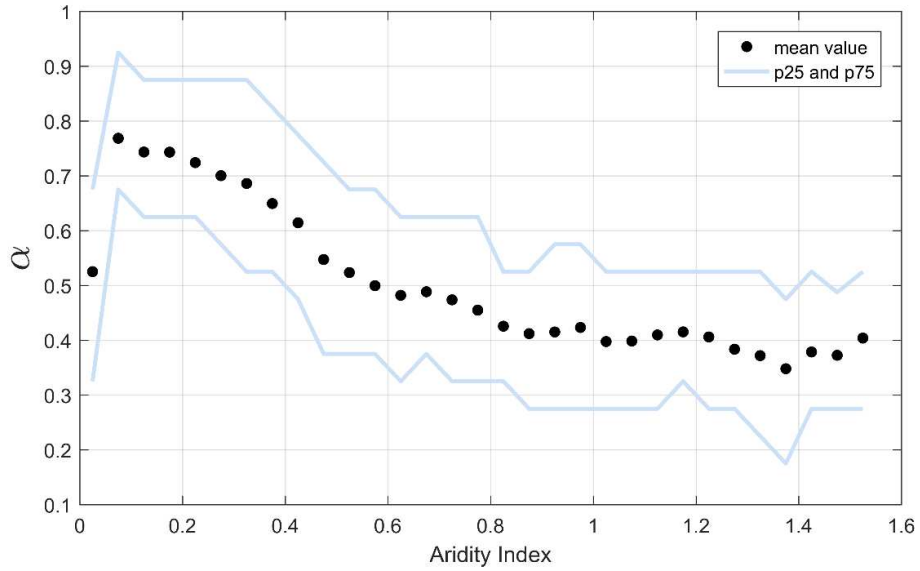

Figure 5.10 – Relation between α and the aridity index. Black dots represent the mean of α in an interval of 0.05 in aridity index. Blue lines represent the 25th and 75th percentiles.

5.3.2.2. Canonical Correlation Analysis

Figure 5.11 shows the global map of the combination of coefficients α and β (both positive, both negative, or one positive and the other negative), as obtained through the canonical correlation analysis approach.

Table 5.3 shows the number of pixels with statistically significant correlations that belong to each combination. More than 60% of the pixels have both coefficients with positive sign. This means that for most of the pixels SPEI positively correlates with VCI and TCI. Furthermore, Table 5.3 shows that, for this particular combination of coefficients, there are slightly more cases where α is greater than β (57% against 43%, respectively). In the cases where α is greater than β the relative importance of VCI to the overall vegetation health is greater, while in the opposite cases TCI is the dominant term to estimate VHI. Conversely, a small number of cases where both coefficients are negative (about 3% of the pixels; Table 5.3) is found. In these cases, SPEI negatively correlates with both VCI and TCI, which implies that a drought episode is related to lower (higher) than normal temperatures (NDVI). In about two thirds of these pixels the module of α is greater than the

module of β, implying that VCI is the dominant negative term to VHI. Moreover, Table 5.3 shows that about 15% of the total number of pixels have a positive value of α and a negative value of β, meaning that SPEI positively correlates with VCI and negatively correlates with TCI. Here, the great majority of pixels (93%) have a larger positive contribution of VCI to the estimation of VHI than a negative contribution of TCI (about 7% of the pixels). Finally, 19% of the pixels show negative correlation between SPEI and VCI ($\alpha < 0$) and a positive correlation of SPEI and TCI ($\beta > 0$). This is the only combination of coefficients where for most of the pixels (72%) VHI is estimated with a larger contribution of TCI (in module) than VCI (28%).

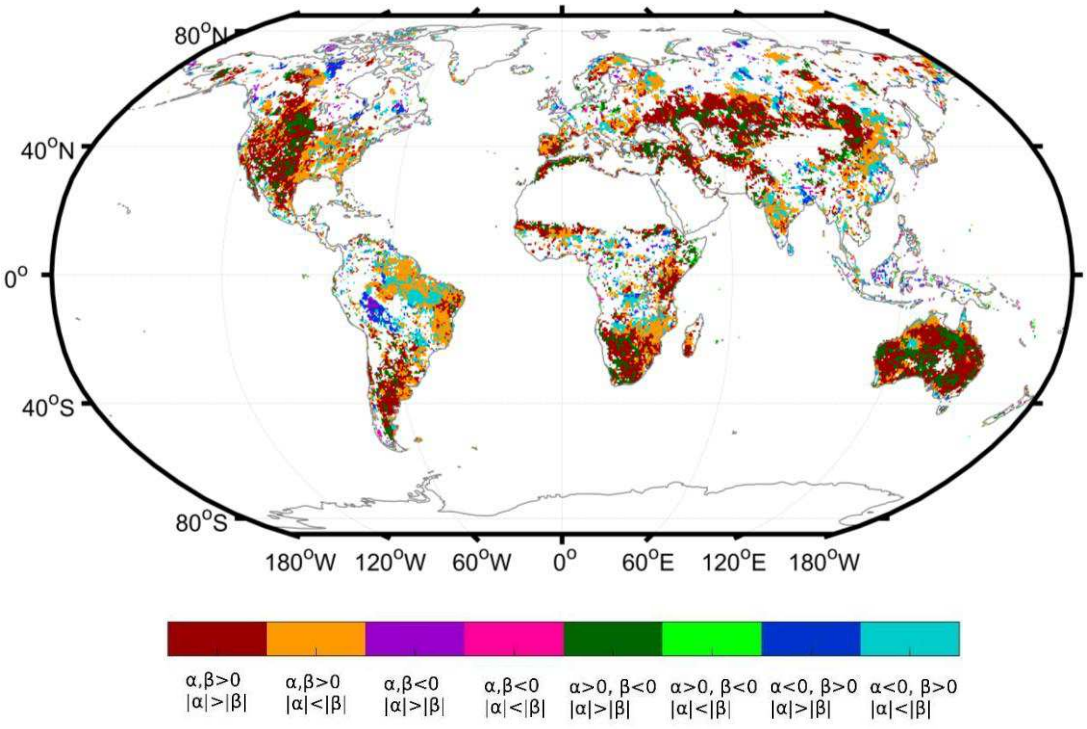

Figure 5.11 – Global map of α and β coefficient combinations as estimated through canonical correlation analysis.

These results show that for the majority of the pixels (63%) the approach followed here is consistent with that developed by (Kogan 1997), where both coefficients are positive, i.e., the assumption that vegetation health is poor when NDVI is low and temperature is high works well for most cases. Furthermore, Table 5.3 shows that for cases where one of the coefficients is positive and the other is negative, the positive term has always the greater contribution to VHI. This is particularly striking in the case where $\alpha > 0$ and $\beta < 0$. This means that although

lower than normal temperatures ($\alpha > 0$ and $\beta < 0$) or higher than normal NDVI values ($\alpha < 0$ and $\beta > 0$) are related to drought in a given region, the predominant contribution to vegetation health is the lower than normal NDVI values and higher than normal temperatures, respectively.

Figure 5.12 shows the relationship between pixels with a given combination of coefficients and its predominant land cover and aridity distributions. Results show that only two combinations of coefficients have the semiarid climate class represented as their median: the combination of $\alpha, \beta > 0$ and the one where $\alpha > 0, \beta < 0$, with both presenting $|\alpha| > |\beta|$ (representing 10,122 and 3,807 pixels – about 37% of the total pixels –, respectively). These are the only combinations (of the eight possible) where $\alpha > 0$ and $|\alpha| > |\beta|$, i.e. VCI correlates positively with SPEI and is the dominant term in the estimation of VHI. The only difference between them is the sign of β: VCI correlates positively with SPEI in the first and negatively in the latter case. These regions are also defined by a predominance of shrubland and grassland biomes (Figure 5.12), typically defined by warm and dry conditions and low altitude vegetation.

Table 5.3 – Number and percentage of pixels for each coefficient α and β combination (and its rationale). Only pixels with statistically significant correlations are considered.

	# pixels (% of total)		# pixels (% of total in the combination)	Rationale
$\begin{cases}\alpha > 0\\ \beta > 0\end{cases}$	17,799 (63%)	$\lvert\alpha\rvert > \lvert\beta\rvert$	10,122 (57%)	SPEI correlates positively with both VCI and TCI
		$\lvert\alpha\rvert < \lvert\beta\rvert$	7,677 (43%)	
$\begin{cases}\alpha < 0\\ \beta < 0\end{cases}$	861 (3%)	$\lvert\alpha\rvert > \lvert\beta\rvert$	574 (67%)	SPEI correlates negatively with both VCI and TCI
		$\lvert\alpha\rvert < \lvert\beta\rvert$	287 (33%)	
$\begin{cases}\alpha > 0\\ \beta < 0\end{cases}$	4,111 (15%)	$\lvert\alpha\rvert > \lvert\beta\rvert$	3,807 (93%)	SPEI correlates positively with VCI and negatively with TCI
		$\lvert\alpha\rvert < \lvert\beta\rvert$	304 (7%)	
$\begin{cases}\alpha < 0\\ \beta > 0\end{cases}$	5,313 (19%)	$\lvert\alpha\rvert > \lvert\beta\rvert$	1,500 (28%)	SPEI correlates positively with TCI and negatively with VCI
		$\lvert\alpha\rvert < \lvert\beta\rvert$	3,813 (72%)	

On the other hand, the positive combination of coefficients, with $|\alpha| < |\beta|$ (representing the second larger individual combination with 7,677 pixels – about 27% of the total) has its distribution median centred on the moist sub-humid class

(with the 25th and 75th percentiles in the dry sub-humid and humid classes, respectively), and the main biomes represented are croplands, savannas and forests. In these regions the relative importance of TCI to the overall vegetation health is larger than VCI. When comparing the two combinations of coefficients where α and β are positive it is possible to check their complementarity: (1) when $|\alpha| > |\beta|$ (drier and warmer biomes like grasslands and shrublands) the limiting factor to vegetation growth is water and vegetation health is more determined by the condition of the vegetation measured by NDVI; (2) when $|\alpha| < |\beta|$ (moister biomes like savannas, croplands and forests) the limiting factor is solar energy and vegetation health is more determined by temperature.

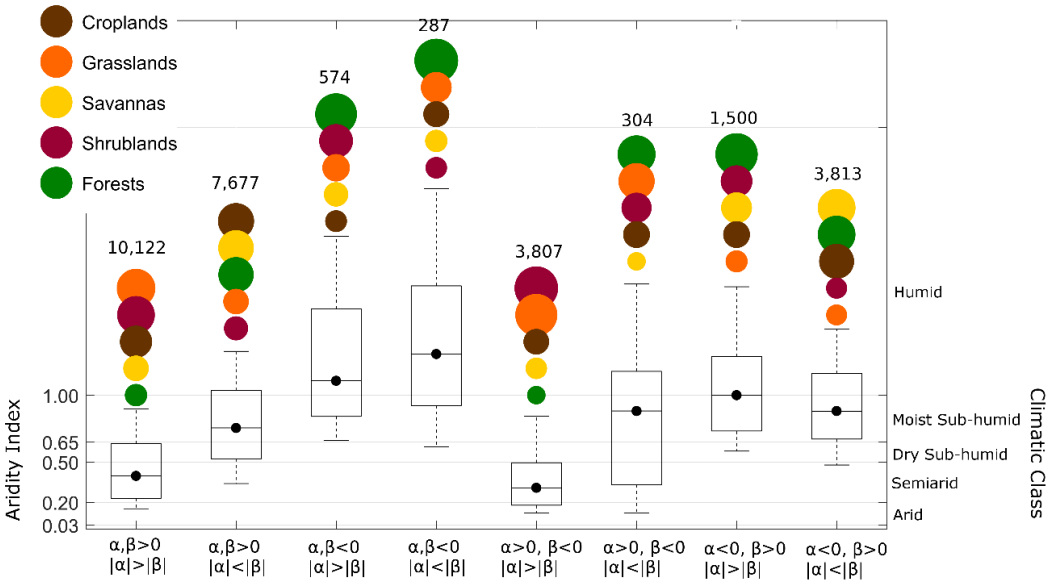

Figure 5.12 – Boxplots representing the aridity index distribution and its associated climatic class over the different coefficient combinations. The black dot represents the median value, the box represents the 25th and 75th percentiles, and the whiskers the 5th and 95th percentiles. The coloured circles represent the landcovers associated to that combination of coefficients. The size of the circles is proportional to the percentage of the total number of pixels (numbers above the circles) in each combination (as displayed in Table 5.3). The sum of the coloured circles in each combination is 100%.

Using CCAs to estimate the contributions of VCI and TCI to the overall vegetation health is a promising methodology since, by definition, the correlation between VCI, TCI and SPEI is maximised. However, results where one or two of the coefficients are negative are very difficult to explain on a physical basis. Instead, they may be viewed as a purely statistical result, without physical meaning. One example is the case where the two weights are taken negative: this means that, e.g.,

a drought episode is related to higher than normal NDVI (greener than normal) and lower than normal temperatures – following Figure 5.12 this is mainly found in forest regions. Another example is the case where $\alpha < 0$ and $\beta > 0$: here a drought episode is related to higher than normal temperatures, which is expected, but it is also related to greener than normal conditions (high NDVI values), which is in contradiction with the expected drought effects. It is also important to refer that the dataset of SPEI used in this work relies on Climate Research Unit (CRU) data. Errors may arise in regions where observations are very sparse.

When comparing Figure 5.9 with Figure 5.12 it is noticeable that the boxplots estimated with the iterative maximisation (Figure 5.9) and the two boxplots where $\alpha, \beta > 0$ estimated with the CCAs (Figure 5.11) are very similar. The main difference found in the two is the (small) change in the percentage of forests for the TCI-dominant cases.

Another problem of the CCA methodology is related to the correlations between VCI and TCI. If these two variables are highly correlated it is possible to have, for example, a positive correlation between VCI and SPEI with the CCA method and a negative one when the simple correlation is computed. This may lead to interpretation problems. One process to avoid this problem is to orthogonalize VCI and TCI with the help of a Principal Components Analysis (PCA). However, this process would lead to even more ambiguous results and interpretation, since the canonical correlation would not be fed with VCI and TCI but with some combination of the two that would explain the maximum amount of variance.

5.4. Using Meteosat LST CDR

The analysis performed in the previous sections can also be applied to the Meteosat LST CDR developed in Chapter 3, which as opposed to Princeton University LST is not an assimilated merged variable, but a pure remotely sensed clear-sky LST, with the added benefit of being estimated with the pixel emissivity (instead of a unitary value). Furthermore, a set of coefficients estimated using a fully observational Meteosat TCI may be important for implementing real time drought monitoring using MSG/SEVIRI.

As described in Chapter 3, the CM SAF LST consists of two databases: one estimated with Physical Mono-Window (PMW) algorithm; and one estimated with the Statistical Mono-Window (SMW) algorithm, with information spanning the period from 1991 to 2009. LST is organised as monthly diurnal cycle means, i.e., each month consists of 24 values containing the hourly means for the respective month, or instantaneous values. For this analysis the first are used. From these, monthly means of a mean day are then estimated (one value per month), and the same procedure previously detailed is applied in order to remove each pixels' time series trend. Then, TCI is estimated using both datasets. On the other hand, VCI is estimated exactly as described in the previous sections but for the 1991 – 2009 period.

Princeton University LST is also used with the aim of comparing the weight α estimated with the three different LSTs. However, a new setting of this dataset is required, since in the previous chapters the procedure relied in picking the maximum daily mean LST value of each fortnight. To keep consistency with CM-SAF's variables, the monthly means of the diurnal cycle are estimated for the Princeton LST, from the hourly data. Then, the methodology of trend removal and TCI estimation is followed.

The iterative maximisation of VHI and SPEI with the aim of estimating α is then applied, TCI being estimated with the three datasets. Figure 5.13 shows the derived maps of α when using PMW LST and SMW LST and when estimated with Princeton University LST (1991 – 2009).

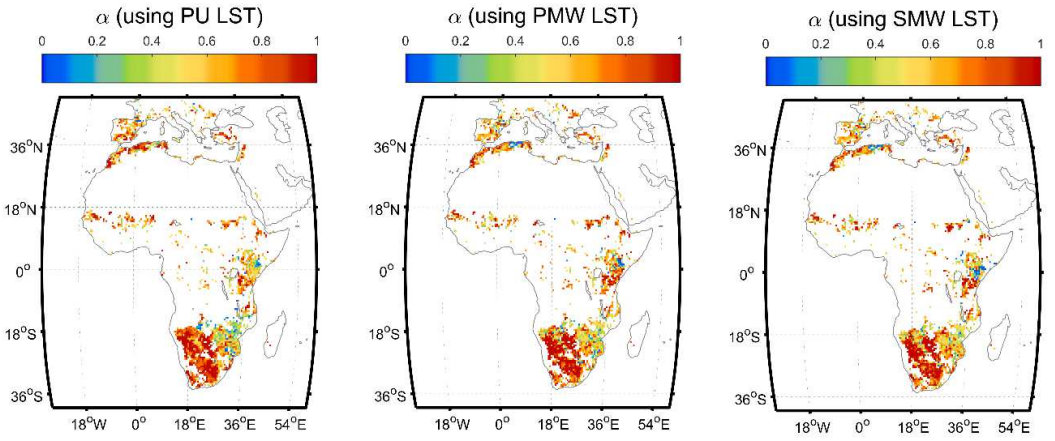

Figure 5.13 – Comparison of α estimated with TCI dependent on: Princeton University (PU) merged LST (left), CM SAF PMW LST (center), CM SAF SMW LST (right).

Histograms of the differences between α estimated with PMW LST, SMW LST and PU LST are shown in Figure 5.14. Distributions of α derived from PMW and SMW LST against the one derived from PU LST, and the distribution of the weight estimated from PMW against SMW LSTs are also shown in Figure 5.14. The patterns in Figure 5.13 show great similarity among the datasets. Differences between values of α are larger in various regions, which puts into evidence the sensitivity of this analysis to the input data being used. Nevertheless, the magnitude and spatial distribution of α are coherent among these datasets; the RMSDs of α derived with PU and the clear sky LSTs are about 0.2. Furthermore, it is worth noticing that the differences between α estimated with PMW and SMW LSTs are smaller, with a RMSD of about 0.1. The average differences of α estimated with the different LST datasets are negligible, which means that the use of any of these datasets is not introducing any overall systematic error in this type of analysis.

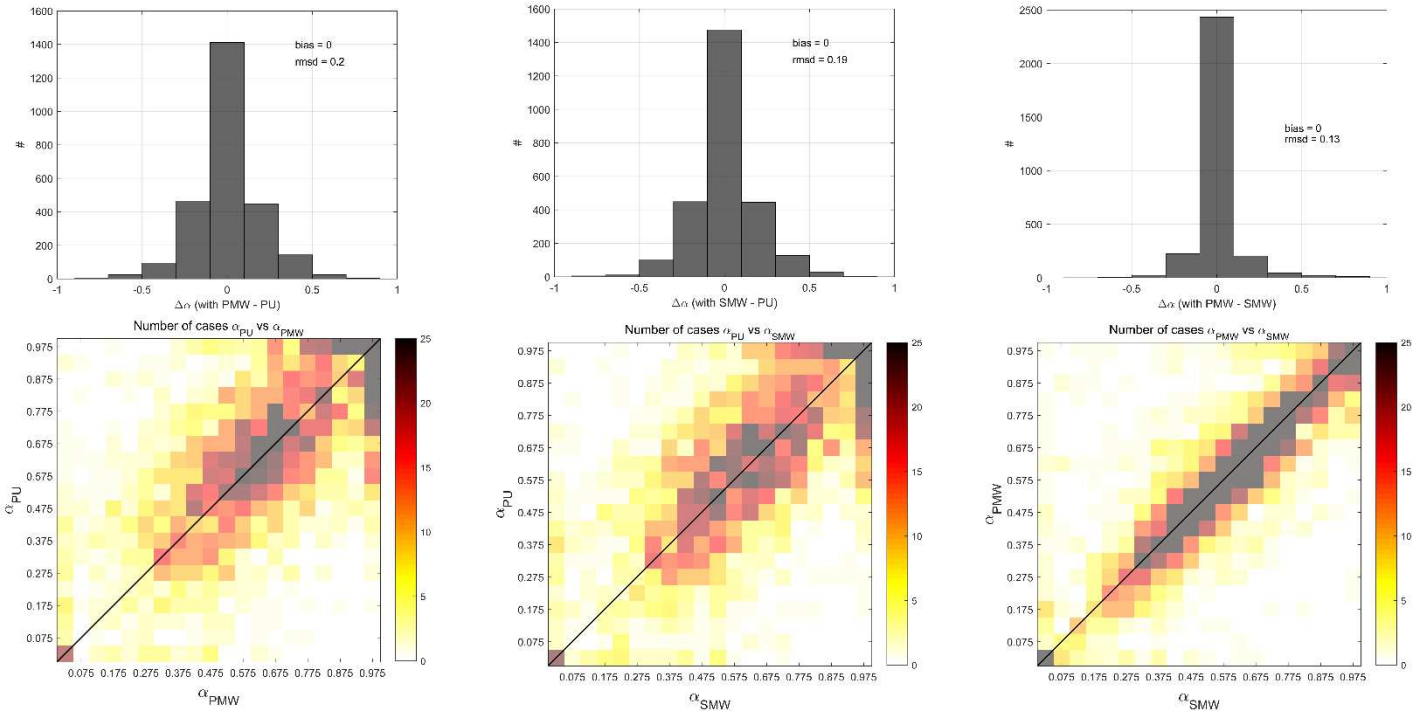

Figure 5.14 – Histogram of the differences between estimated with PMW – PU (top left), SMW – PU (top center) and PMW – SMW (top right); and distribution of the number of pixels with values of α with PMW against PU (bottom left), SMW against PU (bottom center) and SMW against PMW (bottom right). The black line represents the diagonal.

5.5. Conclusions

The Vegetation Health Index (VHI) has been widely used to study and monitor droughts all over the globe using remote sensing observations. VHI is based on a linear combination of two indices, namely the Vegetation Condition Index (VCI) that uses information from visible and near infrared channels (usually NDVI) and the Thermal Condition Index (TCI) based on data in the thermal infrared channels (usually top-of-atmosphere brightness temperature or land surface temperature). Since there is no a priori knowledge about the contribution of VCI and TCI to vegetation health, equal weights are usually assigned to both (Kogan, 2001). The aim of this paper was to analyse, for the period 1982-2009, the relative contributions of VCI and TCI to VHI, for different types of vegetation over Europe.

The study area was divided into clusters with different vegetation characteristics. These were based in the climatological maximum month of NDVI, i.e. the month at which the impact of vegetation and thermal stress is the greatest. Five clusters were retained, representing regions where maximum NDVI occurs in months from March to July. Following the CGIAR-CSI aridity index and UNESCO definition of aridity classes, it is shown that clusters with maximum NDVI earlier in the year (March, April) are mainly located in semiarid regions, while clusters with later occurrences of maximum NDVI (July) are mostly located in regions defined by a humid climate class. Furthermore, pixel-based correlations between VHI of the month defined by the respective cluster and SPEI of the previous month (computed over different time-scales) were estimated. Significant correlations were found mainly in semiarid and dry sub-humid regions, i.e. vegetation health is more (less) determined by drought in semiarid (humid) regions, with the notable exception of the humid northern Iberia and some mountainous regions. For the areas with significant VHI-SPEI correlations the contributions of VCI and TCI to VHI were assessed. The comparison between VCI versus SPEI correlations and TCI versus SPEI ones, indicates that the relative contribution of VCI and TCI depends mostly on vegetation cover, – with VCI being more relevant in water dependent semiarid regions and TCI being more relevant in solar radiation dependent humid regions. As such, the corresponding weights to VHI are not necessarily equal. With the aim of accounting for this variability the relative contribution of VCI and TCI, as obtained by the parameter α – varying between 0 and 1 – was identified by

maximising the correlation between VHI and SPEI. It was found that regions where α is higher (and therefore VCI is largely driven by drought) correspond to the semiarid climate class, while a decrease in the value of the weight was found when evolving to moistier classes (i.e. TCI is more affected by drought).

Given the above dependence on vegetation type of the weights related to VCI and TCI contributions to VHI, the following should be taken in account: i) it is advantageous to monitor and study drought events using VCI and TCI on a separate basis and considering this information when analysing VHI in space and time; ii) the use of appropriate weights to estimate VHI for different vegetation types may be an asset.

LST and NDVI climate data records are then used to assess global maps of the relative contributions of VCI and TCI to estimate a global SPEI-based VHI. A map with this information would be an asset to use in drought monitoring, decreasing the error associated with the general use of equal weights associated to each term. Here, two methodologies are used to derive the contributions of VCI and TCI to VHI on a global scale. The first methodology is similar to the one previously used, where the maximum correlation between VHI and SPEI of the previous month is found by a stepwise maximisation problem. The second methodology relies in a canonical correlation analysis (CCA) which finds the linear combinations between VCI, TCI and SPEI that maximises its correlation.

Results obtained with both methodologies are very similar. The CCA method is a promising approach since it directly maximises the correlation between VCI, TCI and SPEI with no need to assign and iterate a priori values of α. However, problems of interpretation may arise when canonical coefficients are assigned negative signs. However, if dismissing these cases, the majority of the pixel correlations behave as physically expected (following Kogan, 1997). For these pixels, and for both methodologies, results show that VCI and TCI contributions depend on the aridity class in the region: VCI dominates for water limited semiarid regions while TCI dominates for energy limited moistier regions. These results are in agreement with the work developed in the previous section.

This work paves the way to a general set of global weights to be used on VHI to a better monitoring of drought. Further work is necessary to understand the cause

of the negative CCA coefficients – if it is of physical character or a statistical relic – and to evaluate the best methodology to estimate the relative contributions.

Finally, the methodology of the iterative maximisation of VHI and SPEI is applied to the Meteosat disk. Here, the LST CDR developed in Chapter 3 and available to the public at the CM SAF website, is used to estimate TCI. Preliminary results show small discrepancies between results using the merged Princeton University LST and the CM SAF LST. Future work is needed to further analyse these results, specially having in consideration the missing values due to cloud contamination.

The next step may consist of using the estimated weights and apply them to a few different regions in order to understand if the SPEI-based VHI derived in this chapter does a better work in capturing drought episodes when compared to the traditional VHI estimated with equal weights for VCI and TCI.

Chapter 6

During the previous chapters a Climate Data Record of Land Surface Temperature was developed and improved, and an application that relies in such a dataset was studied. This chapter aims at summarising the overall conclusions, while linking all the work done throughout the PhD.

6. Overall Conclusions and Final Remarks

The main drive of the present thesis was to explore satellite derived LST climatologies: from its development to its application in climate problems.

Satellite-based remote sensing for meteorological applications has been used since more than 50 years ago, so in the present days it is possible to gather the first +30 years climatologies of these data. LST, as the driving force in the exchange of long-wave radiation and turbulent fluxes between the surface and atmosphere, is one of the most important satellite-derived variables. Climatologies of LST may be very appealing to a wide range of applications. However, the retrieval of LST to be used in these applications is not trivial since the procurement of data spanning decades of measurements may be a difficult task to achieve.

Within this scope the first objective of this work was to develop an algorithm capable of retrieving LST from the geostationary series of satellites Meteosat First and Second Generation (MFG, MSG), to further implement it with the aim of developing an LST CDR on the CM SAF. The outcome of this task includes two single-channel algorithms: the PMW and the SMW. These algorithms were comprehensively validated with a set of in situ LST measurements (for very different atmospheric conditions) provided by KIT, and with the GSW – algorithm operational at the LSA SAF. Results show that the single-channel algorithms can retrieve LST within or very close to the 2 K target accuracy. The second objective of this work focused on problems that emerged during the development of the algorithms. The first problem was related to orography. Algorithms like the PMW

and SMW depend on reanalysed water vapor profiles defined in a grid associated to a smoothed orography, which leads to misestimations in the water vapor profile. With the aim of improving LST retrievals over mountainous regions, two orographic correction methodologies were designed: a correction directly on the water vapor profile used by the PMW algorithm; and a correction to the integrated profile (TCWV) used by the SMW. Improvements in the LST retrieval vary depending on the method used but may reach a RMSD of 1.7 K (in the Alpine region), an extremely large discrepancy for climatological applications. The second problem was related to the calibration of the coefficients used in the statistical retrievals (SMW, GSW). A sensitivity analysis of those algorithms revealed that selecting a set of atmospheric profiles that spans the full range of surface temperatures and total column water vapor combinations that are physically possible is a difficult task. The third and final objective of this thesis was to use an LST climatology and apply it to improve drought monitoring. Within this scope, LST (and NDVI) was applied to estimate VHI, a very common remote sensing-based drought index. This index relies on the weighted sum of a term dependent on LST and another dependent on NDVI. Since usually there is no *a priori* knowledge about the weights of each term, the LST and NDVI climatologies were used as a benefit to understand if the usually used weights of 0.5 are appropriate when applied to different ecosystems and aridity regions. With this purpose VHI was correlated with the multi-scalar drought index SPEI to understand the effect of drought episodes on the vegetation health components (thermal component TCI – dependent on LST –, and vegetation component VCI – dependent on NDVI). Results presented in Chapter 5 show that there is a dependency of the contribution of each term on the region aridity and biome, and the use of an equal weight of 0.5 in both terms to estimate VHI may not be the most appropriate choice. The final topic of the thesis aims at ensuring that VHI is accurately used, and the development of global maps of VCI and TCI weights is envisioned. Preliminary results are also shown in Chapter 5. The maps show that there is a strong global dependency on aridity, with moister regions displaying larger weights on the TCI term, while arid regions show larger weights for the VCI term. Finally, the same procedure was used with TCI estimated with the previously developed PMW and SMW LSTs. Preliminary results show that the weights estimated with those are very similar with the ones estimated with the Princeton University LSTs used in the above-mentioned analysis. This is

a very promising result, since it may pave the way for a MSG/MTG real-time drought monitoring in the future.

The main common thread of this thesis was related to the use of remotely sensed LST, which is now a variable that spans over 30 years of records, for climate monitoring applications. Since to the best of our knowledge there were no climate records of LST based on geostationary satellites, with high spatial and temporal resolutions and for the European/African regions, the third and fourth chapters of this thesis were dedicated to the development, improving and implementation of algorithms to retrieve LST from the Meteosat constellation of satellites. This was a complex task involving the joint effort between the LSA SAF and CM SAF, representing two thirds of this thesis. The final third, enclosed in chapter 5, was related to the application of LST climatologies (which included the ones developed with the above-mentioned algorithms) for climate monitoring, more specifically, to the improvement of drought monitoring techniques. Since the inception of the LST CDR on the CM SAF was a time-consuming task, this last part was mainly performed with a different record: a merged LST CDR (between polar satellite LSTs and reanalysed LSTs). However, the last section of this chapter included a brief and promising analysis with the CM-SAF LST CDRs.

New possibilities on climate monitoring arise from the brand new remotely sensed LST CDRs developed during this thesis. Here, one of these applications was investigated paving the way for a better understanding on how to monitor droughts using the Vegetation Health Index.

As a final remark, it is worth mentioning that the outcome of research linked to this thesis includes 3 papers published and one submitted in *Remote Sensing*:

- Duguay-Tetzlaff, A.; Bento, V.A.; Göttsche, F.M.; Stöckli, R.; Martins, J.P.A.; Trigo, I.; Olesen, F.; Bojanowski, J.S.; da Camara, C.; Kunz, H. Meteosat Land Surface Temperature Climate Data Record: Achievable Accuracy and Potential Uncertainties. Remote Sens. 2015, 7, 13139-13156.

- Martins, J.P.A.; Trigo, I.F.; Bento, V.A.; da Camara, C. A Physically Constrained Calibration Database for Land Surface Temperature Using Infrared Retrieval Algorithms. Remote Sens. 2016, 8, 808.

- Bento, V.A.; DaCamara, C.C.; Trigo, I.F.; Martins, J.P.A.; Duguay-Tetzlaff, A. Improving Land Surface Temperature Retrievals over Mountainous Regions. Remote Sens. 2017, 9, 38.

- Bento, V.A.; Trigo, I.F.; Gouveia, C.M.; DaCamara, C.C. Contribution of Land Surface Temperature to Vegetation Health Index: a comparative study using clear sky and all-weather Climate Data Records. Submitted to Remote Sens.

Another paper published in *Agricultural and Forest Meteorology*:

- Bento, V.A., Gouveia, C.M., DaCamara, C.C., Trigo, I.F. A Climatological assessment of drought impact on Vegetation Health Index. Agricultural and Forest Meteorology, *Agric. For. Meteorol. 2018, 259, 286–295.*

A paper is currently being prepared:

- Bento, V.A., DaCamara, C.C., Gouveia, C.M., Trigo, I.F. On the global assessment of vegetation and temperature contributions to a SPEI based vegetation health index. In preparation.

Research work was presented in 9 national and international conference presentations (in both oral and poster format) and led to a publicly available climate data record of LST held by the CM-SAF:

- Duguay-Tetzlaff, A.; Bento, V.A.; Stöckli, R.; Trigo, I.F.; Hollmann, R.; Werscheck, M. CM-SAF, Algorithm Theoretical Basis for Land Surface Temperature (LST), SUMET Edition 1, May 12, 2017. SAF/CM/MeteoSwiss/ATBD/MET/LST, Issue 1, Revision 3. Available: http://www.cmsaf.eu

I also had the opportunity to attend a two-week EOS-COST action on data assimilation and data analysis methods in Italy and participate in two summer schools held by the EARTHSYSTEMS doctoral programme.

Bibliography

Aminou, D. M., and Coauthors, 2009: Meteosat Third Generation (MTG) status of space segment definition. *SPIE*, **7474**, 747406-747406–747410, doi:10.1117/12.830969.

Anderson, M. C., J. M. Norman, J. R. Mecikalski, J. A. Otkin, and W. P. Kustas, 2007: A climatological study of evapotranspiration and moisture stress across the continental United States based on thermal remote sensing: 1. Model formulation. *J. Geophys. Res. Atmos.*, **112**, D10117, doi:10.1029/2006JD007506.

Baldauf, M., and Coauthors, 2011: Operational Convective-Scale Numerical Weather Prediction with the COSMO Model: Description and Sensitivities. *Mon. Weather Rev.*, **139**, 3887–3905, doi:10.1175/MWR-D-10-05013.1.

Barducci, A., and I. Pippi, 1996: Temperature and emissivity retrieval from remotely sensed images using the "grey body emissivity" method. *IEEE Trans. Geosci. Remote Sens.*, **34**, 681–695, doi:10.1109/36.499748.

Basili, P., S. Bonafoni, V. Mattioli, P. Ciotti, and N. Pierdicca, 2004: Mapping the atmospheric water vapor by integrating microwave radiometer and GPS measurements. *IEEE Trans. Geosci. Remote Sens.*, **42**, 1657–1665, doi:10.1109/TGRS.2004.830943.

Becker, F., and Z. L. Li, 1990a: Towards a local split window method over land surfaces. *Int. J. Remote Sens.*, **11**, 369–393, doi:10.1080/01431169008955028.

——, and ——, 1990b: Temperature-independent spectral indices in thermal infrared bands. *Remote Sens. Environ.*, **32**, 17–33, doi:10.1016/0034-4257(90)90095-4.

Beguería, S., S. M. Vicente-Serrano, F. Reig, and B. Latorre, 2014: Standardized precipitation evapotranspiration index (SPEI) revisited: Parameter fitting, evapotranspiration models, tools, datasets and drought monitoring. *Int. J. Climatol.*, **34**, 3001–3023, doi:10.1002/joc.3887.

Bento, V., 2013: Exploring RTTOV to Retrive Land Surface Temperature from a Geostationary Satellite Constellation. University of Lisbon, .

——, C. DaCamara, I. F. Trigo, J. Martins, and A. Duguay-Tetzlaff, 2017: Improving Land Surface Temperature Retrievals over Mountainous Regions. *Remote Sens.*, **9**, 38, doi:10.3390/rs9010038.

Berk, A., G. Anderson, P. Acharya, J. Ghetwynd, L. Bernstein, E. Shettle, M. Matthew, and S. Adler-Golden, 1999: *MODTRAN4 User's Manual; Air Force Research Laboratory: Hanscom, MA, USA, 1999*.

BESSHO, K., and Coauthors, 2016: An Introduction to Himawari-8/9 - Japan's New-Generation Geostationary Meteorological Satellites. *J. Meteorol. Soc. Japan. Ser. II*, **94**, 151–183, doi:10.2151/jmsj.2016-009.

Bhuiyan, C., R. P. Singh, and F. N. Kogan, 2006: Monitoring drought dynamics in the Aravalli region (India) using different indices based on ground and remote sensing data. *Int. J. Appl. Earth Obs. Geoinf.*, **8**, 289–302, doi:10.1016/j.jag.2006.03.002.

Bodas-Salcedo, A., M. A. Ringer, and A. Jones, 2008: Evaluation of the surface radiation budget in the atmospheric component of the Hadley Centre Global Environmental Model (HadGEM1). *J. Clim.*, **21**, 4723–4748, doi:10.1175/2008JCLI2097.1.

Bojinski, S., M. Verstraete, T. C. Peterson, C. Richter, A. Simmons, and M. Zemp, 2014: The concept of essential climate variables in support of climate research, applications, and policy. *Bull. Am. Meteorol. Soc.*, **95**, 1431–1443, doi:10.1175/BAMS-D-13-00047.1.

Borbas, E. E., S. S. Wetzel, H. L. Huang, and J. Li, 2005: Global profile training database for satellite regression retrievals with estimates of skin temperature and emissivity. *Proceedings of the XIV International ATOVS Study Conference*, Beijing, China, 763–770.

Borel, C., 2008: Error analysis for a temperature and emissivity retrieval algorithm for hyperspectral imaging data. *Int. J. Remote Sens.*, **29**, 5029–5045, doi:10.1080/01431160802036540.

Bork-Unkelbach, A., 2012: Extrapolation von in-situ Landoberflächentemperaturen auf Satellitenpixel. Karlsruhe Institute of Technology, .

Bosilovich, M. G., J. D. Radakovich, A. da Silva, R. Todling, and F. Verter, 2007: Skin temperature analysis and bias correction in a coupled land-atmosphere data assimilation system. *J. Meteorol. Soc. Japan*, **85**, 205–228, doi:10.2151/jmsj.85A.205.

Caparrini, F., F. Castelli, and D. Entekhabi, 2004: Variational estimation of soil and vegetation turbulent transfer and heat flux parameters from sequences of multisensor imagery. *Water Resour. Res.*, **40**, 1–15, doi:10.1029/2004WR003358.

Chedin, A., N. A. Scott, C. Wahiche, and P. Moulinier, 1985: The improved initialisation inversion method: A high- resolution physical method for temperature retrievals from the TIROS-N series. *J. Clim. Appl. Meteorol.*, **24**, 128–143, doi:10.1175/1520-0450(1985)024<0128:TIIIMA>2.0.CO;2.

Clerbaux, C., and Coauthors, 2009: Monitoring of atmospheric composition using the thermal infrared IASI/MetOp sounder. *Atmos. Chem. Phys.*, **9**, 6041–6054, doi:10.5194/acp-9-6041-2009.

Coccia, G., A. L. Siemann, M. Pan, and E. F. Wood, 2015: Creating consistent datasets by combining remotely-sensed data and land surface model estimates through Bayesian uncertainty post-processing: The case of Land Surface Temperature from HIRS. *Remote Sens. Environ.*, **170**, 290–305, doi:10.1016/j.rse.2015.09.010.

Coll, J. R., E. Aguilar, and L. Ashcroft, 2017: Drought variability and change across the Iberian Peninsula. *Theor. Appl. Climatol.*, **130**, 901–916, doi:10.1007/s00704-016-1926-3.

Cook, E. R., R. Seager, M. A. Cane, and D. W. Stahle, 2007: North American drought: Reconstructions, causes, and consequences. *Earth-Science Rev.*, **81**, 93–134, doi:10.1016/j.earscirev.2006.12.002.

Crago, R. D., and R. J. Qualls, 2014: Use of land surface temperature to estimate surface energy fluxes: Contributions of Wilfried Brutsaert and collaborators. *Water Resour. Res.*, **50**, 3396–3408, doi:10.1002/2013WR015223.

Cristóbal, J., J. C. Jiménez-Muñoz, J. A. Sobrino, M. Ninyerola, and X. Pons, 2009: Improvements in land surface temperature retrieval from the Landsat series thermal band using water vapor and air temperature. *J. Geophys. Res. Atmos.*, **114**, D08103, doi:10.1029/2008JD010616.

Dai, A., 2012: Increasing drought under global warming in observations and models. *Nat. Clim. Chang.*, **3**, 52–58, doi:10.1038/nclimate1633.

Dash, P., F. M. Göttsche, F. S. Olesen, and H. Fischer, 2002: Land surface temperature and emissivity estimation from passive sensor data: Theory and practice-current trends. *Int. J. Remote Sens.*, **23**, 2563–2594, doi:10.1080/01431160110115041.

——, ——, ——, and ——, 2005: Separating surface emissivity and temperature using two-channel spectral indices and emissivity composites and comparison with a vegetation fraction method. *Remote Sens. Environ.*, **96**, 1–17, doi:10.1016/j.rse.2004.12.023.

Davis, G., 2007: History of the NOAA satellite program. *J. Appl. Remote Sens.*, **1**, 12504, doi:10.1117/1.2642347.

Dee, D. P., and Coauthors, 2011: The ERA-Interim reanalysis: Configuration and performance of the data assimilation system. *Q. J. R. Meteorol. Soc.*, **137**, 553–597, doi:10.1002/qj.828.

Derrien, M., and H. Le Gléau, 2011: MSG/SEVIRI cloud mask and type from SAFNWC. *http://dx.doi.org/10.1080/01431160500166128*,.

Detsch, F., I. Otte, T. Appelhans, A. Hemp, and T. Nauss, 2016: Seasonal and long-term vegetation dynamics from 1-km GIMMS-based NDVI time series at Mt. Kilimanjaro, Tanzania. *Remote Sens. Environ.*, **178**, 70–83, doi:10.1016/j.rse.2016.03.007.

Diffenbaugh, N. S., D. L. Swain, and D. Touma, 2015: Anthropogenic warming has increased drought risk in California. *Proc. Natl. Acad. Sci.*, **112**, 3931–3936, doi:10.1073/pnas.1422385112.

Ding, M., L. Li, Y. Zhang, X. Sun, L. Liu, J. Gao, Z. Wang, and Y. Li, 2015: Start of vegetation growing season on the Tibetan Plateau inferred from multiple methods based on GIMMS and SPOT NDVI data. *J. Geogr. Sci.*, **25**, 131–148, doi:10.1007/s11442-015-1158-y.

Ding, Y., M. J. Hayes, and M. Widhalm, 2011: Measuring economic impacts of drought: a review and discussion. *Disaster Prev. Manag. An Int. J.*, **20**, 434–446, doi:10.1108/09653561111161752.

Duguay-Tetzlaff, A., and Coauthors, 2015: Meteosat Land Surface Temperature Climate Data Record: Achievable Accuracy and Potential Uncertainties. *Remote Sens.*, **7**, 13139–13156, doi:10.3390/rs71013139.

Elachi, C., and J. J. van Zyl, 2006: *Introduction to the physics and techniques of remote sensing*. Wiley-Interscience, 616 pp.

Fensholt, R., and S. R. Proud, 2012: Evaluation of Earth Observation based global long term vegetation trends - Comparing GIMMS and MODIS global NDVI time series. *Remote Sens. Environ.*, **119**, 131–147, doi:10.1016/j.rse.2011.12.015.

Freitas, S. C., I. F. Trigo, J. M. Bioucas-Dias, and F. M. Göttsche, 2010: Quantifying the uncertainty of land surface temperature retrievals from SEVIRI/Meteosat. *IEEE Trans. Geosci. Remote Sens.*, **48**, 523–534, doi:10.1109/TGRS.2009.2027697.

——, ——, J. Macedo, R. Silva, and R. Perdigão, 2013: Land surface temperature from multiple geostationary satellites. *Int. J. Remote Sens.*, **34**, 3051–3068, doi:10.1080/01431161.2012.716925.

Gao, X., and F. Giorgi, 2008: Increased aridity in the Mediterranean region under greenhouse gas forcing estimated from high resolution simulations with a regional climate model. *Glob. Planet. Change*, **62**, 195–209, doi:10.1016/j.gloplacha.2008.02.002.

Garand, L., 2003: Toward an integrated land-ocean surface skin temperature analysis from the variational assimilation of infrared radiances. *J. Appl. Meteorol.*, **42**, 570–583, doi:10.1175/1520-0450(2003)042<0570:TAILSS>2.0.CO;2.

GCOS, 2011: *Systematic Observation Requirements For Satellite-Based Data Products for Climate - 2011 Update*. 127 pp.

Ghent, D., J. Kaduk, J. Remedios, J. Ardö, and H. Balzter, 2010: Assimilation of land surface temperature into the land surface model JULES with an ensemble Kalman filter. *J. Geophys. Res.*, **115**, D19112, doi:10.1029/2010JD014392.

Gillespie, A., S. Rokugawa, T. Matsunaga, J. Steven Cothern, S. Hook, and A. B. Kahle, 1998: A temperature and emissivity separation algorithm for advanced spaceborne thermal emission and reflection radiometer (ASTER) images. *IEEE Trans. Geosci. Remote Sens.*, **36**, 1113–1126, doi:10.1109/36.700995.

Good, E., 2015: Daily minimum and maximum surface air temperatures from geostationary satellite data. *J. Geophys. Res. Atmos.*, **120**, 2306–2324, doi:10.1002/2014JD022438.

Göttsche, F. M., and F. S. Olesen, 2001: Modelling of diurnal cycles of brightness

temperature extracted from meteosat data. *Remote Sens. Environ.*, **76**, 337–348, doi:10.1016/S0034-4257(00)00214-5.

——, and F. S. Olesen, 2009: Modelling the effect of optical thickness on diurnal cycles of land surface temperature. *Remote Sens. Environ.*, **113**, 2306–2316, doi:10.1016/j.rse.2009.06.006.

——, and G. C. Hulley, 2012: Validation of six satellite-retrieved land surface emissivity products over two land cover types in a hyper-arid region. *Remote Sens. Environ.*, **124**, 149–158, doi:10.1016/j.rse.2012.05.010.

——, F. S. Olesen, and A. Bork-Unkelbach, 2011: Validation of operational land surface temperature products with three years of continuous in-situ measurements. *Proceedings of the EUMETSAT Meteorological Satellite Conference2*, Oslo, Norway.

——, F.-S. Olesen, and A. Bork-Unkelbach, 2013: Validation of land surface temperature derived from MSG/SEVIRI with in situ measurements at Gobabeb, Namibia. *Int. J. Remote Sens.*, **34**, 3069–3083, doi:10.1080/01431161.2012.716539.

Gouveia, C., R. M. Trigo, S. Beguería, and S. M. Vicente-Serrano, 2017: Drought impacts on vegetation activity in the Mediterranean region: An assessment using remote sensing data and multi-scale drought indicators. *Glob. Planet. Change*, **151**, 15–27, doi:10.1016/j.gloplacha.2016.06.011.

——, R. M. Trigo, and C. C. DaCamara, 2009: Drought and vegetation stress monitoring in Portugal using satellite data. *Nat. Hazards Earth Syst. Sci.*, **9**, 185–195, doi:10.5194/nhess-9-185-2009.

Guillevic, P. C., A. Bork-Unkelbach, F. M. Gottsche, G. Hulley, J. P. Gastellu-Etchegorry, F. S. Olesen, and J. L. Privette, 2013: Directional viewing effects on satellite land surface temperature products over sparse vegetation canopies-a multisensor analysis. *IEEE Geosci. Remote Sens. Lett.*, **10**, 1464–1468, doi:10.1109/LGRS.2013.2260319.

Hargreaves, G. H., 1994: Defining and using reference evapotranspiration. *J. Irrig. Drain. Eng.*, **120**, 1132–1139, doi:10.1061/(asce)0733-9437(1994)120:6(1132).

Harris, I., P. D. Jones, T. J. Osborn, and D. H. Lister, 2014: Updated high-resolution grids of monthly climatic observations - the CRU TS3.10 Dataset. *Int. J. Climatol.*, **34**, 623–642, doi:10.1002/joc.3711.

Hartmann, D. L., and Coauthors, 2013: Observations: Atmosphere and surface. *Climate Change 2013 the Physical Science Basis: Working Group I Contribution to the Fifth Assessment Report of the Intergovernmental Panel on Climate Change*, Intergovernmental Panel on Climate Change, Ed., Vol. 9781107057 of, Cambridge University Press, Cambridge, 159–254.

Heidinger, A. K., I. Laszlo, C. C. Molling, and D. Tarpley, 2013: Using SURFRAD to verify the NOAA single-channel land surface temperature algorithm. *J. Atmos. Ocean. Technol.*, **30**, 2868–2884, doi:10.1175/JTECH-

D-13-00051.1.

Heim, R. R., 2002: A review of twentieth-century drought indices used in the United States. *Bull. Am. Meteorol. Soc.*, **83**, 1149–1165, doi:10.1175/1520-0477(2002)083<1149:AROTDI>2.3.CO;2.

Hewison, T. J., and M. König, 2008: Inter-calibration of Meteosat imagers and IASI. *Proceedings of the EUMETSAT Meteorological Satellite Conference*, Darmstadt, Germany.

Hillier, D., and B. Dempsey, 2012: A dangerous delay: The cost of late response to early warnings in the 2011 drought in the Horn of Africa. *Oxfam Policy Pract. Agric. Food L.*, **12**, 1–34, doi:ISBN: 978-1-78077-034-5.

Hocking, J., P. J. Rayer, D. Rundle, R. W. Saunders, M. Matricardi, A. Geer, P. Brunel, and J. Vidot, *RTTOV v11 Users Guide; Nowcasting Satellite Application Facility (NWC-SAF): Darmstadt, Germany, 2014*.

Hoerling, M., J. Eischeid, J. Perlwitz, X. Quan, T. Zhang, and P. Pegion, 2012: On the increased frequency of mediterranean drought. *J. Clim.*, **25**, 2146–2161, doi:10.1175/JCLI-D-11-00296.1.

Hollmann, R., and Coauthors, 2013: The ESA climate change initiative: Satellite data records for essential climate variables. *Bull. Am. Meteorol. Soc.*, **94**, 1541–1552, doi:10.1175/BAMS-D-11-00254.1.

House, F. B., A. Gruber, G. E. Hunt, and A. T. Mecherikunnel, 1986: History of satellite missions and measurements of the Earth Radiation Budget (1957–1984). *Rev. Geophys.*, **24**, 357–377, doi:10.1029/RG024i002p00357.

Idso, S. B., R. D. Jackson, P. J. Pinter, R. J. Reginato, and J. L. Hatfield, 1981: Normalizing the stress-degree-day parameter for environmental variability. *Agric. Meteorol.*, **24**, 45–55, doi:10.1016/0002-1571(81)90032-7.

Iglesias, A., L. Garrote, and F. Martín-Carrasco, 2009: Drought risk management in Mediterranean river basins. *Integr. Environ. Assess. Manag.*, **5**, 11–16.

Jackson, R. D., S. B. Idso, R. J. Reginato, and P. J. Pinter, 1981: Canopy temperature as a crop water stress indicator. *Water Resour. Res.*, **17**, 1133–1138, doi:10.1029/WR017i004p01133.

Jiménez-Muñoz, J. C., and J. A. Sobrino, 2003: A generalized single-channel method for retrieving land surface temperature from remote sensing data. *J. Geophys. Res.*, **109**, 8112, doi:10.1029/2004JD004804.

——, and J. A. Sobrino, 2007: Error sources on the land surface temperature retrieved from thermal infrared single channel remote sensing data. *http://dx.doi.org/10.1080/01431160500075907*,.

——, J. Cristobal, J. A. Sobrino, G. Sòria, M. Ninyerola, and X. Pons, 2009: Revision of the single-channel algorithm for land surface temperature retrieval from landsat thermal-infrared data. *IEEE Trans. Geosci. Remote Sens.*, **47**, 339–349, doi:10.1109/TGRS.2008.2007125.

de Jong, R., S. de Bruin, A. de Wit, M. E. Schaepman, and D. L. Dent, 2011: Analysis of monotonic greening and browning trends from global NDVI time-series. *Remote Sens. Environ.*, **115**, 692–702, doi:10.1016/j.rse.2010.10.011.

——, J. Verbesselt, A. Zeileis, and M. Schaepman, 2013: Shifts in Global Vegetation Activity Trends. *Remote Sens.*, **5**, 1117–1133, doi:10.3390/rs5031117.

Kabsch, E., F. S. Olesen, and F. Prata, 2008: Initial results of the land surface temperature (LST) validation with the Evora, Portugal ground-truth station measurements. *Int. J. Remote Sens.*, **29**, 5329–5345, doi:10.1080/01431160802036326.

Kalman, R. E., 1960: A New Approach to Linear Filtering and Prediction Problems. *J. Basic Eng.*, **82**, 35, doi:10.1115/1.3662552.

——, and R. S. Bucy, 1961: New Results in Linear Filtering and Prediction Theory. *J. Basic Eng.*, **83**, 95, doi:10.1115/1.3658902.

Karnieli, A., M. Bayasgalan, Y. Bayarjargal, N. Agam, S. Khudulmur, and C. J. Tucker, 2006: Comments on the use of the Vegetation Health Index over Mongolia. *Int. J. Remote Sens.*, **27**, 2017–2024, doi:10.1080/01431160500121727.

——, and Coauthors, 2010: Use of NDVI and land surface temperature for drought assessment: Merits and limitations. *J. Clim.*, **23**, 618–633, doi:10.1175/2009JCLI2900.1.

Klos, R. J., G. G. Wang, W. L. Bauerle, and J. R. Rieck, 2009: Drought impact on forest growth and mortality in the southeast USA: An analysis using Forest Health and Monitoring data. *Ecol. Appl.*, **19**, 699–708, doi:10.1890/08-0330.1.

Kogan, F. N., 1997: Global Drought Watch from Space. *Bull. Am. Meteorol. Soc.*, **78**, 621–636.

——, 2000: Satellite-Observed Sensitivity of World Land Ecosystems to El Niño/La Niña. *Remote Sens. Environ.*, **74**, 445–462, doi:10.1016/S0034-4257(00)00137-1.

——, 2001: Operational space technology for global vegetation assessment. *Bull. Am. Meteorol. Soc.*, **82**, 1949–1964.

——, L. Salazar, and L. Roytman, 2012: Forecasting crop production using satellite-based vegetation health indices in Kansas, USA. *Int. J. Remote Sens.*, **33**, 2798–2814, doi:10.1080/01431161.2011.621464.

Kondratyev, K. Y., 1969: *Radiation in the Atmosphere*. Academic Press, New York, USA,.

Kustas, W., and J. Norman, 1996: Use of remote sensing for evapotranspiration monitoring over land surfaces. *Hydrol. Sci. J.*, **41**, 495–516, doi:10.1080/02626669609491522.

De La Taille, L., S. Rota, C. Hartley, and R. Stuhlmann, 2015: Meteosat third generation programme status. *Proceedings of the Annual EUMETSAT Meteorological Satellite Conference*.

Lakshmi, V., 2017: *Remote Sensing of Hydrological Extremes*. Springer International Publishing,.

Lawrimore, J. H., M. J. Menne, B. E. Gleason, C. N. Williams, D. B. Wuertz, R. S. Vose, and J. Rennie, 2011: An overview of the Global Historical Climatology Network monthly mean temperature data set, version 3. *J. Geophys. Res. Atmos.*, **116**, D19121, doi:10.1029/2011JD016187.

Li, L., Z. Ying, Y. Feng, and S. Guoqiang, 1998: Monitoring drought of Guizhou using remote sensing vegetation index. *J. Guizhou Meteorol.*, **22**, 50–54.

Li, Z.-L., B.-H. Tang, H. Wu, H. Ren, G. Yan, Z. Wan, I. F. Trigo, and J. A. Sobrino, 2013: Satellite-derived land surface temperature: Current status and perspectives. *Remote Sens. Environ.*, **131**, 14–37, doi:10.1016/j.rse.2012.12.008.

Lillesand, T. M., R. W. Kiefer, and J. W. Chipman, 2004: *Remote sensing and image interpretation*. 763 pp.

Lindner, M., and Coauthors, 2010: Climate change impacts, adaptive capacity, and vulnerability of European forest ecosystems. *For. Ecol. Manage.*, **259**, 698–709, doi:10.1016/j.foreco.2009.09.023.

Loveland, T. R., B. C. Reed, J. F. Brown, D. O. Ohlen, Z. Zhu, L. Yang, and J. W. Merchant, 2000: Development of a global land cover characteristics database and IGBP DISCover from 1 km AVHRR data. *Int. J. Remote Sens.*, **21**, 1303–1330, doi:10.1080/014311600210191.

Ma, X. L., Z. Wan, C. C. Moeller, W. P. Menzel, and L. E. Gumley, 2002: Simultaneous retrieval of atmospheric profiles, land-surface temperature, and surface emissivity from Moderate-Resolution Imaging Spectroradiometer thermal infrared data: extension of a two-step physical algorithm. *Appl. Opt.*, **41**, 909–924, doi:10.1364/AO.41.001174.

Mariotti, A., 2010: Recent changes in the mediterranean water cycle: A pathway toward long-term regional hydroclimatic change? *J. Clim.*, **23**, 1513–1525, doi:10.1175/2009JCLI3251.1.

Martins, J., I. F. Trigo, V. Bento, and C. da Camara, 2016: A Physically Constrained Calibration Database for Land Surface Temperature Using Infrared Retrieval Algorithms. *Remote Sens.*, **8**, 808, doi:10.3390/rs8100808.

Masiello, G., C. Serio, I. De Feis, M. Amoroso, S. Venafra, I. F. Trigo, and P. Watts, 2013: Kalman filter physical retrieval of surface emissivity and temperature from geostationary infrared radiances. *Atmos. Meas. Tech.*, **6**, 3613–3634, doi:10.5194/amt-6-3613-2013.

——, ——, S. Venafra, G. Liuzzi, F. Göttsche, I. F. Trigo, and P. Watts, 2015: Kalman filter physical retrieval of surface emissivity and temperature from SEVIRI infrared channels: a validation and intercomparison study. *Atmos.*

Meas. Tech., **8**, 2981–2997, doi:10.5194/amt-8-2981-2015.

Matricardi, M., F. Chevallier, and S. Tjemkes, 2001: An improved general fast radiative transfer model for the assimilation of radiance observations. *ECMWF Tech. Memo.*, **345**, 153–173, doi:10.1256/qj.02.181.

Mattar, C., C. Durán-Alarcón, J. C. Jiménez-Muñoz, A. Santamaría-Artigas, L. Olivera-Guerra, and J. A. Sobrino, 2015: Global Atmospheric Profiles from Reanalysis Information (GAPRI): a new database for earth surface temperature retrieval. *Int. J. Remote Sens.*, **36**, 5045–5060, doi:10.1080/01431161.2015.1054965.

Mckee, T. B., N. J. Doesken, and J. Kleist, 1993: The relationship of drought frequency and duration to time scales. *AMS 8th Conf. Appl. Climatol.*, 179–184, doi:citeulike-article-id:10490403.

McMillin, L. M., 1975: Estimation of sea surface temperatures from two infrared window measurements with different absorption. *J. Geophys. Res.*, **80**, 5113, doi:10.1029/JC080i036p05113.

McVicar, T. R., and D. L. B. Jupp, 1998: The current and potential operational uses of remote sensing to aid decisions on drought exceptional circumstances in Australia: A review. *Agric. Syst.*, **57**, 399–468, doi:10.1016/S0308-521X(98)00026-2.

Menzel, W. P., and J. F. W. Purdom, 1994: Introducing GOES-I: The First of a New Generation of Geostationary Operational Environmental Satellites. *Bull. Am. Meteorol. Soc.*, **75**, 757–781, doi:10.1175/1520-0477(1994)075<0757:IGITFO>2.0.CO;2.

Milly, P. C. D., R. T. Wetherald, K. A. Dunne, and T. L. Delworth, 2002: Increasing risk of great floods in a changing climate. *Nature*, **415**, 514–517, doi:10.1038/415514a.

Mishra, A. K., and V. P. Singh, 2009: Analysis of drought severity-area-frequency curves using a general circulation model and scenario uncertainty. *J. Geophys. Res. Atmos.*, **114**, D06120, doi:10.1029/2008JD010986.

Mishra, A. K., and V. P. Singh, 2010: A review of drought concepts. *J. Hydrol.*, **391**, 202–216, doi:10.1016/j.jhydrol.2010.07.012.

Mitra, D. S., and T. J. Majumdar, 2004: Thermal inertia mapping over the Brahmaputra basin, India using NOAA-AVHRR data and its possible geological applications. *Int. J. Remote Sens.*, **25**, 3245–3260, doi:10.1080/01431160310001632701.

Moran, M. S., T. R. Clarke, Y. Inoue, and A. Vidal, 1994: Estimating crop water deficit using the relation between surface-air temperature and spectral vegetation index. *Remote Sens. Environ.*, **49**, 246–263, doi:10.1016/0034-4257(94)90020-5.

Morland, J., and C. Mätzler, 2007: Spatial interpolation of GPS integrated water vapour measurements made in the Swiss Alps. *Meteorol. Appl.*, **14**, 15–26, doi:10.1002/met.2.

Mountain Research Initiative EDW Working Group, 2015: Elevation-dependent warming in mountain regions of the world. *Nat. Clim. Chang.*, **5**, 424–430, doi:10.1038/nclimate2563\rhttp://www.nature.com/nclimate/journal/v5/n5/abs/nclimate2563.html#supplementary-information.

Myneni, R. B., F. G. Hall, P. J. Sellers, and A. L. Marshak, 1995: The interpretation of spectral vegetation indexes. *IEEE Trans. Geosci. Remote Sens.*, **33**, 481–486, doi:10.1109/36.377948.

Neeck, S. P., T. J. Magner, and G. E. Paules, 2005: NASA's small satellite missions for Earth observation. *Acta Astronautica*, Vol. 56 of, Pergamon, 187–192.

Oyler, J. W., S. Z. Dobrowski, Z. A. Holden, S. W. Running, J. W. Oyler, S. Z. Dobrowski, Z. A. Holden, and S. W. Running, 2016: Remotely Sensed Land Skin Temperature as a Spatial Predictor of Air Temperature across the Conterminous United States. *http://dx.doi.org/10.1175/JAMC-D-15-0276.1*,.

Palmer, W. C., 1965: *Meteorological Drought. US Department of Commerce, Weather Bureau, Research Paper No. 45, p. 58*.

Páscoa, P., C. M. Gouveia, A. Russo, and R. M. Trigo, 2017: Drought Trends in the Iberian Peninsula over the Last 112 Years. *Adv. Meteorol.*, **2017**, 1–13, doi:10.1155/2017/4653126.

Peres, L. F., and C. C. DaCamara, 2004: Land surface temperature and emissivity estimation based on the two-temperature method: Sensitivity analysis using simulated MSG/SEVIRI data. *Remote Sens. Environ.*, **91**, 377–389, doi:10.1016/j.rse.2004.03.011.

——, and ——, 2005: Emissivity maps to retrieve land-surface temperature from MSG/SEVIRI. *IEEE Trans. Geosci. Remote Sens.*, **43**, 1834–1844, doi:10.1109/TGRS.2005.851172.

——, and ——, 2006: Improving two-temperature method retrievals based on a nonlinear optimization approach. *IEEE Geosci. Remote Sens. Lett.*, **3**, 232–236, doi:10.1109/LGRS.2005.862274.

Phillips, O. L., and Coauthors, 2009: Drought Sensitivity of the Amazon Rainforest. *Science (80-.).*, **323**, 1344–1347, doi:10.1126/science.1164033.

Prata, A. J., 1993: Land surface temperatures derived from the advanced very high resolution radiometer and the along-track scanning radiometer: 1. Theory. *J. Geophys. Res.*, **98**, 16689–16702, doi:10.1029/93JD01206.

Qin, J., K. Yang, S. Liang, and X. Guo, 2009: The altitudinal dependence of recent rapid warming over the Tibetan Plateau. *Clim. Change*, **97**, 321–327, doi:10.1007/s10584-009-9733-9.

Qin, Z., A. Karnieli, and P. Berliner, 2001: A mono-window algorithm for retrieving land surface temperature from Landsat TM data and its application to the Israel-Egypt border region. *Int. J. Remote Sens.*, **22**, 3719–3746, doi:10.1080/01431160010006971.

Quiring, S. M., and S. Ganesh, 2010a: Evaluating the utility of the Vegetation Condition Index (VCI) for monitoring meteorological drought in Texas. *Agric. For. Meteorol.*, **150**, 330–339, doi:10.1016/j.agrformet.2009.11.015.

——, and ——, 2010b: Evaluating the utility of the Vegetation Condition Index (VCI) for monitoring meteorological drought in Texas. *Agric. For. Meteorol.*, **150**, 330–339, doi:10.1016/j.agrformet.2009.11.015.

Reichle, R. H., S. V. Kumar, S. P. P. Mahanama, R. D. Koster, and Q. Liu, 2010: Assimilation of Satellite-Derived Skin Temperature Observations into Land Surface Models. *J. Hydrometeorol.*, **11**, 1103–1122, doi:10.1175/2010JHM1262.1.

Reutter, H., F.-S. Olesen, and H. Fischer, 1994: Distribution of the brightness temperature of land surfaces determined from AVHRR data. *Int. J. Remote Sens.*, **15**, 95–104, doi:10.1080/01431169408954053.

Riebsame, W. E., S. A. Changnon Jr., and T. R. Karl, 1991: *Drought and natural resources management in the United States. Impacts and implications of the 1987-89 drought*. Westview Press, 174 pp.

Rivas-martínez, S., and Coauthors, 2011: Worldwide bioclimatic classification system. *Glob. Geobot.*, **1**, 1–634.

Rodriguez, A., R. Stuhlmanna, S. Tjemkesa, D. M. Aminoub, H. Starkb, and P. Blytheb, 2009: Meteosat Third Generation (MTG): Mission and system concepts. *Infrared Spaceborne Remote Sensing and Instrumentation XVII*, M. Strojnik, Ed., Vol. 7453 of, International Society for Optics and Photonics, 74530C.

Rossow, W. B., and R. A. Schiffer, 1999: Advances in Understandig Clouds from ISCCP. *Bull. Amer. Meteor. Soc.*, **80**, 2261–2287, doi:10.1175/1520-0477(1999)080<2261:AIUCFI>2.0.CO;2.

Sabins, F. F., 1997: *Remote sensing : principles and interpretations.* Waveland Press, 494 pp.

Sandholt, I., K. Rasmussen, and J. Andersen, 2002: A simple interpretation of the surface temperature/vegetation index space for assessment of surface moisture status. *Remote Sens. Environ.*, **79**, 213–224, doi:10.1016/S0034-4257(01)00274-7.

Saunders, R., M. Matricardi, and P. Brunel, 1999: An improved fast radiative transfer model for assimilation of satellite radiance observations. *Q. J. R. Meteorol. Soc.*, **125**, 1407–1425, doi:10.1002/qj.1999.49712555615.

Savtchenko, A., D. Ouzounov, S. Ahmad, J. Acker, G. Leptoukh, J. Koziana, and D. Nickless, 2004: Terra and Aqua MODIS products available from NASA GES DAAC. *Advances in Space Research*, Vol. 34 of, Pergamon, 710–714.

Scarino, B., P. Minnis, R. Palikonda, R. H. Reichle, D. Morstad, C. Yost, B. Shan, and Q. Liu, 2013: Retrieving clear-sky surface skin temperature for numerical weather prediction applications from geostationary satellite data. *Remote Sens.*, **5**, 342–366, doi:10.3390/rs5010342.

Schmetz, J., P. Pili, S. Tjemkes, D. Just, J. Kerkmann, S. Rota, and A. Ratier, 2002: An introduction to Meteosat Second Generation (MSG). *Bull. Am. Meteorol. Soc.*, **83**, 977–992, doi:10.1175/BAMS-83-7-Schmetz-1.

Schmit, T. J., M. M. Gunshor, W. P. Menzel, J. J. Gurka, J. Li, and A. S. Bachmeier, 2005: Introducing the next-generation advanced baseline imager on GOES-R. *Bull. Am. Meteorol. Soc.*, **86**, 1079–1096, doi:10.1175/BAMS-86-8-1079.

Schott, J. R., 2007: *Remote Sensing: The Image Chain Approach*. Oxford University Press, 688 pp.

Sheffield, J., E. F. Wood, and M. L. Roderick, 2012: Little change in global drought over the past 60 years. *Nature*, **491**, 435–438, doi:10.1038/nature11575.

Siemann, A. L., G. Coccia, M. Pan, and E. F. Wood, 2016: Development and Analysis of a Long-Term, Global, Terrestrial Land Surface Temperature Dataset Based on HIRS Satellite Retrievals. *J. Clim.*, **29**, 3589–3606, doi:10.1175/JCLI-D-15-0378.1.

Singh, R. P., S. Roy, and F. Kogan, 2003: Vegetation and temperature condition indices from NOAA AVHRR data for drought monitoring over India. *Int. J. Remote Sens.*, **24**, 4393–4402, doi:10.1080/0143116031000084323.

Smakhtin, V. U., and E. L. F. Schipper, 2008: Droughts: The impact of semantics and perceptions. *Water Policy*, **10**, 131–143, doi:10.2166/wp.2008.036.

Smith, T. M., and R. L. Smith, 2015: *Elements of Ecology*. 9th ed. Pearson,.

Snyder, W. C., Z. Wan, Y. Zhang, and Y. Z. Feng, 1998: Classification-based emissivity for land surface temperature measurement from space. *Int. J. Remote Sens.*, **19**, 2753–2774, doi:10.1080/014311698214497.

Sobrino, J. A., and J. C. Jiménez-Muñoz, 2005: Land surface temperature retrieval from thermal infrared data: An assessment in the context of the Surface Processes and Ecosystem Changes Through Response Analysis (SPECTRA) mission. *J. Geophys. Res. D Atmos.*, **110**, 1–10, doi:10.1029/2004JD005588.

——, C. Coll, and V. Caselles, 1991: Atmospheric correction for land surface temperature using NOAA-11 AVHRR channels 4 and 5. *Remote Sens. Environ.*, **38**, 19–34, doi:10.1016/0034-4257(91)90069-I.

——, Z. L. Li, M. P. Stoll, and F. Becker, 1994: Improvements in the Split-Window Technique for Land Surface Temperature Determination. *IEEE Trans. Geosci. Remote Sens.*, **32**, 243–253, doi:10.1109/36.295038.

——, Z. L. Li, M. P. Stoll, and F. Becker, 1996: Multi-channel and multi-angle algorithms for estimating sea and land surface temperature with atsr data. *Int. J. Remote Sens.*, **17**, 2089–2114, doi:10.1080/01431169608948760.

——, G. Sòria, and A. J. Prata, 2004: Surface temperature retrieval from along track scanning radiometer 2 data: Algorithms and validation. *J. Geophys. Res. D Atmos.*, **109**, D11101, doi:10.1029/2003JD004212.

Stuhlmann, R., A. Rodriguez, S. Tjemkes, J. Grandell, A. Arriaga, J. L. Bézy, D. Aminou, and P. Bensi, 2005: Plans for EUMETSAT's Third Generation Meteosat geostationary satellite programme. *Advances in Space Research*, Vol. 36 of, Pergamon, 975–981.

Sun, D., and R. T. Pinker, 2003: Estimation of land surface temperature from a Geostationary Operational Environmental Satellite (GOES-8). *J. Geophys. Res.*, **108**, 4326, doi:10.1029/2002JD002422.

——, and M. Kafatos, 2007: Note on the NDVI-LST relationship and the use of temperature-related drought indices over North America. *Geophys. Res. Lett.*, **34**, L24406, doi:10.1029/2007GL031485.

——, R. T. Pinker, and J. B. Basara, 2004: Land Surface Temperature Estimation from the Next Generation of Geostationary Operational Environmental Satellites: GOES M–Q. *J. Appl. Meteorol.*, **43**, 363–372, doi:10.1175/1520-0450(2004)043<0363:LSTEFT>2.0.CO;2.

Sun, H., C. Yunhao, and S. Hongquan, 2011: Comparisons and classification system of typical remote sensing indexes for agricultural drought. *Trans. Chinese Soc. Agric. Eng.*, **28**, 147–154(8).

Tang, B., and Z. L. Li, 2008: Retrieval of land surface bidirectional reflectivity in the mid-infrared from MODIS channels 22 and 23. *Int. J. Remote Sens.*, **29**, 4907–4925, doi:10.1080/01431160802036573.

Tang, H., and Z.-L. Li, 2014: *Quantitative Remote Sensing in Thermal Infrared. Theory and Applications*. 298 pp.

Tessier, R., 1989: The Meteosat Programme. *ESA Bull.*, **58**, 45–57.

Theocharous, E., E. Usadi, and N. P. Fox, 2010: *CEOS comparison of IR Brightness Temperature Measurements in Support of Satellite Validation. Part I: Laboratory and Ocean Surface Temperature Comparison of Radiation Thermometers*. National Physical Laboratory: Teddington, UK,.

Trenberth, K. E., A. Dai, G. van der Schrier, P. D. Jones, J. Barichivich, K. R. Briffa, and J. Sheffield, 2013: Global warming and changes in drought. *Nat. Clim. Chang.*, **4**, 17–22, doi:10.1038/nclimate2067.

Trigo, I. F., P. Viterbo, I. F. Trigo, and P. Viterbo, 2003: Clear-Sky Window Channel Radiances: A Comparison between Observations and the ECMWF Model. *http://dx.doi.org/10.1175/1520-0450(2003)042<1463:CWCRAC>2.0.CO;2*,.

——, I. T. Monteiro, F. Olesen, and E. Kabsch, 2008a: An assessment of remotely sensed land surface temperature. *J. Geophys. Res.*, **113**, 1–12, doi:10.1029/2008JD010035.

——, L. F. Peres, C. C. DaCamara, and S. C. Freitas, 2008b: Thermal land surface emissivity retrieved from SEVIRI/Meteosat. *IEEE Transactions on Geoscience and Remote Sensing*, Vol. 46 of, IEEE, 307–315.

——, S. C. Freitas, J. M. Bioucas-Dias, C. Barroso, I. T. Monteiro, and P.

Viterbo, 2009: *Algorithm Theoretical Basis Document for Land Surface Temperature (LST), LSA-4 (MLST); Land Surface Analysis Satellite Aplication Facility: Darmstadt, Germany, 2009*.

——, and Coauthors, 2011: The Satellite Application Facility for Land Surface Analysis. *Int. J. Remote Sens.*, **32**, 2725–2744, doi:10.1080/01431161003743199.

——, S. Boussetta, P. Viterbo, G. Balsamo, A. Beljaars, and I. Sandu, 2015: Comparison of model land skin temperature with remotely sensed estimates and assessment of surface-atmosphere coupling. *J. Geophys. Res. Atmos.*, **120**, 12,096-12,111, doi:10.1002/2015JD023812.

Tucker, C., J. Pinzon, M. Brown, D. Slayback, E. Pak, R. Mahoney, E. Vermote, and N. El Saleous, 2005: An extended AVHRR 8-km NDVI dataset compatible with MODIS and SPOT vegetation NDVI data. *Int. J. Remote Sens.*, **26**, 4485–4498, doi:10.1080/01431160500168686.

Ulivieri, C., M. M. Castronuovo, R. Francioni, and A. Cardillo, 1994: A split window algorithm for estimating land surface temperature from satellites. *Adv. Sp. Res.*, **14**, 59–65, doi:10.1016/0273-1177(94)90193-7.

UNESCO, 1979: *Map of the world distribution of arid regions: Map at scale 1:25,000,000 with explanatory note*. Paris,.

Valor, E., and V. Caselles, 1996: Mapping land surface emissivity from NDVI: Application to European, African, and South American areas. *Remote Sens. Environ.*, **57**, 167–184, doi:10.1016/0034-4257(96)00039-9.

Verstraeten, W. W., F. Veroustraete, C. J. Van Der Sande, I. Grootaers, and J. Feyen, 2006: Soil moisture retrieval using thermal inertia, determined with visible and thermal spaceborne data, validated for European forests. *Remote Sens. Environ.*, **101**, 299–314, doi:10.1016/j.rse.2005.12.016.

Vicente-Serrano, S. M., S. Beguería, and J. I. López-Moreno, 2010: A multiscalar drought index sensitive to global warming: The standardized precipitation evapotranspiration index. *J. Clim.*, **23**, 1696–1718, doi:10.1175/2009JCLI2909.1.

——, and Coauthors, 2014: Evidence of increasing drought severity caused by temperature rise in southern Europe. *Environ. Res. Lett.*, **9**, 44001, doi:10.1088/1748-9326/9/4/044001.

——, D. Cabello, M. Tomás-Burguera, N. Martín-Hernández, S. Beguería, C. Azorin-Molina, and A. El Kenawy, 2015: Drought variability and land degradation in semiarid regions: Assessment using remote sensing data and drought indices (1982-2011). *Remote Sens.*, **7**, 4391–4423, doi:10.3390/rs70404391.

Wan, Z., and J. Dozier, 1996: A generalized split-window algorithm for retrieving land-surface temperature from space. *IEEE Trans. Geosci. Remote Sens.*, **34**, 892–905, doi:10.1109/36.508406.

——, and Z. L. Li, 1997: A physics-based algorithm for retrieving land-surface

emissivity and temperature from eos/modis data. *IEEE Trans. Geosci. Remote Sens.*, **35**, 980–996, doi:10.1109/36.602541.

——, P. Wang, and X. Li, 2004: Using MODIS Land Surface Temperature and Normalized Difference Vegetation Index products for monitoring drought in the southern Great Plains, USA. *Int. J. Remote Sens.*, **25**, 61–72, doi:10.1080/0143116031000115328.

Wang, N., B. H. Tang, C. Li, and Z. L. Li, 2010: A generalized neural network for simultaneous retrieval of atmospheric profiles and surface temperature from hyperspectral thermal infrared data. *International Geoscience and Remote Sensing Symposium (IGARSS)*, IEEE, 1055–1058.

——, H. Wu, F. Nerry, C. Li, and Z. L. Li, 2011: Temperature and emissivity retrievals from hyperspectral thermal infrared data using linear spectral emissivity constraint. *IEEE Trans. Geosci. Remote Sens.*, **49**, 1291–1303, doi:10.1109/TGRS.2010.2062527.

Wardlow, B. D., M. C. Anderson, and J. P. Verdin, 2012: *Remote sensing of drought innovative monitoring approaches*. CRC Press, xxii, 409 pp.

Watson, K., 1992: Two-temperature method for measuring emissivity. *Remote Sens. Environ.*, **42**, 117–121, doi:10.1016/0034-4257(92)90095-2.

Wilhite, D. A., and M. H. Glantz, 1985: Understanding: The drought phenomenon: The role of definitions. *Water Int.*, **10**, 111–120, doi:10.1080/02508068508686328.

——, M. D. Svoboda, and M. J. Hayes, 2007: Understanding the complex impacts of drought: A key to enhancing drought mitigation and preparedness. *Water Resour. Manag.*, **21**, 763–774, doi:10.1007/s11269-006-9076-5.

WMO, 2016: The Global Observing System for Climate (GCOS): Implementation Needs. **200**, 325, doi:GCOS-200.

Yu, X., X. Guo, and Z. Wu, 2014: Land surface temperature retrieval from landsat 8 TIRS-comparison between radiative transfer equation-based method, split window algorithm and single channel method. *Remote Sens.*, **6**, 9829–9852, doi:10.3390/rs6109829.

Zargar, A., R. Sadiq, B. Naser, and F. I. Khan, 2011: A review of drought indices. *Environ. Rev.*, **19**, 333–349, doi:10.1139/a11-013.

Zhu, Z., and Coauthors, 2016: Greening of the Earth and its drivers. *Nat. Clim. Chang.*, **6**, 791–795, doi:10.1038/nclimate3004.

Zomer, R. J., A. Trabucco, O. Van Straaten, and D. A. Bossio, 2006: *Carbon, Land and Water:A Global Analysis of the Hydrologic Dimensions of Climate Change Mitigation through Afforestation/Reforestation*. 44 pp.

——, ——, D. A. Bossio, and L. V Verchot, 2008: Climate change mitigation: A spatial analysis of global land suitability for clean development mechanism

afforestation and reforestation. *Agric. Ecosyst. Environ.*, **126**, 67–80, doi:10.1016/j.agee.2008.01.014.

Annexes

Annex A

Martins, J.P.A.; Trigo, I.F.; Bento, V.A.; da Camara, C. A Physically Constrained Calibration Database for Land Surface Temperature Using Infrared Retrieval Algorithms. Remote Sens. 2016, 8, 808.

Annex B

Duguay-Tetzlaff, A.; Bento, V.A.; Göttsche, F.M.; Stöckli, R.; Martins, J.P.A.; Trigo, I.; Olesen, F.; Bojanowski, J.S.; da Camara, C.; Kunz, H. Meteosat Land Surface Temperature Climate Data Record: Achievable Accuracy and Potential Uncertainties. Remote Sens. 2015, 7, 13139-13156.

remote sensing

MDPI

Article

A Physically Constrained Calibration Database for Land Surface Temperature Using Infrared Retrieval Algorithms

João P. A. Martins [1,2,*], Isabel F. Trigo [1,2], Virgílio A. Bento [2] and Carlos da Camara [2]

[1] Instituto Português do Mar e da Atmosfera, 1749-077 Lisbon, Portugal; isabel.trigo@ipma.pt

[2] Instituto Dom Luiz, University of Lisbon, IDL, Campo Grande, Ed C1, 1749-016 Lisbon, Portugal; vabento@fc.ul.pt (V.A.B.); cdcamara@fc.ul.pt (C.d.C.)

* Correspondence: joao.p.martins@ipma.pt; Tel.: +351-21-844-7055 (ext. 1555)

Academic Editors: Zhaoliang Li, Richard Müller and Prasad S. Thenkabail
Received: 5 August 2016; Accepted: 15 September 2016; Published: 28 September 2016

Abstract: Land surface temperature (LST) is routinely retrieved from remote sensing instruments using semi-empirical relationships between top of atmosphere (TOA) radiances and LST, using ancillary data such as total column water vapor or emissivity. These algorithms are calibrated using a set of forward radiative transfer simulations that return the TOA radiances given the LST and the thermodynamic profiles. The simulations are done in order to cover a wide range of surface and atmospheric conditions and viewing geometries. This study analyzes calibration strategies while considering some of the most critical factors that need to be taken into account when building a calibration dataset, covering the full dynamic range of relevant variables. A sensitivity analysis of split-windows and single channel algorithms revealed that selecting a set of atmospheric profiles that spans the full range of surface temperatures and total column water vapor combinations that are physically possible seems beneficial for the quality of the regression model. However, the calibration is extremely sensitive to the low-level structure of the atmosphere, indicating that the presence of atmospheric boundary layer features such as temperature inversions or strong vertical gradients of thermodynamic properties may affect LST retrievals in a non-trivial way. This article describes the criteria established in the EUMETSAT Land Surface Analysis—Satellite Application Facility to calibrate its LST algorithms, applied both for current and forthcoming sensors.

Keywords: land surface temperature; thermal infrared; calibration; generalized split-window; mono-window; database; radiative transfer

1. Introduction

Land surface temperature (LST) is an important parameter in the physics of the Earth's surface. LST controls the surface-emitted long-wave radiation and is thereby essential to quantify sensible and latent heat fluxes between the Earth's surface and the atmosphere. These interactions are crucial for a variety of applications related to land surface processes, such as climate and drought monitoring [1,2], hydrological cycle [3–5], model assessment [6–9], and data assimilation [10–12], among others. LST has been retrieved in remote sensing platforms using a variety of algorithms that rely on sensor channels in the so-called atmospheric window region of the infrared spectrum [13]. Within this band, surface-emitted radiances reach the sensor with relatively little absorption by the atmosphere. Moreover, in the thermal infrared atmospheric window (TIR), surface emissivity can be determined with relatively less uncertainty than in other regions in the infrared, such as in the middle infrared, making it ideal to retrieve surface properties [14]. Previous studies proposed the use of channels in the middle infrared for LST estimation [13,15,16]; however, these are far less common than algorithms based on the thermal infrared observations and therefore will not be considered here.

The choice of LST algorithm, which is often a semi-empirical function of top-of-atmosphere (TOA) brightness temperatures in TIR, is intrinsically linked to the characteristics of the sensor being used. As such, LST algorithms may rely on a single channel (the mono-window algorithms, MW), when measurements are available in only one TIR band [15,17–19], or in a combination of TIR channels using the so-called generalized split-windows (GSW) approach [13,20,21]. In general, this type of algorithm is based on a linear regression between the measured quantities at the top of the atmosphere and LST, using ancillary data such as spectral emissivity, total column water vapor (TCWV), zenith viewing angle (ZVA), land cover and also day/night flags. Usually these parameters are divided into classes, and for each combination a set of model coefficients is estimated [13,20]. The whole procedure therefore requires setting up a comprehensive calibration database which is usually generated ad hoc, with a high risk of leaving out unforeseen situations that lead to systematic biases in operational retrievals. To the best of our knowledge, no study has been devoted to the process of building a calibration database. This paper focuses on the factors that need to be taken into account when building a calibration database for such regressions, providing a general methodology that can be applied when developing an algorithm for infrared LST estimates and providing a systematic discussion of the impact of all the choices that are made when building a calibration database.

In order to make the model coefficients robust enough to deal with any combination of input parameters, it is necessary to calibrate the model for a wide range of atmospheric and surface conditions as well as viewing geometries. A good calibration of the model coefficients can only be achieved if the calibration database is designed carefully, covering the range of variations that are expected to affect the problem [21]. Usually, the models are calibrated using criteria that are considered reasonable, covering a wide range of atmospheric and surface conditions [20,22], but here we propose an objective approach to prepare a calibration database that minimizes the overall model error statistics and their variations among the range of input parameters.

This article summarizes the procedure used in the EUMETSAT LSA SAF [23] to calibrate LST algorithms for the Spinning Enhanced Visible and InfraRed Imager (SEVIRI, e.g., [20]) onboard the Meteosat Second Generation (MSG), the Advanced Very-High Resolution Radiometer (AVHRR) on Metop and the Meteosat Visible and InfraRed Imager (MVIRI) onboard Meteosat First Generation (MFG; e.g., [17]). The current standard methodology within the LSA SAF uses a criterion for setting up the calibration database with a good compromise, addressing the widest possible retrieval conditions (which are a pre-requisite for a global LST product), but a sensitivity analysis was required to ensure that the most robust possible model coefficients are in use. A similar exercise will be soon performed for the Flexible Combined Imager (FCI) on board the Meteosat Third Generation (MTG; [24]) to design the follow-on of LSA SAF operational LST products.

2. Methodology

2.1. The Problem

Considering the Earth surface as a lambertian emitter-reflector, a cloud-free atmosphere under local thermodynamic equilibrium and negligible atmospheric scattering, the monochromatic top of atmosphere radiance L_i, in a given channel i, and measured by a sensor onboard a satellite observing the Earth's surface under zenith angle θ is expressed by (e.g., [13]):

$$L_i(\theta) = B(T_{bi}) = \epsilon_i B_i\left(T_{sfc}\right)\tau_i(\theta) + L^{\uparrow}_{atm,i}(\theta) + (1-\epsilon_i)\,L^{\downarrow}_{atm,i}\tau_i(\theta) \quad (1)$$

where ϵ_i is the surface emissivity on channel i, $B_i\left(T_{sfc}\right)$ is the equivalent black-body radiance at temperature T_{sfc} (or LST), τ_i is the transmissivity, $L^{\uparrow}_{atm,i}$ is the upward atmosphere-emitted radiance, and $L^{\downarrow}_{atm,i}$ is the downward atmosphere-emitted radiance. LST is often estimated from linearized inversions of Equation (1), applied to one or more channels in the TIR, as mentioned above. There are a few formulations of these inversions in the literature [25] which mostly depend on how the Taylor

expansion of the radiative transfer equation is made in order to derive a formulation that is suitable to a particular application. In this work, the sensitivity to the used model is not fully addressed, although some of the results could be slightly different if different LST algorithms were used. However, it is important to assess the differences of using a GSW model or a MW model, as they serve two different purposes: the first is widely used in state-of-the-art retrieval schemes in sensors with two or more channels in the thermal atmospheric window, while the second is left for sensors with only one channel in that band. Here, only one formulation for each case is considered—one GSW and one MW algorithm—which will serve as testbeds for the calibration datasets under analysis. The GSW formulation used for operational LST estimates both from the Moderate Resolution Imaging Spectroradiometer (MODIS; [21]) and from SEVIRI ([20]):

$$LST = C + \left(A_1 + A_2 \frac{1-\epsilon}{\epsilon} + A_3 \frac{\Delta\epsilon}{\epsilon^2} \right) \frac{T_{IR1} + T_{IR2}}{2} + \left(B_1 + B_2 \frac{1-\epsilon}{\epsilon} + B_3 \frac{\Delta\epsilon}{\epsilon^2} \right) \frac{T_{IR1} - T_{IR2}}{2} \quad (2)$$

where A_1, A_2, A_3, B_1, B_2, B_3 and C are the model coefficients, T_{IR1} and T_{IR2} are the equivalent brightness temperatures, ϵ and $\Delta\epsilon$ are the average and the difference of the emissivities in both split-windows channels. For the MW model, the formulation derived by Duguay-Tetzlaff et al. [17] to derive LST from Meteosat First Generation is used:

$$LST = A \frac{T_{IR1}}{\epsilon_{IR1}} + B \frac{1}{\epsilon_{IR1}} + C, \quad (3)$$

where A, B, and C are again the regression coefficients. In both cases, the regression coefficients are fit for classes of TCWV and ZVA, and they must somehow simulate atmospheric absorption and emission, while the effect of surface emissivity is in these cases, explicitly resolved. The atmospheric transmissivity is mainly constrained by the radiative optical path. Hence, a good calibration database to fit model coefficients in Equations (2) and (3) needs to ensure that a scene may be observed by a wide range of viewing geometries (ZVA) and water vapor contents, which is the most relevant and variable absorber/emitter in the TIR window region.

The weighting functions (given by the vertical derivative of transmissivity) of atmospheric window channels peak close to the surface, where the strongest vertical gradients of humidity are found. However, in the presence of well-developed moist planetary boundary layers, their peak will be higher above (although always relatively close to the ground), which means the temperature and humidity vertical structure at the lower levels in the profiles represented in the calibration database might play a role in the database robustness, especially considering the occurrence of temperature inversions close to the surface. This effect may be taken into account not only by introducing a large variety of atmospheric profiles at different locations and observation times, but also by artificially varying the difference between the surface skin temperature and the near-surface air temperature ($LST - T_{air}$), which in turn has a significant role in the control of the thermal structure of the lower atmosphere, through the turbulent sensible heat flux (e.g., [26,27]). This difference varies across the diurnal cycle, among surface types and for different large scale atmospheric conditions, and may be either positive or negative. Particular attention should be paid to its distribution within calibration databases and to the impact on algorithm performance.

The difference between TOA brightness temperatures in the split-window channels is aimed at capturing differential absorption within those bands which is associated to atmospheric water vapor content. In the case of a GSW algorithm, Equation (3), the difference between the spectral emissivities of the window channels are also taken into account. This difference is related to surface type and moisture in the sense that moister surfaces show less spectral variations in emissivity [28].

2.2. Radiative Transfer Simulations

The development of LST algorithms, such as those represented by Equations (2) and (3) (see e.g., [20,21,25]) is usually based on a set of radiative transfer simulations performed for a

calibration database (for algorithm fit) and a validation one (for algorithm test), both representing a wide range of clear sky conditions. The databases must be independent and, while the former should encapsulate the widest possible atmospheric conditions for the area of interest together with broad distributions of surface emissivity and sensor viewing geometry that are needed for robust parameter estimation, the latter should contain the largest possible set of profiles/surface conditions to allow a comprehensive characterization of LST algorithm uncertainty. By LST algorithm uncertainty, we mean deviations of LST retrievals from the "true value" that are not associated to uncertainties in the input data, but solely to the retrieval method. The characterization of the individual sources of uncertainty (such as the algorithm uncertainty studied here or the uncertainty due to emissivity or to the sensor noise, for example) has been recognized as crucial for the uncertainty validation of remotely sensed surface temperature products [29]. It is worth emphasizing that the comparison of LST estimates obtained using actual remote sensing observations against ground-based observations is part of a product validation exercise. In that case, which is often limited to a relatively small number of available sites, the deviations will be the result of both algorithm and input errors and their contributions to the total error are impossible to disentangle. The radiative transfer simulations aim to determine the TOA spectral radiances for each profile in the respective databases, so that the forward problem is solved with full knowledge of the surface emission and atmospheric absorption. It is important that those simulations are performed with an accurate radiative transfer model. For the example analyzed in this study, the MODTRAN4 code [30] was used, which returns spectral radiances with a resolution of 1 cm^{-1}. For the sake of simplicity, MODTRAN4 TOA radiances were convoluted with SEVIRI response functions for channels centered at 10.8 μm (IR1 channel) and 12.0 μm (IR2 channel, only used in the GSW algorithm), and then subject to the inverse Planck function to obtain the respective channels brightness temperatures, T_{IR1} and T_{IR2} (for more details see, e.g., [15]). The calibration of the coefficients is performed using a least-squares technique, aimed to provide the best fit for the semi-empirical relationships between the simulated brightness temperatures and the set of prescribed LSTs, atmospheric conditions and viewing geometries in the calibration database. In the case of Equations (2) and (3) used in this study, the coefficients are calibrated in classes of ZVA and TCWV, as those formulations do not explicitly model their effect on the atmospheric correction. Finally, the algorithm uncertainty is characterized using the independent validation database, through comparisons of estimated LST obtained with one of the semi-empirical models (Equation (2) or (3)) and the LST_{True} value. The latter corresponds to the T_{Skin} values in the databases, which together with the respective atmospheric profiles, surface emissivity and prescribed view zenith angle, led to the TOA brightness temperature(s) used in the LST algorithms. The use of independent databases for algorithm calibration and validation, relying on accurate radiative transfer simulations, is the best way of characterizing the algorithm uncertainty and its performance for a wide range of scenarios.

2.3. Characteristics of Atmospheric Profiles Relevant for Radiative Transfer in the TIR Window

We have opted to select the calibration dataset from a comprehensive collection of clear-sky profiles of temperature, water vapor and ozone, as well as ancillary variables such as spectral emissivity, land cover, elevation, skin temperature, and surface pressure compiled by Borbas et al. [31]. This dataset, hereafter referred to as SeeBor database, includes over 15,000 profiles and will be used in this work for convenience. We could have made use of other datasets also specifically gathered for satellite retrievals under clear sky conditions (e.g., [22]), but our focus is on the criteria to be taken into account for the subset of calibration data for LST algorithms.

Figure 1 shows the geographical distribution of profiles contained in the SeeBor database; the dots representing the profile locations are colored according to their TCWV. This dataset covers the whole globe, including oceans. Regions with more frequent cloud cover are, as expected, somewhat less populated. In general, low values of TCWV are found near the poles and high values close to the Equator. However there are notable exceptions, especially in some continental regions where it is possible to observe both very dry and very moist atmospheres. From this large set of profiles only a

few will be selected to calibrate an LST retrieval algorithm, while the rest is used for its validation, i.e., characterization of algorithm uncertainty as mentioned above. The task of selecting these calibration profiles is tricky and impacts the model robustness, as will be shown below.

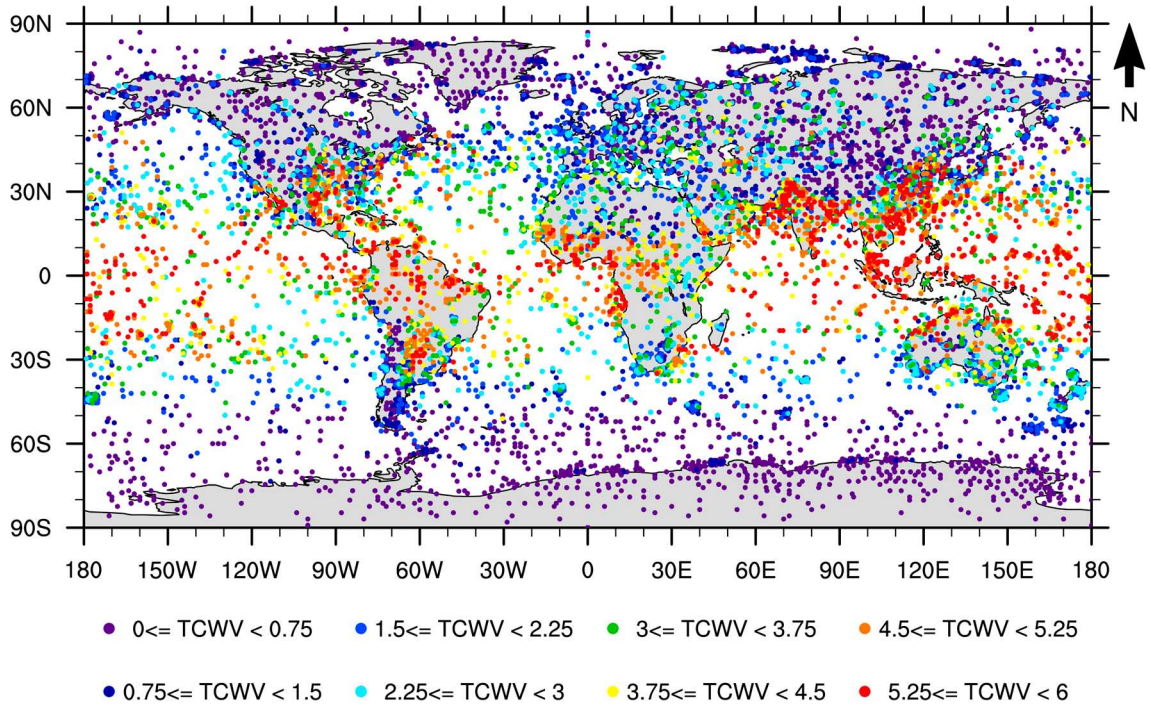

Figure 1. Distribution of the SeeBor (clear sky) profiles, colored by TCWV class (in cm).

The statistical distributions of TCWV and skin temperature are shown in Figure 2a,b, respectively. Both distributions are highly skewed. The majority of the profiles are on the drier side of the TCWV distribution and almost no profiles show values of more than 6 cm since those conditions are within the physical limit for an atmosphere with no clouds. Skin temperatures show a wide dynamic range, roughly between 210 and 330 K, the distribution being negatively skewed. Thus, in principle, it would only be necessary to uniformly span these ranges of values to have a comprehensive calibration database. However, some combinations of both parameters are unphysical, which in turn leads to less accurate coefficients and worse performance by the regression model. The bivariate distribution shown in Figure 2c reveals that not surprisingly very moist (clear sky) atmospheres only occur over the warmer surfaces, while towards lower TCWV values, the skin temperature range increases. In other words, the very dry atmospheres can be very warm or very cold, whereas the moister atmospheres are only found over warmer surfaces.

In Figure 3 the distribution of $LST - T_{air}$ is shown, for each class of TCWV. T_{air} corresponds to the temperature at the first pressure level above the ground. The separation in classes of TCWV shows that drier atmospheres support somewhat larger temperature gradients close to the surface. The dynamic range of this parameter needs to be chosen carefully, since it has a large impact on the resulting coefficients (see sensitivity tests in Section 3). Cases with the largest differences should also be accounted for in the linear regression; otherwise, the calibration would miss some of the most extreme low-level temperature profiles and this would degrade the quality of the regression, especially when the algorithm needs to deal with such profiles in practice. For very dry atmospheres, the distribution is nearly normal with maximum absolute differences of about 20 K. In the case of moister atmospheres, the distributions become positively skewed with maximum positive differences of about 25 K for only a few cases but almost no values below -10 K. In general, most cases lie between -15 K and 15 K.

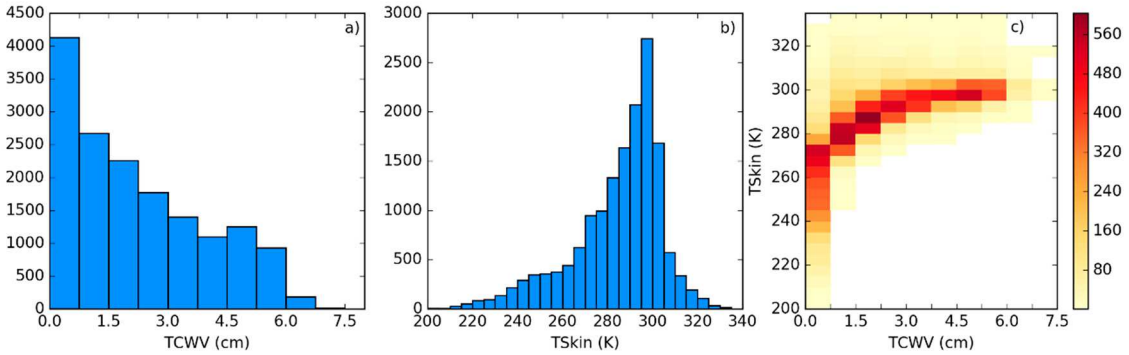

Figure 2. Distributions of (**a**) TCWV and (**b**) skin temperature on the SeeBor database; (**c**) Bivariate distribution of the previous parameters.

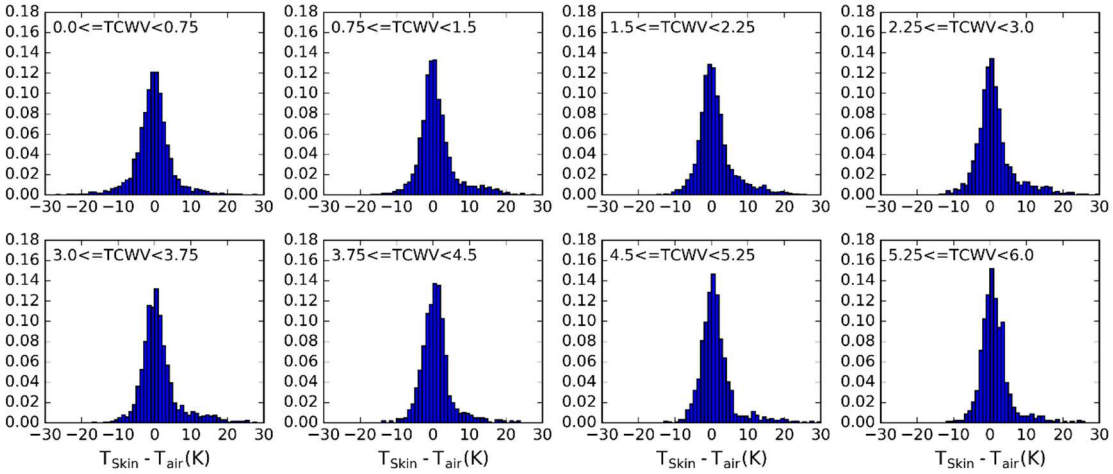

Figure 3. Distributions of the difference between the skin temperature and the temperature at the first level above the surface on SeeBor, by class of TCWV. Histograms are normalized by the number of cases in each TCWV class.

The diversity of land surfaces and the radiative properties of their materials need to be taken into account through an appropriate range of surface emissivities. This quantity adds an extra level of complexity to the calibration database. Depending on the algorithm that is chosen, only one value is used in the case of a single-channel algorithm, or the values on two bands need to be specified in the case of a GSW model. Some GSWs, such as that considered here (Equation (2)) rely on the average value of the emissivity in the two channels and also the difference between them. Therefore it was decided to prescribe a range of emissivity values for the channel around 10.8 µm and then prescribe a range of differences of the emissivities in both channels, $\Delta\epsilon = \epsilon_{IR2} - \epsilon_{IR1}$. The range of spectral emissivities at 10.8 µm and 12.0 µm, close to typical central wavelengths of split-window channels (e.g., MODIS, SEVIRI), available in the SeeBor database are shown in Figure 4. There are quite a few cases with very high emissivities which correspond to SeeBor profiles over water bodies and ice. In general, cases over land have higher emissivities in the 12.0 µm compared to the 10.8 µm. The larger spectral variations are found over deserts and semi-arid surfaces.

The viewing angle also affects the calibration and the appropriate range to be considered will depend on each sensor. In this work the analysis will be for a sensor on board a geostationary platform, or for a large swath polar orbiting sensor, and therefore we will also consider a wide range of view zenith angles.

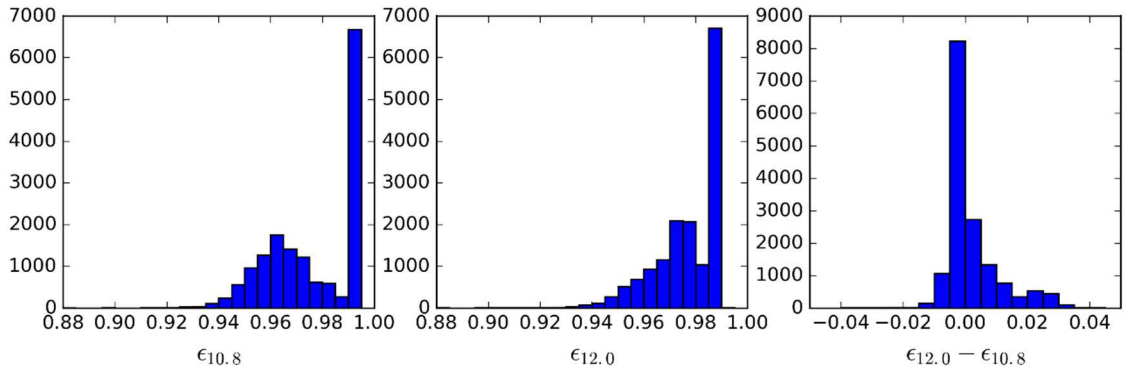

Figure 4. Distribution of the SeeBor spectral emissivities at 10.8 and 12.0 μm, and their difference.

2.4. A Calibration Database

Given the physical constraints of the problem and the range of the input parameters detailed in the previous section, the following methodology is proposed to select the subset of calibration profiles:

(1) Define classes of T_{Skin} (from 200 K to 330 K in steps of 5 K) and $TCWV$ (from 0 to 6 cm in classes of 0.75 cm—values greater than this should be treated with the coefficient corresponding to the last $TCWV$ class).

(2) Iterate in the SeeBor clear-sky profile database to fill each class in the $TCWV/T_{Skin}$ phase space (as in Figure 2c) with one case each. When a new profile is selected, it is ensured that its great-circle distance to the already selected profiles is greater than an initial distance of 15 degrees, which guarantees a wide geographical coverage. After a sufficiently large number of tries (in this case 30,000), the distance criterion is relaxed in steps of minus 1 degree, until the whole $TCWV/T_{Skin}$ phase space is filled.

(3) For each of the previously selected profiles, assign a new T_{Skin} based on the ranges of $T_{Skin} - T_{air}$ observed in Figure 3. The choice of the range of perturbations to apply is key to the performance of the chosen model and may depend on the region of interest. In the case of this work, a range of $\pm$15 K around T_{air} in steps of 5 K showed an overall good performance. As will be seen, large biases arise when non-physical cases are included or if the somewhat more extreme cases are not taken into account.

(4) Each of these conditions may be sensed from angles ranging from 0 (nadir view) to 70° in steps of 2.5°. It is important to discretize the viewing geometry in this way because this is an intrinsically non-linear problem. The upper limit of the ZVA might be adapted for the sensor under analysis. Previous calibration exercises show that above this viewing angle limit the retrieval errors are generally too high, especially for moister atmospheres [15].

(5) For the emissivity, a range of possible values are attributed to each of the cases above: values of $\epsilon_{10.8}$ from 0.93 to 1.0 in steps of 0.01, and then, in the case of a GSW model, it is appropriate to prescribe departures from this value for $\epsilon_{12.0}$: -0.015 to 0.035 in steps of 0.01 (excluding cases where $\epsilon_{12.0} > 1.0$), as suggested by Figure 4.

Figure 5 shows the statistical and geographical properties of the database gathered following those steps, which total 116 profiles. By combining these profiles with the prescribed viewing geometries and surface/low-level conditions proposed in steps 3 to 5, the total number of cases used in the calibration is 906,192. This number is around ten times larger than the number of simulations made for the validation dataset, which contains the remaining profiles in the SeeBor database, simulated with five random angles (within the ZVA range of each sensor) per profile. Note that the TCWV distribution (Figure 5a) is close to that of the whole SeeBor data set (Figure 2a), although moister profiles are relatively over-represented, so that a robust fit of LST algorithms can be achieved for these

cases. Nevertheless, low humidity profiles still dominate within the distribution, to ensure a proper coverage of the $TCWV/T_{Skin}$ phase space (Figure 5c) and its large dynamic range of T_{Skin} towards low TCWV values (as seen in Figure 2c).

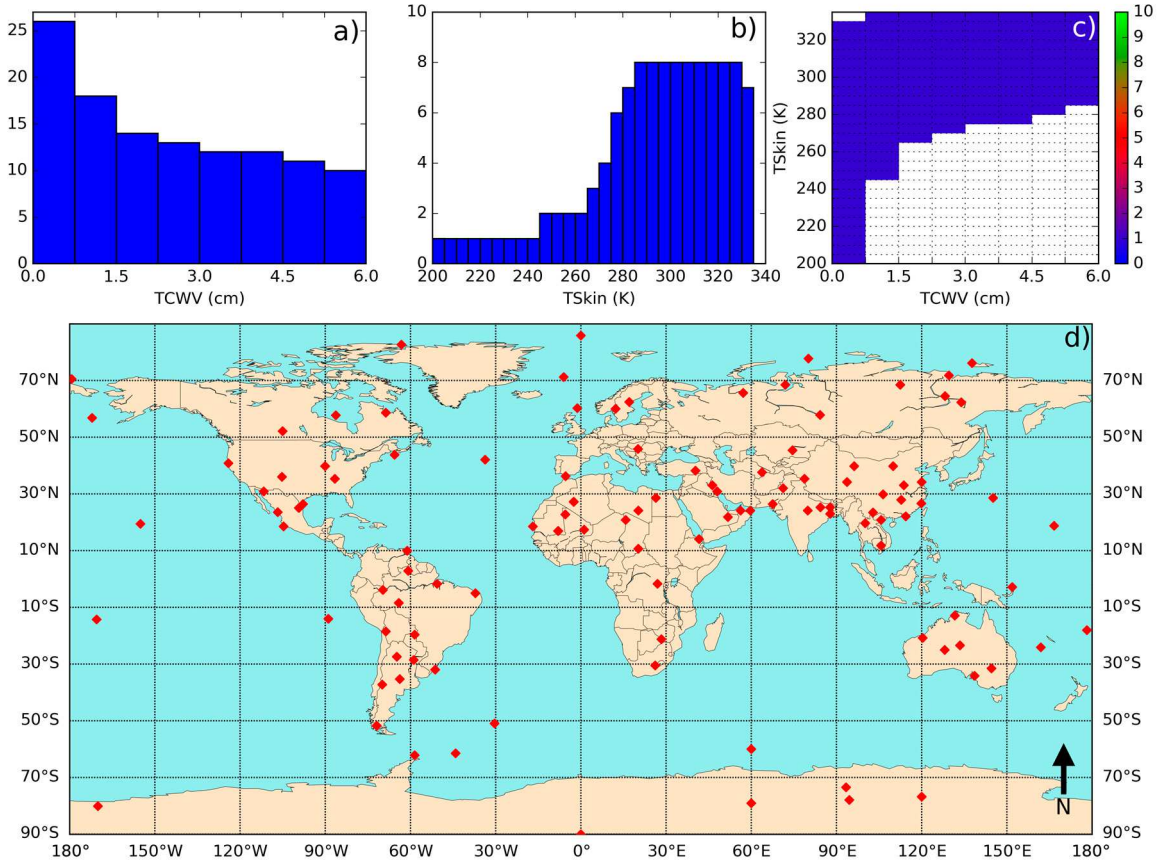

Figure 5. Main properties of the proposed calibration database: (**a**) TCWV distribution; (**b**) T_{Skin} distribution; (**c**) bivariate $TCWV/T_{Skin}$ distribution and (**d**) geographical distribution.

The way the database is built also leads to a greater frequency of profiles gathered over land, since some of the most extreme conditions are only found there. The presence of some marine profiles is not problematic because algorithms also need to cover cases where the LST retrieval is made over small islands or coastal regions. Validation of LST products over large water bodies is also a common practice (e.g., [32]).

3. Results

3.1. Error Statistics of the Proposed Calibration Database

Figure 6 shows the error statistics of the GSW algorithm adjusted using the proposed calibration database; the algorithm error (i.e., $LST_{GSW} - LST_{True}$) statistics are evaluated for the independent validation database. Globally, this reveals a bias of around -0.09 K and a Root Mean Square Error (RMSE) of 0.776 K, the scatterplot shows larger dispersions towards larger LSTs which is mainly caused by the greater water vapor content of such atmospheres. Especially when combined with large viewing angles, this kind of profile is responsible for the largest retrieval errors. This is confirmed by the diagram on the center of Figure 6 which shows the RMSE per class of ZVA and TCWV: larger RMSE values of above 3 K appear for classes with larger optical path (larger ZVA and larger TCWV). On the other hand, nearly all classes below 3 cm and below 50 degrees show RMSEs of 0.5 K or lower. The distribution of the bias over the TCWV/ZVA diagram shows that this statistic does not

change much across the different classes with only a few classes with positive and negative biases of magnitudes around 0.2 K, towards higher values of TCWV.

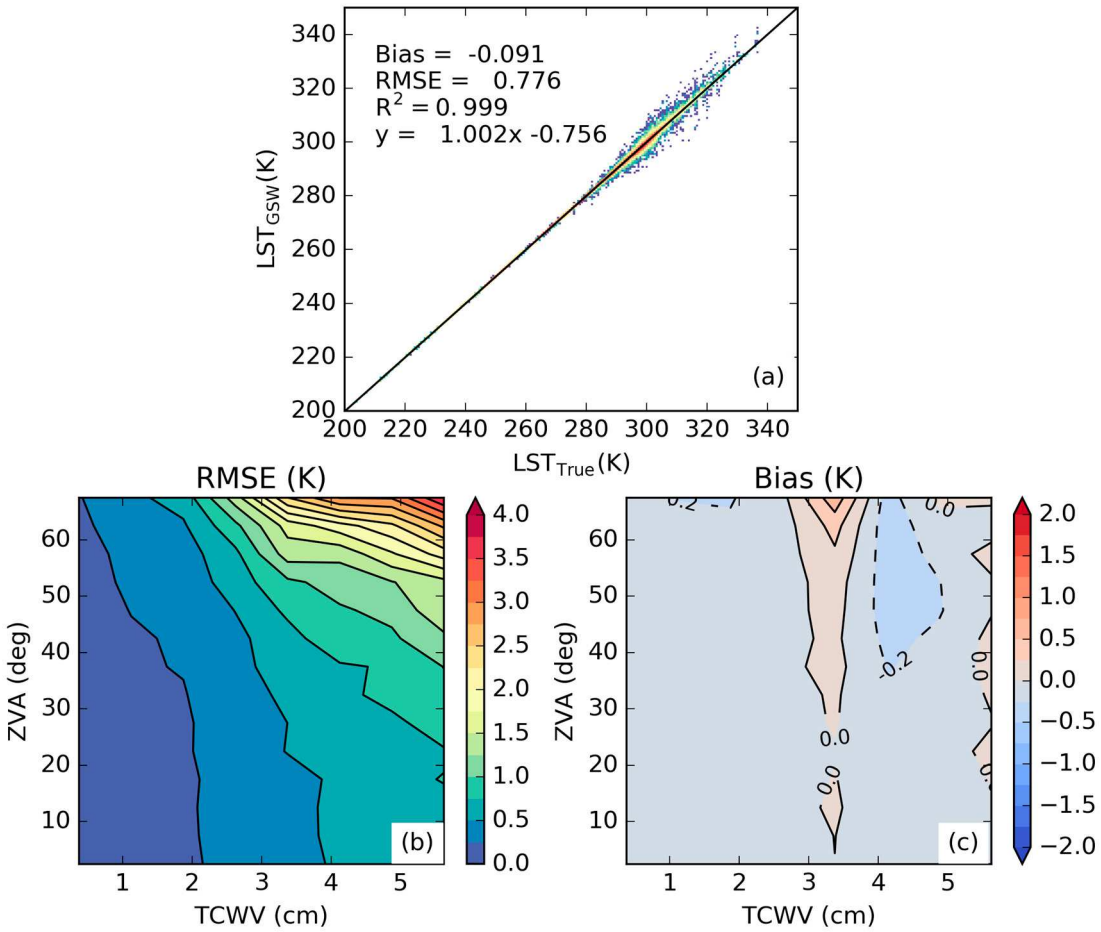

Figure 6. Error statistics for the proposed calibration database using the GSW model. (**a**) Scatterplot with all the cases in the database. The global bias and RMSE are indicated. The black line represents the best linear fit; (**b**) RMSE distribution as a function of TCWV and ZVA; (**c**) Bias distribution as a function of TCWV and ZVA.

In Figure 7 the same statistics are analyzed in the case of the MW model. Although this model shows nearly the same overall bias (0.086 K), its RMSE is almost three times larger (of about 2.20 K). The way the RMSE is distributed along the classes of TCWV and ZVA is much less linear than in the case of the GSW model and presents a stronger dependency on TCWV even for low ZVAs. Moreover, there are more classes with retrieval errors that are close to the limit acceptable for LST algorithms (e.g., LSA-SAF LST products consider 4 K to be their threshold accuracy requirement; [20]). The bias also has a more complex structure among the TCWV/ZVA classes, some of them reaching more than 1 K, both positive and negative showing that the overall bias results from the cancellation of values between different classes. The differences between Figures 6 and 7, and in particular the steeper increase in RMSE with TCWV in the MW, emphasize the importance of using GSW-type schemes whenever possible.

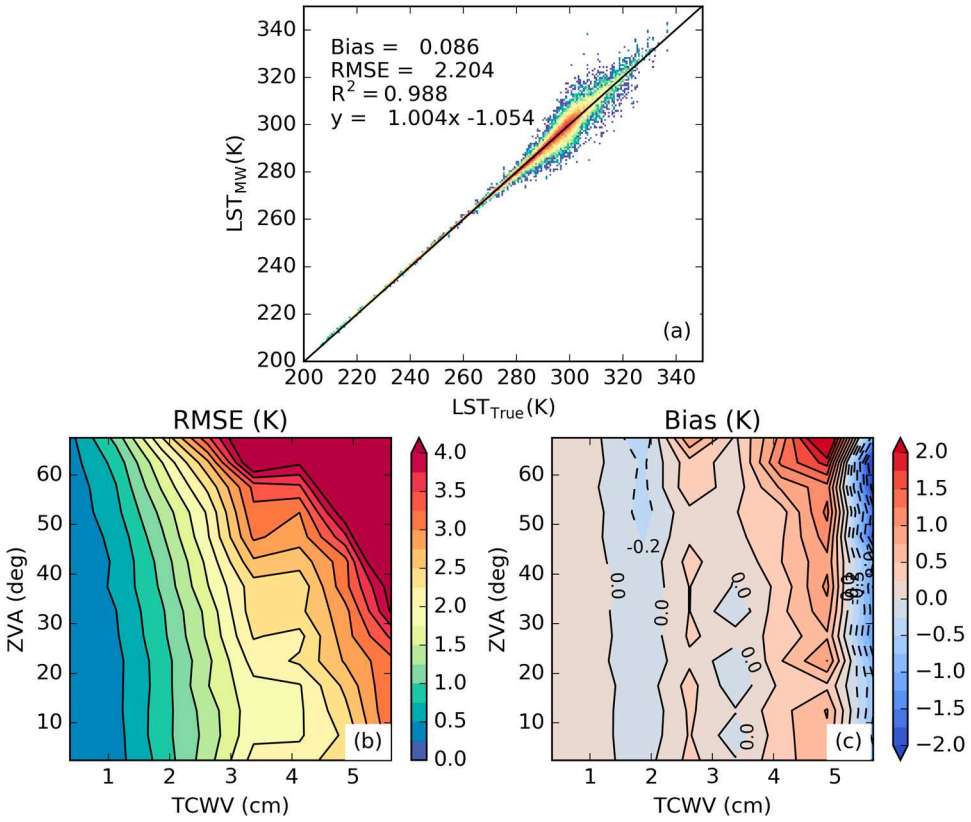

Figure 7. Error statistics for the proposed calibration database using the MW model. (**a**) Scatterplot with all the cases in the database. The global bias and RMSE are indicated. The black line represents the best linear fit; (**b**) RMSE distribution as a function of TCWV and ZVA; (**c**) Bias distribution as a function of TCWV and ZVA.

3.2. Sensitivity to the Distribution of Relevant Variables

In order to study the sensitivity of the proposed database to some of the choices that were made, a set of experiments was performed. The baseline calibration dataset, which is based on a choice of profiles that is adequate to fill the TCWV/LST diagram, is referred to as WTS_−15_15 (TCWV is sometimes represented as W in the literature and TS stands for T_{Skin}). A different criterion could have been adopted to choose a few calibration profiles from the more than 15000 profiles in the SeeBor database, such as ensuring a flat distribution of TCWV. This criterion was adopted, together with the wide geographical distribution criterion of WTS_−15_15, for experiments FLAT14_−15_15 and FLAT10_−15_15. The difference between these two is that for the first, 14 profiles per TCWV class were chosen (112 profiles vs. 116 in WTS_−15_15) and for the latter only 10 (leading to a total of 80 profiles). The goal was to test the relevance of the number of profiles and of the respective joint LST /TCWV distribution for the robustness of the regression coefficients. The statistical and geographical distributions of these databases are illustrated in Figures 8 and 9. Large parts of the TCWV/LST diagram are not covered such as the most extreme LST classes. In the intermediate TCWV classes, a large number of the cases fall in the same LST range, as these combinations are globally more frequent for clear sky conditions, and therefore also more frequent in the SeeBor database. Note that a few of the profiles are common to FLAT14_−15_15 and to FLAT10_−15_15; this is because the algorithm is initiated with the same random seed, which generated the same random number sequence for all the experiments. The geographical distributions show that relatively fewer profiles over land are selected, which might be explained by the fact that the inclusion of more extreme situations was not a requirement.

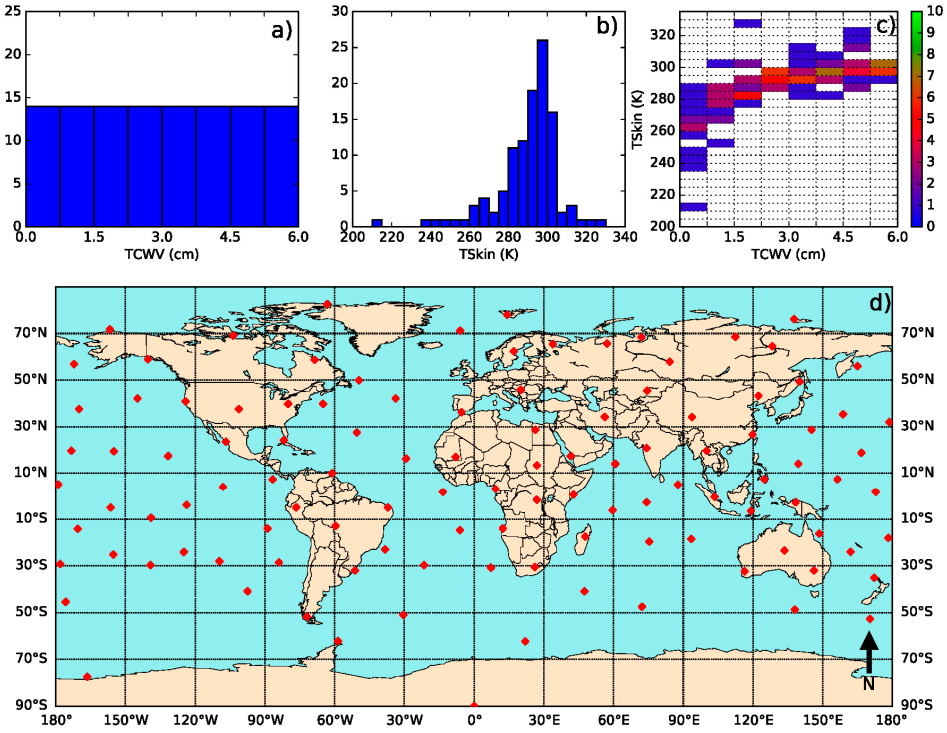

Figure 8. Main properties of the FLAT14_−15_15 calibration database: (**a**) TCWV distribution; (**b**) T_{Skin} distribution; (**c**) bivariate TCWV/T_{Skin} distribution and (**d**) geographical distribution.

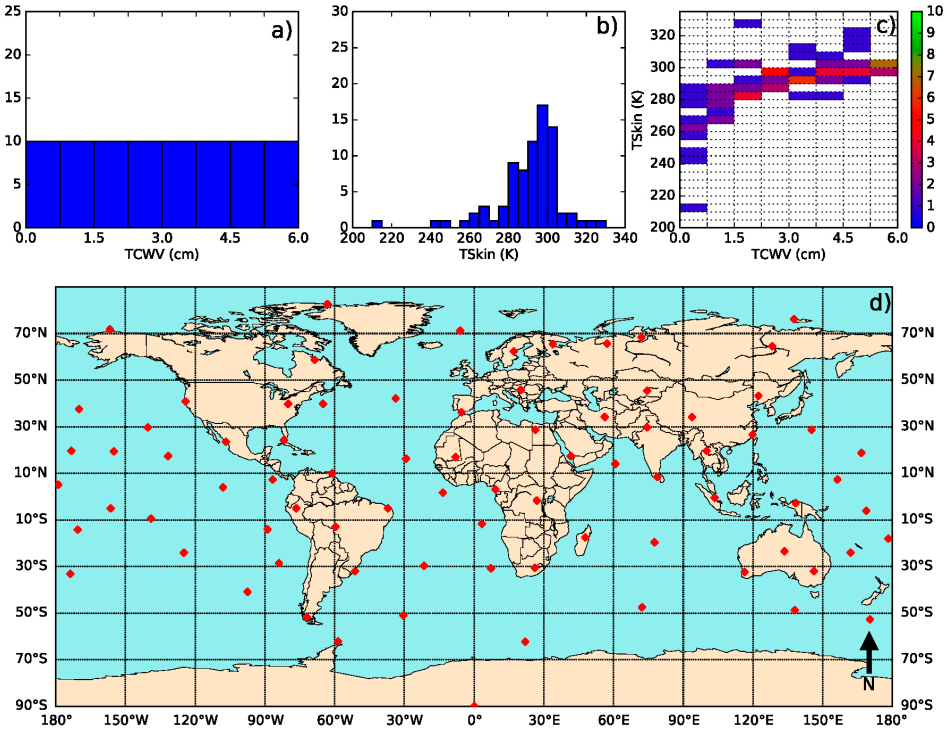

Figure 9. Main properties of the FLAT10−15_15 calibration database: (**a**) TCWV distribution; (**b**) T_{Skin} distribution; (**c**) bivariate TCWV/T_{Skin} distribution and (**d**) geographical distribution.

Another factor that greatly influences the robustness of the coefficients is the $LST - T_{air}$ difference. Therefore, we tested a few variants of the WTS_−15_15 database varying the lower and upper limits

of the prescribed $LST - T_{air}$ difference, always using steps of 5 K. These experiments are referred to as WTS_−10_10, WTS_−10_15, WTS_−10_20, WTS_−15_20, WTS_−20_15, WTS_−20_20, WTS_−20_25 and WTS_−25_25 (the numbers in the experiment name refer to the lower and upper limits of $LST - T_{air}$). All these choices of calibration databases were tested in both the GSW and the MW formulations and the same validation database was used to assess their statistical properties. The set of sensitivity experiments is described in Table 1.

Table 1. Description of the calibration database sensitivity experiments.

Database	Selection of Profiles	Number of Profiles	Prescribed $LST - T_{air}$ Range (K)
Baseline: WTS_−15_15	Full coverage of the LST/TCWV phase space	116	−15 to +15
FLAT14_−15_15	Flat distribution of TCWV with 14 profiles per TCWV class	112	−15 to +15
FLAT10_−15_15	Flat distribution of TCWV with 10 profiles per TCWV class	80	−15 to +15
WTS_−10_10	Full coverage of the LST/TCWV phase space	116	−10 to +10
WTS_−10_15	Full coverage of the LST/TCWV phase space	116	−10 to +15
WTS_−10_20	Full coverage of the LST/TCWV phase space	116	−10 to +20
WTS_−15_20	Full coverage of the LST/TCWV phase space	116	−15 to +20
WTS_−20_15	Full coverage of the LST/TCWV phase space	116	−20 to +15
WTS_−20_20	Full coverage of the LST/TCWV phase space	116	−20 to +20
WTS_−20_25	Full coverage of the LST/TCWV phase space	116	−20 to +25
WTS_−25_25	Full coverage of the LST/TCWV phase space	116	−25 to +25

The results of the sensitivity experiments are summarized in Tables 2 and 3 for the GSW and MW algorithms, respectively. Both algorithms were adjusted using the different calibration databases described above and assessed using a common and independent validation database. In Tables 2 and 3, values of the overall bias and RMSE are indicated, as well as their variability among the TCWV/ZVA classes (via the standard deviation of the bias and RMSE, respectively, obtained per TCWV/ZVA class). The GSW model shows a slightly higher bias and RMSE using the FLAT approach when compared to the WPS. Their variabilities are also larger for the FLAT-type databases, which means that there are classes that are not so well represented when using this approach.

Table 2. Error statistics for the sensitivity experiments. The bias is calculated by averaging the difference $LST_{GSW} - LST_{True}$ for the validation database. The database with the best statistic is highlighted in red.

Database	Bias (K)	RMSE (K)	Bias Stdev (K)	RMSE Stdev (K)
Baseline: WTS_−15_15	−0.09	0.78	0.14	0.67
FLAT14_−15_15	−0.12	0.81	0.38	0.70
FLAT10_−15_15	−0.11	0.82	0.32	0.72
WTS_−10_10	0.05	0.74	0.26	0.64
WTS_−10_15	0.07	0.76	0.34	0.69
WTS_−10_20	0.09	0.81	0.41	0.73
WTS_−15_20	−0.02	0.76	0.21	0.67
WTS_−20_15	−0.11	0.79	0.14	0.68
WTS_−20_20	−0.12	0.78	0.14	0.68
WTS_−20_25	−0.11	0.78	0.15	0.68
WTS_−25_25	−0.25	0.87	0.22	0.73

The set of experiments summarized in Table 1 also suggest high sensitivity to the lower and upper limits of the prescribed $LST - T_{air}$ difference prescribed in the calibration databases as this range is the only condition changing among experiments denoted by "WTS". The results presented in Table 1 suggest that it is hard to tell which combination is the best. In general, widening the $LST - T_{air}$ range of possible values seems to make the overall RMSE worse, although there are a few exceptions. Another discernible pattern regards the sign and magnitude of the overall bias: increasing the upper limit increases the bias (i.e., it becomes "more positive"); conversely, decreases in the lower limit seem

to make the bias more negative. Well-balanced ranges (absolute value of the lower and the upper limits close to each other) seem to lower the variability of the statistics.

Table 3. Same as Table 2 but for the MW model.

Database	Bias (K)	RMSE (K)	Bias Stdev (K)	RMSE Stdev (K)
Baseline: WTS_−15_15	0.09	2.02	0.71	1.63
FLAT14_−15_15	0.11	2.08	0.73	1.42
FLAT10_−15_15	−0.04	2.05	0.69	1.38
WTS_−10_10	0.55	1.97	0.70	1.35
WTS_−10_15	0.76	2.19	0.92	1.54
WTS_−10_20	0.89	2.39	1.09	1.72
WTS_−15_20	0.43	2.28	0.83	1.69
WTS_−20_15	−0.13	2.23	0.71	1.67
WTS_−20_20	0.04	2.34	0.76	1.68
WTS_−20_25	0.16	2.46	0.83	1.89
WTS_−25_25	−0.28	2.67	0.89	2.07

In the case of the MW model, the experiments show even less linear results. In fact, the case with more favorable error statistics is arguably FLAT10_−15_15, with a lower absolute value of the bias and bias variability, an overall RMSE that is comparable to that of the baseline experiment and with less variability among classes. For the MW model, the experiment with the smallest RMSE is WTS_−10_10 (of about 1.97 K); however, it has also the worst absolute value for the bias, 0.55 K. Like in the case of the GSW model, there is also a tendency to get worse RMSE values towards wider ranges of $LST - T_{air}$ difference.

These results suggest that the configuration of an appropriate calibration database may vary with the algorithm to be used and area coverage, as the distribution of the variables analyzed above (most notably $LST - T_{air}$) over the area of interest may support the exclusion of more extreme cases and non-relevant. The choice of profiles from a SeeBor-like database is non-trivial, but basing the choice on fully covering the bivariate TCWV/LST distribution over the respective region of interest seems to have some advantages. It is worth noting that covering the most frequent classes in the TCWV/LST diagram leads, as expected, to better overall statistics, as those will be the most frequent in the validation database (and also in real applications). In Figure 10, the overall statistics are analyzed for the FLAT14_−15_15 calibration database, which, despite having a comparable number of profiles to WTS_−15_15 and much more than FLAT10_−15_15, shows overall worse performance than those cases. The analysis of the bias (Figure 10c) as a function of TCWV clearly shows that some classes are affected by large negative biases (between 2 and 3 cm, and around 5 cm) while between 3 and 4 cm the bias is positive; the ZVA dependency seems less important in the analyzed case. This shows that even with a flat distribution of TCWV, the performance of the model will depend on the TCWV, suggesting that combined distributions of variables relevant to the problem need to be taken into account. In practice this would translate in a roughly latitude-dependent bias (following the latitude dependence of TCWV), which is something that should be avoided in global datasets.

In order to explore the effect of the prescribed $LST - T_{air}$ differences in the representation of the most extreme cases, boxplots of the error distribution (as given by $LST_{MW} - LST_{True}$) were calculated by classes of $LST - T_{air}$ in the validation database, and also as a function of the TCWV class, for two of the proposed experiments: MW calibrated using WTS_−15_15 and WTS_−25_25, respectively, as shown in Figures 11 and 12. There were some classes with only few cases, reflecting the fact that largely negative differences rarely occur and they do so in very dry atmospheres, so we merged them into a single class $-25K \leq LST - T_{air} < 10K$ to increase the figure readability. Large positive differences are more frequent and may occur in all types of atmospheres. The comparison of the error distributions shown in Figures 11 and 12 indicates that only a few classes seem to be statistically affected by the temperature difference range that is applied. In drier atmospheres (TCWV < 3 cm) the effect is in fact

negligible, since under these conditions the TOA brightness temperatures will be highly dominated by the surface emitted signal (i.e., by LST and surface emissivity). In most cases, the only noticeable effect is the increase in the range of the error when the temperature difference increases, even in those classes that are "covered" by both calibration databases (e.g., $5\ K \leq LST - T_{air} < 10\ K$). This is what causes the overall loss of performance of the database with the wider temperature ranges, since those classes are more populated than those with more extreme temperature differences. It is also worth noticing that extending the temperature difference range does not necessarily lead to a better representation of the extreme cases. When $LST - T_{air}$ is positive and large, it likely means the surface sensible heat flux may generate a convective boundary layer, which is often topped by a temperature inversion [33]. It is well known that large LST retrieval errors occur under very moist atmospheres (e.g., [20]). If on top of such conditions we have the development of a convective boundary layer, the height of the largest thermal and moisture gradients may be shifted upwards and therefore the peak of thermal weighting function of (split-)window channels may also be shifted upwards [34–36], which makes it harder to disentangle surface emission (LST and emissivity) from the signal emitted by the lower atmosphere. Some currently used schemes address this issue using different coefficients for day and night retrievals (e.g., [37]), which somewhat tunes the LST algorithms to different structures of the atmospheric boundary layer but introduces an additional discontinuity in the algorithm coefficients, while other schemes use additional information from numerical weather prediction models regarding near-surface air temperature (which may also bring additional model forecast errors into the retrieval). Although not shown, the GSW model seems much less sensitive to these effects, as the boxplot diagrams for the cases illustrated in Figures 11 and 12 for the MW algorithm are much closer to each other in the GSW case. In summary, extending the $LST - T_{air}$ values to include the most extreme cases may not be beneficial for the overall performance of the retrievals because it can lead to higher errors in the classes that are more frequent, without significant compensation from the classes with more extreme situations.

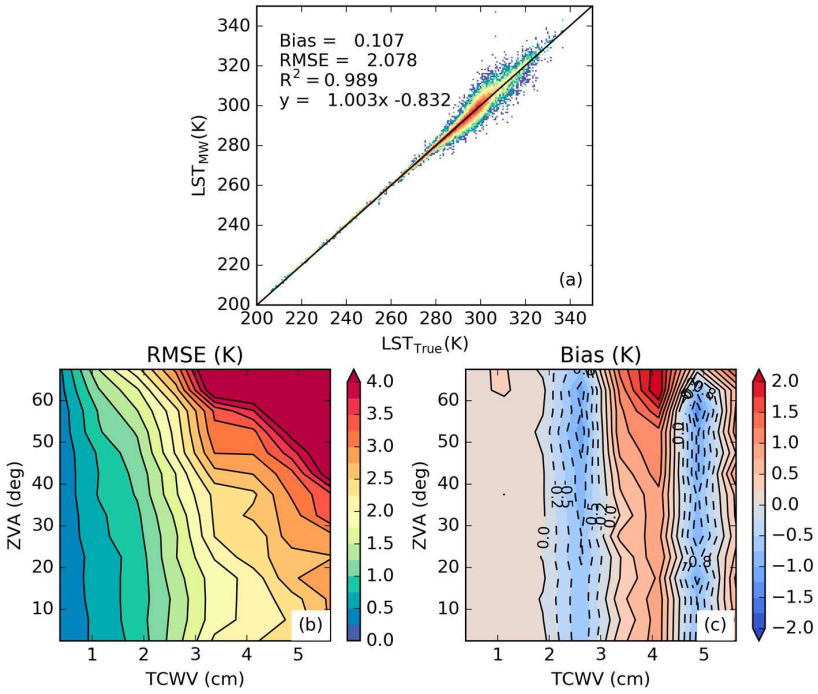

Figure 10. Error statistics for the FLAT14_−15_15 calibration database using the MW model: (**a**) Scatterplot with all the cases in the database. The global bias and RMSE are indicated. The black line represents the best linear fit; (**b**) RMSE distribution as a function of TCWV and ZVA; (**c**) Bias distribution as a function of TCWV and ZVA.

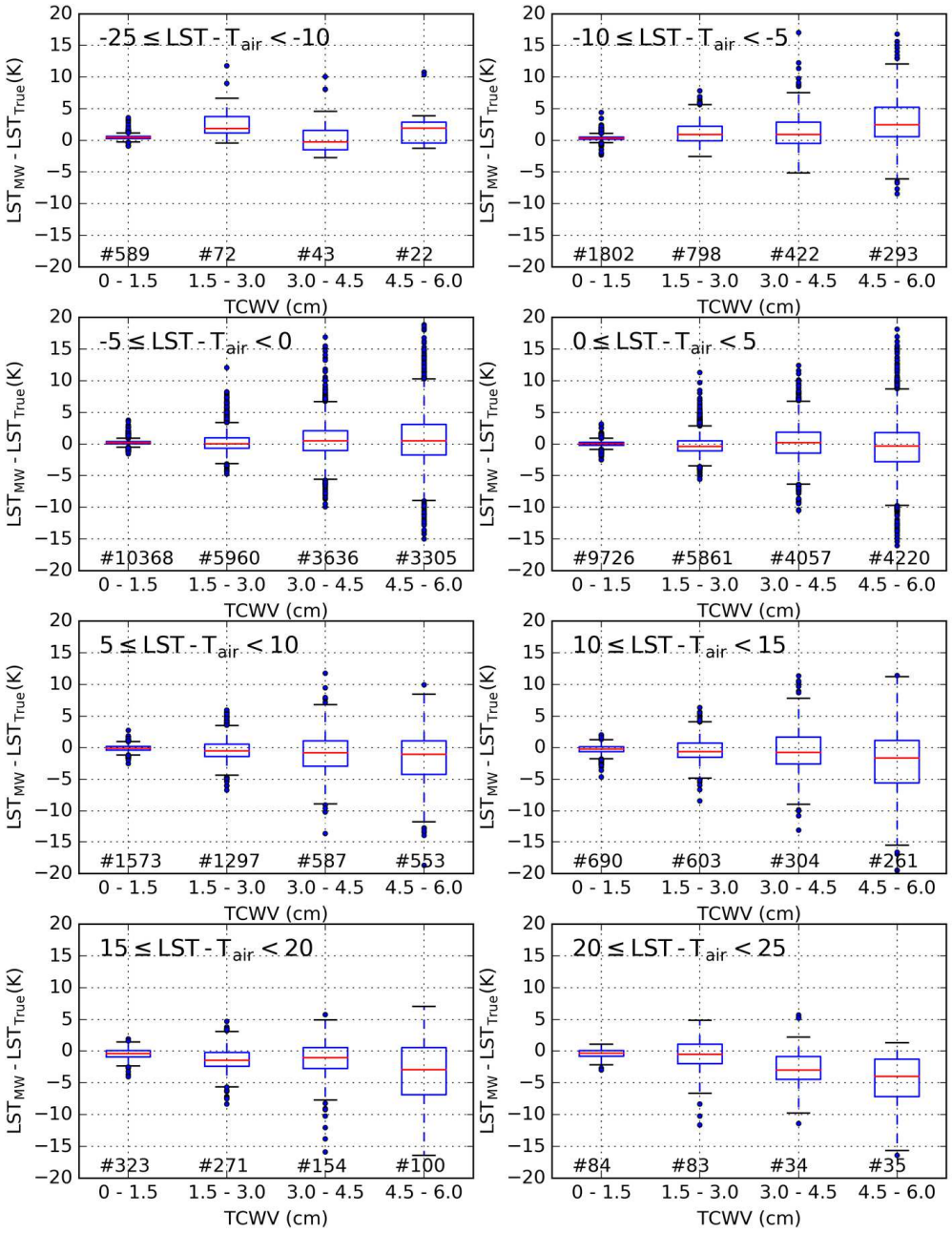

Figure 11. Boxplot diagrams of the $LST_{MW} - LST_{True}$ difference (K) discriminated in classes of $LST - T_{air}$ difference (K) and TCWV, using the WTS_−15_15 database. Below each diagram the number of cases is indicated. Note that the $LST - T_{air}$ range in the top left plot is broader than in the remaining plots.

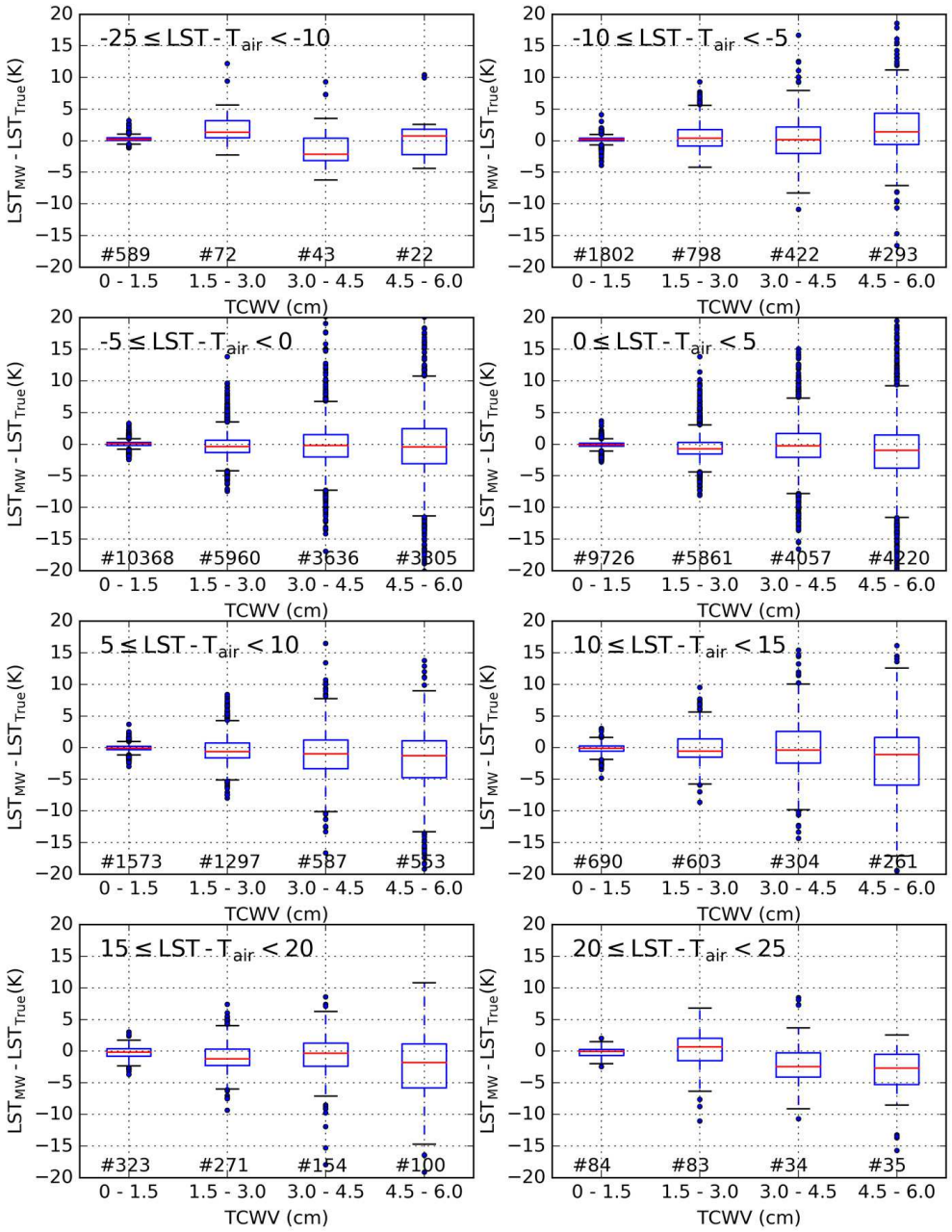

Figure 12. Same as Figure 11 but using WTS_−25_25.

4. Conclusions

The problem of how to design a calibration database for semi-empirical retrieval methods for LST is addressed here by identifying the factors that may influence the quality of the calibration (and therefore of the retrieval) and then investigating their physical range of variability. Considering the equation of radiative transfer between the surface and the TOA within the thermal infrared window, particular attention should be paid to three main factors, namely: (1) the atmospheric transmissivity and its vertical structure, which in turn is conditioned by the water vapor profile, as the main absorber/emitter and most variable gas in the wavelengths of interest, together with the viewing geometry; (2) the surface emissivity and its spectral variations; and finally (3) the low level thermal structure of the atmosphere, which may affect the vertical level at which the sensor is more sensitive in the channels of interest.

Assuming that we would like to design algorithm calibration databases that would lead to good fit under all possible conditions, one of the main questions is whether it is possible to improve the representation of the most extreme cases without compromising the performance of the overall retrieval. In this work it is shown that the answer to this question is not trivial. The selection of a set of atmospheric profiles that spans the range of surface temperatures and total column water vapor combinations that are physically possible seems beneficial for the quality of the regression model, but only modestly. Nevertheless, this ensures that a thorough representation of the possible cases is achieved when the model coefficients are trained, thus avoiding biases in certain classes of input parameters or retrieval conditions. The effects are amplified when a MW model is used instead of a GSW.

In terms of the representation the thermal structure of the low-levels in the atmosphere, the situation is slightly more complex. The inclusion of more extreme temperature differences between the surface and the near-surface air in the calibration database, rather than restricting them to more frequent/moderate cases, degrades the performance of the models especially under moist atmospheres, on which atmospheric emission is non-negligible. Also, such atmospheres are often characterized by well-developed boundary layers and as such, temperature inversions and strong vertical gradients may be present, complicating the atmospheric correction problem. Fully addressing this issue is left for future work.

Regardless of the calibration database used, the errors of LST estimations obtained for an independent validation database can be used to fully characterize the uncertainty of the LST algorithm, which heavily depends on retrieval conditions. The uncertainty budget of LST satellite products will then be the result of that of the algorithm together with the propagation of input uncertainties.

This article summarizes the procedure currently in practice within the EUMETSAT LSA SAF to calibrate the retrieval algorithms for a variety of LST products. The previously used methodology [20] gathered experience from a number of studies (e.g., [16,21,38,39]) but missed an objective criterion to physically constrain the selection of profiles used for calibration, which leads to an algorithm with lower uncertainty. The methodology designated here as WTS_−15_15 is a good compromise addressing the widest possible retrieval conditions, which is a pre-requisite for a global LST product. Future LST products, especially with inputs from the Flexible Combined Imager on board Meteosat Third Generation [24] will benefit from the knowledge provided by this study. It is possible, though, that for different applications (e.g., regional LST products) a different choice of calibration database is more suitable. As such, LST developers should consider the joint distributions of the relevant variables, as detailed above, for their area of interest and to perform similar sensitivity analyses to their algorithms.

Acknowledgments: This study was carried out as part of the EUMETSAT Satellite Application Facility on Land Surface Analysis (LSA SAF). Research by Virgílio Bento was funded by the Portuguese Foundation for Science and Technology (SFRH/BD/52559/2014).

Author Contributions: All authors contributed equally to this work. J.P.M. designed the research, performed the radiative transfer simulations, analyzed the data, and wrote the major part of the manuscript. I.T. guided the whole study including research contents, methodology, etc. and made the greatest contribution to the revisions of the manuscript. V.B. provided ideas for the data analysis and revised the manuscript with a focus on literature research. C.C. contributed to the overall interpretation of the results and provided fundamental ideas for the research design. All the authors worked on the revisions of the manuscript.

Conflicts of Interest: The authors declare no conflict of interest.

References

1. Dirmeyer, P.A.; Cash, B.A.; Kinter, J.L.; Stan, C.; Jung, T.; Marx, L.; Towers, P.; Wedi, N.; Adams, J.M.; Altshuler, E.L.; et al. Evidence for enhanced land-atmosphere feedback in a warming climate. *J. Hydrometeorol.* **2012**, *13*, 981–995. [CrossRef]

2. Wan, Z.; Wang, P.; Li, X. Using MODIS land surface temperature and normalized difference vegetation index products for monitoring drought in the southern Great Plains, USA. *Int. J. Remote Sens.* **2004**, *25*, 61–72. [CrossRef]
3. Guillod, B.P.; Orlowsky, B.; Miralles, D.G.; Teuling, A.J.; Seneviratne, S.I. Reconciling spatial and temporal soil moisture effects on afternoon rainfall. *Nat. Commun.* **2015**, *6*, 6443. [CrossRef] [PubMed]
4. Kustas, W.P.; Norman, J.M. Use of remote sensing for evapotranspiration monitoring over land surfaces. *Hydrol. Sci. J.* **1996**, *41*, 495–516. [CrossRef]
5. Taylor, C.M.; Gounou, A.; Guichard, F.F.; Harris, P.P.; Ellis, R.J.; Couvreux, F.; De Kauwe, M. Frequency of sahelian storm initiation enhanced over mesoscale soil-moisture patterns. *Nat. Geosci.* **2011**, *4*, 430–433. [CrossRef]
6. Trigo, I.F.; Viterbo, P. Clear-sky window channel radiances: A comparison between observations and the ECMWF model. *J. Appl. Meteorol.* **2003**, *42*, 1463–1479. [CrossRef]
7. Trigo, I.F.; Boussetta, S.; Viterbo, P.; Balsamo, G.; Beljaars, A.; Sandu, I. Comparison of model land skin temperature with remotely sensed estimates and assessment of surface-atmosphere coupling. *J. Geophys. Res. Atmos.* **2015**, *120*, 12096–12111. [CrossRef]
8. Wang, A.; Barlage, M.; Zeng, X.; Draper, C.S. Comparison of land skin temperature from a land model, remote sensing, and in situ measurement. *J. Geophys. Res. Atmos.* **2014**, *119*, 3093–3106. [CrossRef]
9. Zheng, W.; Wei, H.; Wang, Z.; Zeng, X.; Meng, J.; Ek, M.; Mitchell, K.; Derber, J. Improvement of daytime land surface skin temperature over arid regions in the NCEP GFS model and its impact on satellite data assimilation. *J. Geophys. Res. Atmos.* **2012**, *117*, D06117. [CrossRef]
10. Caparrini, F.; Castelli, F.; Entekhabi, D. Variational estimation of soil and vegetation turbulent transfer and heat flux parameters from sequences of multisensor imagery. *Water Resour. Res.* **2004**, *40*, 1–15. [CrossRef]
11. English, S.J. The importance of accurate skin temperature in assimilating radiances from satellite sounding instruments. *IEEE Trans. Geosci. Remote Sens.* **2008**, *46*, 403–408. [CrossRef]
12. Ghent, D.; Kaduk, J.; Remedios, J.; Ardö, J.; Balzter, H. Assimilation of land surface temperature into the land surface model JULES with an ensemble Kalman filter. *J. Geophys. Res.* **2010**, *115*, D19112. [CrossRef]
13. Li, Z.L.; Tang, B.H.; Wu, H.; Ren, H.; Yan, G.; Wan, Z.; Trigo, I.F.; Sobrino, J.A. Satellite-derived land surface temperature: Current status and perspectives. *Remote Sens. Environ.* **2013**, *131*, 14–37. [CrossRef]
14. Trigo, I.F.; Peres, L.F.; DaCamara, C.C.; Freitas, S.C. Thermal land surface emissivity retrieved from SEVIRI/Meteosat. *IEEE Trans. Geosci. Remote Sens.* **2008**, *46*, 307–315. [CrossRef]
15. Freitas, S.C.; Trigo, I.F.; Macedo, J.; Barroso, C.; Silva, R.; Perdigão, R. Land surface temperature from multiple geostationary satellites. *Int. J. Remote Sens.* **2013**, *34*, 3051–3068. [CrossRef]
16. Sun, D.; Pinker, R.T. Estimation of land surface temperature from a geostationary operational environmental satellite (GOES-8). *J. Geophys. Res.* **2003**, *108*, 4326. [CrossRef]
17. Duguay-Tetzlaff, A.; Bento, V.; Göttsche, F.; Stöckli, R.; Martins, J.; Trigo, I.; Olesen, F.; Bojanowski, J.; da Camara, C.; Kunz, H. Meteosat land surface temperature climate data record: Achievable accuracy and potential uncertainties. *Remote Sens.* **2015**, *7*, 13139–13156. [CrossRef]
18. Jiménez-Muñoz, J.C. A generalized single-channel method for retrieving land surface temperature from remote sensing data. *J. Geophys. Res.* **2003**, *108*, 4688. [CrossRef]
19. Sobrino, J.A.; Jiménez-Muñoz, J.C. Land surface temperature retrieval from thermal infrared data: An assessment in the context of the Surface Processes and Ecosystem Changes Through Response Analysis (SPECTRA) mission. *J. Geophys. Res. D Atmos.* **2005**, *110*, 1–10. [CrossRef]
20. Freitas, S.C.; Trigo, I.F.; Bioucas-dias, J.M.; Göttsche, F. Quantifying the uncertainty of land surface temperature retrievals from SEVIRI/Meteosat. *IEEE Trans. Geosci. Remote Sens.* **2010**, *48*, 523–534. [CrossRef]
21. Wan, Z.; Dozier, J. A generalized split-window algorithm for retrieving land-surface temperature from space. *IEEE Trans. Geosci. Remote Sens.* **1996**, *34*, 892–905.
22. Mattar, C.; Durán-Alarcón, C.; Jiménez-Muñoz, J.C.; Santamaría-Artigas, A.; Olivera-Guerra, L.; Sobrino, J.A. Global atmospheric profiles from reanalysis information (GAPRI): A new database for earth surface temperature retrieval. *Int. J. Remote Sens.* **2015**, *36*, 5045–5060. [CrossRef]
23. Trigo, I.F.; Dacamara, C.C.; Viterbo, P.; Roujean, J.L.; Olesen, F.; Barroso, C.; Camacho-de-Coca, F.; Carrer, D.; Freitas, S.C.; García-Haro, J.; et al. The satellite application facility for land surface analysis. *Int. J. Remote Sens.* **2011**, *32*, 2725–2744. [CrossRef]

24. De La Taille, L.; Rota, S.; Hartley, C.; Stuhlmann, R. Meteosat third generation programme status. In Proceedings of the Annual EUMETSAT Meteorological Satellite Conference, Toulouse, France, 21–25 September 2015.
25. Yu, Y.; Privette, J.L.; Pinheiro, A.C. Evaluation of split-window land surface temperature algorithms for generating climate data records. *IEEE Trans. Geosci. Remote Sens.* **2008**, *46*, 179–192. [CrossRef]
26. Brutsaert, W. *Hydrology: An Introduction*; Cambridge Univ. Press: Cambridge, UK, 2005.
27. Crago, R.D.; Qualls, R.J. Use of land surface temperature to estimate surface energy fluxes: Contributions of Wilfried Brutsaert and collaborators. *Water Resour. Res.* **2014**, *50*, 3396–3408. [CrossRef]
28. Hulley, G.C.; Hook, S.J.; Abbott, E.; Malakar, N.; Islam, T.; Abrams, M. The ASTER Global Emissivity Dataset (ASTER GED): Mapping earth's emissivity at 100 meter spatial scale. *Geophys. Res. Lett.* **2015**, *42*, 7966–7976. [CrossRef]
29. Bulgin, C.E.; Embury, O.; Merchant, C.J. Sampling uncertainty in gridded sea surface temperature products and Advanced Very High Resolution Radiometer (AVHRR) Global Area Coverage (GAC) data. *Remote Sens. Environ.* **2016**, *177*, 287–294. [CrossRef]
30. Berk, A.; Anderson, G.P.; Bernstein, L.S.; Acharya, P.K.; Dothe, H.; Matthew, M.W.; Adler-Golden, S.M.; Chetwynd, J.H., Jr.; Richtsmeier, S.C.; Pukall, B.; et al. MODTRAN4 radiative transfer modeling for atmospheric correction. *Proc. SPIE* **1999**, *3756*, 348–353.
31. Borbas, E.E.; Seemann, S.W.; Huang, H.L.; Li, J.; Menzel, W.P. Global profile training database for satellite regression retrievals with estimates of skin temperature and emissivity. In Proceedings of International TOVS Study Conference-XIV, Beijing, China, 25–31 May 2005.
32. Wan, Z. New refinements and validation of the MODIS land-surface temperature/emissivity products. *Remote Sens. Environ.* **2008**, *112*, 59–74. [CrossRef]
33. Stull, R.B. *An Introduction to Boundary Layer Meteorology*; Kluwer Academic: Dordrecht, The Netherlands, 1988; p. 666.
34. Rodgers, C.D. *Inverse Methods for Atmospheric Sounding: Theory and Practice*; World Scientific: Hackensack, NV, USA, 2000; Volume 2.
35. Maddy, E.S.; Member, A.; Barnet, C.D. Vertical resolution estimates in version 5 of AIRS operational retrievals. *IEEE Trans. Geosci. Remote Sens.* **2008**, *46*, 2375–2384. [CrossRef]
36. Martins, J.P.A.; Teixeira, J.; Soares, P.M.M.; Miranda, P.M.A.; Kahn, B.H.; Dang, V.T.; Irion, F.W.; Fetzer, E.J.; Fishbein, E. Infrared sounding of the trade-wind boundary layer: AIRS and the RICO experiment. *Geophys. Res. Lett.* **2010**, *37*. [CrossRef]
37. Yu, Y.; Tarpley, D.; Privette, J.L.; Goldberg, M.D.; Rama Varma Raja, M.K.; Vinnikov, K.Y.; Xu, H. Developing algorithm for operational GOES-R land surface temperature product. *IEEE Trans. Geosci. Remote Sens.* **2009**, *47*, 936–951.
38. Jiménez-Muñoz, J.C.; Sobrino, J.A. Error sources on the land surface temperature retrieved from thermal infrared single channel remote sensing data. *Int. J. Remote Sens.* **2006**, *27*, 999–1014. [CrossRef]
39. Trigo, I.F.; Monteiro, I.T.; Olesen, F.; Kabsch, E. An assessment of remotely sensed land surface temperature. *J. Geophys. Res.* **2008**, *113*. [CrossRef]

Remote Sens. **2015**, *7*, 13139-13156; doi:10.3390/rs71013139

OPEN ACCESS

remote sensing

ISSN 2072-4292

www.mdpi.com/journal/remotesensing

Article

Meteosat Land Surface Temperature Climate Data Record: Achievable Accuracy and Potential Uncertainties

Anke Duguay-Tetzlaff [1,*], Virgílio A. Bento [2,†], Frank M. Göttsche [3,†], Reto Stöckli [1,†], João P. A. Martins [2,4,†], Isabel Trigo [2,4,†], Folke Olesen [3,†], Jędrzej S. Bojanowski [1,†], Carlos da Camara [4,†] and Heike Kunz [1]

[1] Federal Office of Meteorology and Climatology MeteoSwiss, Operation Center 1, CH-8058 Zurich-Airport, Switzerland; E-Mails: reto.stoeckli@meteoswiss.ch (R.S.); jedrzej.bojanowski@meteoswiss.ch (J.S.B.); heike.kunz@meteoswiss.ch (H.K.)

[2] Instituto Dom Luiz, University of Lisbon, IDL, Campo Grande, Ed C1, 1749-016 Lisbon, Portugal; E-Mails: vabento@fc.ul.pt (V.A.B.); joao.p.martins@ipma.pt (J.P.A.M.); isabel.trigo@ipma.pt (I.T.);

[3] Karlsruhe Institute of Technology, KIT, Hermann-von-Helmholtz-Platz 1, D-76344 Eggenstein-Leopoldshafen, Germany; E-Mails: frank.goettsche@kit.edu (F.M.G.); folke.olesen@kit.edu (F.O.)

[4] Instituto Português do Mar e da Atmosfera, I.P., Rua C do Aeroporto, 1749-077 Lisbon, Portugal; E-Mail: cdcamara@fc.ul.pt

† These authors contributed equally to this work.

* Author to whom correspondence should be addressed; E-Mail: anke.tetzlaff@meteoswiss.ch; Tel.: +41-58-460-9645; Fax: +41-58-460-9001.

Academic Editors: George P. Petropoulos, Richard Müller and Prasad S. Thenkabail

Received: 29 July 2015 / Accepted: 25 September 2015 / Published: 2 October 2015

Abstract: The European Organization for the Exploitation of Meteorological Satellites' (EUMETSAT) Meteosat satellites provide the unique opportunity to compile a 30+ year land surface temperature (LST) climate data record. Since the Meteosat instrument on-board Meteosat 2–7 is equipped with a single thermal channel, single-channel LST retrieval algorithms are used to ensure consistency across Meteosat satellites. The present study compares the performance of two single-channel LST retrieval algorithms: (1) A physical radiative transfer-based mono-window (PMW); and (2) a statistical mono-window model (SMW). The performance of the single-channel algorithms is assessed using a database of synthetic radiances for a wide range of atmospheric profiles and surface variables. The two single-channel algorithms are evaluated against the commonly-used generalized split-window

(GSW) model. The three algorithms are verified against more than 60,000 LST ground observations with dry to very moist atmospheres (total column water vapor (TCWV) 1–56 mm). Except for very moist atmospheres (TCWV > 45 mm), results show that Meteosat single-channel retrievals match those of the GSW algorithm by 0.1–0.5 K. This study also outlines that it is possible to put realistic uncertainties on Meteosat single-channel LSTs, except for very moist atmospheres: simulated theoretical uncertainties are within 0.3–1.0 K of the *in situ* root mean square differences for TCWV < 45 mm.

Keywords: thermal infrared; LST; Meteosat; single channel; climate data record; radiative transfer

1. Introduction

Land surface temperature (LST) is an important climate state variable. Precise estimates of the radiative surface skin temperature are essential to compute the surface radiative and sensible heat balance [1]. Moreover, LST is a key variable for a wide range of applications related to land surface processes, such as drought [2] and evaporation monitoring [3]. Satellite-based LSTs are important for the evaluation of surface-emitting temperatures in climate models at various time scales [1]. Ideally, they can also be assimilated into land surface models [4–6] to improve numerical weather and climate model predictions.

This wide range of applications makes a long-term homogeneous LST climate data record (CDR) highly desirable [7]. Large-scale LST can only be measured by satellite instruments [8] and is best represented by measurements of geostationary satellite sensors, as it is subject to strong diurnal variation [9,10]. Geostationary LST climate data records (CDRs) are available from the International Satellite Cloud Climatology Project (ISCCP) [11] and the Pathfinder Atmospheres-Extended dataset (PATMOS-x) [8]. The global ISCCP LST CDR has several limitations, as the primary goal of the ISCCP analysis was the retrieval of cloud properties and not LST. The strongest limitation is the very coarse 30 km spatial resolution and, to a lesser extent, the 3-h temporal resolution [11]. Moreover, the original ISCCP retrieval assumes that all surfaces behave like a black body with unit emissivity, which can lead to significant LST retrieval errors, particularly in dry regions (e.g. [12]). The PATMOS-x geostationary LST CDR is only available for the Geostationary Operational Environmental Satellite (GOES) field of view (North and South America).

Starting in 1983, the European's Organization for the Exploitation of Meteorological Satellites (EUMETSAT) Meteosat First (MFG) and Second Generation (MSG) satellites have provided the unique opportunity to compile a 30+ year LST CDR with a 30-min temporal and 5-km spatial resolution over Africa and Europe. Since the Meteosat Visible and Infra-Red Imager (MVIRI) on-board Meteosat 2–7 is equipped with a single thermal infrared channel, single-channel LST retrieval models can ensure consistency across all Meteosat satellites. A consistent approach maximizes long-term and inter-satellite consistency [8].

Most state-of-the-art satellite-based LST retrieval models, such as the Meteosat LST model from the Satellite Application Facility on Land Surface Analysis (LSA SAF), employ the generalized split-window model (GSW) [13–15], where atmospheric absorption is estimated through a two-channel regression of

top-of-atmosphere (TOA) brightness temperatures. This atmospheric correction is less dependent on atmospheric ancillary data than single-channel LST models, which depend completely on ancillary data from numerical weather prediction (NWP) models to estimate the atmospheric state. They range from statistical mono-window models (SMW), which use the observed 11 μm radiance, the total column water vapor (TCWV) from NWP models and *a priori* fitted LST model parameters [16,17] to physical mono-window models (PMW), which are based on radiative transfer modelling [8,18,19,]. PMWs require significantly more processing time than SMWs, as PMW algorithms run radiative transfer models for each satellite acquisition, while SMW algorithms estimate the correction term using a pre-computed statistical relationship. Reported accuracies are 1–2 K for GSW [12,20,21], 2.5 K or less for PMW [8,19] and 2–4 K for SMW [22]. Those performance metrics from the literature cannot be compared, since they refer to different satellite sensors with distinct viewing geometries, with variations in instrument calibration and different validation data for a physical parameter (LST), which is highly variable in time and space [8,10,23]. In order to investigate the achievable accuracy of Meteosat single-channel LST models, the models have to be exercised in a comparable setting. This study tries to answer the following questions: To what extent can a single-channel LST model achieve the accuracy of a two-channel LST model? Does a PMW outperform an SMW? Can we characterize uncertainties for single-channel Meteosat LSTs?

To address those questions, we compare SMW, PMW and GSW using identical satellite observations from MSG. The evaluation is based on more than 60,000 *in situ* LST measurements from four dedicated LST validation stations operated by the Karlsruhe Institute of Technology (KIT). The stations are located in different climate zones and include dry to very moist atmospheres. Furthermore, we perform a series of sensitivity analyses to test the robustness of single-channel LST models to input uncertainties. The characterization of input uncertainty and its propagation towards the final LST retrievals is important for the estimation of product uncertainties, which can ultimately be used as quality indicators by users. This study is unique in that it compares PMW, SMW and GSW LST retrievals from identical satellite acquisitions with a large number of *in situ* measurements across different climate zones.

2. Data and Methods

2.1. Satellite Data

We used data from the EUMETSAT MSG satellite. The MSG satellite carries the Spinning Enhanced Visible and Infrared Imager (SEVIRI), a radiometer that measures the Earth every 15 min with a footprint of about 3 km at nadir. MSG is positioned at 0° longitude over the equator and views KIT's four validation stations at low (25°, Dahra site) to moderate satellite viewing angles (45°, Evora site). LST was estimated in this study from TOA radiances of SEVIRI's 10.8 μm channel. The standard calibration provided by EUMETSAT is applied in the study to generate TOA radiances and brightness temperatures.

The LSA SAF team provided MSG 2 TOA 10.8 μm brightness temperatures, the LSA SAF cloud mask, the LSA SAF surface emissivity and the LSA SAF generalized split-window (GSW) LST retrieval on a 3 × 3 pixel window centered on the ground stations for the year 2010. The extracted time series had a temporal resolution of 15 minutes. We collocated satellite data and available KIT *in situ* measurements

from the year 2010 and ran a PMW and an SMW model using the TOA 10.8-μm brightness temperature together with the LSA SAF surface emissivity. We only considered satellite data that were classified as cloud free in the entire 3 × 3 pixel window by the cloud masking. Overall, this analysis included about 60,000 collocated *in situ* and satellite observations. The *in situ* data, as well as the different LST models are described in detail in the following sections.

2.2. Generalized Split-Window Model

The LSA SAF applies the GSW model with a formulation similar to that proposed by Wan and Dozier [13,14] and adapted by Trigo *et al.* [15] and Freitas *et al.* [12] to the SEVIRI split-window channels. LST is obtained through a semi-empirical regression of SEVIRI 10.8- and 12.0-μm TOA brightness temperatures, where the correction of atmospheric influences is based on the different absorption of two adjacent infra-red bands [12]. The LST is estimated through a linear regression of the split-window TOA brightness temperatures. The regression coefficients depend explicitly on the land surface emissivity and implicitly on the TCWV obtained from the European Centre for Medium-Range Weather Forecasts (ECMWF) operational forecasts and the satellite view zenith angles (VZA) [15]. The surface emissivity is provided for the split-window channels using a method based on the fraction of vegetation cover (FVC), also estimated by the LSA SAF from seviri visible and near-infrared channels [12,24]. Thus, the emissivity computation is driven by the vegetation state and takes into account daily FVC estimates from SEVIRI measurements and a global land cover classification [12,24].

Reported uncertainties for the LSA SAF LST dataset are in the range of 1–2 K [12], except for very moist atmospheres. A detailed description of the LSA SAF model can be found in the corresponding Algorithm Technical Base Document [15]; see also [12]. We used LST data from the LSA SAF archive for model inter-comparisons, which we label "GSW" LST in the following.

2.3. Physical Mono-Window Model

We applied a PMW model to the Meteosat time series described in Section 2.1. The PMW model used here is based on radiative transfer runs. Radiative transfer models can be used to estimate the upward and downward atmospheric path radiance ($L^{\uparrow}$, $L^{\downarrow}$) and the atmospheric transmittance (τ) in the thermal infrared for a specific atmospheric profile [18]. The downward atmospheric path radiance ($L^{\downarrow}$) is the hemispherically-averaged downward radiance. Approximating the Earth's surface as a Lambertian emitter-reflector and neglecting atmospheric scattering, the radiance $L_c(\theta)$, recorded in channel c of a sensor onboard a satellite observing the Earth's surface under view zenith angle θ may be written as (e.g., [25]):

$$L_c(\theta) = \varepsilon_c B_c(T_s)\tau_c(\theta) + L_c^{\uparrow}(\theta) + L_c^{\downarrow}(1-\varepsilon_c)\tau_c(\theta) \quad (1)$$

where ε_c and T_s denote land surface emissivity and LST, respectively. The calibrated Planck function $B_c(T_s)$ provides the radiance emitted by a blackbody at temperature T_s in channel c. The parameters τ_c, $L_c^{\uparrow}(\theta)$ and $L_c^{\downarrow}$ in Equation (1) are the corresponding surface to top of the atmosphere (TOA) transmittance and the atmospheric upward and downward radiances, respectively. These three parameters can be estimated based on the atmospheric humidity and temperature profiles. For a channel of finite spectral band width, the calibrated Planck function in the frequency domain may be approximated as:

$$B_c(T_s) \approx \frac{c_1 \nu_c^3}{\exp\left(\frac{c_2 \nu_c}{\alpha T_s + \beta}\right) - 1} \quad (2)$$

where c_1, c_2 are constants and α, β and ν_c depend on the spectral characteristics of the channel to be used. Inverting Equations (1) and (2) (e.g., [21,25]), the thermal radiance $L_c(\theta)$ measured at the sensor level can then be used to estimate LST:

$$T_s \approx \left(\frac{c_2 \nu_c}{\ln\left(\frac{c_1 \nu_c^3 \tau_c(\theta) \varepsilon_c}{L_c(\theta) - L_c^{\uparrow}(\theta) - L_c^{\downarrow}(1 - \varepsilon_c)\tau_c(\theta)} + 1\right)} - \beta \right) / \alpha \quad (3)$$

The PMW LST in this study was calculated with Equation (3) for SEVIRI 10.8-µm clear-sky TOA brightness temperatures described in Section 2.1, together with surface emissivities (ε_c) taken from the operational LSA SAF dataset [26]. Values of $L_c^{\uparrow}(\theta)$, $L_c^{\downarrow}$ and $\tau_c(\theta)$ were obtained via the Radiative Transfer for the Television Infrared Observation Satellite Operational Vertical Sounder code (RTTOV, Version 11.2), which is a fast radiative transfer model used operationally at the ECMWF [27]. RTTOV is significantly faster than the commonly-used Moderate Resolution Atmospheric Transmission (MODTRAN) line-by-line radiative transfer code [28]. It uses pre-computed transmittance look-up-tables (LUTs) calculated from a spectroscopic database [29]. PMWs require radiative transfer runs during the satellite data processing. For large data processing, it is hence crucial to run a fast radiative transfer model. Bento [30] has recently compared simulated MODTRAN and RTTOV TOA brightness temperatures and reports an overall bias of about 0.2 K in the SEVIRI spectral range, which is close to the SEVIRI instrumental noise.

RTTOV runs performed in this study used atmospheric profiles (temperature and specific humidity) from the ECMWF ERA-Interim reanalysis dataset as input [31], which are available 6-hourly at a spatial resolution of about 75 km. RTTOV simulations for model atmospheres with 21 pressure levels (1000–1 hPa) were performed using the ERA-Interim profiles closest in time and space to each satellite observation.

2.4. Statistical Mono-Window Model

The third LST model we tested is an SMW model. SMWs consist of empirical approaches that relate TOA brightness temperatures of a single atmospheric window channel to LST [16,22,25], generally via a simple linear regression. Here, we linearized the radiative transfer equation, while at the same time maintaining an explicit dependency on surface emissivity:

$$T_s = A \frac{T_b(\theta)}{\varepsilon_c} + B \frac{1}{\varepsilon_c} + C \quad (4)$$

where T_b is the TOA brightness temperature in channel c and ε_c stands for the corresponding spectral surface emissivity.

We estimated the regression coefficients A, B and C for different classes of TCWV and VZA. Following Freitas *et al.* [12] for the operational LSA SAF GSW model and Freitas *et al.* [22] for a single-channel LST model for the GOES satellite series, the calibration/validation of Equation (4) made use of synthetic radiances obtained with the radiative transfer model MODTRAN 4.0. We selected MODTRAN and not RTTOV to tune the SMW model, as we assume the line-by-line MODTRAN model to be slightly more

accurate than the "broad band" RTTOV model. In contrast to the PMW model, the processing speed of the radiative transfer model is more or less irrelevant for SMW, as the radiative transfer simulations are only computed once to establish the model coefficients.

MODTRAN simulations were performed for a range of clear sky atmospheric profiles and surface variables representative for global conditions [32]. The synthetic radiances were split into two subsets: (1) A training dataset for determining the statistical mono-window coefficients (Equation 4); and (2) an independent dataset for model verifications. The training dataset comprises 116 carefully-chosen profiles to encompass the bivariate distribution of TCWV and LST. A total of over 845,000 simulations was obtained by varying the viewing geometry and surface conditions for each profile over the following ranges: (1) VZA from 0° to 75°; (2) surface emissivity between 0.926 and 0.998; and (3) surface temperatures ranging from near surface air temperature minus 15 K to near surface air temperature plus 15 K. Following the approach of Freitas *et al.* [22], coefficients A, B and C in Equation (4) were then determined for 8 different TCWV classes (0 cm–6 cm in steps of 7.5 mm) and 15 VZA classes (0°–75° in steps of 5°).

We applied the above described SMW model to the extracted SEVIRI 10.8-μm clear-sky TOA brightness temperature time series. As for the PMW and GSW model, surface emissivities (ε_c) for the SMW are taken from the operational LSA SAF dataset [26].

2.5. Theoretical Uncertainty Characterization

Potential LST retrieval errors were assessed through the use of the synthetic validation database described in Section 2.4, which contained over 15,500 independent simulations. For the uncertainty analysis presented in this study, we followed the approach of Freitas *et al.* [12]. We provided TOA brightness temperatures, surface and atmospheric information from the database as input to the SMW and PMW model; the calculated LST output was then compared with the corresponding ("true") surface temperature from the database. In addition to the model error, we assessed the sensitivity of the SMW and PMW to radiometric noise, uncertainty in surface emissivity and NWP by superimposing artificial errors to PMW and SMW inputs.

The value used for SEVIRI 10.8-μm radiometric noise is based on radiometric performances for SEVIRI IR 10.8 μm compared to the Infrared Atmospheric Sounding Interferometer (IASI) (bias < 0.2 K) [33]. Values for noise in brightness temperature were generated from a uniform random distribution within the conservative interval (−0.3 K, 0.3 K).

For the estimation of the surface emissivity error, we took into account that bare ground and semi-arid surfaces (generally with lower emissivities) present higher variability and, therefore, higher uncertainty than areas covered by vegetation. As such, emissivity uncertainties used in this study were obtained from random uniform distributions within the intervals (−0.04, 0.04) for $\varepsilon_c < 0.95$, (−0.02, 0.04) for $0.95 \leq \varepsilon_c < 0.98$ and (−0.01, 0.01) for $\varepsilon_c \geq 0.98$ The rationale for this choice is based on emissivity variability for bare ground surfaces ($\varepsilon_c < 0.95$), sparsely- ($0.95 \leq \varepsilon_c < 0.98$) and densely- ($\varepsilon_c \geq 0.98$) vegetated areas [12].

The PMW model requires a characterization of the errors associated with the atmospheric profiles. Since these are obtained from ERA-Interim nearest in space and time to the satellite observation, we assume that the uncertainty in collocation may be used as a measure of the profile uncertainty. Thus, the

impact of profile errors on retrieved LST values was estimated by replacing the profiles at hour h by the corresponding ones at hour h + 6. A similar procedure was used to determine the impact of TCWV errors on LST estimates from the SMW. It is worth recalling that TCWV is an implicit input to the SMW: This variable is used to determine the regression coefficients (Equation (4)). Therefore, and as explained in detail in Freitas *et al.* [12], studies of the impact of TCWV uncertainties on LST need to combine: (i) The effect on the LST estimate due to the choice of the wrong set of coefficients; and (ii) the probability of that event.

2.6. Ground-Based LST Measurements

The KIT operates four permanent validation stations for satellite-based LST retrieval. The stations, being part of LSA-SAF's validation effort and supported by EUMETSAT, were specifically chosen and designed to validate LST derived from MSG/SEVIRI. They are located in large homogenous areas within the field of view of the METEOSAT satellites and lie in different climate zones, which provides a broad range of atmospheric conditions for product validation [34]. The locations of the four validation stations on the SEVIRI Earth disk are indicated in Figure 1. An overview of the KITs validation sites is provided in Table 1.

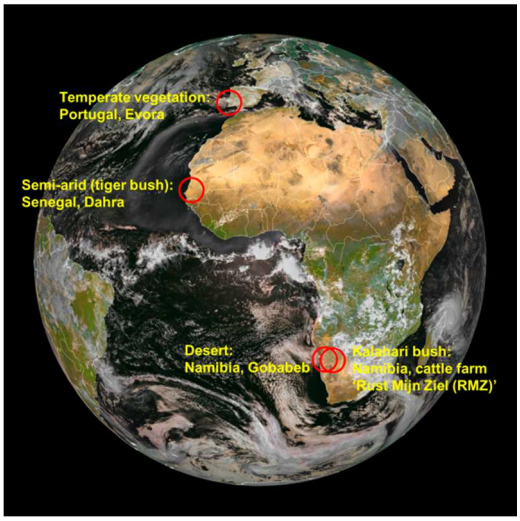

Figure 1. Locations of the Karlsruhe Institute of Technology's (KIT) validation stations on the Meteosat Second Generation (MSG)/Spinning Enhanced Visible and Infrared Imager (SEVIRI) disk.

In principle, LST datasets can readily be validated with ground-truth radiometric measurements. However, this so-called 'temperature-based validation' is largely complicated by the spatial scale mismatch between satellite- and ground-based sensors: areas observed by ground radiometers usually cover about 10 m^2, whereas satellite measurements in the thermal infrared typically cover between 1 km^2 and 100 km^2 [34]. Furthermore, natural land covers and the corresponding land surface temperatures are spatially quite heterogeneous: therefore, for validation measurements to be representative for satellite-derived LST, they have to be performed in areas that are homogenous at the satellite pixel scale. The size of the area that needs to be viewed by the validation instrument at the ground depends on the within-pixel variability of the surface and on how well measurements of several "end members" can be

mixed in order to obtain a representative value for the satellite pixel. This so-called end-member-cover method is based on a linear spectral mixing approach and assumes that the total IR radiance emitted by the land surface within a satellite pixel can be reasonably well approximated by a linear mixture of the IR radiance emitted by the relevant surface cover types within that area [35]. The mixing of measurements obtained for different end-members requires information on their respective fractions within the sensor's field of view and also on scene emissivity [26,36,37]. At KIT's validation sites, the relevant spectral end-members (e.g., trees, grassland and background soil) were determined from an independent component analysis of high-resolution satellite data (visible and near-infrared). The fractional coverages of the determined end-members were then obtained by land cover classification [35].

Table 1. Overview of KITs validation stations. TCWV, total column water vapor.

	Dahra	**RMZ**	**Gobabeb**	**Evora**
Location	Senegal Lat.: 15.402336 Lon.: −15.432744	Namibia Lat.: −23.010532 Lon.:18.352897	Namibia Lat.: −23.550956 Lon.: 15.05138	Portugal Lat.: 38.540244 Lon.: −8.003368
Elevation	90 m	1450 m	406 m	230 m
Climate Zone	Tropical Wet-Dry	Steppe	Desert	Mediterranean
TCWV 2010	17 to 56 mm	2 to 28 mm	1 to 38 mm	2 to 43 mm
Vegetation	Grassland; 96% grass, 4% tree	Savanna; 85% grass/soil, 15% tree	Baren; 32% tree, 68% grass	Woody savanna with isolated groups of evergreen oak trees

The main instrument for the *in situ* determination of LST at KIT's validation stations is the precision radiometer "KT15.85 IIP" produced by Heitronics GmbH, Wiesbaden, Germany. KT15.85 IIP radiometers measure thermal infra-red radiance between 9.6 μm and 11.5 μm, have a temperature resolution of 0.03 K and an accuracy of ±0.3 K over the relevant temperature range [38]. The KT15.85 IIP has a drift of less than 0.01% per month: The high stability is achieved by linking the radiance measurements via beam-chopping (a differential method) to internal reference temperature measurements and was confirmed by a long-term parallel run with the self-calibrating radiometer "RotRad" from Commonwealth Scientific and Industrial Research Organisation (CSIRO), which is continuously stabilized with 2 blackbodies [37]. The parallel run at the Evora site started in April 2005; a year later, the agreement between the instruments was still excellent (correlation 0.99). Due to the KT-15.85 IIP's narrow spectral response function and the small distance between the radiometers and the surface atmospheric attenuation of the surface-leaving, thermal infrared radiation is negligible. However, the measurements of the surface-observing KT-15.85 IIPs contain radiance emitted by the surface (*i.e.*, the target signal), as well as reflected downward IR radiance from the atmosphere, which needs to be corrected for [34]. Therefore, at each station, an additional KT-15.85 IIP measures downward longwave IR radiance from the atmosphere at 53° VZA: measurements under that specific zenith angle are directly related to downward hemispherical radiance [39], so that no ancillary data for deriving ground truth LST are needed.

Accurate estimations of land surface emissivity (LSE) are essential for obtaining satellite LST products, but also for limiting the uncertainty of ground-based LST estimates. Especially sites with larger fractions of bare ground are prone to be misrepresented in satellite-retrieved LSEs: Comparisons with *in situ* LSE revealed that over arid regions, satellite-retrieved LSEs differ by more than 3% [36]. Since for

vegetated sites, LSE is a dynamic quantity, we use LSA-SAF's daily LSE to derive *in situ* LST from the *in situ* radiance measurements at Dahra (Senegal, tiger bush, 45 m a.s.l.), Rust Mijn Ziel (RMZ) (Namibia, Kalahari bush, 1450 m a.s.l.) and Evora (Portugal, cork-oak tree forest, 230 m a.s.l.). *In situ* LST at the desert site Gobabeb (Namibia, gravel plains, 450 m a.s.l.) is derived using a static emissivity obtained from *in situ* measurements [36].

3. Results and Discussions

3.1. Theoretical Uncertainty Analysis

The total impact of model and input uncertainties, including uncertainties in surface emissivity, NWP and sensor calibration, measured as the root mean square difference (RMSD) of retrieved LST *versus* the "true" surface temperature in the database, is presented in Figure 2 for different values of VZA and TCWV. RMSD and bias obtained for the validation database are shown in Table 2.

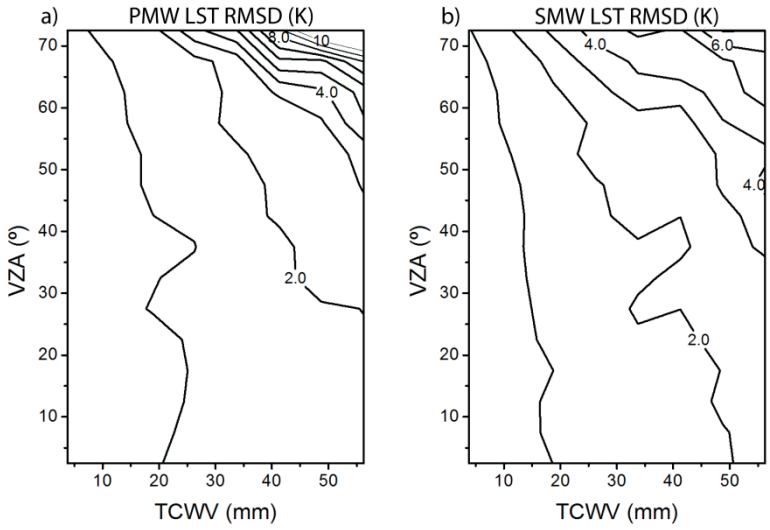

Figure 2. Theoretical uncertainty for MSG/SEVIRI LST estimates. (**a**) Physical radiative transfer-based mono-window model (PMW); (**b**) statistical mono-window model (SMW). The values are the root mean square differences, assuming model and input uncertainties. VZA, satellite viewing angle.

The 2 K target accuracy (RMSD) of the LSA SAF LST dataset is reached for the majority of angles and TCWV classes for PMW and SMW, degrading into larger errors for very moist atmospheres with high angles, *i.e.*, for very large optical paths. The slopes of the lines in Figure 2 suggest that TCWV errors are most relevant for low-to-moderate view angles. For very moist atmospheres (TCWV > 50 mm) and high viewing angles (VZA > 55 mm), the SMW performed slightly better than the PMW. We hypothesize that this reflects the implicit sensitivity of the PMW to the NWP input: Freitas *et al.* [12] showed that uncertainties in atmospheric profiles can have a strong impact on LST retrievals. While SMWs only require TCWV as input, PMWs require atmospheric temperature and water vapor profiles, which can introduce additional uncertainties, especially for very moist atmospheres. We found that LST errors associated with emissivity uncertainties are expected to be within 1.0 K and 2.8 K in 90% of the

estimates obtained with the SWM and PWM model, respectively. However, the impact of emissivity in both models is much smaller under moist atmospheres.

Table 2. Theoretical uncertainty for MSG/SEVIRI LST estimates for the PMW and SMW. RMSD and bias associated with both model and input uncertainty.

	PMW		SMW	
	RMSD (K)	**BIAS (K)**	**RMSD (K)**	**BIAS (K)**
TCWV ≤ 45 mm	1.6	−0.2	1.6	−0.1
TCWV > 45 mm	3.3	−1.1	3.4	−0.6

The PMW and SMW uncertainties we simulated for TCWVs ≤ 45 mm (RMSD of 1.6 K) more or less correspond to the uncertainties reported by Freitas *et al.* [12] for GSW. For moister atmospheres (TCWVs > 45 mm) the PMW and SMW uncertainties (RMSD of up to 10 K and 6 K, respectively) significantly exceed the simulated GSW uncertainties (max. error about 4.5 K; Freitas *et al.* [12]), particularly for high VZAs. This very likely demonstrates the different sensitivity of the single-channel and GSW models to uncertainties related to inaccurate NWP input. Single-channel models rely entirely on NWP data to estimate the atmospheric state, while the two split-window channels provide additional information about the atmospheric absorption for the GSW model [8].

3.2. Ground-Based Validation

For a range of atmospheric conditions, the two investigated single-channel LST models match the accuracy of the GSW model (Figure 3). A summary of the bias and the RMSD associated with the different LST models is provided in Tables 3 and 4.

For dry to medium-moist atmospheres (TCWV up to 45 mm), RMSDs of the PMW and the SMW model ranged between 1.8 K and 2.6 K (Table 3). This is close to the 2 K target accuracy of the GSW-based LSA SAF dataset. For the Evora and RMZ sites, the PMW model matched the accuracy of the GSW with RMSDs of 1.9 K (PMW) and 1.9–2.0 K (GSW) and had an absolute bias < 1 K. For the sites Gobabeb and Dahra, the PMW (RMSD 1.8 K and 2.6 K) was slightly less accurate than the GSW (RMSD 1.5 K and 2.3 K), while the SMW's RMSD was up to 0.5 K larger (TCWV up to 45 mm; Table 3). Yu *et al.* [21] have recently compared PMW and GSW LSTs from the Landsat satellite against 41 ground observations from the Surface Radiation (SURFRAD) Budget Network in moderate climate zones. They have reported the highest accuracy for the PMW with a difference in RMSD of only 0.1 K compared to the GSW: Our analysis does not confirm this finding. We show that PMW agrees with GSW to within 0.1–0.5 K for most atmospheric conditions tested here.

In Gobabeb, RMZ and Dahra, the PMW and SMW performed very similarly (ΔRMSD 0.2 K) for TCWV < 45 mm. In Evora, the PMW had a 0.6 K lower RMSD and 0.7 K lower bias compared to the SMW. At very high TCWVs (>45 mm), we observe a 1 K higher RMSD for the PMW compared to the SMW at Dahra. Hence, the computationally-expensive PMW model outperforms the SMW only at one out of four investigated stations.

Observed RMSD matches the theoretical uncertainties (Section 3.1) to within 0.3–1 K for dry to medium-moist atmospheres (Tables 2 and 3). Slightly larger RMSDs can reflect uncertainty and scaling differences of the ground measurements not included in the theoretical uncertainty analysis.

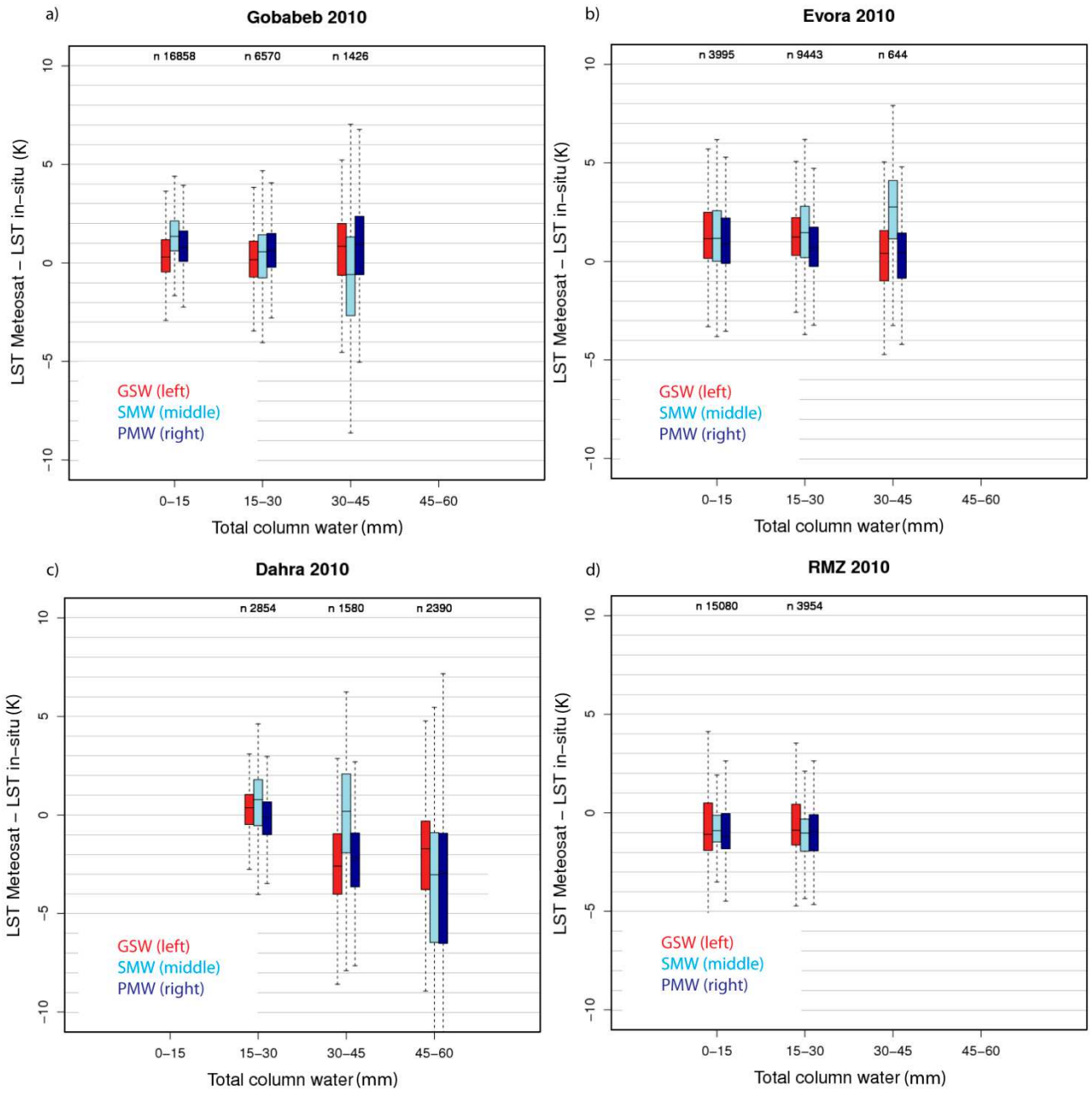

Figure 3. Comparison of LST between *in situ* measurements from the KIT sites and Meteosat-based retrievals for different TCWV classes. The boxplots show the median, the first and third quartile with whiskers at the 95th and fifth percentiles. GSW: the Satellite Application Facility on Land Surface Analysis's (LSA SAF) operational GSW. (**a**) KIT Gobabeb station; (**b**) KIT Evora station; (**c**) KIT Dahra station; (**d**) KIT RMZ station.

For very moist atmospheres, which are only encountered at the Dahra station, we observed a distinctly higher RMSD (Δ2.9 K–Δ1.9 K) and bias (Δ2.1–Δ0.8 K) for the two single-channel models compared to the GSW (Table 4) and a higher RMSD (>3 K) compared to the theoretical error analysis (Figure 2). In addition, we observed different model performances for selected TCWV classes and sites (Figure 3). We investigated those differences and provide possible explanations in the following sections.

Table 3. Statistics for the comparison of LST between *in situ* measurements and the operational LSA SAF dataset for dry to medium-moist atmospheres (TCWV ≤ 45 mm).

TCWV ≤ 45 mm	GSW		PMW		SMW	
	RMSD (K)	BIAS (K)	RMSD (K)	BIAS (K)	RMSD (K)	BIAS (K)
Gobabeb	1.5	0.4	1.8	0.8	2.0	0.9
Evora	2.0	1.2	1.9	0.7	2.5	1.4
Dahra	2.3	−0.8	2.6	−1.2	2.4	0.4
RMZ	1.9	−0.5	1.9	−0.8	1.7	−0.8

Table 4. Statistics for the comparison of LST between *in situ* measurements and the operational LSA SAF dataset for very moist atmospheres (TCWV > 45 mm) experienced at the KIT 'Dahra' station.

TCWV > 45 mm	GSW		PMW		SMW	
	RMSD (K)	BIAS (K)	RMSD (K)	BIAS (K)	RMSD (K)	BIAS (K)
Dahra	3.4	−2.2	6.3	−4.3	5.3	−3.0

3.2.1. Gobabeb Station

For the desert station Gobabeb mono-window LSTs met the LSA SAF target accuracy requirement (RMSD ≥ 2 K and bias < 1 K; Table 3 and Figures 3a and 4).

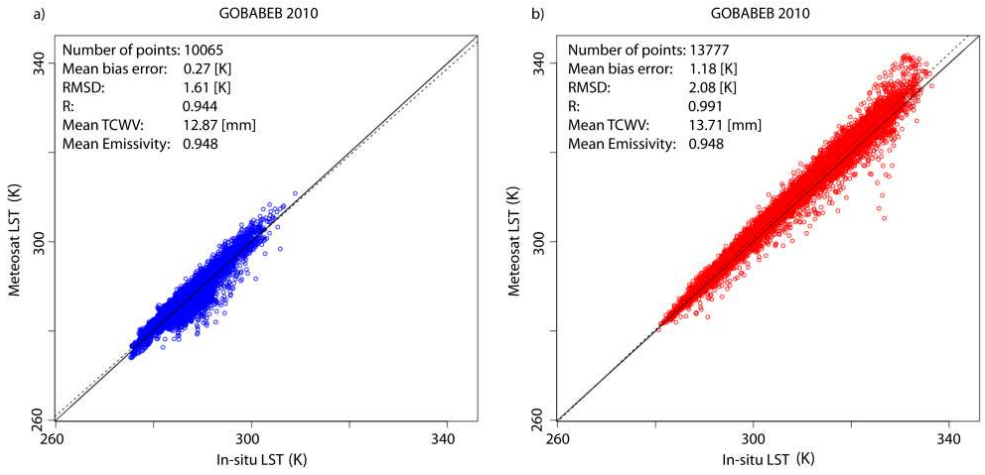

Figure 4. Comparison between *in situ* LST (KIT Gobabeb station, 2010) and Meteosat LST from the PMW for TCWVs < 35 mm: (**a**) Nighttime; (**b**) daytime.

Due to the exceptionally wet January/February and October/November 2010, the presented analysis included a large number of observations for a wide range of atmospheric conditions, including also rather moist atmospheres (Figure 3a). Despite the overall good model performances, the two single-channel models had a distinct positive bias for dry atmospheres compared to the LSA SAF dataset (0.8–1.2 K *versus* 0.1–0.2 K, respectively; Figure 3a). This single-channel bias is close to zero during nighttime, but is greater than 1 K during daytime (Figure 4). Other studies (e.g., [8]) also report that the largest single-channel biases occur at LST values greater than 310 K, which is in line with our observations. The observed daytime LST bias likely demonstrates the implicit sensitivity of the mono-channel models

on NWP errors. The GSW model, which is less dependent on accurate NWP input, does not show a significant daytime bias in Gobabeb.

3.2.2. Dahra Station

In Dahra, single-channel LSTs reached the LSA SAF target accuracy for TCWV up to 30 mm (RMSD < 2 K, bias < 0.5 K; Figure 3c). For higher TCWVs, the PMW, SMW and GSW models had a high negative Meteosat LST minus *in situ* LST bias (−4.3 K, −3.0 K and −2.2 K, respectively; Table 4, Figure 5). RMSD are significantly higher for PMW and SMW compared to GSW (Δ 2.9 and 1.9 K, respectively; Table 4) and the theoretically-expected error (Δ 3–4 K; Table 4 and Figure 2).

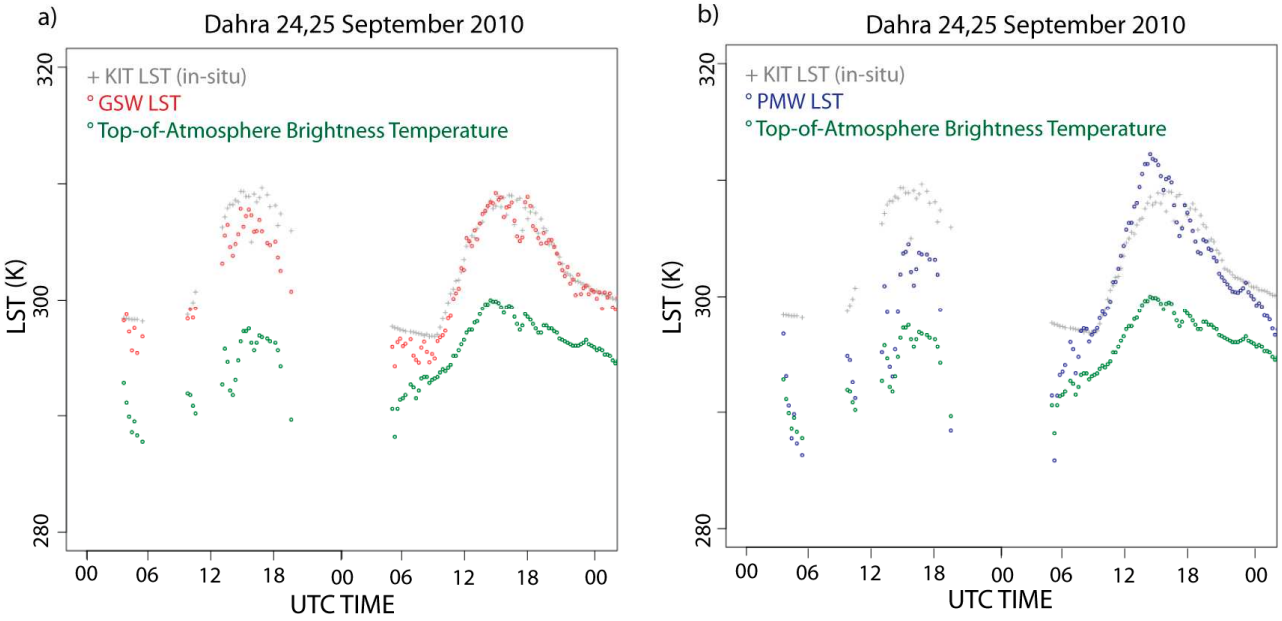

Figure 5. (**a**) LSA SAF's operational GSW; (**b**) PMW.

Cloud contaminations and/or uncertainties in NWP (ECMWF), together with the limitations of the mono-channel methods under analysis, might explain the difference between the observed RMSD and the theoretical uncertainties.

Errors due to cloud contamination are not accounted for in the theoretical uncertainty analysis. Clouds are usually significantly colder than the land surface, and cloud contamination should hence result in negative LST biases [8]. This hypothesis is supported by the high temporal scatter of the TOA-brightness temperature (example: Figure 5, 24 September 2010). Clear sky TOA brightness temperature is mainly driven by solar heating and follows a continuous diurnal cycle [10]. This is clearly not the case on 24 September 2010.

In addition, uncertainties in TCWV fields might be higher in Dahra than the NWP uncertainties accounted for in the sensitivity study (Section 2.5). This second hypothesis is supported by the observed 1–2 K lower GSW bias compared to PMW and SMW (Table 4). As detailed in Section 3.1, GSWs perform atmospheric correction rather independently from the NWP model input, while PMW and SMW are quite sensitive to errors in NWP models. For a given (measured) TOA brightness temperature and a very dry atmospheric profile, which is wrongly assumed to be more moist by the NWP model, this can

lead to a considerable underestimation of LST retrieved by single-channel models: As the true atmosphere becomes dryer, it also becomes more transparent, and the retrieved LST decreases [8]. We have characterized the NWP error in the sensitivity study by replacing the profiles at hour h by the corresponding ones at hour h + 6. This approach might not be valid for tropical conditions. Moreover, differences in viewing geometry between the ground and satellite radiometer can introduce uncertainties related to inaccurate emissivity in Dahra, where the surface emissivities varies strongly over the seasons [20].

3.2.3. RMZ and Evora Stations

The radiative transfer-based single-channel approach (PMW) met LSA SAF target accuracy at the Evora and RMZ sites (RMSD around 2.0 K, bias < 1.0 K; Table 3 and Figure 3b,d).

For Evora, all models, including GSW, had a significant positive bias, while we observed a negative bias for all models at the RMZ station (0.7–1.2 K and −0.5–−0.9 K, respectively; Table 3 and Figure 3b,d). The biases are known from previous validation studies of the operational LSA SAF LST dataset and are given [20] as 0.8 K and −0.4 K for Evora and RMZ, respectively. These biases partially reflect the achievable accuracy with *in situ* LST. These have to represent large-scale satellite footprints covering several square kilometers: although the land cover at the Evora and RMZ validation sites is spatially quite homogeneous [35], they represent a mixture of grass, background soil and trees, which cause shadows and complicate the ground-based LST determination [40]. The negative biases observed for RMZ are thought to be related to the site's high elevation (1360 m a.s.l.), which may not be correctly accounted for by the LST retrieval algorithms. The PMW and SMW do not perform an orographic correction, *i.e.*, we use atmospheric profiles as the model input, which corresponds to the ECMWF grid cell height and not to the elevation at the station.

4. Conclusions

Long-term LST climate data records with a high temporal and spatial resolution are useful for climate monitoring and climate applications [7]. This requirement can be met by extending LST data records from geostationary satellites into the past. Since heritage sensors provide only one thermal infrared band, multi-channel LST retrieval approaches cannot be used. This study thus evaluated the performance of single-channel retrieval models developed for the geostationary Meteosat satellite against *in situ* LST and the GSW-based LSA SAF dataset. The key question that we investigated is to what extent a single-channel LST model can achieve the accuracy of a two channel GSW model.

This comprehensive validation study, which included more than 60,000 *in situ* LST measurements for very different atmospheric conditions, demonstrates that Meteosat-based single-channel LSTs agree with those from GSW to within 0.1–0.5 K and are within or very close to the 2 K target accuracy of the LSA SAF Meteosat LST data, except for very moist atmospheres (TCWV > 45 mm), but with the added benefit that they can be applied across satellite generations. TCWVs above 45 mm primarily occur in tropical and subtropical regions, which are regularly cloud covered and correspond to less than 5% of the MSG disk. We can hence expect the overall majority of MSG single-channel LSTs to meet the 2–3 K "currently achievable performance" defined by the Global Climate Observing System (GCOS) [7].

However, this study also reveals a significant negative bias (−4.3 K) for the PMW for very moist atmospheres (TCWV > 45 mm) at Dahra station, Senegal. We found some indications that cloud

contamination and/or inaccurate NWP input contributes to this strong negative bias. This issue needs to be investigated before generating a CDR.

This study also demonstrates that it is possible to characterize retrieval uncertainties for Meteosat single-channel LST, except for very moist atmospheres, which will simplify, for instance, the assimilation of those data into land surface models. RMSDs estimated from a theoretical, radiative transfer-based sensitivity study matched RMSDs from the ground-based comparison within 0.3–1 K for TCWVs ≤ 45 mm. For very moist atmospheres with TCWV > 45 mm, we observe a distinct higher RMSD (>3 K) compared to the theoretical uncertainties. We found indications that this is partly due to cloud contamination, which is not accounted for in the theoretical error analysis. Moreover, the adapted approach to characterize NWP uncertainties by simply replacing NWP profiles might not be realistic for tropic conditions. More advanced TCWV error characterizations, such as, e.g., an error characterization based on the NWP background error covariance matrix, as proposed by Peres and Camara [41], should be tested. The authors propose to put a "low quality" flag on Meteosat single-channel LST retrievals for TCWV > 45 mm and to inform users that associated LST uncertainties might not be realistic for very moist atmospheres. Additional LST validation stations in very moist climate zones will be highly valuable to find realistic LST model uncertainty for those conditions.

The results of this study suggest that computationally more expensive PMWs do not necessarily outperform SMWs. We observed a distinct higher accuracy (ΔRMSD > 0.2 K) for the PMW compared to SMW only at one at of four validation stations.

Possible improvements of the current PMW and SMW model should be addressed in future studies. The presented single-channel models might be improved by including an orographic correction for the atmospheric profiles and by an improved cloud screening in tropical regions.

The results presented here are strictly only valid for MSG, since the MFG thermal sensor has a slightly different spectral response function, a lower digital quantification and a less accurate absolute radiometric accuracy. Accordingly, the LST retrieval errors may be greater than the errors presented in this study. Inaccuracies arising from emissivity retrieval and satellite calibration were not considered here, despite their relevance for the quality of a Meteosat LST CDR. Therefore, future work needs to investigate these error sources. Although it might be difficult to remove inter-Meteosat calibration errors completely, the present work demonstrates that, for the investigated ground stations, LST retrievals from well-calibrated MFG data can reach the accuracy of LSA SAF's operational GSW.

Acknowledgments

This study was carried out as part of the EUMETSAT Satellite Application Facility on Climate Monitoring (CM SAF) and on Land Surface Analysis (LSA SAF). The Swiss National Supercomputing Centre (CSCS) is acknowledged for providing computing and archiving resources for this project. We want to thank the Karlsruhe Institute of Technology (KIT) for maintaining the LST *in situ* stations and for kindly providing the validation data. Research by Virgílio Bento was funded by the Portuguese Foundation for Science and Technology (SFRH/BD/52559/2014).

Author Contributions

All authors contributed equally to this work. Virgílio A. Bento, Isabel F. Trigo and Carlos da Camara designed the SMW model and the methodology for the sensitivity analysis and error budget estimation. João P.A. Martins performed MODTRAN simulations and designed the calibration database for the SMW model. Folke Olesen and Frank-M. Göttsche derived and provided the KIT validation stations' data. Frank-M. Göttsche is responsible for Section 2.6 and contributed to the interpretation of the results. Jedrzej S. Bojanowski supported the software development and the ground-based validation. Reto Stöckli and Heike Kunz initiated the project and reviewed the paper. Reto Stöckli programmed the Meteosat processing system (pre-processing). Anke Duguay-Tetzlaff established the PMW model, implemented the single-channel LST retrieval models, performed the ground-based validation and compiled the manuscript.

Conflicts of Interest

The authors declare no conflict of interest.

References

1. Bodas-Salcedo, A.; Ringer, M.; Jones, A. Evaluation of the surface radiation budget in the atmospheric component of the Hadley Centre Global Environmental Model (HADGEM1). *J. Clim.* **2008**, *21*, 4723–4748.
2. Wan, Z.; Wang, P.; Li, X. Using MODIS land surface temperature and normalized difference vegetation index products for monitoring drought in the southern Great Plains, USA. *Int. J. Remote Sens.* **2004**, *25*, 61–72.
3. Kustas, W.; Norman, J. Use of remote sensing for evapotranspiration monitoring over land surfaces. *Hydrol. Sci. J.* **1996**, *41*, 495–516.
4. Bosilovich, M.; Radakovich, J.; da Silva, A.; Todling, R.; Verter, F. Skin temperature analysis and bias correction in a coupled land-atmosphere data assimilation system. *J. Meteorol. Soc. Japan* **2007**, *85*, 205–22
5. Reichle, R.; Kumar, S.; Mahanama, S.; Koster, R.; Liu, Q. Assimilation of satellite-derived skin temperature observations into land surface models. *J. Hydrometeorol.* **2010**, *11*, 1103–1122.
6. Ghent, D.; Kaduk, J.; Remedios, J.; Ardo, J.; Balzter, H. Assimilation of land surface temperature into the land surface model JULES with an ensemble Kalman filter. *J. Geophys. Res.-Atmos.* **2010**, *115*, 19–19.
7. GCOS 2011 Report: Systematic Observation Requirements for Satellite-Based Datasets for Climate 2011 Update. Available online: https://www.wmo.int/pages/prog/gcos/Publications/gcos-154.pdf (accessed on 21 May 2015).
8. Heidinger, A.; Laszlo, I.; Molling, C.; Tarpley, D. Using SURFRAD to verify the NOAA single-channel land surface temperature algorithm. *J. Atmos. Ocean. Technol.* **2013**, *30*, 2868–2884.
9. Garand, L. Toward an integrated land-ocean surface skin temperature analysis from the variational assimilation of infrared radiances. *J. Appl. Meteorol.* **2003**, *42*, 570–583.
10. Göttsche, F.; Olesen, F. Modelling the effect of optical thickness on diurnal cycles of land surface temperature. *Remote Sens. Environ.* **2009***, 113*, 2306–2316.

11. Rossow, W.; Schiffer, R. Advances in understanding clouds from ISCCP. *Bull. Am. Meteorol. Soc.* **1999**, *80*, 2261–2287.
12. Freitas, S.; Trigo, I.; Bioucas-Dias, J.; Göttsche, F. Quantifying the uncertainty of land surface temperature retrievals from Seviri/Meteosat. *IEEE Trans. Geos. Remote Sens.* **2010**, *48*, 523–534.
13. Wan, Z.; Dozier, J. A generalized split-window algorithm for retrieving land-surface temperature from space. *IEEE Trans. Geos. Remote Sens.* **1996**, *34*, 892–905.
14. Trigo, I.; Monteiro, I.; Olesen, F.; Kabsch, E. An assessment of remotely sensed land surface temperature. *J. Geophys. Res.-Atmos.* **2008**, *113*, D17.
15. Trigo, I.; Freitas, S.C.; Bioucas-Dias, J.; Barroso, C.; Monteiro, I.T.; Viterbo, P. *Algorithm Theoretical Basis Document for Land Surface Temperature (LST)*, *LSA-4 (MLST)*; Land Surface Analysis Satellite Application Facility: Darmstadt, Germany, 2009.
16. Sun, D.; Pinker, R.; Basara, J. Land surface temperature estimation from the next generation of geostationary operational environmental satellites: GOES M-Q. *J. Appl. Meteorol.* **2004**, *43*, 363–372.
17. Jimenez-Munoz, J.; Sobrino, J. A generalized single-channel method for retrieving land surface temperature from remote sensing data. *J. Geophys. Res.-Atmos.* **2004**, *109*, D22.
18. Reutter, H.; Olesen, F.; Fischer, H. Distribution of the brightness temperature of land surfaces determined from AVHRR data. *Int. J. Remote Sens.* **1994**, *15*, 95–104.
19. Scarino, B.; Minnis, P.; Palikonda, R.; Reichle, R.; Morstad, D.; Yost, C.; Shan, B.; Liu, Q. Retrieving clear-sky surface skin temperature for numerical weather prediction applications from geostationary satellite data. *Remote Sens.* **2013**, *5*, 342–366.
20. Göttsche, F.; Olesen, F.; Bork-Unkelbach, A. Validation of operational land surface temperature products with three years of continuous in-situ measurements. In Proceedings of the EUMETSAT Meteorological Satellite Conference, Oslo, Norway, 5–9 September, 2011.
21. Yu, X.; Guo, X.; Wu, Z. Land surface temperature retrieval from LANDSAT 8 TIRS-comparison between radiative transfer equation-based method, split window algorithm and single channel method. *Remote Sens.* **2014**, *6*, 9829–9852.
22. Freitas, S.; Trigo, I.; Macedo, J.; Barroso, C.; Silva, R.; Perdigao, R. Land surface temperature from multiple geostationary satellites. *Int. J. Remote Sens.* **2013**, *34*, 3051–3068.
23. Göttsche, F.; Olesen, F. Modelling of diurnal cycles of brightness temperature extracted from METEOSAT data. R*emote Sens. Environ.* **2001**, *76*, 337–348.
24. Peres, L.F.; da Camara, C.C. Emissivity maps to retrieve land-surface temperature from MSG/SEVIRI. *IEEE Trans. Geos. Remote Sens.* **2005**, *43*, 1834–1844.
25. Li, Z.-L.; Tang, B.-H.; Wu, H.; Ren, H.; Yan, G.; Wan, Z.; Trigo, I.F.; Sobrino, J.A. Satellite-derived land surface temperature: Current status and perspectives. *Remote Sens. Environ.* **2013**, *131*, 14–37.
26. Trigo, I.; Peres, L.; da Carnara, C.; Freitas, S. Thermal land surface emissivity retrieved from SEVIRI/METEOSAT. *IEEE Trans. Geos. Remote Sens.* **2008**, *46*, 307–315.
27. Saunders, R.; Matricardi, M.; Brunel, P. An improved fast radiative transfer model for assimilation of satellite radiance observations. *Q. J. Royal Meteorol. Soc.* **1999**, *125*, 1407–1425.
28. Berk, A.; Anderson, G.; Acharya, P.; Ghetwynd, J.; Bernstein, L.; Shettle, E.; Matthew M.; Adler-Golden, S. *MODTRAN4 User's Manual*; Air Force Research Laboratory: Hanscom, MA, USA, 1999.

29. Hocking, J.; Rayer, P.J.; Rundle, D.; Saunders R.W.; Matricardi, M.; Geer, A.; Brunel, P.; Vidot, J. *RTTOV v11 Users Guide*; Nowcasting Satellite Application Facility (NWC-SAF): Darmstadt, Germany, 2014.
30. Bento, V. Exploring RTTOV to Retrieve Land Surface Temperature from a Geostationary Satellite Constellation. Master's Thesis, University Lisbon, Lisbon, Portugal, 2013.
31. Dee, D.; Uppala, S.; Simmons, A.; Berrisford, P.; Poli, P.; Kobayashi, S.; Andrae, U.; Balmaseda, M.; Balsamo, G.; Bauer, P.; *et al.* The ERA-Interim reanalysis: Configuration and performance of the data assimilation system. *Q. J. Royal Meteorol. Soc.* **2011**, *137*, 553–597.
32. Borbas, E.E.; Wetzel, S.S.; Huang, H.L.; Li, J. Global profile training database for satellite regression retrievals with estimates of skin temperature and emissivity. In Proceedings of the XIV International ATOVS Study Conference, Beijing, China, 25–31 May 2005; pp. 763–770.
33. Hewison, T.J.; König, M. Inter-calibration of Meteosat imagers and IASI. In Proceedings of the EUMETSAT Meteorological Satellite Conference, Darmstadt, Germany, 8–12 September 2008.
34. Göttsche, F.; Olesen, F.; Bork-Unkelbach, A. Validation of land surface temperature derived from MSG/SEVIRI with *in situ* measurements at Gobabeb, Namibia. *Int. J. Remote Sens.* **2013**, *34*, 3069–3083.
35. Bork-Unkelbach, A. Extrapolation von *in-situ* Landoberflächentemperaturen auf Satellitenpixel. Ph.D. Thesis, Karlsruhe Institute of Technology, Karlsruhe, Germany, 2012.
36. Göttsche, F.; Hulley, G. Validation of six satellite-retrieved land surface emissivity products over two land cover types in a hyper-arid region. *Remote Sens. Environ.* **2012**, *124*, 149–158.
37. Kabsch, E.; Olesen, F.; Prata, F. Initial results of the land surface temperature (LST) validation with the Evora, Portugal ground-truth station measurements. *Int. J. Remote Sens.* **2008**, *29*, 5329–5345.
38. Theocharous, E.; Usadi, E.; Fox, N.P. *CEOS Comparison of IR Brightness Temperature Measurements in Support of Satellite Validation. Part. I: Laboratory and Ocean Surface Temperature Comparison of Radiation Thermometers*; National Physical Laboratory: Teddington, UK, 2010.
39. Kondratyev, K.Y. *Radiation in the Atmosphere*; Academic Press: New York, NY, USA, 1969.
40. Guillevic, P.C.; Bork-Unkelbach, A.; Göttsche, F.M.; Hulley, G.;Gastellu-Etchegorry, J.-P; Olesen, F.S.; Privette, J.L. Directional viewing effects on satellite land surface temperature products over sparse vegetation canopies—A multisensor analysis. *IEEE Geos. Remote Sens. Lett.* **2013**, *10*, 1464–1468.
41. Peres, L.F.; da Camara, C.C. Land surface temperature and emissivity estimation based on the two-temperature method: Sensitivity analysis using simulated MSG/SEVIRI data. *Remote Sens. Environ.* **2004**, *91*, 377–389.